Summer 7-15-2021

Petrology and Geochemistry of Evolved Achondrites: Planetesimal Mantles and Crusts

Zoltan Vaci
University of New Mexico

Zoltan Vaci

Candidate

Earth and Planetary Sciences

Department

This dissertation is approved, and it is acceptable in quality and form for publication:

Approved by the Dissertation Committee:

Carl Agee, Chairperson

Charles Shearer

Horton Newsom

Adrian Brearley

James Day

PETROLOGY AND GEOCHEMISTRY OF EVOLVED ACHONDRITES: PLANETESIMAL MANTLES AND CRUSTS

By

Zoltan Vaci

B.S. Geology, Rutgers University, 2012
M.S. Earth and Planetary Sciences, University of New Mexico, 2017

DISSERTATION

Submitted in partial fulfillment of the requirements for the degree of

Doctor of Philosophy
Earth and Planetary Sciences

The University of New Mexico
Albuquerque, New Mexico

July 2021

ACKNOWLEDGMENTS

I would like to extend my thanks first and foremost to my former master's and current PhD advisor, Carl Agee, who has provided invaluable scientific discussion, advice, academic connections, meteorite samples, and funding for my five years at UNM. Carl is a leader in his field and his direction of the Institute of Meteoritics has yielded incredible breakthroughs in planetary science, some of which I have been privileged to participate in. I am thankful for the Institute for giving me a chance to try my hand at original research and providing the tools I needed to advance in the field.

I am grateful for the scientific support of Chip Shearer, who is my co-advisor on my PhD committee. Chip has an uncanny ability to take a tortuous mess of a PhD project and render it with laser-like focus through an informal discussion of its merits and flaws. This dissertation would not be what it is without his guidance. I am also grateful for weekly discussions with his research group, which included Jim Papike, Aaron Bell, Paul Burger, and Steve Simon. These meetings were where some of our best ideas were produced, and I am thankful the group kept their door open for me. In particular, I would like to thank Aaron Bell for training me to use the gas-mixing furnace lab and always being available for advice and support.

The UNM Earth and Planetary Sciences faculty has provided invaluable support throughout my academic career. I owe thanks to Mike Spilde for training me to use the electron microprobe and keeping our arguably most useful instrument in top working order. I am grateful to Adrian Brearley and Elena Dobrica for their help with transmission electron microscopy and for the scientific discussions they provided. I would also like to thank Karen Ziegler, Zach Sharp, and the rest of the Center for Stable Isotopes for introducing me to stable isotopic analysis of extraterrestrial material. Yemane Asmerom and Victor Polyak were also instrumental to my scientific career by training me and allowing me to use their radiogenic isotope lab.

I am thankful for all of my co-authors and collaborators who have performed analyses and provided excellent scientific discussions during the publication process. These include Munir Humayun, Chris Herd, Erin Walton, Oliver Tschauner, James Day, Matt Heizler, Henner Busemann, Daniela Kreitsch, and Qing-Zhu Yin. I am indebted to a greater scientific community that has never been anything but welcoming, supportive, and insightful.

I could not have made it far in this journey without the support of my friends at UNM and elsewhere: Thanks to The Hoodoos and Friends for providing musical escape from the rigors of academia, thanks to everyone that shared in my river and mountain adventures in New Mexico, thanks to The Squad for being the longest-running group chat and best group of friends I could ask for, and thanks to the people I have lived with these years for putting up with me.

Finally, I thank my mother Agnes who is an unlimited source of emotional support and kindness. Thanks to the rest of my Hungarian family as well for cheering me on. Thanks to my academic support cat Mylar Flannigan for chasing gloom and mice away from my house.

PETROLOGY AND GEOCHEMISTRY OF EVOLVED ACHONDRITES: PLANETESIMAL MANTLES AND CRUSTS

By

ZOLTAN VACI

B.S. Geology, Rutgers University, 2012
M.S. Earth and Planetary Sciences, University of New Mexico, 2017
Ph.D., Earth and Planetary Sciences, University of New Mexico, 2021

ABSTRACT

Melting and differentiation are fundamental to early solar system evolution on planetary bodies that accreted enough material to heat up radioactively or through impacts and breach their solidi. Partially and fully melted material is present in the meteorite record in the form of primitive achondrites and achondrites, which are fragments of planetesimals that underwent heating events in the first few million years of solar system history. Although the vast majority of this material is mafic or ultramafic, new evolved samples, recovered in the last few decades, are pushing the petrologic and geochemical boundaries of planetesimal melting, differentiation, and crust formation. The goal of this study is to analyze the composition and interpret the petrogenesis of some of this newly discovered evolved material, which includes deep crustal or mantle cumulates and evolved crustal basaltic andesites and trachyandesites. The formation conditions of these rocks are debated in a terrestrial setting, and on planetesimals their petrogenesis has until now remained mysterious.

Chapter 1 is a study of the petrology and geochemistry of the dunitic monomict fragmental breccias Northwest Africa (NWA) 12217 and 12562. These rocks represent large

melting events on a unique parent body that resulted in the formation of deep crustal or mantle cumulates. Chapter 2 focuses on evolved planetesimal crustal material by characterizing NWA 6698, an evolved diorite with a cumulate texture. The oxygen isotopic composition of this rock links it to the ureilite parent body, and the potential for the melting and differentiation of this object is explored. Chapter 3 is a project in experimental petrology in which chondritic bulk compositions are melted under varying temperatures and oxygen fugacities at 1 atmosphere of pressure. This is an attempt to explain the unique evolved compositions of these recent meteorite finds relative to their potentially chondritic precursors. Chapter 4 is a review paper providing a synoptic view of Martian magmatism through geologic time via the study of meteorite chronology.

TABLE OF CONTENTS

PREFACE

This dissertation is composed of three chapters and an analytical appendix. Each chapter represents an independent manuscript with its own introduction, methods, results, discussion, conclusions, and references. Thus, some repetition between chapters is inevitable. Each chapter has several co-authors whose contributions include analytical measurements and scientific discussions. The majority of the analytical work was done by me and as such I will be the first author of the publications that manifest from these manuscripts.

Chapter 1 focuses on the mineralogy, petrology, and geochemistry of three monomict fragmental dunitic breccias, NWA 12217, 12319, and 12562. These meteorites have oxygen isotopic compositions akin to the HED meteorites, brachinites, and angrites, but their olivine abundance and chemistry sets them apart as likely belonging to Vesta or an unknown differentiated parent body. These unique samples are important pieces of the puzzle that is "The Great Dunite Shortage" (Chapman 1986) or the "Missing Mantle Problem" (Burbine et al. 1996), the apparent paucity of olivine-rich material among asteroids and in the meteorite record. The microanalytical data was gathered by me at UNM and presented at the 2019 Lunar and Planetary Science Conference (LPSC) (Vaci et al. 2019a) and the 2019 Annual Meeting of the Meteoritical Society (MetSoc) (Vaci et al. 2019b). Oxygen isotopic composition was analyzed by Karen Ziegler and included in the 2019 abstracts. Trace element compositions were measured by James Day and Marine Paquet at Scripps Institution of Oceanography and was submitted as an abstract to LPSC 2020. Chromium isotopic compositions were measured by Qing-zhu Yin at the Department of Earth and Planetary Sciences at the University of California, Davis. The manuscript this chapter is based on has been accepted by *Nature Communications*.

Chapter 2 is a study of the mineralogy, petrology, and geochemistry of NWA 6698, a diorite with oxygen isotopes similar to carbonaceous chondrites, ureilites, and the trachyandesite ALM-A. This highly evolved meteorite is the second complete rock that samples the partial melting of a chondritic protolith that formed the ureilites as residues on the ureilite parent body (Bischoff et al. 2014; Barrat et al. 2016). Initially, this diorite was thought to be associated with the ordinary chondrites, and thus it was included in a study on magmatism among ordinary chondrite-like material which was presented by me at LPSC 2018 (Vaci et al. 2018). I gathered additional microanalytical data on NWA 6698 at UNM, as well as trace element data under the supervision of Munir Humayun at the National Magnetic Lab, Florida State University. This was submitted as an abstract to LPSC 2020 and presented at LPSC 2021 (Vaci et al. 2021).

Chapter 3 is a departure from the study of natural samples and presents an experimental investigation into the melting and differentiation of chondritic material. This study draws from earlier melting experiments (Jurewicz et al. 1993, 1995; Usui et al. 2015) and attempts to expand their scope by incorporating alkalis and lower oxygen fugacities to produce more evolved run products. All experiments were performed by me at the UNM gas mixing lab in a 1-atmosphere furnace, and I analyzed the run products using the electron microprobe and scanning electron microscope at UNM. Aaron Bell and Chip Shearer provided the laboratory expertise and research insight necessary for this project.

Chapter 4 is a review paper on martian chronology derived from meteorites, published in the journal *Geosciences.* I provide a synoptic view of the history of the planet derived from meteorite geochemistry, including modelling of accretion, core formation, and differentiation timescales, the earliest evolved magmatism gleaned from the martian crustal breccia NWA 7034, and the ongoing volcanism as sampled by the shergottites, nakhlites, and chassignites (SNC).

References

Barrat J. A., Jambon A., Yamaguchi A., Bischoff A., Rouget M. L., and Liorzou C. 2016. Partial melting of a C-rich asteroid: Lithophile trace elements in ureilites. Geochimica et Cosmochimica Acta 194:163–178.

Bischoff A., Horstmann M., Barrat J.-A., Chaussidon M., Pack A., Herwartz D., Ward D., Vollmer C., and Decker S. 2014. Trachyandesitic volcanism in the early Solar System. Proceedings of the National Academy of Sciences 111:12689–12692. http://www.pnas.org/cgi/doi/10.1073/pnas.1404799111.

Burbine T. H., Meibom A., and Binzel R. P. 1996. Mantle material in the main belt: Battered to bits? Meteoritics and Planetary Science 31:607–620.

Chapman C. R. 1986. Implications of the inferred compositions of asteroids for their collisional evolution. Mem. Soc. Astron. Italiana 57:103–114.

Jurewicz A. J. G., Mittlefehldt D. W., and Jones J. H. 1993. Experimental partial melting of the Allende (CV) and Murchison (CM) chondrites and the origin of asteroidal basalts. Geochimica et Cosmochimica Acta 57:2123–2139.

Jurewicz A. J. G., Mittlefehldt D. W., and Jones J. H. 1995. Experimental partial melting of the St. Severin (LL) and Lost City (H) chondrites. Geochimica et Cosmochimica Acta 59:391–408.

Usui T., Jones J. H., and Mittlefehldt D. W. 2015. A partial melting study of an ordinary (H) chondrite composition with application to the unique achondrite Graves Nunataks 06128 and 06129. Meteoritics and Planetary Science 50:759–781.

Vaci Z., Agee C. B., Ziegler K., and Heizler M. T. 2018. Magmatic Evolution Trends Within the Ungrouped Achondrite Meteorite Record. 49th Lunar and Planetary Science Conference Abstract #1256. http://www.lpi.usra.edu/meetings/lpsc2018/pdf/1256.pdf.

Vaci Z., Agee C. B., and Ziegler K. 2019a. Unique Dunite Breccia Northwest Africa 12217: Mineralogy, Petrology, and Oxygen Isotopes. 50th Lunar and Planetary Science Conference Abstract #1175. http://www.lpi.usra.edu/meetings/lpsc2019/pdf/1175.pdf.

Vaci Z., Agee C. B., and Ziegler K. 2019b. Dunite breccias Northwest Africa 12217, 12562: Possible planetesimal mantles. In MetSoc 82. p. 6459.

Vaci Z., Yang S., Humayun M., and Agee C. B. 2021. Northwest Africa 6698: Partial melt of the ureilite parent body. Lunar and Planetary Science Conference LII 52.

CHAPTER 1

Olivine-rich achondrites and the missing mantle problem in the asteroid belt

Abstract

Seismic data of Earth's interior, the mineralogy of natural samples, and modelling results confirm that the mantles of rocky planets are dominantly composed of olivine and its high-pressure polymorphs (Ringwood 1975; McDonough and Sun 1995). Dunites are rocks consisting of >90% olivine. The missing mantle problem represents the paucity of olivine-rich material among meteorite samples and remote observation of asteroids, given the ubiquity of differentiated planetesimals in the early Solar System (Bell et al. 1989; Burbine et al. 1996). Here we report the discovery of new olivine-rich meteorites that have asteroidal origins and are related to V-type asteroids or vestoids. Northwest Africa 12217, 12319, and 12562 are dunites and lherzolite cumulates that have siderophile element abundances consistent with origins on highly differentiated asteroidal bodies that experienced core formation, and with trace element, oxygen isotopic, and chromium isotopic compositions associated with the isotopically anomalous howardite-eucrite-diogenite (HED) meteorites and the isotope-anomalous eucrites. These meteorites mark an end to the shortage of olivine-rich material, allowing for full examination of differentiation processes acting on planetesimals in the earliest epoch of the Solar System.

1. Introduction

The mantle compositions of terrestrial planets are well constrained compared with those of small bodies and asteroids, although it is widely held that differentiated planets with metallic cores also have olivine-dominated silicate mantles. For example, the asteroid 4 Vesta, though

only about 500 km in diameter, is suggested to have undergone core formation and differentiation to form an olivine-rich mantle during a magma ocean phase (Ikeda and Takeda 1985; Righter and Drake 1997; Mandler and Elkins-Tanton 2013), through partial melting (Stolper 1975, 1977; Jones 1984), or through serial magmatism and fractional crystallization (Shearer et al. 1997; Beck and McSween 2010). If differentiated bodies were ubiquitous throughout the early Solar System, as planetesimal accretion theory suggests (Hevey and Sanders 2006; Weiss and Elkins-Tanton 2013), then olivine-rich asteroid interiors, and meteorite samples of them, should be quite common.

Based on the currently available meteorites and remote sensing of bodies in the asteroid belt, olivine-rich asteroid materials appear to be remarkably sparse, implying a 'missing mantle problem' (Bell et al. 1989). Notably, the diversity of iron meteorite types suggests the presence of at least 50 different parent bodies with iron cores and complementary olivine-dominated mantles not observed by remote sensing (Goldstein et al. 2009). In the asteroid belt, objects with spectral signatures suggesting that their compositions are olivine-rich (>80%) are classified as A-type asteroids (Cruikshank and Hartmann 1984), and these account for less than 0.16% of all objects larger than 2 km (DeMeo et al. 2019). In the meteorite record, diogenites, thought to represent deep crustal cumulate material from Vesta, are mostly orthopyroxenites with under 40 vol% olivine(Mittlefehldt 2015), and only small clasts of dunite have thus far been identified in a mesosiderite breccia (Beck et al. 2011). Other olivine-rich asteroid-derived rocks include the brachinites, brachinite-like achondrites, and ureilites. The brachinites and brachinite-like achondrites contain 68-95 modal% olivine, which is somewhat ferroan (Fo_{64-74}) (Day et al. 2012a, 2019). Their nearly chondritic trace element compositions indicate that they are dominantly residues formed by partial melt extraction from a chondritic source(Day et al. 2012a;

Gardner-Vandy et al. 2013), with some meteorites (ALH 84025, Brachina, EET 99402/99407, and Eagles Nest) possibly representing cumulates (Warren and Kallemeyn 1989; Swindle et al. 1998; Mittlefehldt et al. 2003). Ureilites are also primitive achondrites that are likely to represent samples from a planetary mantle that was catastrophically disrupted before it could fully differentiate (Goodrich et al. 2015). They range in composition from dunite to peridotite (olivine Fo_{74-97}) (Brugier et al. 2019), but like brachinites and brachinite-like achondrites, they are not from a fully differentiated asteroid.

Several hypotheses have been put forward to explain the apparently low abundance of olivine-rich mantle material in the Solar System. The most obvious of these is that olivine-rich material is not easily detected in the asteroid belt, and there have not been enough impacts involving this undetected material to bring samples of it to Earth. Such a biasing could be due to space weathering, which could darken the spectra of A-type asteroids and obscure them from optical observation (Pieters et al. 1993; Clark et al. 2003), or to catastrophic impacts that have systematically destroyed olivine-rich planetary mantles in the early Solar System (Burbine et al. 1996). Dynamical modelling demonstrates that large impacts primarily occurred in the final stages of planetesimal accretion and were capable of stripping away the silicate portions of early planets, leaving behind Fe-rich cores (Asphaug 2017). The disrupted mantle material from these 'stripping' events must then be removed from the accretion disc, presumably by being incorporated into the terrestrial planets or falling into the Sun. Such a scenario cannot account for the largest asteroids Vesta or Ceres, which retain plentiful silicate materials (Russell et al. 2012, 2016).

The paucity of olivine-rich material is potentially due to collisional transport processes. Recent asteroid surveys have concluded that there are no olivine-rich bodies in the asteroid belt

above ~2 km in size other than A-type asteroids (DeMeo et al. 2019), and therefore, there is no statistically significant evidence for widespread differentiation into Fe-rich cores, olivine-rich mantles, and basaltic crusts in the asteroid belt (Bottke et al. 2006). The distribution of the A-type asteroids instead supports differentiation of planetesimals in the inner Solar System, where the abundance of aluminum-26 allowed for early enhanced melting of these bodies, followed by later migration and implantation into the asteroid belt. The Nice (Tsiganis et al. 2005) and Grand Tack (Walsh et al. 2011) models provided dynamical explanations for such early disruptions through large-scale orbital excitations, migrations and ejections in the early solar system. Later models (Turrini et al. 2012; Raymond and Izidoro 2017) have suggested that the in-situ formation of Jupiter was enough to trigger widespread orbital instabilities in the asteroid belt necessary for both the collisional erosion of early planetesimals and their migration to different parts of the Solar System.

Here we reevaluate the missing mantle problem in light of the discovery of the olivine-rich ultramafic achondrite meteorites Northwest Africa (NWA) 12217, 12319, and 12562. These samples contain abundant Mg-rich olivine, are consistent with a cumulate origin, and probably represent materials similar to Vesta or the vestoids.

2. Samples and Methods

Northwest Africa 12217 was purchased by Jay Piatek in 2015 from a Moroccan meteorite dealer, and a 20.7 g deposit sample resides at the University of New Mexico (UNM). Northwest Africa 12319 was discovered in 2018 as thirteen fragments and splinters totaling 35.3 g, and it was sold by a meteorite dealer in Agadir, Morocco, to Alan Mazur in July 2018. Deposit samples reside at the Universities of Kiel (5.07 g) and Münster (1.05 g). Northwest Africa 12562 was

found in Algeria in 2017 as a single 3930 g stone, and it was purchased by Zuokai Ke in May 2018 in Chenzhou, China. A 21 g deposit sample resides at the University of New Mexico. Fragments from the deposit samples of NWA 12217 and 12562 were mounted in epoxy and polished to 0.05 μm smoothness. Thin sections were also produced from fragments of NWA 12217 and 12319 (BC2920.2). These samples were analyzed by optical microscopy, electron probe microanalysis (EPMA), and scanning electron microscopy (SEM) at the Institute of Meteoritics, UNM, Albuquerque, NM (NWA 12217, 12319, and 12562) and the Institut für Geowissenschaften, Christian-Albrechts-Universität in Kiel, Germany (NWA 12319).

Several fragments from deposit samples of NWA 12217 and 12562 were mounted in epoxy and polished to 0.05 μm smoothness. Two polished thin sections were also produced from fragments of NWA 12217 and 12319 (BC2920.2). These samples were analyzed by optical microscopy, electron probe microanalysis (EPMA), and scanning electron microscopy (SEM) at the Institute of Meteoritics, UNM, Albuquerque, NM (NWA 12217, 12319, and 12562) and the Institut für Geowissenschaften, Christian-Albrechts-Universität in Kiel, Germany (NWA 12319).

Six fresh fragments of interior materials of NWA 12217 and NWA 12562, weighing between 1-2 mg, were selected using a stereomicroscope to avoid any possible contamination from fusion crust. Oxygen isotopic analyses were performed using a CO_2 laser + BrF_5 fluorination system following modified procedures outlined in Sharp (1990). The analyses in Göttingen were performed following the protocol described in Pack et al. (2016) and Peters et al. (2020), and details regarding the UNM technique are given in Wostbrock et al. (2020). Oxygen isotope compositions were calculated using the following procedure: the $\delta^{17,18}O$ values refer to the per mil deviation of a sample's ($^{17}O/^{16}O$) and ($^{18}O/^{16}O$) ratios from the V-SMOW standard values, respectively, expressed as $\delta^{17,18}O = [(^{17,18}O/^{16}O)_{sample}/(^{17,18}O/^{16}O)_{V\text{-}SMOW} - 1]*10^3$. The

delta values were then converted to logarithmic δ′ in which $\delta^{17,18}O' = \ln(\delta^{17,18}O/1000 + 1)*1000$. The $\Delta^{17}O'$ values were obtained from the δ′ values following $\Delta^{17}O' = \delta^{17}O' - 0.528 * \delta^{18}O'$. Typical analytical precision of the laser-fluorination technique is better than ± 0.02‰ for $\Delta^{17}O'$.

Whole-rock fragments of all three meteorites were partially disaggregated to obtain small chips that were subsequently crushed with limited force in an agate mortar and pestle to make a partially representative (~0.3 g) whole-rock powder for each sub-fragment. Bulk rock major- and trace-element abundances were determined at the *Scripps Isotope Geochemistry Laboratory (SIGL)* on sample powders by digestion in sealed Teflon vessels at 140°C in Optima grade concentrated HF and HNO_3 (4:1V/V) for >72 hours on a hot plate, along with total analytical blanks and terrestrial basalt standards. Samples were sequentially dried and taken up in concentrated HNO_3 to remove fluorides, followed by dilution and doping with indium to monitor instrumental drift during analysis. Major- and trace-element abundance analyses were obtained using a *ThermoScientific* iCAP Qc quadrupole inductively coupled plasma mass spectrometer in normal mode. Reference materials were analyzed as "unknowns" (BIR-1, BHVO-2, HARZ-01, and BCR-2) to assess external reproducibility and accuracy (see also Day et al. 2015). For major and trace elements, reproducibility of reference materials was better than 5% (RSD).

Osmium isotope and HSE abundance analyses were performed at the SIGL using methods described in Day et al. (2016a). Homogenized powder aliquots of the samples and total procedural blanks were digested in sealed borosilicate Carius tubes, with isotopically enriched multi-element spikes (^{99}Ru, ^{106}Pd, ^{185}Re, ^{190}Os, ^{191}Ir, ^{194}Pt), and 6 mL of a 1:2 mixture of multiply Teflon distilled HCl and HNO_3 that was treated with H_2O_2 to expunge Os. Samples were digested to a maximum temperature of 270˚C in an oven for 72 hours. Osmium was triply extracted from the acid using CCl_4 and then back-extracted into HBr, prior to purification by

micro-distillation that was performed twice. Rhenium and the other HSE were recovered and purified from the residual solutions using standard anion exchange separation techniques. Isotopic compositions of Os were measured in negative-ion mode on a *ThermoScientific* Triton thermal ionization mass spectrometer at the SIGL. Rhenium, Pd, Pt, Ru and Ir were measured using a *Cetac* Aridus II desolvating nebulizer coupled to a *ThermoScientific* iCAP q ICP-MS. Offline corrections for Os involved an oxide correction, an iterative fractionation correction using $^{192}Os/^{188}Os = 3.08271$, a ^{190}Os spike subtraction, and finally, an Os blank subtraction. Precision for $^{187}Os/^{188}Os$, determined by repeated measurement of the UMCP Johnson-Matthey standard was better than ±0.2% (2 St. Dev.; 0.11390 ±20; n = 5). Measured Re, Pd, Pt, Ru, and Ir isotopic ratios for sample solutions were corrected for mass fractionation using the deviation of the standard average run of the day over the natural ratio for the element. External reproducibility on HSE analyses was better than 0.5% for 0.5 ppb solutions and all reported values are blank corrected. The total analytical blank run with samples had $^{187}Os/^{188}Os = 0.177 \pm 0.02$, with quantities (in picograms) of 0.9 [Re], 1.9 [Pd], 1.4 [Pt], 2.1 [Ru], 1.2 [Ir] and 0.3 [Os]. Blank contributions represent <10% in NWA 12562, but >40% for Re, Pd, Pt and Ru for NWA 12217. We measured NWA 12217 and NWA 12562 in duplicate and NWA 12319 once during the course of this study.

An interior fusion-crust free chip of each sample was ground to a powder using an agate mortar and pestle. For dissolution, an aliquot (~15 mg) of the whole-rock powder was placed into a PTFE capsule with a 3:1 mixture of concentrated HF:HNO_3 that was sealed in a stainless-steel Parr bomb jacket. The Parr bomb was heated at 190°C for 96 hours in an oven. After complete dissolution, the sample was processed through a 3-column chemistry extraction procedure to separate Cr from all other matrix elements(Yamakawa et al. 2009). The purified Cr

fractions were loaded onto outgassed W filaments (the total Cr load split among four filaments) and each set of sample filaments bracketed with two filaments loaded with a similar amount of terrestrial Cr standard (NIST SRM 979) before and after. The Cr isotopic composition was measured at UC Davis using a Thermo Triton Plus thermal ionization mass spectrometer (Sanborn et al. 2019). Each filament analysis consisted of 1,200 ratios with 8 s integrations times. A gain calibration was made at the beginning of each filament, the baseline was measured, and the amplifiers were rotated between each block of 25 ratios. The mass fractionation was corrected using an exponential law and a $^{50}Cr/^{52}Cr$ ratio of 0.051859 (Shields et al. 1966). The $^{53}Cr/^{52}Cr$ and $^{54}Cr/^{52}Cr$ ratios are expressed in ε-notation (that is, parts per 10,000 deviation from the NIST SRM 979 Cr standard).

3. Results

3.1 Mineralogy and Petrology

The NWA 12217, 12319, and 12562 meteorites are monomict fragmental breccias predominantly composed of olivine fragments up to 1 cm in size that appear cream-colored to light green in hand sample (Fig. 1A). All three breccia assemblages are crosscut by dark veins. Dunite NWA 12217 is composed of 93 modal% olivine, 4 modal% low and high-Ca pyroxene, minor chromite, FeNi metal, andesine plagioclase, Fe-sulfide, merrillite, and trace alkali feldspar and silica, whereas lherzolites NWA 12319 and NWA 12562 have lesser olivine (85-87 modal%) and higher abundances of low and high-Ca pyroxene (9-11 modal%), and minor chromite, FeNi metal, and plagioclase. Northwest Africa 12319 is also notable for having 3 modal% sulfide. The dark veins identified in all three meteorites are composed of variable amounts of sulfide, chromite, and pyroxene, as well as ubiquitous vermicular symplectites composed of chromite

and both low and high-Ca pyroxene. These symplectites appear both as inclusions within veins and on their own. The veins and symplectites are found both along grain boundaries and fully enclosed within olivine grains. Despite being brecciated, all three rocks lack "matrix" material.

All three meteorites have olivine grains and fragments that are forsteritic and contain low CaO (average of 0.06 ±0.04 wt.%) and Cr_2O_3 (average of 0.07 ± 0.05 wt.%) relative to olivine in other primitive achondrites (Goodrich et al. 2017). Olivine compositions are generally more variable in the lherzolites NWA 12319 (Fo_{77-91}) and NWA 12562 (Fo_{73-92}) than in the dunite NWA 12217 (Fo_{86-93}). Pyroxene compositions show similar variability in NWA 12217 (Fs_{3-48}, Wo_{1-43}), NWA 12319 (Fs_{9-46}, Wo_{2-44}), and NWA 12562 (Fs_{14-56}, Wo_{2-37}) (Fig. 2). These phases do not show zonation in major or minor element composition. Feldspar is a minor (<1 vol%) but ubiquitous phase in NWA 12217, 12319, and 12562, and is evenly distributed as brecciated fragments in the lherzolites. Feldspar-bearing fragments are often associated with high-SiO_2 (>70 wt.%) phases or pure silica. In the dunite NWA 12217, feldspar also occurs as small (~200-300 μm) inclusions within olivine, surrounded by radiating fractures, with compositions ranging from andesine to oligoclase to potassium feldspar (Fig. 3 and 4). No potassium feldspar was identified in NWA 12562 or NWA 12319, but a small high-silica (95 wt.%) glassy inclusion was identified in NWA 12562 with 1 wt.% K_2O. Chromite compositions in all three meteorites show a range in Al_2O_3 content up to 25 wt.%. Iron-nickel metal in the meteorites ranges in Ni content between 6 and 40 wt.%, with Ni/Co between 2 and 192. Chemical zonation is not observed in any of the major or minor phases such that variation in composition is attributed to differences between individual grains. A summary of microprobe measurements is shown in Table 1.

3.2 Oxygen and Chromium Isotopes

The ultramafic achondrites NWA 12319 and 12562 overlap in oxygen isotope composition as to be virtually indistinguishable, while NWA 12217 is somewhat heavier in ^{17}O (overall $\delta^{17}O' = 1.62$ to 1.88; $\delta^{18}O' = 3.48$ to 3.87; $\Delta^{17}O' = -0.230$ to -0.136) (Fig. 1B). The chromium isotopic composition of the ultramafic achondrites ranges from $\varepsilon^{54}Cr = -0.26\pm0.08$ for NWA 12217 to $+0.02\pm0.13$ for NWA 12319, while NWA 12319 and 12562 overlap within error (Fig. 5). The coupled $\Delta^{17}O$ and $\varepsilon^{54}Cr$ systematics of the three meteorites plot outside of the main group normal HED meteorites (Fig. 5B/D). While NWA 12217 plots in the vicinity of the oxygen- and chromium-anomalous eucrites (Scott et al. 2009), between Bunburra Rockhole, Asuka 881394, Pasamonte, and Pecora Escarpment 91007 (Sanborn and Yin 2014; Sanborn et al. 2016; Benedix et al. 2017; Wimpenny et al. 2019), NWA 12319 and 12562 plot in a region of non-carbonaceous inner solar system materials where no previous samples have plotted (Fig. 5A/B). Mixing normal HED material with any known chondrite groups cannot explain the coupled chromium-oxygen isotopic compositions of these olivine-rich achondrites (Fig. 5C/D).

The isotopic compositions of the anomalous eucrites argue for multiple parent body origins of basaltic meteorites, and these new samples suggest the same for their ultramafic counterparts. Additionally, while the oxygen isotope data potentially contain enough data points to be representative of these heterogeneous breccias, the chromium isotopic data could be influenced by the diversity in phases hosting Cr. By mass balance, only ~30% of the Cr budget in the ultramafic achondrites is derived from major phases, while the rest resides in chromite grains, chromite-rich veins, and symplectites (discussed below), whose origin is potentially exogenous to the rock.

3.3 Trace Element Compositions and Re/Os

Bulk major, minor, and trace element abundances for NWA 12217, 12319, and 12562 reflect the dominance of olivine, in conjunction with a minor feldspar component. Dunite NWA 12217 has a Mg# [molar Mg/(Mg+Fe)] of 91, higher than lherzolites NWA 12319 and NWA 12562 (Mg# = 85 and 83 respectively). The incompatible trace element (ITE) compositions of NWA 12217, 12319, and 12562 are nearly identical in relative abundances (Fig. 6A). The patterns of NWA 12217 and 12562 contain slight enrichments in the light REE but otherwise are almost flat relative to CI chondrites. The variability in the ITE in brachinites makes meaningful comparison with the ultramafic achondrites difficult. The diogenites, by contrast, show similar trends in ITE depletions to NWA 12217, 12319, and 12562.

Highly siderophile element (HSE) concentrations in NWA 12217, 12319, and 12562 are shown in Figure 6B along with those of the brachinites, diogenites, and bulk silicate Earth and Mars. Abundances of HSE are generally low (<0.002×CI chondrite) with the exceptions of Pd and Re in NWA 12562. All three meteorites have HSE abundances in the intermediate range of the diogenites, with some heterogeneity among aliquots. The osmium isotopic compositions of all three meteorites are almost identical. However, their $^{187}Re/^{188}Os$ ratios vary significantly with four aliquots lying close to a 4.5 Ga Solar System isochron (Fig. 7) whereas one fragment of NWA 12562 has experienced significant Re gain. This combined evidence suggests that the high Re in aliquots of NWA 12562 represent addition from terrestrial weathering, and that the HSE in NWA 12217, 12319, and 12562 are in chondritic-relative abundances. While terrestrial disturbance of Re in meteorites is well documented, disturbance in Pd, especially to the degree noted in NWA 12562, is not (Day et al. 2016). The meteorite also has elevated abundances of Ni, Co, Cu, and Pb, consistent with preferential sampling of monosulfide solid solution (MSS)-rich

fractions. As veins containing sulfide are found throughout each meteorite (Fig. 8), the elevated Pd in NWA 12562 is consistent with MSS injection as veins within the olivine cumulate. It is not currently possible to determine whether this process occurred immediately after petrogenesis or later, as the Re/Os disturbance in the meteorite must be assumed to result from weathering and rusting of sulfides and metals. Not including the additions to NWA 12562, the total measured HSE abundances of all three meteorites are between 1 and 4 ppb, and this is lower than in terrestrial peridotites(Day et al. 2016) and much lower than in brachinites and brachinite-like achondrites(Day et al. 2012a, 2019).

3.5 Symplectites, veins, and shock features

Northwest Africa 12217, 12319, and 12562 contain symplectites composed of chromite, low-Ca pyroxene, and high-Ca pyroxene (Fig. 9 and 10). They occur along grain boundaries, between olivine grains and between olivine and pyroxene grains, as well as inclusions within olivine grains. Their distribution is not associated with any particular phase in either meteorite. The symplectites consist of vermicular chromite lathes of varying thickness that crosscut pyroxene grains. The chromite veins appear zoned in Cr X-ray maps (Fig. 10), but this zonation could be an artifact of the electron beam overlap with other phases, since the scale of chemical heterogeneity within the symplectites is likely smaller than the electron interaction volume. Low-Ca pyroxene associated with symplectites is more magnesian (En_{90}) than pyroxene that is found as a major phase. High-Ca pyroxene within symplectites is variable in modal abundance as well as in Ca content. The averaged bulk composition in wt.% using X-ray map data of three of these symplectites is as follows: SiO_2=37.36±4.54, MgO=22.23±3.52, Cr_2O_3=16.63±6.19,

FeO=10.82±3.02, CaO=4.64±2.71. The high variance in the data reflect the μm-scale chemical heterogeneity in the symplectites.

Dark veins that crosscut major phases are visible in hand sample and from optical microscopy in NWA 12217, 12319, and 12562. These veins sometimes show symplectic textures and are always multi-phased. Chromite is always present in the veins, with variable amounts of sulfide and low- and high-Ca pyroxene (Fig. 8). The veins are not shock features, as several are observed to be crosscut by fractures. Planar fracturing is ubiquitous among major phases as a characteristic shock feature. In cross-polarized light (XPL), olivine grains in NWA 12217 exhibit undulose extinction indicative of shock (Fig. 11). Dark interstitial areas that appear in hand-sample to be fine grained "matrix" material are not evident in optical or electron imagery. Instead, these dark areas appear to be shock-mosaicized areas of olivine grains under optical microscopy (Fig. 11). As these areas are purely crystallographic features, they do not appear in BSE imagery (Fig. 12). Despite the significant shock that these rocks have undergone, there are no shock-melt veins or pockets in either meteorite, and none of the feldspar grains have been transformed to glassy maskelynite. The planar fractures and mosaicism in olivine grains record a maximum shock pressure of 60-65 GPa (Stöffler et al. 2018). However, given the lack of any partial melt veins or pockets, the shock pressures that these meteorites experienced are likely a great deal lower.

4.0 Discussion

4.1 Petrogenesis and Parent Body Origin

The oxygen isotopic compositions of NWA 12217, 12319, and 12562 suggest affinities with the angrites, brachinites, and brachinite-like achondrites (BLA) (Fig. 1B). However, other

aspects rule out association with these groups. The angrites in general appear to be more oxidized than NWA 12217, 12319, and 12562, with analytical and experimental studies suggesting that they crystallized well above the iron-wüstite (IW) buffer (Jurewicz et al. 1993; Keil 2012). The olivine compositions and the presence of Fe-metal in these new meteorites suggest that they were formed in a more reducing environment. A single dunitic angrite, NWA 8535, has been identified(Santos et al. 2016), and though it also contains Mg-rich olivine (Fo_{70-88}), its olivine Fe/Mn is ~90, more than twice that of the new ultramafic achondrites. Its composition is typical of plutonic angrites and angrites in general, which have superchondritic Ca/Al and higher amounts of Cr_2O_3 in their olivines than these new meteorites. Also, these ultramafic meteorites are clearly separated from the angrite field in $\Delta^{17}O$-$\varepsilon^{54}Cr$ systematics (Fig. 5B). It is therefore unlikely that NWA 12217, 12319, or 12562 bear affinity to the angrite parent body.

The brachinites and BLA are the most obvious analogues to the ultramafic achondrites because they are dunites and peridotites. However, they are geochemically distinct in that their range in forsterite content and trace element abundances is much more variable. Olivine CaO and Cr_2O_3 content of brachinites is more variable and in general higher than in the ultramafic achondrites (Fig. 13). As shown in $\Delta^{17}O$-$\varepsilon^{54}Cr$ systematics, brachinites and BLA are distinct from the three ultramafic achondrites (Fig. 5B), suggesting the two lithologies are unlikely to be of common origin. The ITE and HSE abundances of brachinites are also highly variable, likely due to their origin as residues of partial melting on a parent body that never fully differentiated (Day et al. 2012a, 2015; Keil 2014; Goodrich et al. 2017). The HSE abundances of the ultramafic achondrites plot well below those of the brachinites and BLA, effectively ruling out association with those meteorites and any other primitive achondrites that form as residues of low degrees of

partial melting. This distinction is also evident when comparing Fe/Mn versus Fe/Mg (Fig. 14). In a reducing environment, a residue of partial melting produces a linear trend with a near-constant, chondritic Mn/Mg ratio, while a cumulate produced by fractional crystallization results in a range of Fe/Mg with constant Fe/Mn (Goodrich and Righter 2000; Goodrich et al. 2017). The ultramafic achondrites show a constant Fe/Mn ratio and a range of Fe/Mg, as would be expected for cumulate rocks, while many of the primitive achondrites, including brachinites and BLA, show the constant Mn/Mg ratios expected for residues of partial melting.

The ultramafic achondrites are most similar geochemically to diogenites and the Mg-rich harzburgites found as clasts in howardites (Hahn et al. 2018). Low olivine CaO and Cr_2O_3 contents and the low variance in analyses from all three rocks are similar to those reported for the HED clan (Mittlefehldt 2015) (Fig. 13). Olivine from the HED meteorites and Mg-rich harzburgites, like the ultramafic achondrites, show a constant Fe/Mn ratio and variable Fe/Mg. In particular, the Mg-rich harzburgites overlap with NWA 12562 and 12319, with the latter showing significantly more spread in Fe/Mg. Because the ultramafic achondrites are breccias, this greater variability is likely due to impact sampling and mixing of fragments from a large differentiated protolith.

The similar shape of the REE patterns of NWA 12217 and 12562 strongly suggests that they were formed by similar processes, while the bulk abundance differences are likely an artifact of brecciation processes that led to variance in modal pyroxene abundance. While the eucrites and diogenites, as crustal rocks, show LREE enrichments relative to the HREE (Mittlefehldt 2015), residues of partial melting are expected to have LREE/HREE < 1 (Frey 1984). Instead, NWA 12217 and 12562 show enrichments in the LREE relative to the HREE, suggesting different formation conditions such as accumulation in a fractionating magmatic

assemblage within a region of magma storage in their parent body. Although LREE enrichment is also possible through incorporation of crustal material during brecciation or metasomatism, we regard crustal incorporation as unlikely because both meteorites appear to be monomict breccias with no evidence of contamination by a different lithology. NWA 12319 contains three times as much P_2O_5 as the other two rocks, so it is possible that its flat REE pattern is a result of more contributions to its REE budget from phosphates, or potentially a trapped melt component, relative to pyroxenes.

Importantly, the HED meteorites show up to five orders of magnitude of variations in HSE concentrations (Day et al. 2016), so this metric alone is not sufficient to establish a relationship of the ultramafic achondrites to the diogenites. However, in combination with other lines of evidence discussed above, it rules out association with other olivine-rich planetary material. NWA 12217, 12319, and 12562 have broadly chondritic HSE patterns that are found in all planetary bodies that experienced core-mantle differentiation (Day et al. 2016). This implies that they originate from bodies that experienced core formation events and whose mantles were later enriched in HSE from late accretion of chondritic material. Their similarity to diogenites and Mg-rich harzburgites suggests that these parent bodies are sampled by V-type asteroids or vestoids.

The Fe/Mn systematics of the olivines in NWA 12217, 12319, and 12562 argue convincingly for a cumulate origin within a fractionating magma chamber for these meteorites. The diogenites and Mg-rich harzburgites included in howardites are similarly cumulate rocks within this scheme, but whether they originated on the same parent body is not fully resolved. The pyroxene minor element diversity (Fig. 15) exhibited in particular by NWA 12319 and 12562 overlaps and broadens the fields plotted by the diogenites, Mg-rich harzburgites, and

NWA 12217. Coupled with the oxygen and chromium isotopic evidence, this suggests the existence of at least two large, differentiated parent bodies present in the early Solar System, at least one of which has since been annihilated by impact (the other potentially being Vesta). This would favor the 'Battered to Bits' (Burbine et al. 1996) scenario in which planetesimal mantles have been largely eroded away, and NWA 12217, 12319, and 12562 would represent rare examples of such mantle material.

The Dawn mission arguably created more questions regarding Vesta and the HED meteorites than it solved by observing a large metallic core over 100 km in diameter(Ermakov et al. 2014) and failing to observe large volumes of olivine-rich mantle material exposed by deep impact craters (Consolmagno et al. 2015). If the bulk composition of Vesta is chondritic, the elevated REE contents of the crustal eucrites argue for the existence of a complimentary REE-depleted and olivine-rich mantle 7-10 times the size of the crust (Mittlefehldt and Lindstrom 2003; Consolmagno et al. 2015). However, the large Vestan core and the deep crust-mantle boundary suggested by impact craters that excavated olivine-free material from 100 km deep(Clenet et al. 2014), severely limit the potential size of this mantle.

The petrological and geochemical characteristics of the newly discovered ultramafic achondrites favor serial magmatism within fractionating magma chambers on its parent bodies, just as the discovery of olivine-rich material overlying eucritic material favors this model on Vesta (Cheek and Sunshine 2020). The variability in Mg# and pyroxene compositions found within all three breccias suggests that they are sampling heterogeneous igneous bodies, whereas under a magma ocean scenario more homogeneity should be expected. The REE compositions of the ultramafic achondrites are likewise varied and dependent on high-Ca pyroxene content, a phase that is not expected to be in the mantle of a sodium-depleted parent body such as Vesta

(Consolmagno et al. 2015). While bulk analyses of the ultramafic achondrites suggest they are as alkali-depleted as the HED meteorites, brecciated ultramafic rocks are unlikely to represent precisely the volatile budgets of their host bodies (Fig. 16). Thus, the compositions of these meteorites raise additional complexities in piecing together the igneous histories of Vesta, the vestoids, and any other differentiated planetesimals that produced fractionating magmas.

4.2 Symplectites

The possibility of subsolidus introduction of exogenous chromium to planetary materials warrants discussion. The symplectites identified in NWA 12217, 12319, and 12562 are commonly found in ultramafic and mafic rocks, including examples within terrestrial peridotites, lunar troctolites, martian basalts and cumulates, diogenites, and the ungrouped achondrite QUE 93148. The particular type of symplectites found in NWA 12217, 12319, and 12562 are almost identical to those found in the Mg-rich harzburgite clasts in howardites (Hahn et al. 2018). They are composed of vermicular chromite lathes, low-Ca pyroxene, and high-Ca pyroxene (Fig. 9 and 10). The pyroxene included in the symplectites is generally more magnesian (FeO < 2.0 wt.%) than pyroxenes not associated with symplectites. The petrogenesis of symplectites is controversial, with many possible formation mechanisms proposed over decades of research (Bell et al. 1975; Dawson and Smith 1975; Morishita and Arai 2003; Field 2008; Holness et al. 2011; Elardo et al. 2012; Khisina et al. 2013; Špaček et al. 2013; Hahn et al. 2018). These include: (1) crystallization of late-stage trapped melts; (2) diffusion of minor elements out of olivine; (3) breakdown of pre-existing chrome garnets; (4) reaction with a chromium-rich metasomatizing fluid.

It is unlikely that the symplectites are late-stage crystallization products because their bulk composition is not that of a possible melt inclusion or late-stage residuum(Holness et al. 2011). The amount of chromium dissolved in the melt would have to be unreasonably high to crystallize such phases. A likely candidate for such a late-stage melt pocket was identified in NWA 12217. The bulk composition of the pocket is much higher in Si, Al, Ca, than the symplectites and contains negligible amounts of Cr. Similar to the symplectites in a lunar troctolite (Elardo et al. 2012), the symplectites contain highly variable proportions of high- and low-Ca pyroxene, but the compositions of these phases are largely uniform. The composition of a trapped melt would be highly variable depending on the stage of the crystallization sequence of the parent magma, and this variability should be reflected in pyroxene compositional diversity. Conversely, if each trapped pocket was formed at the same time, a uniform distribution of high- and low-Ca pyroxene should be expected. We find neither to be the case.

We also consider it to be unlikely that the symplectites were formed by diffusion of Cr out of olivine. The Cr contents of olivines in all three meteorites are uniformly low (Fig. 13), and there are chromite grains scattered throughout that were likely liquidus phases and the primary Cr carriers. None of the olivine grains contain diffusion gradients in Cr or any other element, which would be expected if Cr was diffusing out of the grains and into the symplectites. Instead, there are elevated Cr compositions in olivines adjacent to the symplectites which implies Cr diffusion from the symplectites into the olivines, as found in the lunar troctolite (Elardo et al. 2012) and in Vestal Mg-rich harzburgites (Hahn et al. 2018). We note that the elevated Cr in olivine grains is only observed one or two μm away from the symplectites, so it is also possible that the measurement is due to symplectite interference with the electron beam's interaction volume during microprobe analysis.

The bulk compositions of the symplectites are stoichiometrically consistent with having been formed through the breakdown of preexisting chromium garnet (Špaček et al. 2013). However, the garnet stability field exists at pressures greater than 1.5 GPa (O'Hara et al. 1971), a regime difficult to reconcile with formation on a small body such as a planetesimal. Even at the high end of a theoretical pressure calculation, assuming a body with a diameter of 1000 km, an average density of 4000 kg/m^3, and a depth of 400 km, the hydrostatic pressure is less than 1 GPa. We suggest that NWA 12217, 12319, and 12562 more likely formed on a smaller body, and therefore the symplectites are unlikely to be garnet breakdown products. However, as the planetesimal size is poorly constrained, this possibility cannot be completely excluded.

There is also the possibility of a Cr-rich metasomatizing melt or fluid crystallizing symplectites like those identified in NWA 12217, 12319, and 12562. Elardo et al. (2012) suggested that a chromite-rich basaltic melt infiltrated cracks and grain boundaries in the lunar troctolite 76535 and crystallized chromite as a liquidus phase. The chromite then reacted metasomatically with bounding olivine and plagioclase, resulting in the formation of symplectites with high Mg# since they were buffered by the high Mg# of adjacent olivine. Additional unreacted chromite was deposited as chromite veins. Hahn et al. (2018) likewise argued for an exogenous origin for the symplectites they identified in Mg-rich harzburgite howardite clasts. They found a glassy melt inclusion high in Cr with a preserved reaction front that was in the process of precipitating a symplectite assemblage. Based on this observation, they argued that a melt that contained both a silicate and metallic component interacted with olivine under changing fO_2 conditions and resulted in the crystallization of the symplectites.

Based on our observations, we do not consider that the mechanisms proposed by Elardo et al. (2012) to be relevant to symplectite formation in NWA 12217, 12319, or 12562, since the

symplectites are ubiquitous as inclusions within olivine and along olivine-olivine and olivine-pyroxene grain boundaries and do not involved plagioclase. Hahn et al. (2018) present an interesting model of formation based on a single melt glass that they identified interacting with a symplectite. However, we found no such melt in NWA 12217, 12319 or 12562. Therefore, we do not find it compelling to associate these symplectites with a hypothetical infiltrating melt. Furthermore, the melt glass(Hahn et al. 2018) remains poorly characterized, and likely finer-scale measurements such as TEM analyses will be necessary to understand how such a melt could accommodate high levels of Cr_2O_3, along with the microstructure of the propagating reaction front. Their suggestion of a metallic melt component necessary to incorporate Cr and an associated increase in fO_2 also remains hypothetical.

The main obstacle to deciphering the origin of the symplectites in NWA 12217, 12319, and 12562 is the origin of chromium. The most obvious source would be the chromite that is ubiquitous throughout all three meteorites, but implicating these requires that they break down spontaneously into symplectites in some regions while remaining pristine in others, with no satisfying explanation as to why. There is also no clear source for the excess silica required to crystallize the pyroxene components of the symplectites. In lieu of any other plausible sources for Cr, we find that the interaction of an exogenous melt is a possible formation mechanism, but there is a paucity of evidence for such an interaction.

5. Conclusions

The discovery of the ultramafic achondrites Northwest Africa 12217, 12319, and 12562 represents an end to the shortage of olivine-rich planetary materials. While they bear geochemical and petrological similarities to the HED meteorites, in particular ultramafic clasts

found within howardites, their stable isotopic compositions suggest that they do not originate from Vesta. Like the isotope-anomalous eucrites, they were instead likely sourced from similar differentiated parent bodies with vestoid spectral characteristics. Their minor element chemistries and bulk compositions demand an origin inside a fractionating magma chamber rather than as residues of partial melting. Their HSE contents suggest that they formed on a parent body that experienced core-mantle differentiation and whose silicate portion was later enriched by a meteoritic component, much like the terrestrial planets and Vesta. These meteorites provide additional evidence for widespread differentiation before disruption among planetesimals and protoplanets during the early solar system.

Figures & Tables

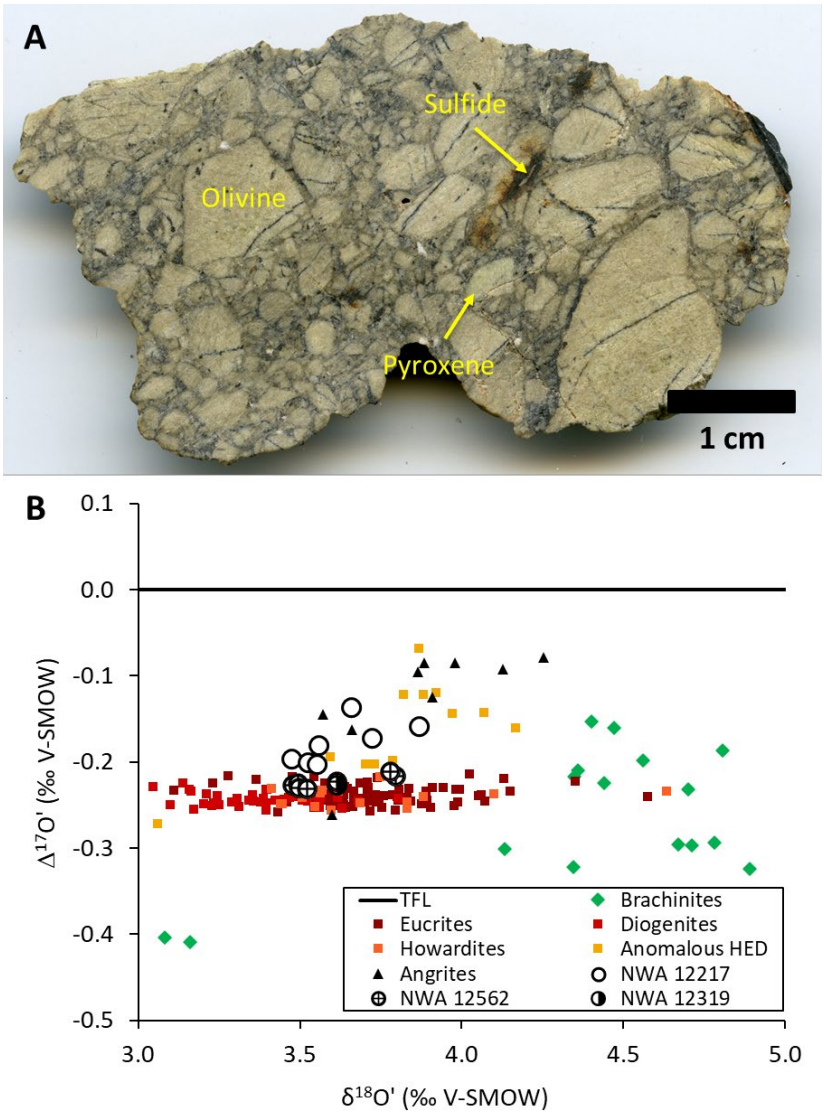

Figure 1. (A) Northwest Africa 12217 showing large olivine fragments. The light to dark brown material which is terrestrial weathering, typically oxidation of metal grains and sulfides. Remnant fusion crust is visible in the top right corner of the meteorite. Interstitial areas between grains have been darkened by shock, and they reflect the primary lithology of the meteorites. (B) $\Delta^{17}O$ diagram showing NWA 12217, 12319, and 12562 in relation to other achondrite groups(Greenwood et al. 2005, 2012; Scott et al. 2009; Zhang et al. 2019). TFL is the mass-dependent terrestrial fractionation line. Errors are smaller than symbols.

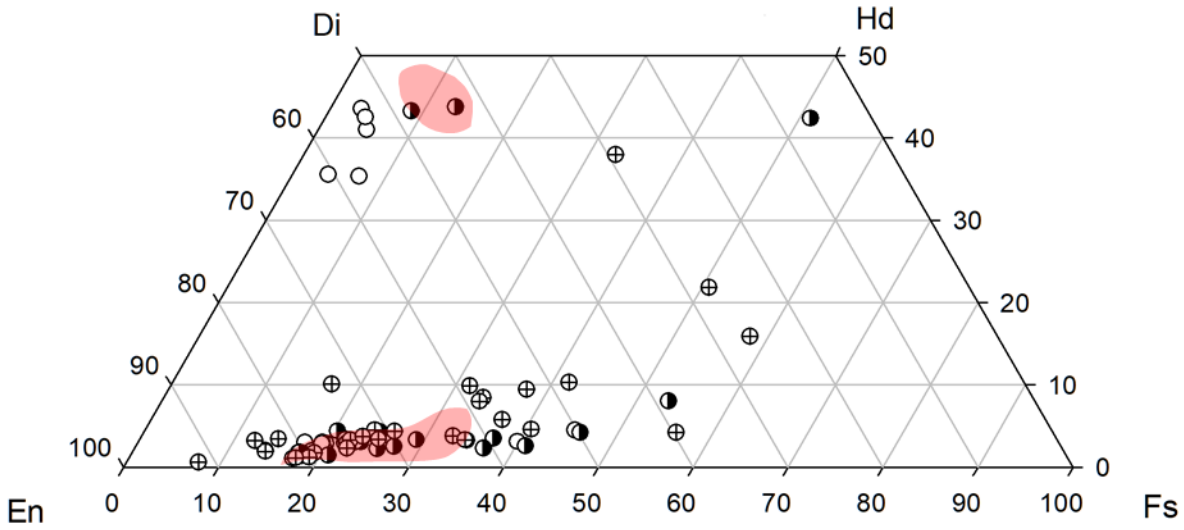

Figure 2. Quadrilateral showing pyroxene compositions of dunite NWA 12217 (open circles), lherzolites NWA 12319 (half-filled circles) and 12562 (crossed circles), and fields of diogenites (Mittlefehldt 2015) (pale red).

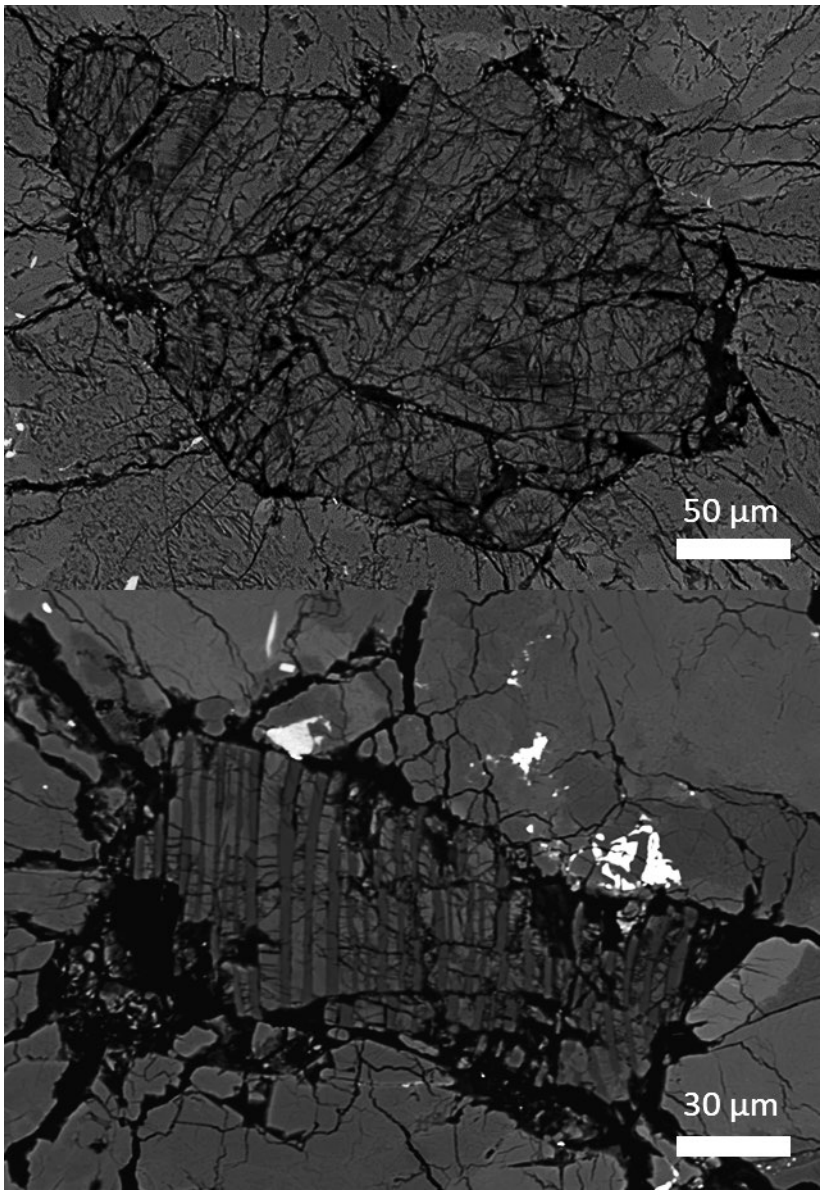

Figure 3. BSE images of plagioclase (top) and alternating lathes of K-feldspar and silica (bottom), both found as inclusions within olivine grains in NWA 12217.

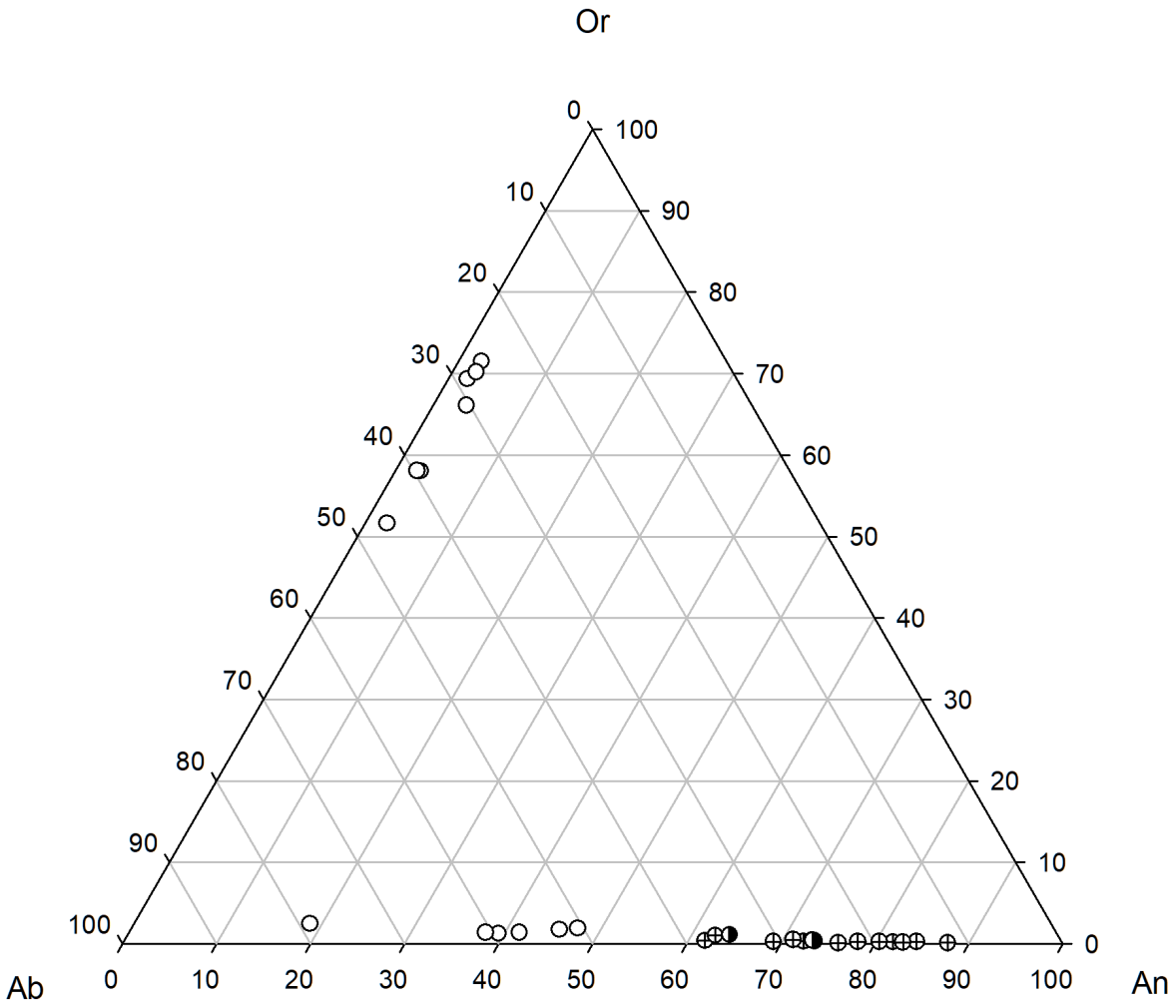

Figure 4. Ternary diagram showing feldspar compositions in NWA 12217 (open circles), 12319 (half-filled circles), and 12562 (crossed circles). Feldspars in NWA 12217 are small (<500 µm) inclusions in olivine and are likely representative of trapped melt, while feldspars in NWA 12319 and 12562 appear as brecciated clasts.

NWA 12217	Olivine (n=90)		Low-Ca Pyroxene (n=18)		High-Ca Pyroxene (n=5)		Chromite (n=6)		Plagioclase (n=5)		K-feldspar (n=9)	
	Avg.	Stdev	Avg.	Stdev	Avg.	Stdev	Avg.	Stdev	Avg.	Stdev	Avg.	Stdev
Al_2O_3	0.03	0.04	0.72	0.28	0.80	0.45	10.10	6.84	26.11	2.04	16.71	1.56
SiO_2	40.19	1.28	52.15	1.54	53.25	0.62	0.03	0.06	57.19	3.94	68.44	2.58
Cr_2O_3	0.10	0.07	0.60	0.23	1.17	0.25	59.80	5.05	n.a.		n.a.	
TiO_2	0.01	0.01	0.19	0.14	0.17	0.21	0.11	0.10	n.a.		n.a.	
Na_2O	0.00	0.01	0.04	0.02	0.50	0.14	0.01	0.01	6.83	1.43	3.94	1.18
MgO	50.36	1.97	24.32	5.34	19.20	1.40	10.23	2.85	0.00	0.00	0.01	0.03
MnO	0.25	0.06	0.69	0.26	0.14	0.05	0.59	0.12	n.a.		n.a.	
FeO	8.91	2.11	17.57	6.88	2.89	0.96	17.17	3.07	0.20	0.06	0.18	0.08
NiO	0.01	0.01	0.01	0.01	0.01	0.02	0.00	0.01	n.a.		n.a.	
K_2O	0.02	0.01	0.02	0.01	0.04	0.02	0.03	0.01	0.30	0.09	9.61	1.21
CaO	0.07	0.05	1.61	0.68	18.96	1.70	0.03	0.05	7.92	2.30	0.51	0.11
Total	99.94		97.91		97.132		98.12		98.54		99.53	
NWA 12319	Olivine (n=102)		Low-Ca Pyroxene (n=20)		High-Ca Pyroxene (n=2)		Chromite (n=10)		Plagioclase (n=4)			
	Avg.	Stdev	Avg.	Stdev	Avg.	Stdev	Avg.	Stdev	Avg.	Stdev		
Al_2O_3	0.03	0.03	0.86	0.29	1.29	0.69	10.88	9.18	31.76	1.08		
SiO_2	40.56	0.90	54.89	2.16	50.21	1.39	0.18	0.18	49.99	1.53		
Cr_2O_3	0.05	0.03	0.61	0.23	0.61	0.73	56.93	10.16	0.01	0.01		
TiO_2	0.02	0.02	0.17	0.15	0.73	0.58	0.51	0.63	0.02	0.02		
Na_2O	0.01	0.01	0.04	0.06	0.16	0.11	0.02	0.01	3.22	0.48		
MgO	45.65	3.32	24.19	5.00	8.27	8.89	7.08	3.48	0.04	0.04		
MnO	0.34	0.08	0.58	0.20	0.55	0.24	0.69	0.18	0.03	0.03		
FeO	13.23	3.49	16.32	6.27	17.93	14.20	22.46	4.53	0.41	0.08		
NiO	0.01	0.01	0.01	0.01	n.a.		n.a.		n.a.			
K_2O	0.01	0.01	0.02	0.01	0.01	0.02	0.02	0.01	0.10	0.06		
CaO	0.06	0.04	2.40	4.41	19.31	1.73	0.02	0.02	14.51	0.95		
Total	99.97		100.06		99.07		98.79		100.08			
NWA 12562	Olivine (n=84)		Low-Ca Pyroxene (n=38)		High-Ca Pyroxene (n=3)		Chromite (n=6)		Plagioclase (n=12)			
	Avg.	Stdev	Avg.	Stdev	Avg.	Stdev	Avg.	Stdev	Avg.	Stdev		
Al_2O_3	0.02	0.01	0.97	0.38	1.17	0.41	7.23	4.83	32.39	1.49		
SiO_2	39.82	0.85	53.81	1.90	49.38	0.38	0.05	0.03	48.76	2.19		
Cr_2O_3	0.05	0.04	0.65	0.21	0.47	0.06	58.40	5.95	0.01	0.01		
TiO_2	0.01	0.01	0.14	0.08	0.51	0.32	0.74	0.40	0.02	0.02		
Na_2O	0.00	0.00	0.03	0.02	0.10	0.08	0.01	0.01	2.75	0.96		
MgO	45.67	3.99	24.84	5.99	8.98	0.26	4.97	1.06	0.09	0.10		
MnO	0.34	0.10	0.58	0.22	0.85	0.18	0.71	0.05	0.01	0.01		
FeO	14.19	4.50	16.52	6.67	25.65	6.05	25.73	2.06	0.41	0.21		
NiO	0.01	0.01	0.01	0.01	0.00	0.00	0.00	0.01	0.01	0.01		
K_2O	0.02	0.01	0.02	0.00	0.02	0.01	0.02	0.00	0.06	0.04		
CaO	0.06	0.03	2.21	1.58	12.12	4.06	0.03	0.02	15.65	1.64		
Total	100.19		99.78		99.25		97.88		100.16			

Table 1. Average electron microprobe analyses for major and minor phases in NWA 12217, 12319, and 12562, in wt.%.

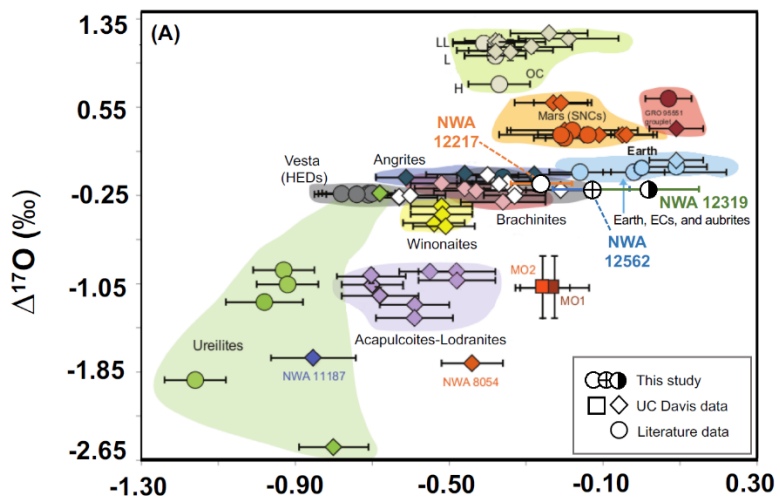
(A)
LL
L
H
OC
Mars (SNCs)
GRO 95551 Grouplet
NWA 12217
Earth
Vesta (HEDs)
Angrites
NWA 12319
Earth, ECs, and aubrites
Brachinites
Winonaites
NWA 12562
MO2
MO1
Acapulcoites-Lodranites
Ureilites
NWA 11187
NWA 8054
This study
UC Davis data
Literature data
Δ17O (‰)
1.35
0.55
-0.25
-1.05
-1.85
-2.65
-1.30
-0.90
-0.50
-0.10
0.30

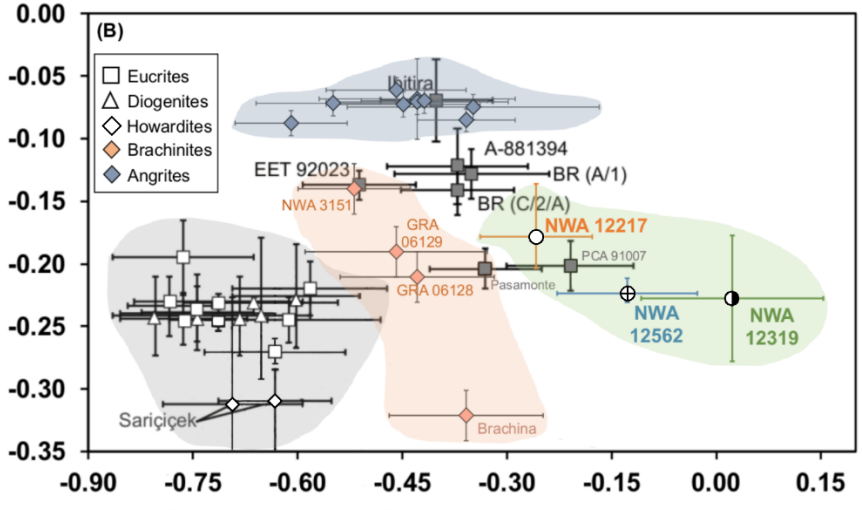
(B)
Eucrites
Diogenites
Howardites
Brachinites
Angrites
Ibitira
A-881394
EET 92023
BR (A/1)
NWA 3151
BR (C/2/A)
NWA 12217
GRA 06129
PCA 91007
GRA 06128
Pasamonte
NWA 12562
NWA 12319
Sariçiçek
Brachina
0.00
-0.05
-0.10
-0.15
-0.20
-0.25
-0.30
-0.35
-0.90
-0.75
-0.60
-0.45
-0.30
-0.15
0.00
0.15

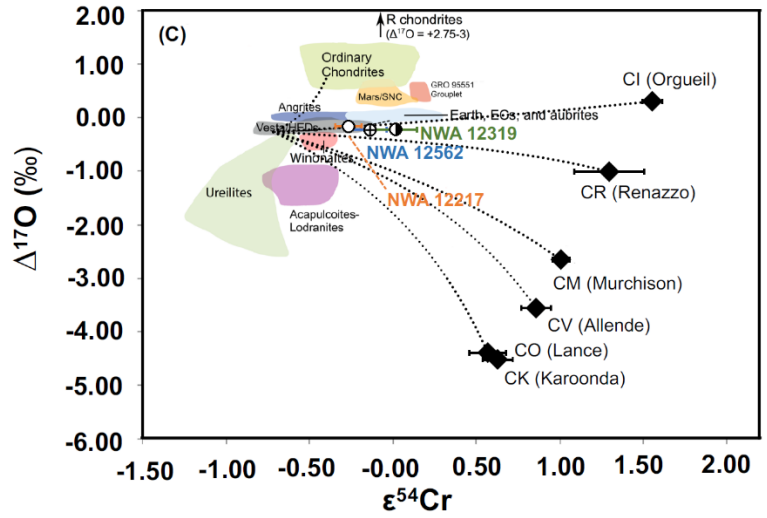
(C)
R chondrites
(Δ17O = +2.75-3)
Ordinary Chondrites
GRO 95551 Grouplet
Mars/SNC
Angrites
Vesta/HEDs
Earth, ECs, and aubrites
NWA 12319
NWA 12562
Winonaites
Ureilites
Acapulcoites-Lodranites
NWA 12217
CI (Orgueil)
CR (Renazzo)
CM (Murchison)
CV (Allende)
CO (Lance)
CK (Karoonda)
Δ17O (‰)
2.00
1.00
0.00
-1.00
-2.00
-3.00
-4.00
-5.00
-6.00
-1.50
-1.00
-0.50
-0.00
0.50
1.00
1.50
2.00
ε54Cr

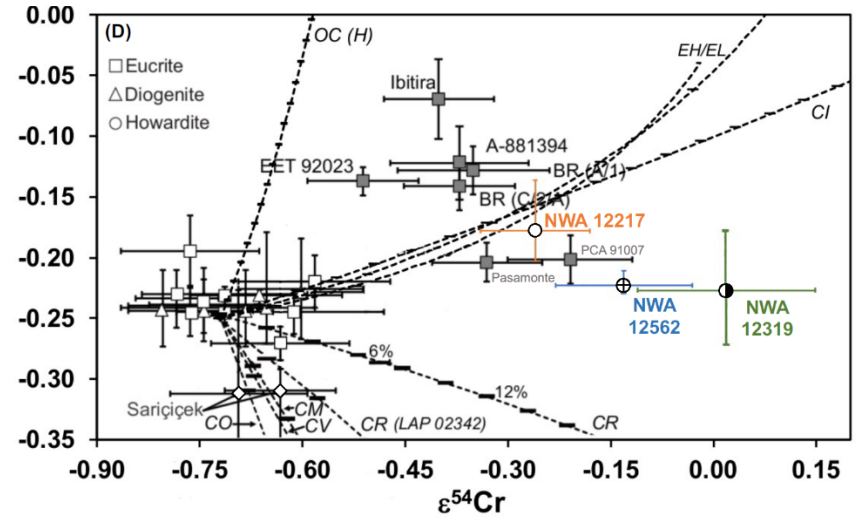
(D)
Eucrite
Diogenite
Howardite
OC (H)
EH/EL
CI
Ibitira
A-881394
EET 92023
BR (A/1)
BR (C/2/A)
NWA 12217
PCA 91007
Pasamonte
NWA 12562
NWA 12319
6%
12%
Sariçiçek
CO
CM
CV
CR (LAP 02342)
CR
0.00
-0.05
-0.10
-0.15
-0.20
-0.25
-0.30
-0.35
-0.90
-0.75
-0.60
-0.45
-0.30
-0.15
0.00
0.15
ε54Cr

Figure 5. (A) $\Delta^{17}O$ versus $\varepsilon^{54}Cr$ isotope systematics of NWA 12217, 12319, and 12562 (graphic circles) shown along with non-carbonaceous chondrites and achondrites. Colored circles represent literature data while the diamonds and squares are data measured at UC Davis. The fields for ordinary chondrites (OC), Mars (SNCs), Earth and earth-likes, Vesta (HEDs), brachinites, ureilites, winonaites (win), acapulcoites (acp)/lodranites/ungrouped achondrites (ung) are marked with select representative samples with available data. Symbol colors indicate meteorite type or grouping. Note that the carbonaceous chondrites and affiliated achondrites plot outside the field of this plot with highly positive $\varepsilon^{54}Cr$ (shown in panel C), with highly positive ε54Cr. Literature data from (Li et al. 2018). (B) $\Delta^{17}O$-$\varepsilon^{54}Cr$ diagram showing NWA 12217, 12319, and 12562 (graphic circles) in comparison with the brachinites, Brachina, GRA 06128, GRA 06129, and NWA 3151 (pink diamonds), angrites, along with the normal HEDs (open symbols) and anomalous eucrites (grey filled squares) (BR = Bunburra Rockhole). The y-axis error bars for NWA 12217 and 12562 represent the range of $\Delta^{17}O$ measured, and for NWA 12319 it is the analytical error of a single measurement. Literature data for eucrites are from (Sanborn and Yin 2014; Sanborn et al. 2016; Benedix et al. 2017; Wimpenny et al. 2019; Zhu et al. 2019) and references therein. (C). Overview $\Delta^{17}O$-$\varepsilon^{54}Cr$ plot showing the three new ultramafic achondrites with relation to major fields of planetary materials in non-carbonaceous (NC) and carbonaceous chondrites (CC) and mixing lines between normal HEDs with ordinary, enstatite, and carbonaceous chondrites. (D). $\Delta^{17}O$-$\varepsilon^{54}Cr$ plot of NWA 12217, 12319, and 12562 (graphic circles) along with the normal HEDs (open symbols) and anomalous eucrites (grey filled squares). Open squares represent literature normal eucrite data. (BR = Bunburra Rockhole). Literature data are from (Wiechert et al. 2004; Greenwood et al. 2005, 2014; Trinquier et al. 2007; Barrat et al. 2008; Scott et al. 2009; Sanborn and Yin 2014; Barrett et al.

2015) and references therein. Various dashed lines represent mixing curves between the average eucrite end member and specific chondritic endmembers as indicated.

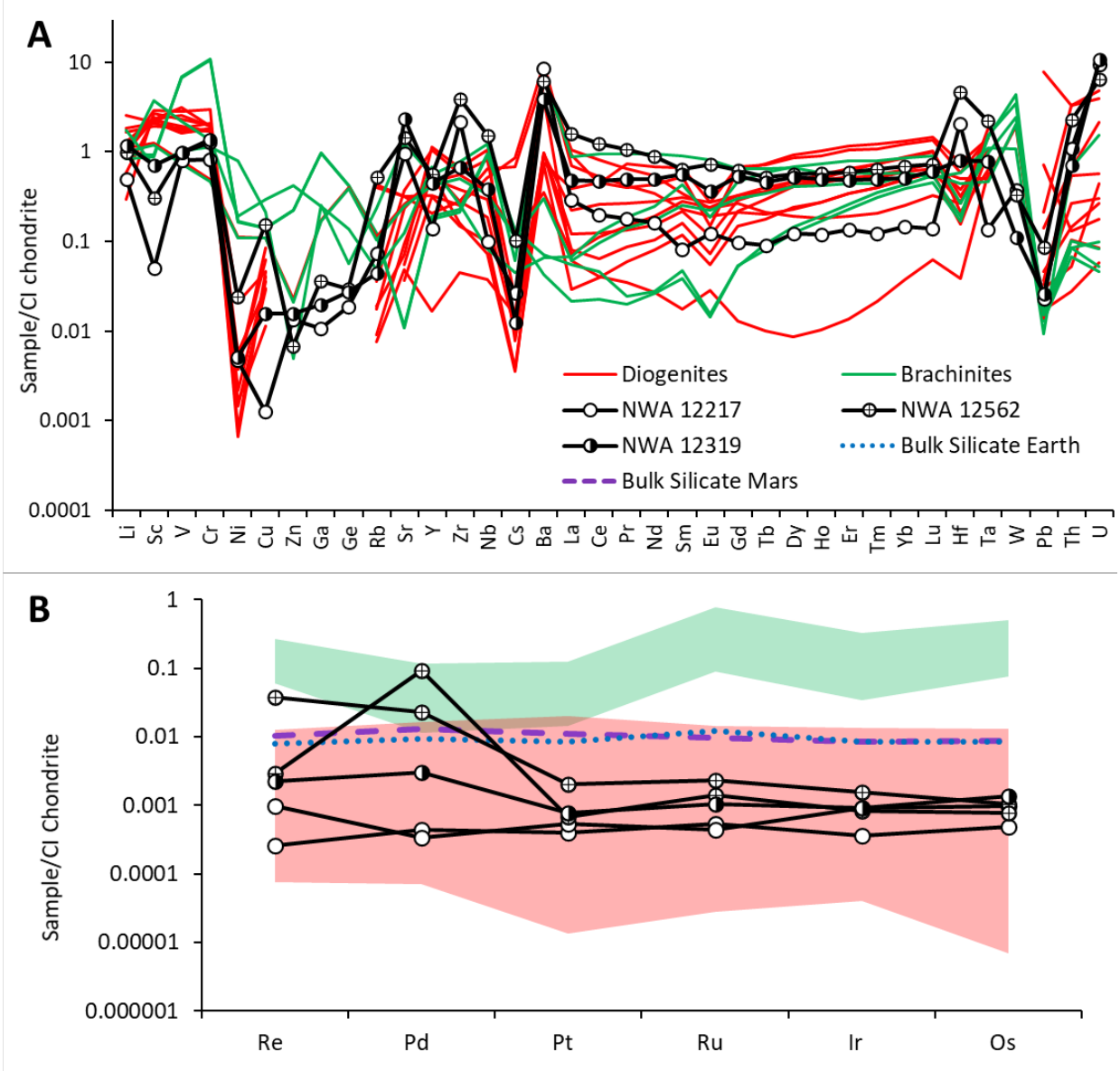

Figure 6. CI-chondrite normalized(Lodders et al. 2009) (A) ITE abundances in NWA 12217 (open circles), NWA 12319 (half-filled circles), NWA 12562 (crossed circles), brachinites(Goodrich et al. 2010; Day et al. 2012a) (green), and diogenites (Mittlefehldt 2015) (red). (B) Bulk CI-normalized HSE abundances of ultramafic achondrites plotted with those of

brachinites (Day et al. 2012a), diogenites (Day et al. 2012b), and estimates for bulk silicate Earth and Mars (Day et al. 2016).

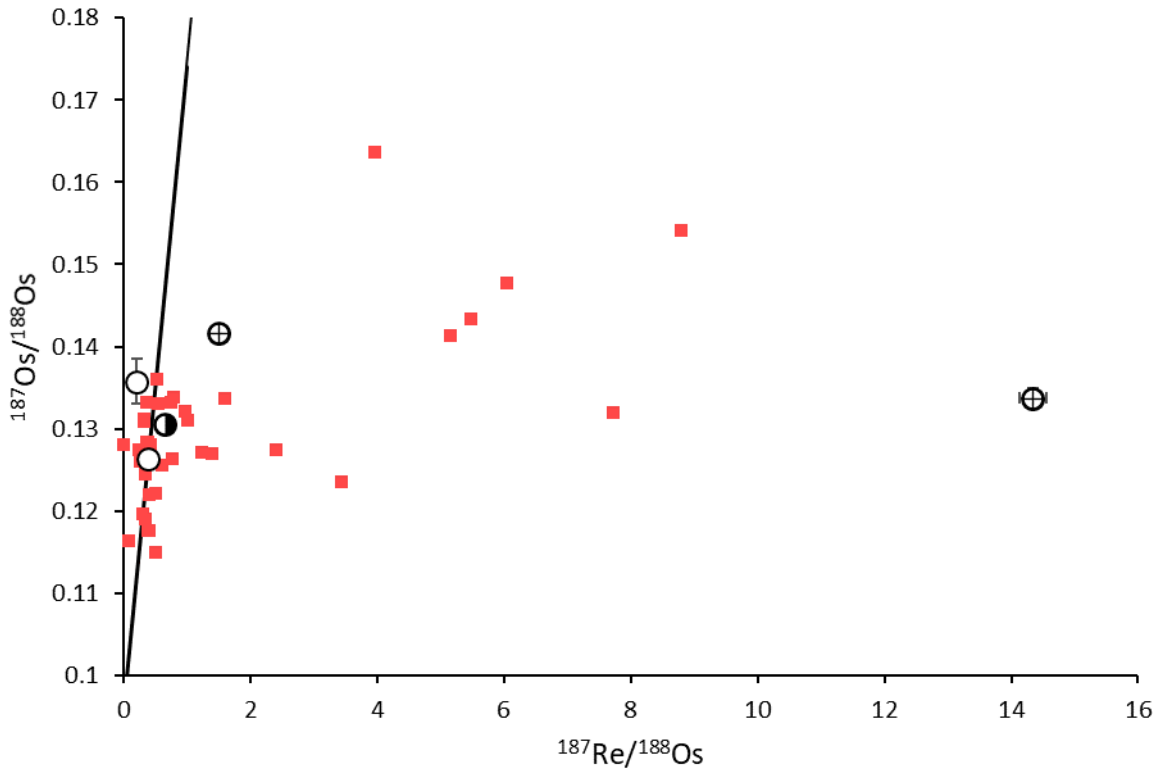

Figure 7. Rhenium-Os Isochron plot showing NWA 12217 (open circles), NWA 12319 (half filled circle), NWA 12562 (crossed circles), HED meteorites (Dale et al. 2012; Day et al. 2012c) (red), and the 4.568 Ga IIIAB iron meteorite isochron (Smoliar et al. 1996).

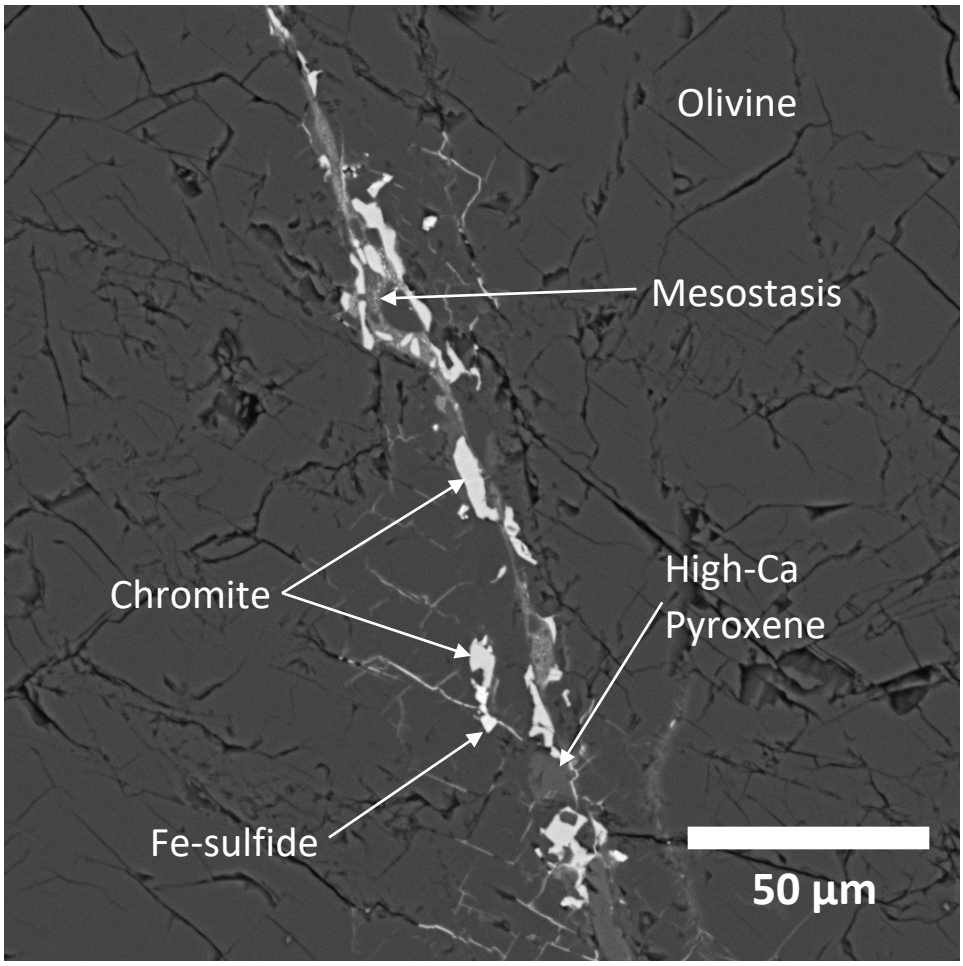

Figure 8. Vein-like feature ubiquitous in NWA 12217 and 12562. Veins are found within olivine grains and along grain boundaries, and some are disturbed by shock. Symplectites (Fig. S1) are sometimes found within veins.

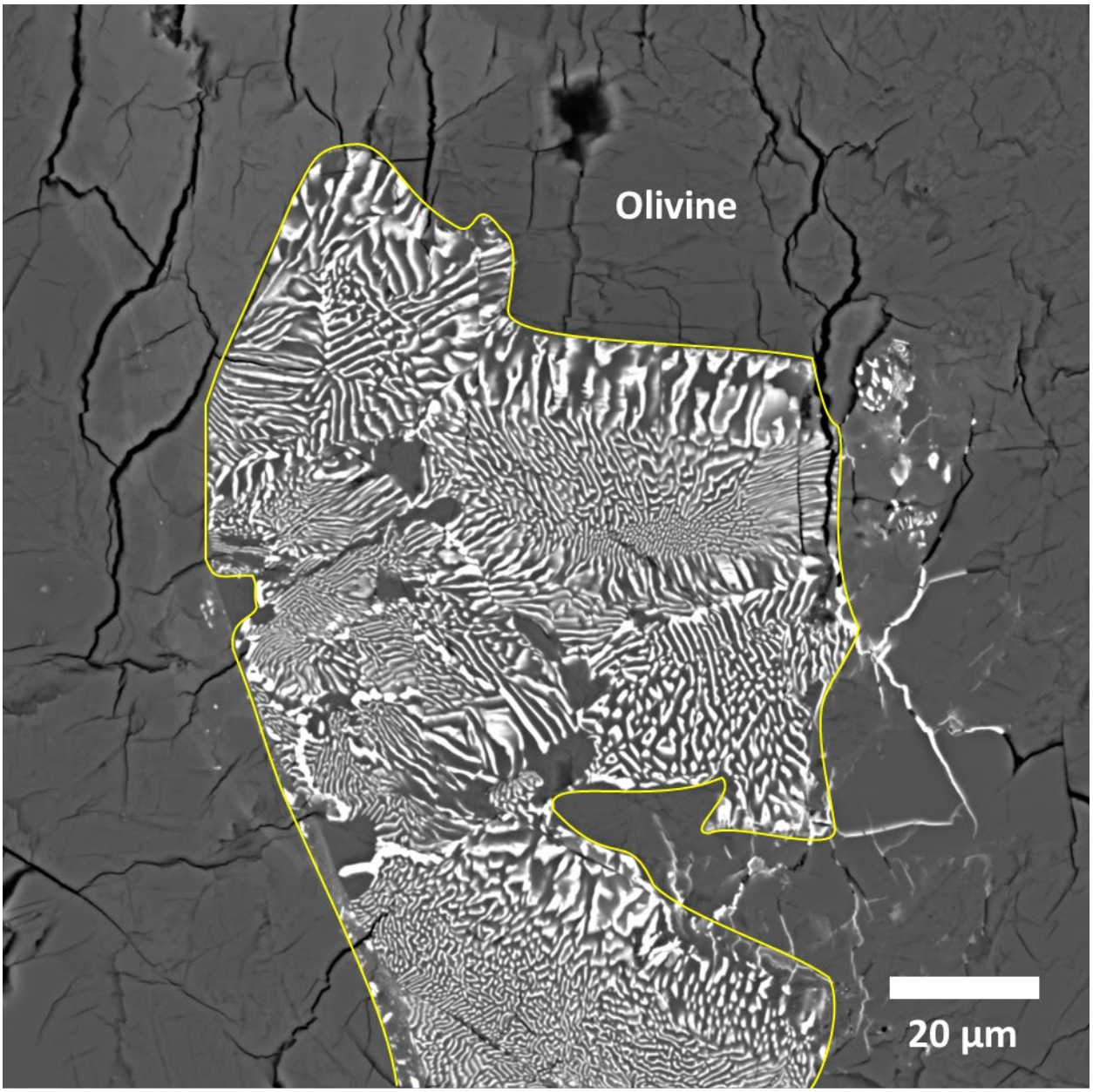

Figure 9. Backscatter electron (BSE) image of a symplectite (yellow outline) composed of chromite and low- and high-Ca pyroxene, completely enclosed within an olivine grain.

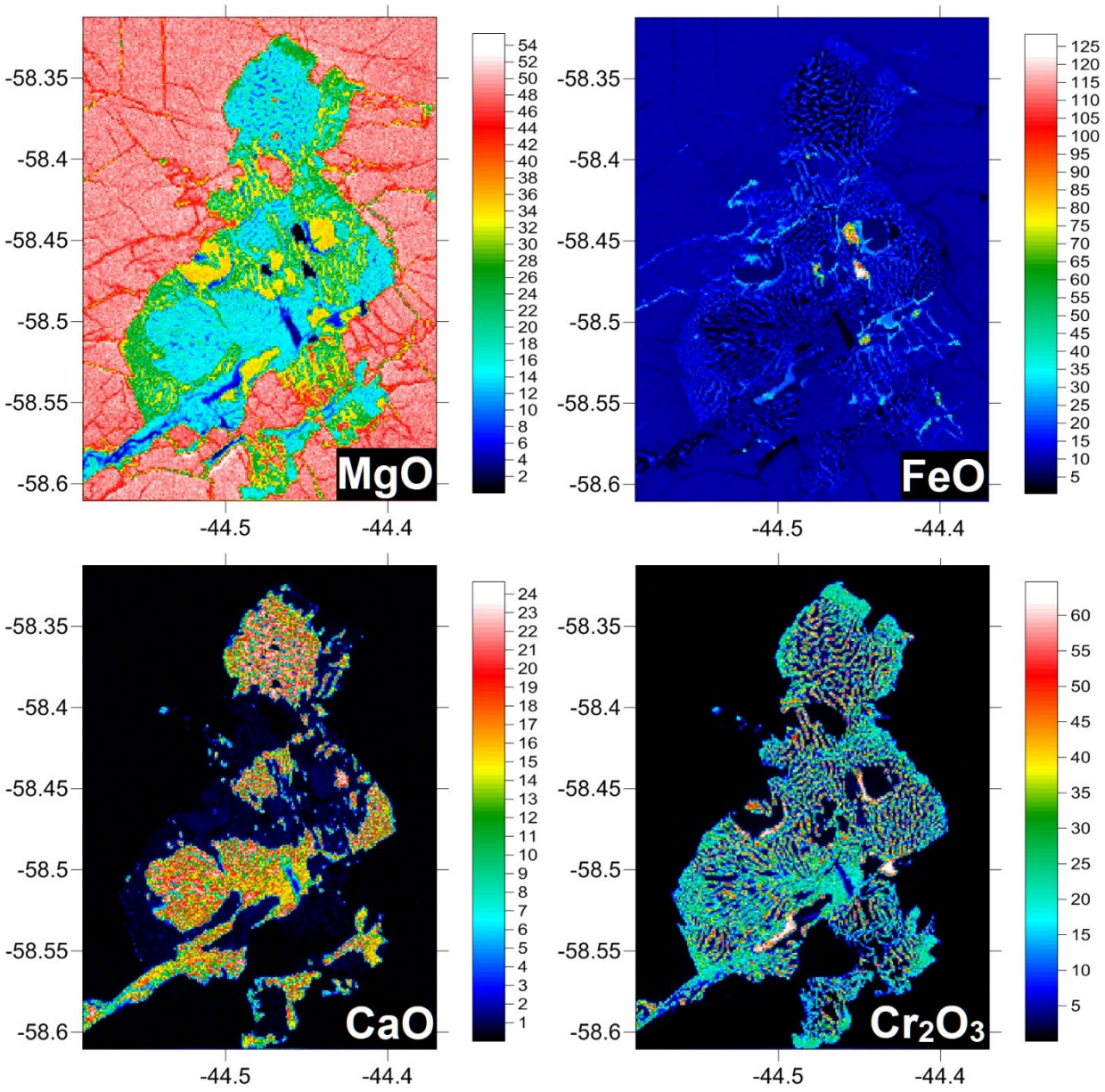

Figure 10. Quantitative X-ray oxide maps of a symplectite in NWA 12217. High FeO spots are FeNi metal or Fe-sulfide grains. Dimensions are in mm; color scale is in wt.%.

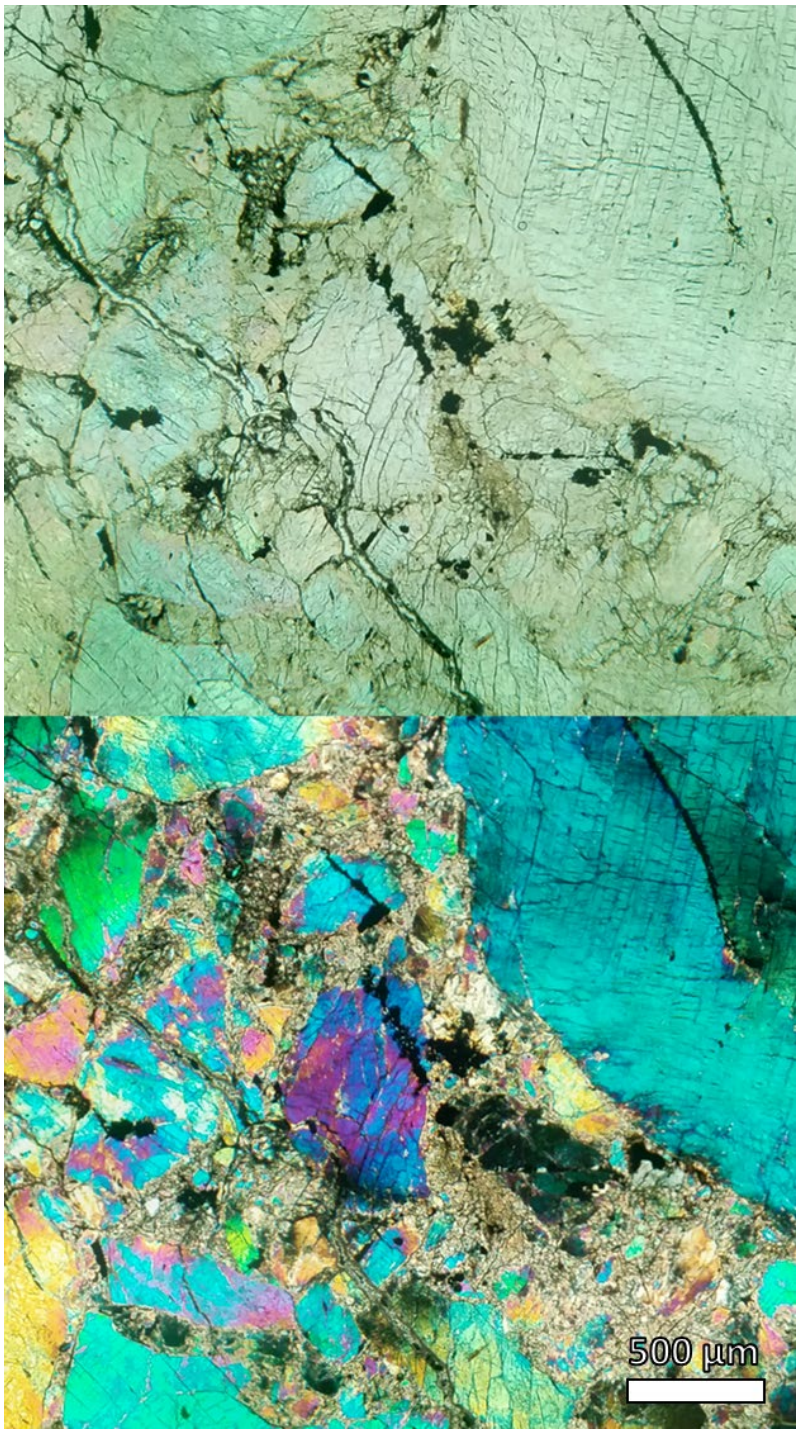

Figure 11. Plane-polarized light (PPL) (top) and cross-polarized light (XPL) (bottom) images of the same area in NWA 12217, showing undulose extinction, fracturing, and shock-mosaicism of compositionally homogenous olivine.

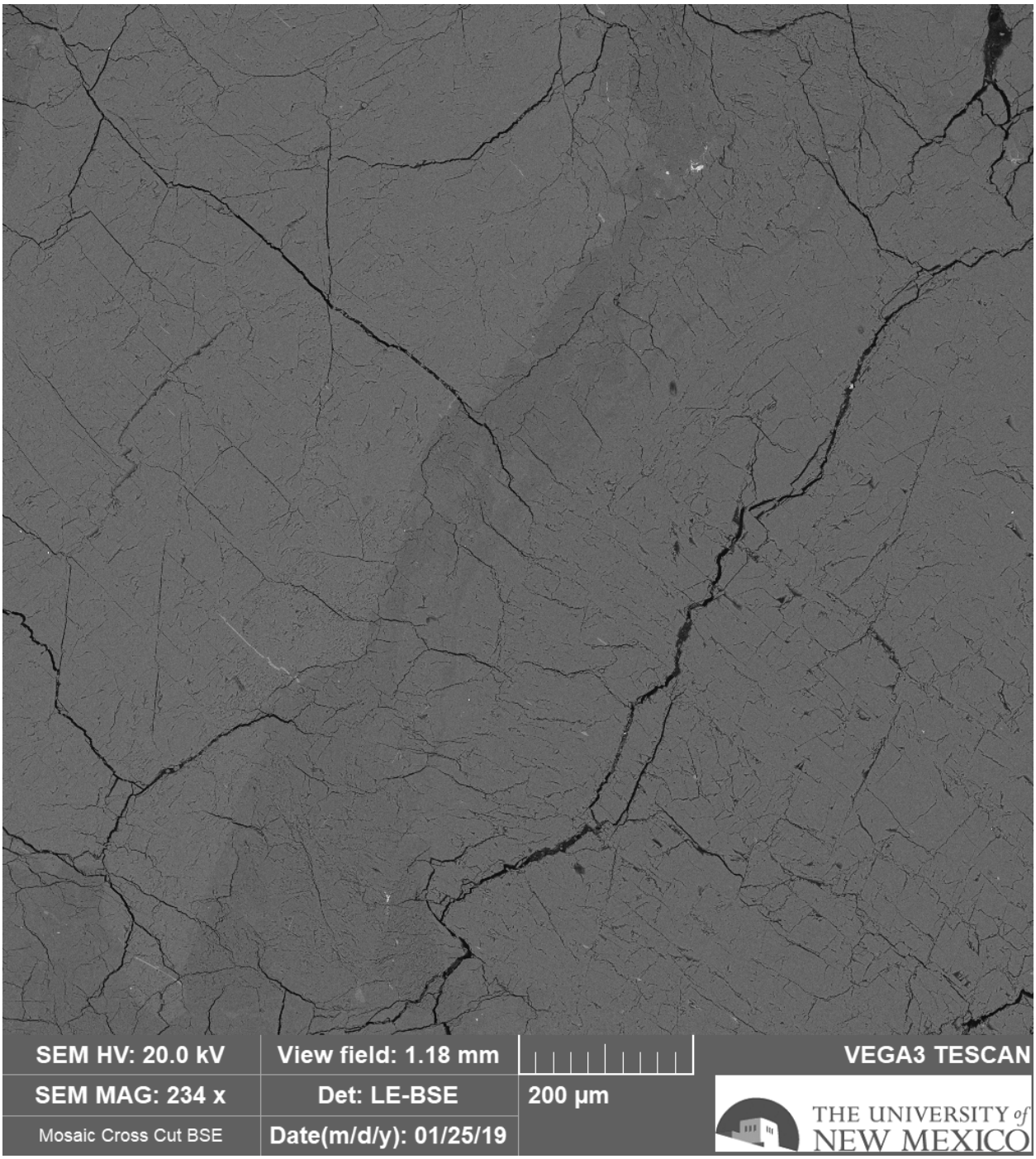

Figure 12. BSE image of typical dunitic lithology present in NWA 12217. The darker areas in the middle of the image appear fine-grained optically (see Fig. 11) but are likely the result of shock-induced mosaicism.

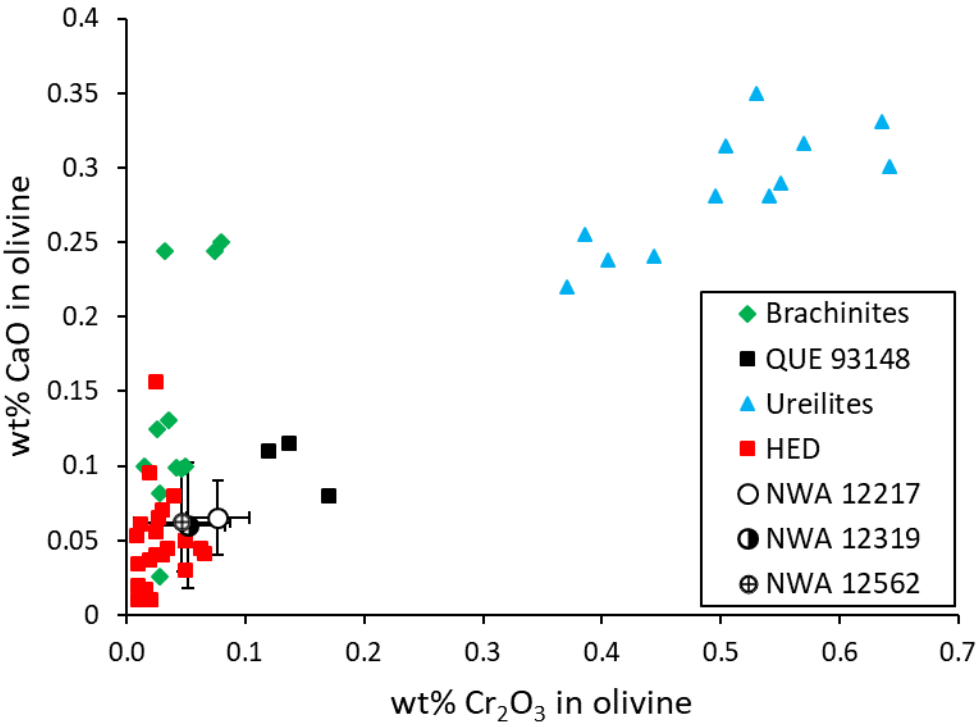

Figure 13. Average CaO versus Cr_2O_3 content in olivine grains in NWA 12217, 12319, and 12562, plotted with olivines from other meteorite groups and QUE 93148 (Goodrich and Righter 2000; Goodrich et al. 2001, 2006; Mittlefehldt et al. 2003; Mittlefehldt 2015).

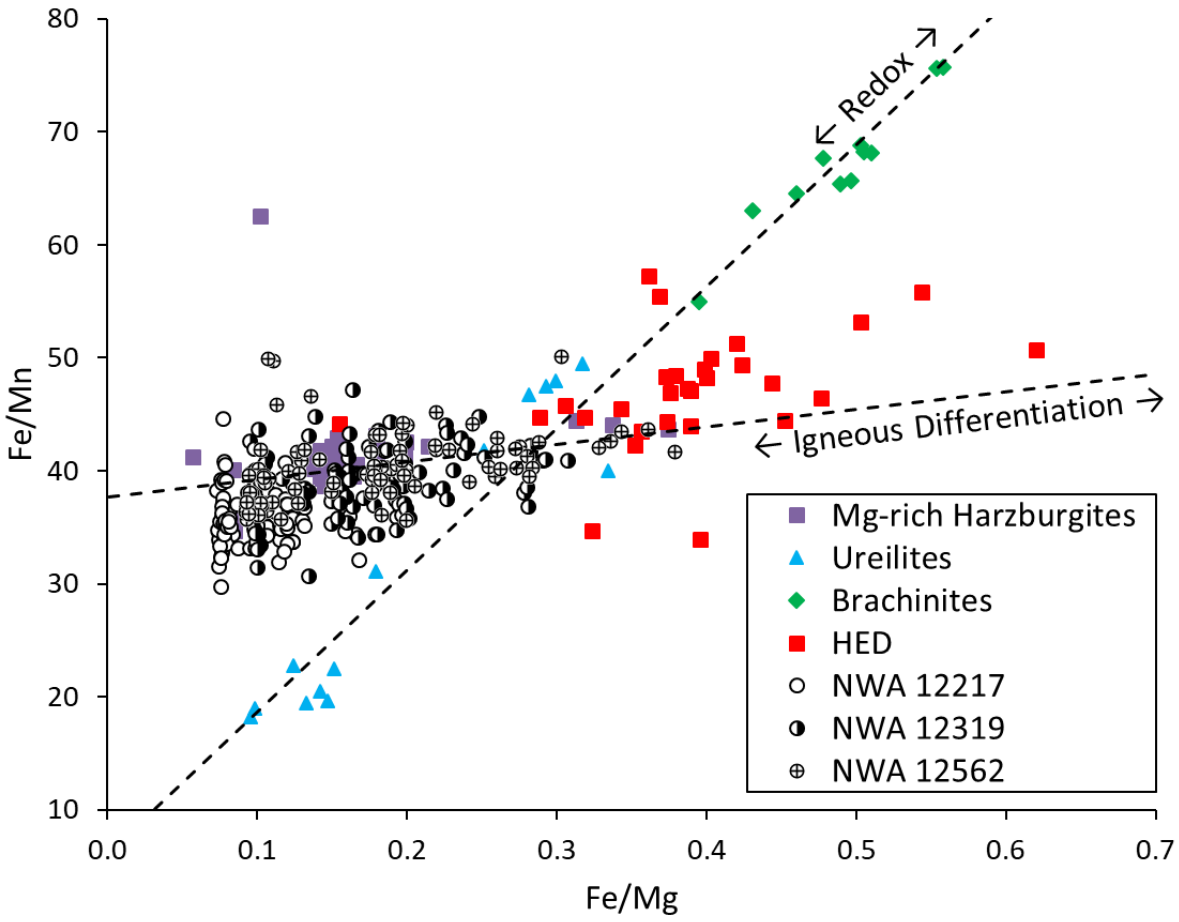

Figure 14. Plot of Fe/Mg versus Fe/Mn of olivine in the ultramafic achondrites and other meteorite groups (Goodrich and Righter 2000; Goodrich et al. 2001, 2006, 2010; Mittlefehldt 2015; Hahn et al. 2018). Mg-rich harzburgites are ultramafic clasts found within howardites. HED olivine analyses are overwhelmingly from diogenites. Primitive achondrites such as the ureilites and brachinites plot with constant Mn/Mg, while NWA 12217, 12319, and 12562 plot with relatively constant Fe/Mn and variable Fe/Mg.

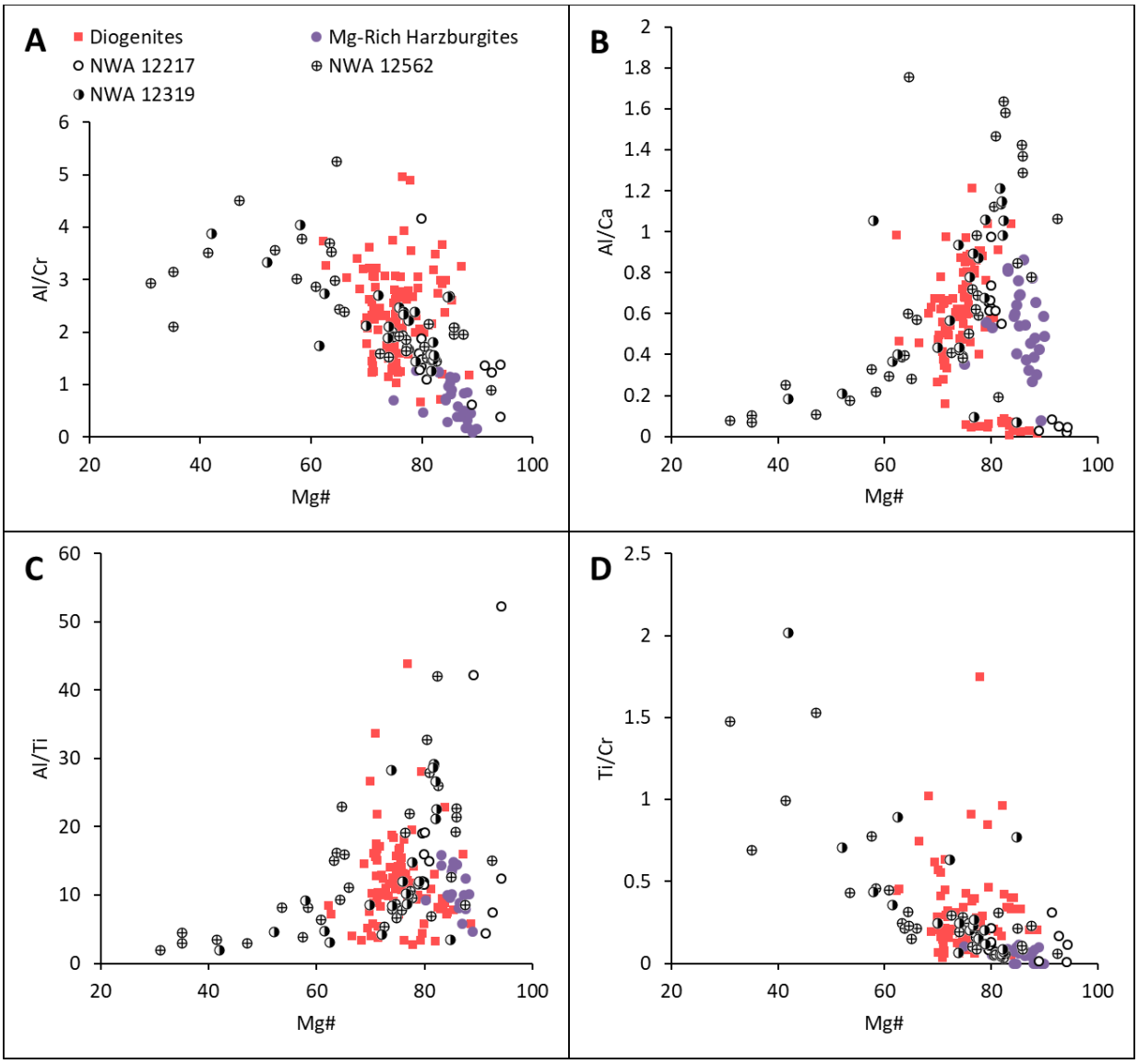

Figure 15. Plots of Mg# versus (a) Al/Cr, (b) Al/Ca, (c) Al/Ti and (d) Ti/Cr in pyroxenes. NWA 12217 and 12562 form largely continuous trends with the Mg-rich harzburgites (Hahn et al. 2018) and diogenites (Mittlefehldt 2015) in all data sets except for Al/Ca, in which the Mg-rich harzburgites show a separate trend.

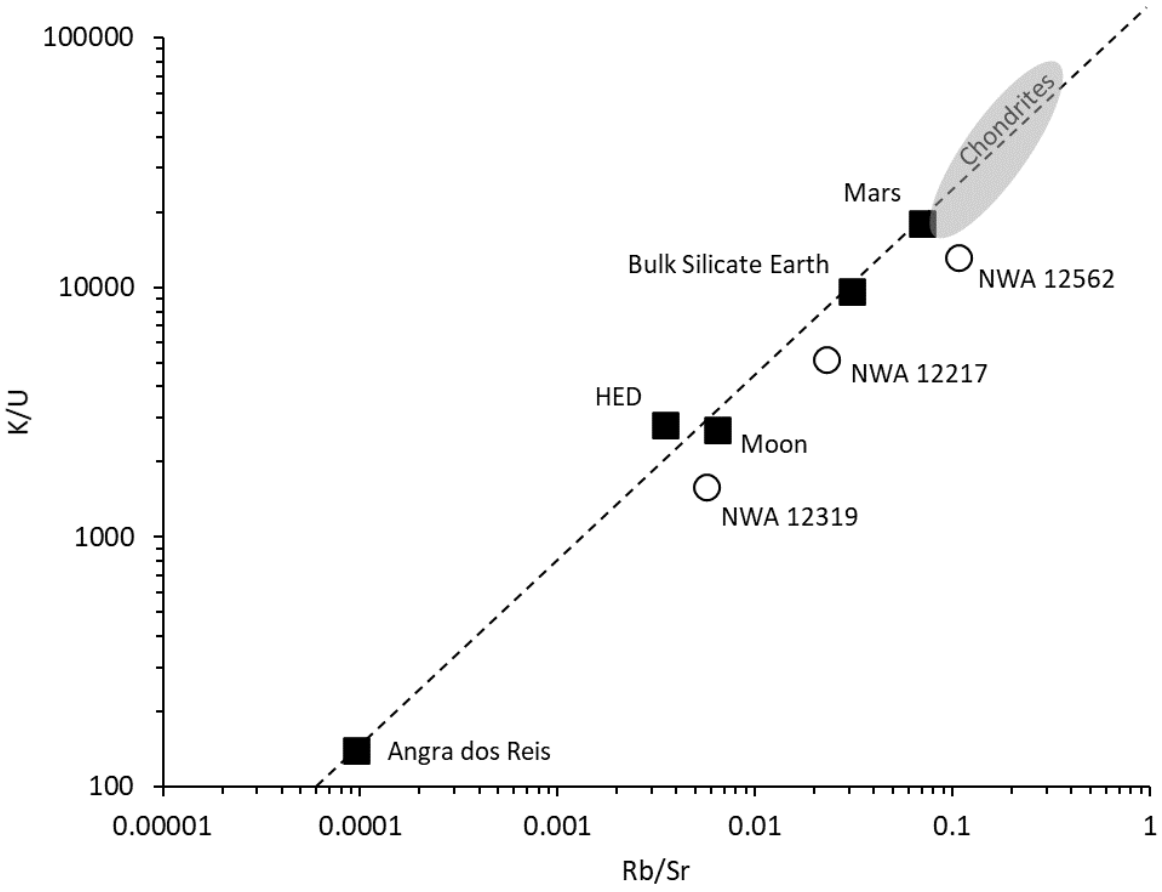

Figure 16. Potassium/U versus Rb/Sr as a proxy for planetary volatile depletion(Halliday and Porcelli 2001). The ultramafic achondrites plot off of the trend formed by the rest of the solar system and show extreme variation, suggesting that they are not representative of their parent bodies. In addition to modification by terrestrial weathering, these elements are subject to 'nugget effects' by brecciation and sample aliquot selection, especially in these olivine-dominated rocks.

References

Asphaug E. 2017. Signatures of hit-and-run collisions. In *Planetesimals: Early Differentiation and Consequences for Planets*. pp. 7–37.

Beck A. W., and McSween H. Y. 2010. Diogenites as polymict breccias composed of orthopyroxenite and harzburgite. *Meteoritics and Planetary Science* 45:850–872.

Beck A. W., Mittlefehldt D. W., Mcsween H. Y., Rumble D., Lee C. T. A., and Bodnar R. J. 2011. MIL 03443, a dunite from asteroid 4 Vesta: Evidence for its classification and cumulate origin. *Meteoritics and Planetary Science* 46:1133–1151.

Bell P. M., Mao H. K., Roedder E., and Weiblen P. W. 1975. The problem of the origin of symplectites in olivine-bearing lunar rocks. *Proceedings lunar science conference 6th* 231–248.

Bell J. F., Davis D. R., Hartmann W. K., and Gaffey M. J. 1989. Asteroids: The Big Picture. In *Asteroids II*. pp. 921–945.

Benedix G. K., Bland P. A., Friedrich J. M., Mittlefehldt D. W., Sanborn M. E., Yin Q. Z., Greenwood R. C., Franchi I. A., and Bevan A. W. R. 2017. Bunburra Rockhole: Exploring the geology of a new differentiated asteroid. *Geochimica et Cosmochimica Acta* 208:145–159. http://dx.doi.org/10.1016/j.gca.2017.03.030.

Bottke W. F., Nesvorný D., Grimm R. E., Morbidelli A., and O'Brien D. P. 2006. Iron meteorites as remnants of planetesimals formed in the terrestrial planet region. *Nature* 439:821–824.

Brugier Y. A., Barrat J. A., Gueguen B., Agranier A., Yamaguchi A., and Bischoff A. 2019. Zinc isotopic variations in ureilites. *Geochimica et Cosmochimica Acta* 246:450–460.

Burbine T. H., Meibom A., and Binzel R. P. 1996. Mantle material in the main belt: Battered to bits? *Meteoritics and Planetary Science* 31:607–620.

Cheek L. C., and Sunshine J. M. 2020. Merging spatial and spectral datasets to place olivine in stratigraphic context at Arruntia crater, a rare window into Vesta's northern hemispheric crust. *Icarus* 345:113718. https://doi.org/10.1016/j.icarus.2020.113718.

Clark B. E., Hapke B., Pieters C., and Britt D. 2003. Asteroid Space Weathering and Regolith Evolution. In *Asteroids III*. pp. 583–599.

Clenet H., Jutzi M., Barrat J. A., Asphaug E. I., Benz W., and Gillet P. 2014. A deep crust-mantle boundary in the asteroid 4 Vesta. *Nature* 511:303–306.

Consolmagno G. J., Golabek G. J., Turrini D., Jutzi M., Sirono S., Svetsov V., and Tsiganis K. 2015. Is Vesta an intact and pristine protoplanet? *Icarus* 254:190–201. http://dx.doi.org/10.1016/j.icarus.2015.03.029.

Cruikshank D. P., and Hartmann W. K. 1984. The Meteorite-Asteroid Connection: Two Olivine-Rich Asteroids. *Science* 223:281 LP – 283. http://science.sciencemag.org/content/223/4633/281.abstract.

Dawson J. B., and Smith J. V. 1975. Chromite-silicate intergrowths in upper-mantle peridotites. *Physics and Chemistry of the Earth* 9:339–350.

Day J. M. D. et al. 2012. Origin of felsic achondrites Graves Nunataks 06128 and 06129, and ultramafic brachinites and brachinite-like achondrites by partial melting of volatile-rich primitive parent bodies. *Geochimica et Cosmochimica Acta* 81:94–128. http://dx.doi.org/10.1016/j.gca.2011.12.017.

Day J. M. D., Corder C. A., Rumble D., Assayag N., Cartigny P., and Taylor L. A. 2015. Differentiation processes in FeO-rich asteroids revealed by the achondrite Lewis Cliff 88763. *Meteoritics and Planetary Science* 50:1750–1766.

Day J. M. D., Brandon A. D., and Walker R. J. 2016. Highly siderophile elements in Earth, Mars, the Moon, and asteroids. *Reviews in Mineralogy and Geochemistry* 81:161–238.

Day J. M. D., Corder C. A., Assayag N., and Cartigny P. 2019. Ferrous oxide-rich asteroid achondrites. *Geochimica et Cosmochimica Acta* 266:544–567. https://doi.org/10.1016/j.gca.2019.04.005.

DeMeo F. E., Polishook D., Carry B., Burt B. J., Hsieh H. H., Binzel R. P., Moskovitz N. A., and Burbine T. H. 2019. Olivine-dominated A-type asteroids in the main belt: Distribution, abundance and relation to families. *Icarus* 322:13–30. https://doi.org/10.1016/j.icarus.2018.12.016.

Elardo S. M., McCubbin F. M., and Shearer C. K. 2012. Chromite symplectites in Mg-suite troctolite 76535 as evidence for infiltration metasomatism of a lunar layered intrusion. *Geochimica et Cosmochimica Acta* 87:154–177. http://dx.doi.org/10.1016/j.gca.2012.03.030.

Ermakov A. I., Zuber M. T., Smith D. E., Raymond C. A., Balmino G., Fu R. R., and Ivanov B. A. 2014. Constraints on Vesta's interior structure using gravity and shape models from the Dawn mission. *Icarus* 240:146–160. http://dx.doi.org/10.1016/j.icarus.2014.05.015.

Field S. W. 2008. Diffusion, discontinuous precipitation, metamorphism, and metasomatism: The complex history of South African upper-mantle symplectites. *American Mineralogist* 93:618–631.

Frey F. A. 1984. Rare Earth Element Abundances in Upper Mantle Rocks, Elsevier B.V. http://dx.doi.org/10.1016/B978-0-444-42148-7.50010-1.

Gardner-Vandy K. G., Lauretta D. S., and McCoy T. J. 2013. A petrologic, thermodynamic and experimental study of brachinites: Partial melt residues of an R chondrite-like precursor. *Geochimica et Cosmochimica Acta* 122:36–57. http://dx.doi.org/10.1016/j.gca.2013.07.035.

Goldstein J. I., Scott E. R. D., and Chabot N. L. 2009. Iron meteorites: Crystallization, thermal history, parent bodies, and origin. *Chemie der Erde* 69:293–325. http://dx.doi.org/10.1016/j.chemer.2009.01.002.

Goodrich C. A., and Righter K. 2000. Petrology of unique achondrite Queen Alexandra Range 93148: A piece of the pallasite (howardite-eucrite-diogenite?) parent body? *Meteoritics and Planetary Science* 35:521–535.

Goodrich C. A., Hartmann W. K., O'Brien D. P., Weidenschilling S. J., Wilson L., Michel P., and Jutzi M. 2015. Origin and history of ureilitic material in the solar system: The view from asteroid 2008 TC3 and the Almahata Sitta meteorite. *Meteoritics and Planetary Science* 50:782–809.

Goodrich C. A., Kita N. T., Sutton S. R., Wirick S., and Gross J. 2017. The Miller Range 090340 and 090206 meteorites: Identification of new brachinite-like achondrites with implications for the diversity and petrogenesis of the brachinite clan. *Meteoritics and Planetary Science* 52:949–978.

Hahn T. M., Lunning N. G., McSween H. Y., Bodnar R. J., and Taylor L. A. 2018. Mg-rich harzburgites from Vesta: Mantle residua or cumulates from planetary differentiation? *Meteoritics and Planetary Science* 53:514–546.

Hevey P. J., and Sanders I. S. 2006. A model for planetesimal meltdown by 26Al and its implications for meteorite parent bodies. *Meteoritics and Planetary Science* 41:95–106. http://doi.wiley.com/10.1111/j.1945-5100.2006.tb00195.x.

Holness M. B., Stripp G., Humphreys M. C. S., Veksler I. V., Nielsen T. F. D., and Tegner C. 2011. Silicate liquid immiscibility within the crystal mush: late-stage magmatic

microstructures in the skaergaard intrusion, east greenland. *Journal of Petrology* 52:175–222.

Ikeda Y., and Takeda H. 1985. A model for the origin of basaltic achondrites based on the Yamato 7308 Howardite. *Journal of Geophysical Research* 90:C649.

Jones J. H. 1984. The composition of the mantle of the eucrite parent body and the origin of eucrites. *Geochimica et Cosmochimica Acta* 48:641–648. http://www.sciencedirect.com/science/article/pii/0016703784900929.

Jurewicz A. J. G., Mittlefehldt D. W., and Jones J. H. 1993. Experimental partial melting of the Allende (CV) and Murchison (CM) chondrites and the origin of asteroidal basalts. *Geochimica et Cosmochimica Acta* 57:2123–2139.

Keil K. 2012. Angrites, a small but diverse suite of ancient, silica-undersaturated volcanic-plutonic mafic meteorites, and the history of their parent asteroid. *Chemie der Erde* 72:191–218. http://dx.doi.org/10.1016/j.chemer.2012.06.002.

Keil K. 2014. Brachinite meteorites: Partial melt residues from an FeO-rich asteroid. *Chemie der Erde* 74:311–329. http://dx.doi.org/10.1016/j.chemer.2014.02.001.

Khisina N. R., Wirth R., Abart R., Rhede D., and Heinrich W. 2013. Oriented chromite-diopside symplectic inclusions in olivine from lunar regolith delivered by “Luna-24” mission. *Geochimica et Cosmochimica Acta* 104:84–98. http://dx.doi.org/10.1016/j.gca.2012.10.050.

Mandler B. E., and Elkins-Tanton L. T. 2013. The origin of eucrites, diogenites, and olivine diogenites: Magma ocean crystallization and shallow magma chamber processes on Vesta. *Meteoritics and Planetary Science* 48:2333–2349.

McDonough W. F., and Sun S. s. 1995. The composition of the Earth. *Chemical Geology* 120:223–253.

Mittlefehldt D. W., Bogard D. D., Berkley J. L., and Garrison D. H. 2003. Brachinites: Igneous rocks from a differentiated asteroid. *Meteoritics and Planetary Science* 38:1601–1625.

Mittlefehldt D. W., and Lindstrom M. M. 2003. Geochemistry of eucrites: Genesis of basaltic eucrites, and Hf and Ta as petrogenetic indicators for altered antarctic eucrites. *Geochimica et Cosmochimica Acta* 67:1911–1934.

Mittlefehldt D. W. 2015. Asteroid (4) Vesta: I. The howardite-eucrite-diogenite (HED) clan of meteorites. *Chemie der Erde - Geochemistry* 75:155–183. http://dx.doi.org/10.1016/j.chemer.2014.08.002.

Morishita T., and Arai S. 2003. Evolution of spinel-pyroxene symplectite in spinel-lherzolites from the Horoman Complex, Japan. *Contributions to Mineralogy and Petrology* 144:509–522.

O'Hara M. J., Richardson S. W., and Wilson G. 1971. Garnet-peridotite stability and occurrence in crust and mantle. *Contributions to Mineralogy and Petrology* 32:48–68.

Pack A., Tanaka R., Hering M., Sengupta S., Peters S., and Nakamura E. 2016. The oxygen isotope composition of San Carlos olivine on the VSMOW2-SLAP2 scale. *Rapid Communications in Mass Spectrometry* 1495–1504.

Peters S. T. M., Alibabaie N., Pack A., McKibbin S. J., Raeisi D., Nayebi N., Torab F., Ireland T., and Lehmann B. 2020. Triple oxygen isotope variations in magnetite from iron-oxide deposits, central Iran, record magmatic fluid interaction with evaporate and carbonate host rocks. *Geology* 48.

Pieters C. M., Fischer E. M., Rode O., and Basu A. 1993. Optical effects of space weathering: the role of the finest fraction. *Journal of Geophysical Research* 98.

Raymond S. N., and Izidoro A. 2017. Origin of water in the inner Solar System: Planetesimals scattered inward during Jupiter and Saturn's rapid gas accretion. *Icarus* 297:134–148.

Righter K., and Drake M. J. 1997. A magma ocean on Vesta: Core formation and petrogenesis of eucrites and diogenites. *Meteoritics and Planetary Science* 32:929–944.

Ringwood A. E. 1975. Composition and petrology of the earth's mantle., New York : McGraw-Hill, [1975] http://libproxy.unm.edu/login?url=https://search.ebscohost.com/login.aspx?direct=true&db=cat05987a&AN=unm.940656&site=eds-live&scope=site.

Russell C. T. et al. 2012. Dawn at vesta: Testing the protoplanetary paradigm. *Science* 336:684–686.

Russell C. T. et al. 2016. Dawn arrives at ceres: Exploration of a small, volatile-rich world. *Science* 353:1008–1010.

Sanborn M. E., and Yin Q.-Z. 2014. Chromium isotopic composition of the anomalous eucrites: An additional geochemical parameter for evaluating their origin. *Lunar and Planetary Science 45th*. #2018 (abstr.).

Sanborn M. E., Yin Q.-Z., and Mittlefehldt D. W. 2016. The diversity of anomalous HEDs: Isotopic constraints on the connection of EET 92023, GRA 98098, and Dhofar 700 with Vesta. *Lunar and Planetary Science Conference XLVII* 2256 (abstract).

Sanborn M. E., Wimpenny J., Williams C. D., Yamakawa A., Amelin Y., Irving A. J., and Yin Q. Z. 2019. Carbonaceous achondrites Northwest Africa 6704/6693: Milestones for early Solar System chronology and genealogy. *Geochimica et Cosmochimica Acta* 245:577–596. https://doi.org/10.1016/j.gca.2018.10.004.

Santos A. R., Agee C. B., Shearer C. K., and McCubbin F. M. 2016. Northwest Africa 8535 and Northwest Africa 10463: New insights into the angrite parent body. In *Lunar and Planetary Science Conference XLVII*. p. 2590.

Scott E. R. D., Greenwood R. C., Franchi I. A., and Sanders I. S. 2009. Oxygen isotopic constraints on the origin and parent bodies of eucrites, diogenites, and howardites. *Geochimica et Cosmochimica Acta* 73:5835–5853. http://dx.doi.org/10.1016/j.gca.2009.06.024.

Sharp Z. D. 1990. A laser-based microanalytical method for the in situ determination of oxygen isotope ratios of silicates and oxides. *Geochimica et Cosmochimica Acta* 54:1353–1357. http://linkinghub.elsevier.com/retrieve/pii/001670379090160M%5Cnpapers3://publication/doi/10.1016/0016-7037(90)90160-M.

Shearer C. K., Fowler G. W., and Papike J. J. 1997. Petrogenetic models for magmatism on the eucrite parent body: Evidence from orthopyroxene in diogenites. *Meteoritics and Planetary Science* 32:877–889.

Shields W. R., Murphy T. J., Catanzaro E. J., and Garner E. L. 1966. Absolute isotopic abundance ratios and the atomic weight of a reference sample of chromium. Journal of *Research of the National Bureau of Standards Section A: Physics and Chemistry* 70A:193.

Špaček P., Ackerman L., Habler G., Abart R., and Ulrych J. 2013. Garnet breakdown, symplectite formation and melting in basanite-hosted peridotite xenoliths from zinst (bavaria, bohemian massif). *Journal of Petrology* 54:1691–1723.

Stöffler D., Hamann C., and Metzler K. 2018. Shock metamorphism of planetary silicate rocks and sediments: Proposal for an updated classification system. *Meteoritics and Planetary Science* 53:5–49.

Stolper E. 1975. Petrogenesis of eucrite, howardite and diogenite meteorites. *Nature* 258:220–222.

Stolper E. 1977. Experimental petrology of eucritic meteorites. *Geochimica et Cosmochimica Acta* 41:587–611. http://www.sciencedirect.com/science/article/pii/0016703777903003.

Swindle T. D., Kring D. A., Burkland M. K., Hill D. H., and Boynton W. V. 1998. Noble gases, bulk chemistry, and petrography of olivine-rich achondrites Eagles Nest and Lewis Cliff 88763: Comparison to brachinites. *Meteoritics and Planetary Science* 33:31–48.

Tsiganis K., Gomes R., Morbidelli A., and Levison H. F. 2005. Origin of the orbital architecture of the giant planets of the Solar System. *Nature* 435:459–461.

Turrini D., Coradini A., and Magni G. 2012. Jovian early bombardment: Planetesimal erosion in the inner asteroid belt. *Astrophysical Journal* 750.

Walsh K. J., Morbidelli A., Raymond S. N., O'Brien D. P., and Mandell A. M. 2011. A low mass for Mars from Jupiter's early gas-driven migration. *Nature* 475:206–209. http://dx.doi.org/10.1038/nature10201.

Warren P. H., and Kallemeyn G. W. 1989. Allan Hills 84025: the second brachinite, far more differentiated than brachina, and an ultramafic achondritic clast from L Chondrite Yamato 75097. *Proc. 19th lunar and planetary science conference* 475–486.

Weiss B. P., and Elkins-Tanton L. T. 2013. Differentiated Planetesimals and the Parent Bodies of Chondrites. *Annual Review of Earth and Planetary Sciences* 41:529–560. http://www.annualreviews.org/doi/10.1146/annurev-earth-040610-133520.

Wimpenny J., Sanborn M. E., Koefoed P., Cooke I. R., Stirling C., Amelin Y., and Yin Q. Z. 2019. Reassessing the origin and chronology of the unique achondrite Asuka 881394: Implications for distribution of ^{26}Al in the early Solar System. *Geochimica et Cosmochimica Acta* 244:478–501. https://doi.org/10.1016/j.gca.2018.10.006.

Wostbrock J. A. G., Cano E. J., and Sharp Z. D. 2020. An internally consistent triple oxygen isotope calibration of standards for silicates, carbonates and air relative to VSMOW2 and SLAP2. *Chemical Geology* 533:119432. https://doi.org/10.1016/j.chemgeo.2019.119432.

Yamakawa A., Yamashita K., Makishima A., and Nakamura E. 2009. Chemical separation and mass spectrometry of Cr, Fe, Ni, Zn, and Cu in terrestrial and extraterrestrial materials using thermal ionization mass spectrometry. *Analytical Chemistry* 81:9787–9794.

CHAPTER 2

Petrology and geochemistry of evolved dioritic material from the ureilite parent body

Abstract

New oxygen isotopic analyses of the dioritic achondrite Northwest Africa (NWA) 6698 suggest it is related to the ureilites and the trachyandesite ALM-A. Its felsic mineralogy, igneous textures, and trace element geochemistry reflect a cumulate rock that formed from an evolved melt coeval with the one that produced ALM-A, possibly an extrusive lava or shallow crustal intrusion. Modelling results from the Rhyolite-MELTS algorithm suggest that a combination of equilibrium and fractional crystallization at one atmosphere of pressure can produce the bulk compositions of both rocks and that of their respective glass inclusions.

1. Introduction

Achondrites are planetary materials that have undergone melting and magmatic differentiation from parent bodies that had chondritic abundances for major elements. Typical achondritic materials include the HED (howardite, eucrite, diogenite) meteorites, angrites, and SNC (shergottite, nakhlite, chassignite) meteorites. Of the silicate achondrites assumed to originate from small bodies, the vast majority are basaltic to ultramafic in composition, suggesting that planetary differentiation in the early solar system was limited to core-mantle segregation and production of basaltic crust. Recently, evolved material has been identified in the meteoritic record (e.g. Day et al. 2009; Bischoff et al. 2014; Srinivasan et al. 2018),

overturning the assumption that small planetary bodies were incapable of producing material analogous to that of continental crust on Earth.

The majority of early solar system magmatism is represented by the HED meteorites. The over 2000 named HEDs are all mafic or ultramafic rocks and are thought to originate from the asteroid 4-Vesta, the second largest body in the asteroid belt (Mittlefehldt 2015). The angrites compose another significant group of basaltic meteorites with a unique parent body and some of the lowest volatile abundances in the solar system (Keil 2012). Meanwhile, the aubrites are a group of igneous rocks composed largely of nearly FeO-free enstatite, and they represent the most reduced magmatism in the solar system (Keil 2010). The SNC meteorites are generally agreed to originate on Mars and include ultramafic cumulate rocks (poikilitic shergottites, nakhlites, and chassignites) and basaltic materials (basaltic, phyric, and gabbroic shergottites), suggesting that the Martian crust is mostly basaltic (Nyquist et al. 2001). However, the martian crustal breccia NWA 7034 is volatile-rich and contains evolved clasts that challenge this view (Agee et al. 2013; Humayun et al. 2013; Santos et al. 2015; Hewins et al. 2017). Likewise, in situ rover observations suggest the presence of evolved continental crust on Mars (Sautter et al. 2015).

Recent challenges to the predominantly basaltic achondrite paradigm include discovery of the paired Antarctic meteorites Graves Nunataks (GRA) 06128 and 06129, which are rich in sodic plagioclase and likely represent low degrees of partial melting of chondritic materials (Shearer et al. 2010). These meteorites show plutonic and granoblastic textures, chemically equilibrated silicates, and andesitic bulk compositions (Day et al. 2009). The brachinites, which are dunitic primitive achondrites, might be residues of the partial melting that produced GRA

06128/9 (Day et al. 2012a). Northwest Africa (NWA) 11119 is a silica-rich andesitic to dacitic rock and is one of the oldest examples of volcanism in the solar system (Srinivasan et al. 2018).

Evolved volcanism is also associated with the ureilite parent body. The ureilites comprise over 500 ultramafic rocks composed primarily of Mg-rich olivine (Fo_{75-90}) and pyroxene that varies in composition with Fo content but is primarily pigeonite (Goodrich et al. 2017). They also contain wt.% levels of interstitial graphite and Fe metal inclusions associated with a partial melting and smelting event (Singletary and Grove 2003, 2006). As residues of partial melting (e.g. Warren and Kallemeyn 1992), they are likely mantle materials of a parent body that was never completely melted before it was disrupted, and whose oxygen isotopic composition was thus not homogenized (Clayton and Mayeda 1996). The Almahata Sitta meteorites, which fell in 2008 in Sudan, contain the trachyandesitic fragment ALM-A, which is an example of extrusive volcanism in the early solar system likely implicated in the partial melting event that left the ureilites as residues (Bischoff et al. 2014; Barrat et al. 2016). A snapshot of ureilite anatexis is also recorded by the quenched trachyandesitic glass present in the ureilite Ramlat as Sahmah 517 (Rosén et al. 2019).

The ^{26}Al-^{26}Mg geochronometer constrains the crystallization ages of GRA 06128/9, NWA 11119, and ALM-A to within 7 Ma of CAI formation (Shearer et al. 2010; Bischoff et al. 2014; Srinivasan et al. 2018). This suggests that they originated from small parent bodies which melted and crystallized early, as opposed to a terrestrial planet such as Mars, which maintained a molten “magma ocean” or was at least partially molten for tens of Ma (Debaille et al. 2007; Borg et al. 2016; Kruijer et al. 2017). On Earth, the formation of andesitic crust is associated with convergent margins, orogenesis, and subducting tectonic plates (e.g. Gómez-Tuena et al. 2014). The petrogenesis of similar materials on smaller bodies, which lack plate tectonics, is much less

well-understood. However, the degree of magmatic evolution on planetary bodies likely depends on factors such as the composition of the starting material, degree of melting, and oxygen fugacity (fO_2).

Oxygen isotopic heterogeneity in the presolar nebula was imprinted onto the planetary bodies that accreted from it (Clayton 2002), allowing for the "fingerprinting" of parent body origin of planetary materials using their oxygen isotopic composition. The present study focuses on the diorite Northwest Africa (NWA) 6698, whose oxygen isotopic composition plots in the region of carbonaceous chondrites and ureilites. The ureilites are generally thought to be low-degree melting residues of a chondritic protolith that first experienced the segregation of Fe-Ni-S from silicates (Warren et al. 2006; Goodrich et al. 2007) and then fractional melting which depleted the incompatible elements in the silicate residues (Barrat et al. 2016).

Feldspar-rich clasts identified within polymict ureilites likely represent basaltic components of this anatexis, and some of these clasts represent more fractionated material as they contain phosphates, ilmenite, silica, and incompatible-enriched glass (Cohen et al. 2004). However, the trachyandesite ALM-A is the only evolved rock ever identified as associated with the ureilites (Bischoff et al. 2014). While ALM-A was generated by extrusive volcanism, NWA 6698 is a cumulate likely generated by similar magmatic processes. Here we present petrological and geochemical analyses and modelling results to better constrain evolved magmatism on the ureilite parent body.

2. Samples and Methods

NWA 6698 was found as a single 38.4 g stone in October, 2009 and purchased from a meteorite dealer in 2010 in Erfoud, Morocco. It was initially characterized as a dioritic

ungrouped achondrite (Bunch et al. 2011). For the present study, some of the 2.8 g deposit sample from Northern Arizona University was mounted in epoxy and polished to 0.05 μm smoothness for electron probe microanalysis (EPMA), scanning electron microscopy (SEM), and laser ablation inductively coupled plasma mass spectrometry (LA-ICP-MS). Several fragments were also used for oxygen isotopic analysis.

Polished mounts were analyzed by electron probe microanalysis (EPMA) using a JEOL 8200 SuperProbe at UNM. Analytical techniques included qualitative energy-dispersive X-ray spectroscopy (EDS) and quantitative wavelength-dispersive X-ray spectroscopy (WDS), including WDS mapping. An accelerating voltage of 15 kV, a beam current of 20 nA, and a spot size of 1 μm were used for analyses. Spot sizes were increased to 10 μm for phases that included volatile elements. Standards for WDS analysis were manufactured by the C.M. Taylor Standard Corporation in Sunnyvale, CA. Averaged microprobe analyses of constituent phases, BSE mosaic images, and mineral densities were used to formulate bulk compositions with ImageJ thresholding software.

Seven fresh fragments of interior materials of NWA 11575 weighing between 1-3 mg were selected under a stereomicroscope to avoid any possible contamination from fusion crust. Oxygen isotopic analyses were performed using a CO_2 laser + BrF_5 fluorination system following modified procedures outlined in Sharp (1990). Oxygen isotope compositions were calculated using the following procedure: The $\delta^{17,18}O$ values refer to the per mil deviation of a sample's ($^{17}O/^{16}O$) and ($^{18}O/^{16}O$) ratios from the V-SMOW standard values, respectively, expressed as $\delta^{17,18}O = [(^{17,18}O/^{16}O)_{sample}/(^{17,18}O/^{16}O)_{V\text{-}SMOW} - 1]*10^3$. The delta values were then converted to logarithmic δ' in which $\delta^{17,18}O' = \ln(\delta^{17,18}O/1000 + 1)*1000$. The $\Delta^{17}O'$ values were

obtained from the δ′ values following $\Delta^{17}O' = \delta^{17}O' - 0.528 * \delta^{18}O'$. Typical analytical precision of the laser-fluorination technique is better than ± 0.02‰ for $\Delta^{17}O'$.

Laser ablation ICP-MS (LA-ICP-MS) measurements were performed on epoxy-mounted sections using an Electro Scientific Instruments New Wave™ UP193FX excimer laser ablation system coupled to a Thermo Element XR™ at the Plasma Analytical Facility, Florida State University. Analytical methods employed followed Yang et al. (2015) and Oulton et al. (2016). Mineral grains were analyzed with laser spot sizes of 50 or 100 μm, with a repetition rate of 50 Hz and a dwell time of 10 s of ablation. The bulk composition was determined by rastering the laser over an area of 3.9 mm^2 using a 150 μm spot size scanned at 25 μm/s with a repetition rate of 50 Hz (about 60 μm depth). Peaks analyzed, interference corrections, and standardization followed Yang et al. (2015, 2018). Major elements were determined using methods described in Humayun et al. (2010). The USGS glasses BHVO-2g, BCR-2g and BIR-1g, NIST SRM 610, NIST 1263, a steel, and the iron meteorites North Chile (Filomena) and Hoba were used as standards to calibrate the abundances of about 60 elements (Humayun 2012; Yang et al. 2018). Detection limits were determined from the 3-sigma standard deviation of the blanks taken with the laser off. Peaks not detected are shown as n.d. Precision of LA-ICP-MS analyses for major elements on spots is in the 2–5% range (Humayun et al. 2010), and for trace elements, it varies as a function of the concentration from 2% to 10%, except for elements near the detection limit where it is larger (Yang et al. 2018).

3. Results

3.1 Mineralogy and Petrology

NWA 6698 is a diorite with a cumulate texture. It is composed of subhedral oligoclase to labradorite plagioclase (61 wt.%), pigeonite (18 wt.%), augite (11 wt.%), interstitial microlitic glass (6 wt.%), phosphates including apatite and merrillite (2 wt.%), a Cr- and Ti-rich spinel (1 wt.%), and trace FeNi metal grains associated with sulfides. Pyroxenes are unzoned and uniform in backscattered electron (BSE) imagery, suggesting that they are well-equilibrated (Fig. 1). While plagioclase compositions are variable (An_{19-52}), pyroxene compositions are uniform ($Fs_{33.8\pm0.4}Wo_{9.0\pm0.1}$; $Fs_{18.8\pm0.2}Wo_{37.8\pm0.3}$) (Fig. 2). Major phase (plagioclase and pyroxene) compositions overlap with those of the trachyandesite ALM-A (Bischoff et al. 2014). Spinels in NWA 6698 are likewise uniform in composition and contain primarily Fe, Cr, and Ti (Fig. 3). The microlitic glass is quartz-normative and contains sub-µm pyroxene lathes. A summary of the microprobe analyses is shown in Table 1.

The major phases in NWA 6698 display a poikilitic texture, with large >1 mm feldspar oikocrysts that enclose 0.1-1 mm pyroxene chadacrysts. Microlitic glass is found in interstitial spaces between the major minerals. The overall composition is andesitic or dioritic, while the glass is trachytic (Fig. 4). In some instances, glass is heavily weathered such that most of it has been removed, leaving a skeletal microstructure. Submicron-sized FeNi-sulfide grains are scattered throughout the meteorite as inclusions in major phases. Approximately one half of accessory phosphate grains are anhydrous Cl-F-apatite, while the other half are merrillite that contain <0.5 wt% F.

3.2 Oxygen Isotopes

Figure 5 shows results of seven laser-fluorination oxygen isotope analyses. The measured values plot in the field of the ureilites and form a linear trend that crosses the carbonaceous chondrite anhydrous mineral (CCAM) line. Previous oxygen isotopic measurements reported by Bunch et al. (2011), which plotted in the field of the ordinary chondrites on the opposite side of the terrestrial fractionation line (TFL), were erroneous. The new measurements overlap with measurements of the trachyandesite ALM-A and define a mass fractionation line with a slope of 0.52 ($R^2 = 0.99$). Measurements of other evolved achondrites such as NWA 7325 and 11119 plot in the vicinity of the NWA 6698 trend line.

3.3 Major and Trace Element Geochemistry

Table 2 shows a summary of major and trace element analyses by LA-ICP-MS on individual phases in NWA 6698 as well as a bulk raster across an area of ~4 mm^2 of the thick section. To ensure that the bulk raster is representative, a correction was applied to compensate for the lack of glass in the raster area and to balance modal mineralogy in line with the bulk rock. Deficiencies and excesses of major phase percentages were eliminated by subtracting or adding, respectively, the average analyses of each element for each phase in proportions determined by modal differences between SEM maps of the bulk rock versus the area rastered by LA-ICP-MS. Major element analyses of minerals by LA-ICP-MS are nearly identical those performed by EPMA, with slight deviations in SiO_2 measurements that show no resolvable influence on trace element analyses.

The trace element composition of NWA 6698 is typical for a cumulate rock rich in plagioclase, as bulk measurements show elevations in Sr and Eu relative to CI chondrites. Rare

earth element (REE) analyses in plagioclase grains show strong Eu anomalies, while other phases show complementary negative Eu anomalies (Fig. 6). Microlitic glass analyses show enrichments in high field strength elements (HFSE) Ti, Zr, Nb, Hf, and Ta relative to the bulk rock and CI-chondrites (Fig. 7), suggesting the crystallization of HFSE-bearing phases such as zircon and titanomagnetite. NWA 6698 is anomalously low in Th/U for an igneous rock, likely due to terrestrial U addition via desert weathering (e.g. Bland et al. 2006). The trace element pattern of NWA 6698 is similar to that of the trachyandesite ALM-A, however the former shows depletions in LREE and stronger positive Eu and Sr anomalies. The extremely high Ba in NWA 6698 is likely a result of terrestrial weathering.

4. Discussion

4.1 Relationship of NWA 6698 to Ureilites and Trachyandesite ALM-A

While NWA 6698 was initially classified as a dioritic ungrouped achondrite related to the ordinary chondrites (Bunch et al. 2011), the oxygen isotopic analyses presented here negate that association. All 7 new analyses overlap with the ureilites, the trachyandesite ALM-A, and the ungrouped achondrite NWA 11119 (Fig. 5). The slope defined by these analyses is parallel to the terrestrial fractionation line (TFL) with a constant $\Delta^{17}O$ of -1.026 ± 0.015, suggesting that the linear trend defined by the oxygen isotopes is a result of igneous differentiation. The overlapping bulk oxygen isotopic and the similar pyroxene and feldspar mineral compositions of NWA 6698 and ALM-A suggest that the two rocks were produced by the same igneous processes on the ureilite parent body.

ALM-A was interpreted as an extrusive lava due to the presence of anorthoclase grains and rhyolitic glass inclusions (Bischoff et al. 2014). While NWA 6698 contains an analogous

interstitial trachytic glass, no anorthoclase was identified despite its identical K content, and its igneous texture represents a cumulate origin. ALM-A contains zoned plagioclase grains with labradorite cores and albite fringes. The plagioclase grains in NWA 6698 are more limited compositionally (albite to oligoclase) and lack such zoning, suggesting that they crystallized more slowly. The CIPW normative feldspar compositions calculated for the bulk composition of NWA 6698 support this, with an average anorthite content of 29%.

NWA 6698 and ALM-A have an identical Mg# [Mg/(Mg+Fe)] of 0.61, which is expected for melts in equilibrium with ureilites given an olivine-melt distribution coefficient K_D $[(Fe/Mg)_{olivine}/(Fe/Mg)_{melt}]$ of 0.28 (Kushiro and Mysen 2002; Bischoff et al. 2014). The positive Eu anomaly in NWA 6698 (Eu/Eu* = 5.61) is much higher than in ALM-A (Eu/Eu* = 1.63), but other than Eu it is lower in REE relative to ALM-A. This suggests that it accumulated in a magma chamber under reducing conditions and was depleted in trace elements relative to the melt that ALM-A crystallized from. Enrichments in HFSE in the glass likely reflect enrichments of those elements in the magma, and these enrichments are likewise shown in ALM-A (Bischoff et al. 2014).

Melting of the ureilite parent body proceeded in at least two steps. First, a chondritic precursor produced a S-rich metallic melt at the FeNiS eutectic, resulting in siderophile element depletions in ureilites and possibly the formation of an S-rich core (Warren et al. 2006; Rankenburg et al. 2008; Goodrich et al. 2013; Barrat et al. 2015). Next, silicate melting and melt extraction from the ureilite precursors resulted in the felsic mineral and lithophile trace element depletions in the ureilites and the formation of the feldspathic clasts, the trachyandesite ALM-A, and the diorite NWA 6698 (Cohen et al. 2004; Kita et al. 2004; Bischoff et al. 2014; Barrat et al. 2016). Previous models have invoked the smelting of graphite and olivine in the ureilite

precursor to produce the pigeonite and secondary metal present in ureilites, and this necessarily produces enough CO and CO_2 gas for explosive volcanism that ejects lavas from the parent body (Warren and Kallemeyn 1992). However, the trace element systematics of the ureilites are independent of their olivine compositions, suggesting that smelting is not necessary to generate the olivine Mg# diversity found in the ureilites (Barrat et al. 2016). The range in ureilite olivine Mg# is instead likely inherited from accretion, as it correlates with oxygen isotopic composition and Fe/Mn ratio (Clayton and Mayeda 1996; Warren and Huber 2006), as well as carbon and chromium isotopic composition (Barrat et al. 2017; Zhu et al. 2020). While ureilite smelting resulted in the forsteritic reduction rims found around their olivine grains, this was probably a late-stage process related to parent body disruption (Warren and Rubin 2010) and not implicated in the melting episodes discussed here.

The trace element systematics of the ureilites suggest that at least two episodes of fractional to dynamic melting are necessary to produce their characteristic depletion patterns (Fig. 7) (Barrat et al. 2016). The first episode would have exhausted most of the plagioclase in the source and thus produced a trachyandesitic melt, while the second must have continued past plagioclase exhaustion to produce an Al-undersaturated melt and further deplete the trace elements in ureilites. Although multiple melts of differing character must be invoked to explain ureilite trace element systematics, NWA 6698 is clearly linked to the trachyandesitic melt, and the second melt composition remains mysterious and unrepresented in the meteorite record. Alternatively, the melts are a continuum, and many more varied melt compositions existed on the ureilite parent body.

4.2 Petrogenetic Modelling and Provenance

To test whether the cumulate-melt relationship between NWA 6698 and ALM-A is viable, we ran several equilibrium and fractional crystallization models using the Rhyolite-MELTS algorithm (Gualda et al. 2012). Models were run at 1 atmosphere of pressure, since the ureilite parent body is generally understood to be less than a few hundred km in diameter, and the MELTS algorithm is only sensitive to kilobar-scale changes in pressure. The bulk composition of ALM-A was allowed to crystallize from the calculated liquidus of 1470° C to its solidus in 10° C steps for equilibrium crystallization sequences and 1° C steps for fractional crystallization sequences in which fractionated all solids. Oxygen fugacity was varied between 3 log units below the iron-wüstite (IW) buffer to one log unit above (IW-3 to IW+1) but showed negligible change in liquid composition. Both equilibrium and fractional crystallization paths produced liquid compositions similar to those of the NWA 6698 glass (Fig. 8). The glass inclusions in ALM-A are lower in alkalis than the equilibrium and fractional liquid lines of descent (LLD), suggesting that a more complex model is needed to explain their composition. Both the fractional and equilibrium crystallization schemes reproduced the feldspar compositions in ALM-A and NWA 6698 (Fig. 9), suggesting that NWA 6698 could have formed as a cumulate in a fractionating magma chamber with the liquid composition of ALM-A.

While the MELTS modelling results suggest that NWA 6698 and ALM-A could be produced by the same magmatic process, in the same magma chamber on the ureilite parent body, they do not prove that this is the case. Moreover, NWA 6698 is a find with unknown crystallization age. ALM-A was recovered from an observed 2008 fall with a crystallization age of 6.5 Ma after CAI (Bischoff et al. 2014). If the two stones are indeed sourced from the same magma chamber, then their crystallization ages should be indistinguishable.

5. Conclusions

The discovery of NWA 6698 provides additional evidence of pervasive silicate melting on the ureilite parent body that produced a wide range of felsic compositions (Cohen et al. 2004; Kita et al. 2004), a trachyandesitic extrusive lava (Bischoff et al. 2014), and now a dioritic cumulate rock. Its oxygen isotopic composition, mineralogy, and major and trace element geochemistry connect it to both the trachyandesite ALM-A and the ureilite parent body. Its composition yields additional constraints that can be applied to ureilite anatexis and melt evolution. The results of petrogenetic modelling suggest that a combination of equilibrium and fractional crystallization within a magma chamber below the surface of the ureilite parent body can produce the diorite NWA 6698 as a plagioclase cumulate. The melt involved in this process can then crystallize the extrusive or shallow crustal trachyandesite ALM-A.

Figures & Tables

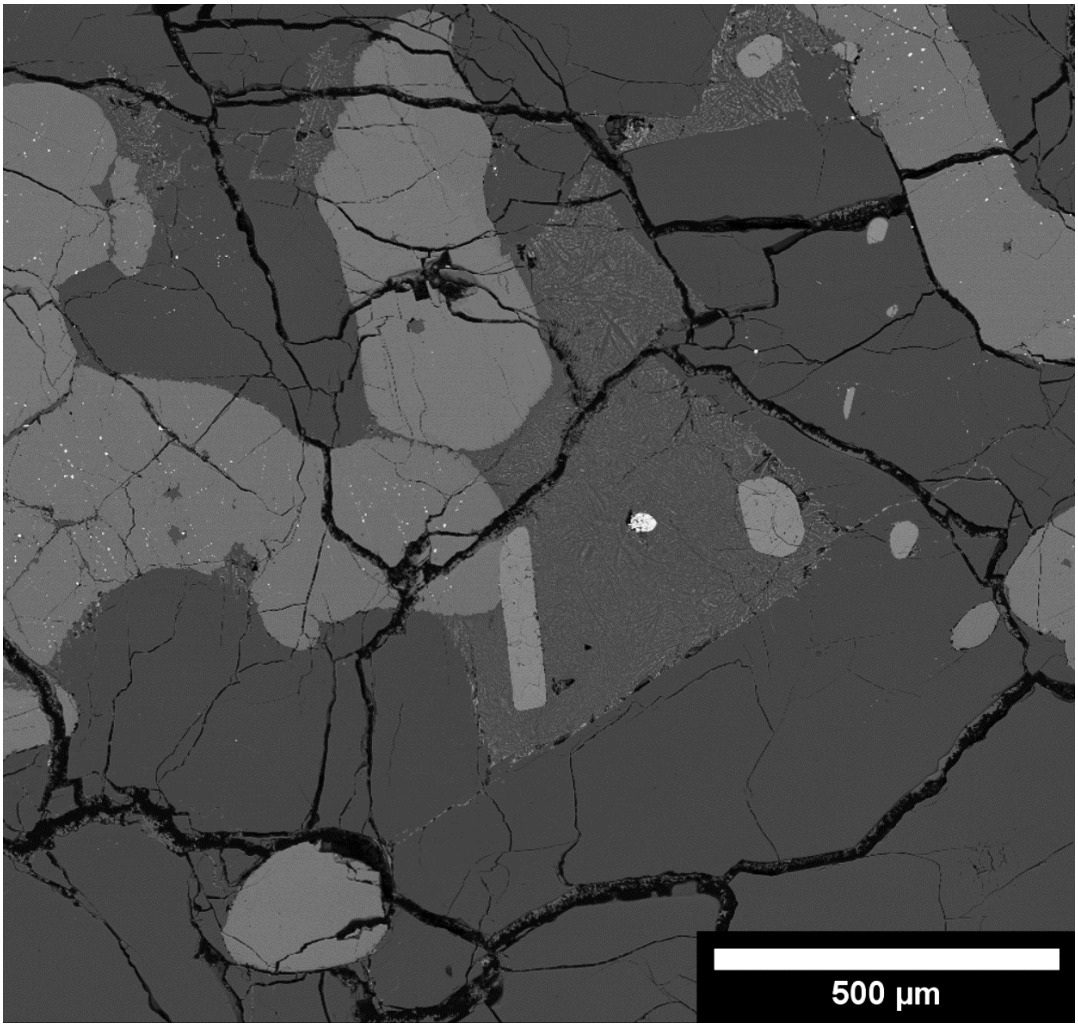

Figure 1. BSE image of NWA 6698. Phases shown are (in ascending brightness) plagioclase, pyroxene, chlorapatite, Fe-sulfide, and FeNi metal. Microlitic glass is seen in the center of the image.

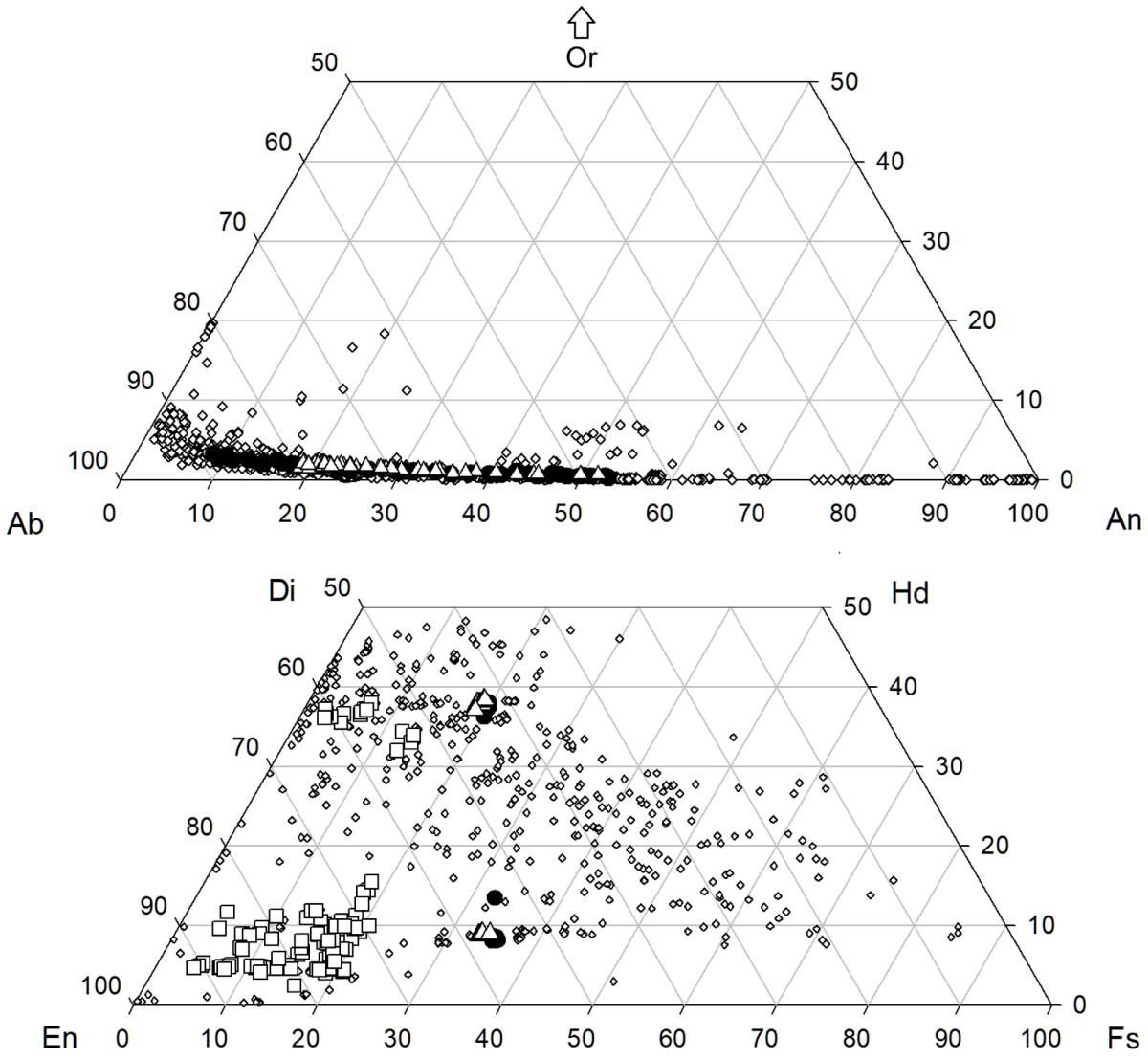

Figure 2. Ternary diagrams showing feldspar and pyroxene compositions in NWA 6698 (white triangles), ALM-A (black circles) (Bischoff et al. 2014) ureilites (white squares) (Collinet and Grove 2020 and references within), and feldspathic clasts in polymict ureilites (white diamonds) (Cohen et al. 2004).

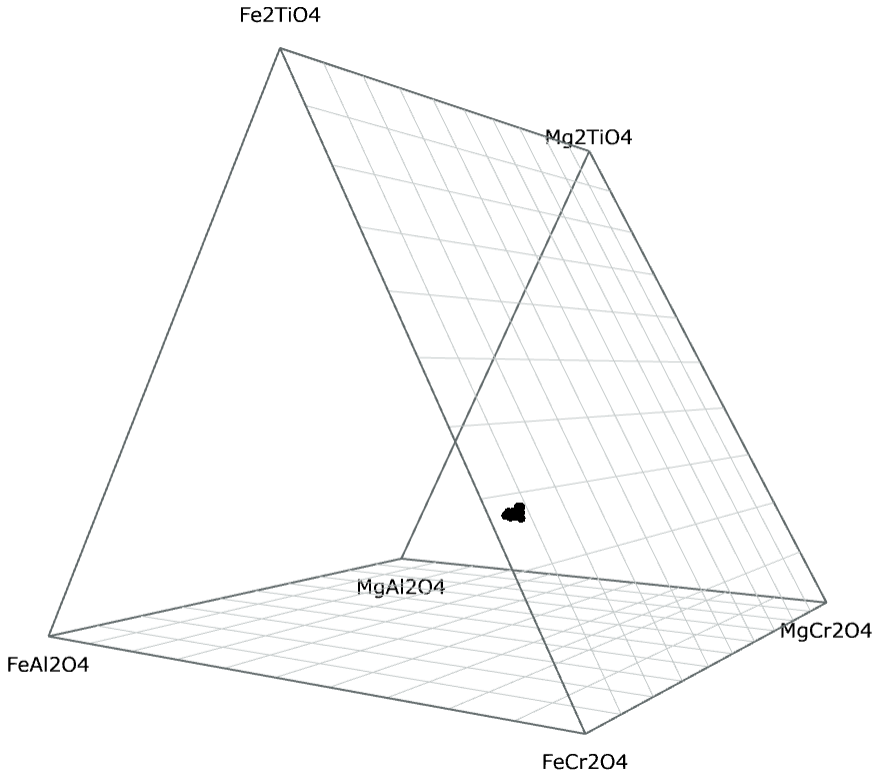

Figure 3. Prism showing composition of spinels in NWA 6698. Plotted with Spinel Web (Antonini et al. 2020).

Table 1. Summary of EPMA measurements for phases in NWA 6698.

NWA 6698	Plagioclase (n=52)		Pigeonite (n=15)		Augite (n=25)		Spinel (n=16)		Glass (n=12)		Merrillite (n=16)		Apatite (n=12)	
	Avg.	Stdev	Avg.	Stdev	Avg.	Stdev	Avg.	Stdev	Avg.	Stdev	Avg.	Stdev	Avg.	Stdev
Al_2O_3	24.10	1.94	0.34	0.01	0.72	0.03	3.51	0.20	13.68	0.99	n.a.		n.a.	
SiO_2	62.22	2.79	53.04	0.34	52.72	0.36	0.04	0.00	67.23	0.50	n.a.		n.a.	
TiO_2	n.a.		0.55	0.02	1.15	0.03	15.47	0.27	1.16	0.08	n.a.		n.a.	
Cr_2O_3	n.a.		0.44	0.01	0.84	0.02	37.86	0.41	0.03	0.02	n.a.		n.a.	
Na_2O	8.47	0.92	0.15	0.01	0.53	0.02	0.02	0.01	7.51	0.46	1.51	0.19	0.58	0.05
MgO	0.04	0.01	19.34	0.25	14.60	0.27	5.06	0.34	1.37	0.26	3.16	0.16	0.51	0.07
MnO	0.01	0.01	1.17	0.02	0.72	0.02	1.01	0.03	0.19	0.04	n.a.		n.a.	
FeO	0.09	0.03	20.35	0.16	11.26	0.08	35.12	0.53	4.78	0.66	1.76	0.25	0.83	0.15
NiO	n.a.		0.01	0.01	0.01	0.01	0.01	0.01	0.01	0.02	n.a.		n.a.	
K_2O	0.28	0.06	0.02	0.01	0.02	0.01	0.03	0.01	1.06	0.16	n.a.		n.a.	
CaO	5.63	1.63	4.23	0.05	17.65	0.10	0.02	0.02	2.50	0.28	47.06	0.17	52.83	0.17
V_2O_3	n.a.		n.a.		n.a.		0.64	0.11	n.a.		n.a.		n.a.	
P_2O_5	n.a.		n.a.		n.a.		n.a.		n.a.		45.21	1.07	40.91	0.98
Cl	n.a.		n.a.		n.a.		n.a.		n.a.		0.00	0.00	3.10	0.09
F	n.a.		n.a.		n.a.		n.a.		n.a.		0.43	0.08	1.79	0.09
OH (calculated)	n.a.		n.a.		n.a.		n.a.		n.a.		n.a.		0.18	0.13
Total	100.83		99.64		100.23		98.78		99.52		99.12		100.73	

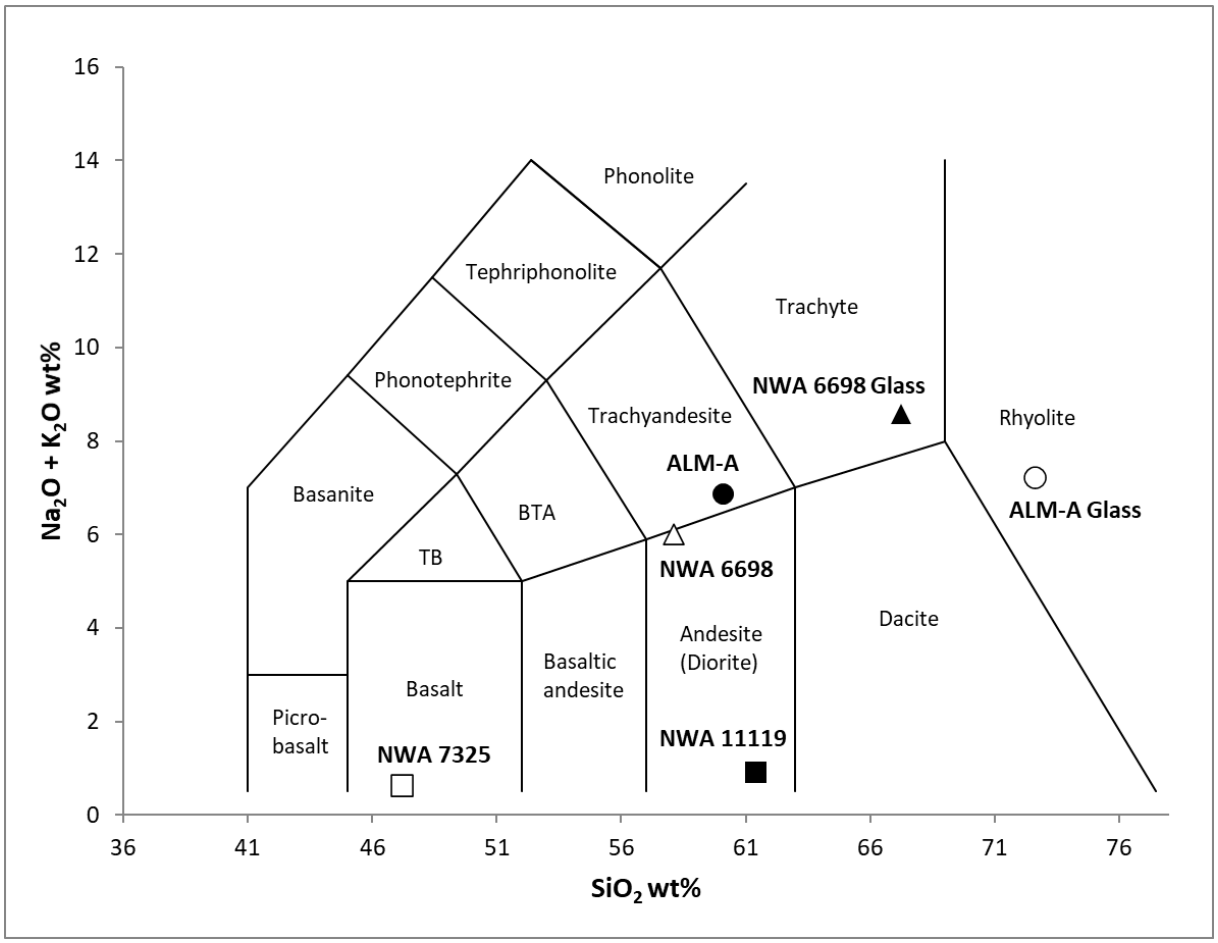

Figure 4. Total alkali-silica (TAS) diagram showing compositions of NWA 6698 and other related achondrites.

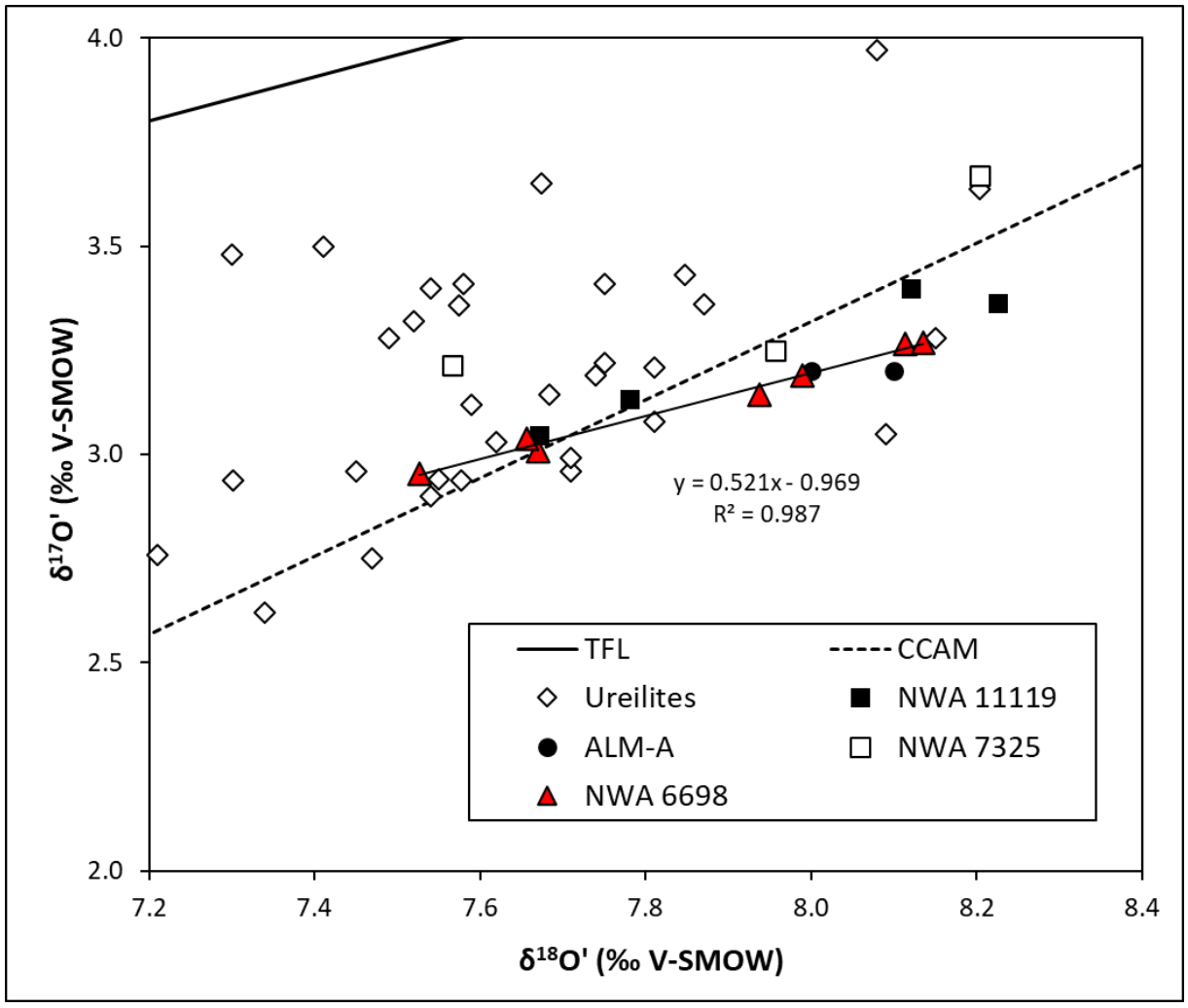

Figure 5. Triple oxygen isotope diagram showing NWA 6698, ureilites (Clayton and Mayeda 1996; Greenwood et al. 2017), and other achondrites (Irving et al. 2013; Bischoff et al. 2014; Srinivasan et al. 2018) that plot in the vicinity. TFL = terrestrial fractionation line; CCAM = carbonaceous chondrite anhydrous minerals line.

Table 2. Summary of LA-ICP-MS measurements for phases in NWA 6698 and bulk raster.

NWA 6698	Plagioclase (n=7)		Pigeonite (n=5)		Augite (n=9)		Glass (n=3)		Phosphate (n=1)	Bulk Raster (n=1)
	Avg.	Stdev	Avg.	Stdev	Avg.	Stdev	Avg.	Stdev		
Na_2O	8.10	0.71	0.14	0.02	0.54	0.07	7.17	0.22	0.85	4.96
MgO	0.04	0.01	19.01	0.44	15.29	1.04	1.66	0.03	2.98	6.83
Al_2O_3	27.18	2.22	0.33	0.04	0.80	0.15	12.86	0.75	0.13	14.06
SiO_2	57.00	3.35	52.94	0.55	49.76	1.57	66.25	0.76	1.30	55.72
P_2O_5	0.032	0.020	0.013	0.006	0.024	0.008	0.798	0.028	52.62	0.680
K_2O	0.25	0.07	0.02	0.01	0.03	0.01	1.59	0.28	0.05	0.28
CaO	7.20	1.68	4.16	0.29	19.19	1.88	2.85	0.08	39.30	8.87
TiO_2	0.09	0.03	0.52	0.03	1.14	0.08	1.34	0.06	0.01	0.46
MnO	0.00	0.00	1.22	0.01	0.77	0.07	0.21	0.01	0.21	0.40
FeO	0.11	0.06	21.66	0.33	12.47	1.24	5.27	0.38	2.54	7.75
V	0	0	39	2	111	22	7	0	11	34
Cr	19	37	3174	62	5752	328	332	30	245	1877
Sc	2	0	39	2	113	12	15	1	51	30
Li	2	1	4	1	3	0	17	2	7	5
Be	0.35	0.39	bdl	bdl	bdl	bdl	0.36	0.10	bdl	0.04
B	0.5	0.3	0.6	0.1	0.6	0.1	15.1	0.9	4.7	2.1
Co	0	0	2	1	1	1	1	1	19	17
Ni	8	13	18	25	12	26	2	3	256	500
Cu	0	0	1	1	2	2	2	1	8	15
Zn	8	2	693	51	256	30	212	23	46	195
Ga	33	4	3	0	6	1	31	0	10	23
Ge	0.20	0.04	0.15	0.03	0.09	0.04	0.16	0.00	1.53	0.13
As	bdl	bdl	0.06	0.02	0.03	0.01	0.07	0.04	0.85	0.19
Se	0.20	0.08	0.18	0.06	0.18	0.09	0.12	0.04	1.10	0.46
Rb	1.27	0.51	0.38	0.24	0.89	0.47	75.65	9.55	0.40	5.77
Sr	177	16	1	1	6	1	36	1	159	102
Y	0.1	0.0	2.6	0.1	9.4	1.1	10.9	0.6	1218.0	4.0
Zr	0.3	0.3	3.2	0.4	17.9	3.2	150.5	24.2	1.8	13.4
Nb	0.02	0.04	0.06	0.01	0.15	0.13	12.99	1.22	0.07	0.87
Mo	bdl	bdl	0.14	0.06	0.07	0.01	0.02	0.01	0.43	0.15
Ag	bdl	bdl	0.01	0.00	0.01	0.00	0.04	0.01	0.05	0.03
Cd	0.04	0.02	0.08	0.03	0.06	0.02	0.09	0.01	0.15	0.06
In	bdl	bdl	bdl	bdl	0.003	0.002	0.041	0.035	bdl	0.006
Sn	0.03	0.01	0.07	0.09	0.03	0.01	0.17	0.04	0.16	0.10
Sb	0.03	0.01	0.02	0.01	0.01	0.00	0.15	0.22	0.05	0.03
Cs	bdl	bdl	bdl	bdl	0.04	0.02	3.96	0.60	0.04	0.32
Ba	24	3	4	2	3	4	31	7	50	43

La	0.08	0.03	0.02	0.01	0.09	0.03	0.94	0.05	149.80	0.31
Ce	0.14	0.04	0.06	0.03	0.34	0.03	2.29	0.05	344.85	0.92
Pr	0.02	0.00	0.01	0.00	0.08	0.01	0.34	0.00	57.51	0.13
Nd	0.07	0.06	0.07	0.02	0.58	0.05	1.72	0.04	307.94	0.71
Sm	0.02	0.00	0.05	0.01	0.36	0.04	0.63	0.02	107.81	0.27
Eu	1.06	0.07	0.01	0.00	0.07	0.01	0.36	0.03	9.26	0.63
Gd	0.02	0.01	0.13	0.01	0.79	0.12	1.07	0.04	172.31	0.43
Tb	0.00	0.00	0.03	0.00	0.17	0.02	0.21	0.01	29.14	0.08
Dy	0.02	0.02	0.34	0.03	1.37	0.16	1.67	0.01	205.72	0.66
Ho	0.00	0.00	0.10	0.00	0.34	0.03	0.40	0.00	43.46	0.15
Er	0.01	0.00	0.40	0.02	1.15	0.11	1.37	0.05	126.59	0.51
Tm	0.00	0.00	0.07	0.01	0.19	0.02	0.24	0.03	17.14	0.08
Yb	0.01	0.01	0.62	0.05	1.41	0.11	1.79	0.03	94.61	0.63
Lu	bdl	bdl	0.12	0.01	0.25	0.02	0.29	0.01	13.94	0.11
Hf	0.02	0.02	0.13	0.01	0.66	0.09	3.98	0.47	0.13	0.41
Ta	bdl	bdl	0.003	0.001	0.008	0.008	0.717	0.103	0.002	0.048
W	0.022	0.028	0.003	0.001	0.007	0.009	0.023	0.004	0.022	0.055
Tl	0.003	0.001	0.001	0.001	0.002	0.001	0.050	0.006	0.011	0.009
Pb	0.080	0.025	0.121	0.086	0.083	0.036	0.507	0.208	5.081	0.834
Bi	0.013	0.023	0.004	0.003	0.002	0.002	0.013	0.010	0.008	0.025
Th	0.007	0.004	0.009	0.005	0.009	0.008	0.395	0.013	10.064	0.067
U	0.003	0.002	0.005	0.005	0.004	0.003	0.240	0.062	0.712	0.070

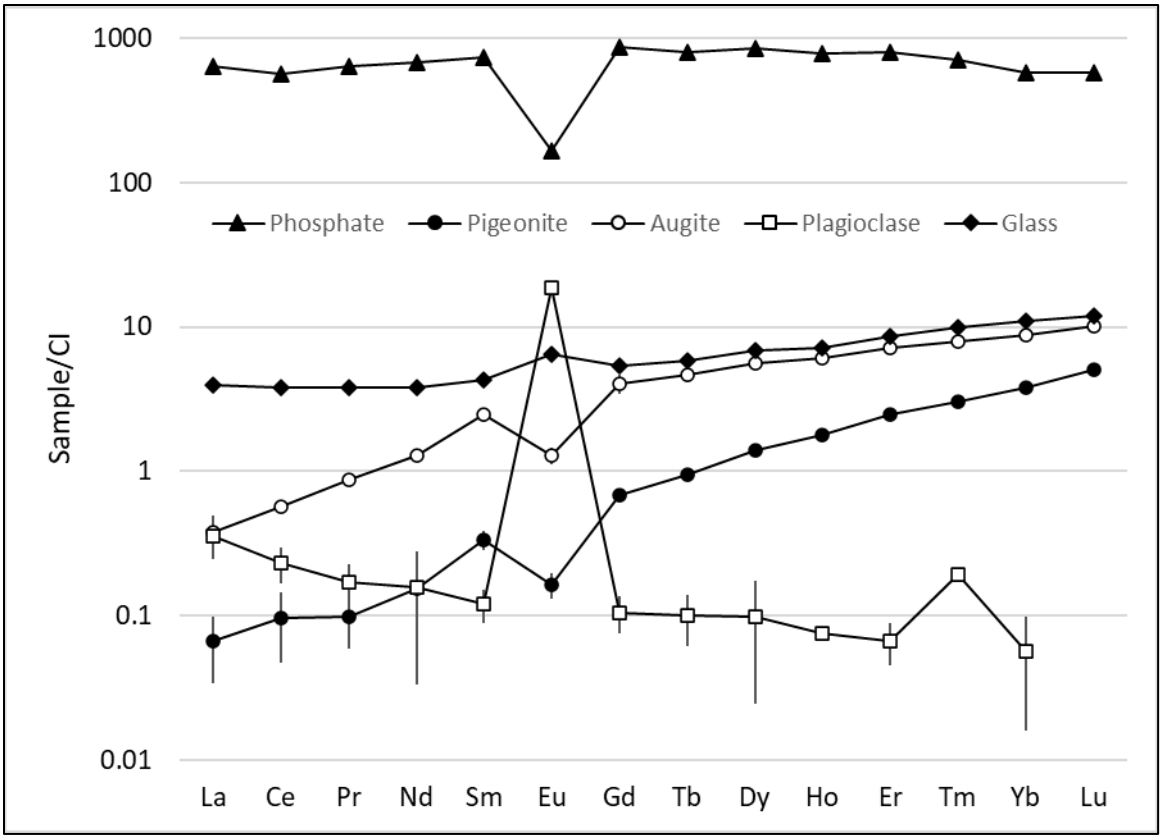

Figure 6. CI-normalized (Anders and Grevesse 1989) REE diagram showing LA-ICP-MS analyzed phases. Error bars are 1σ deviations for phases with multiple analyses.

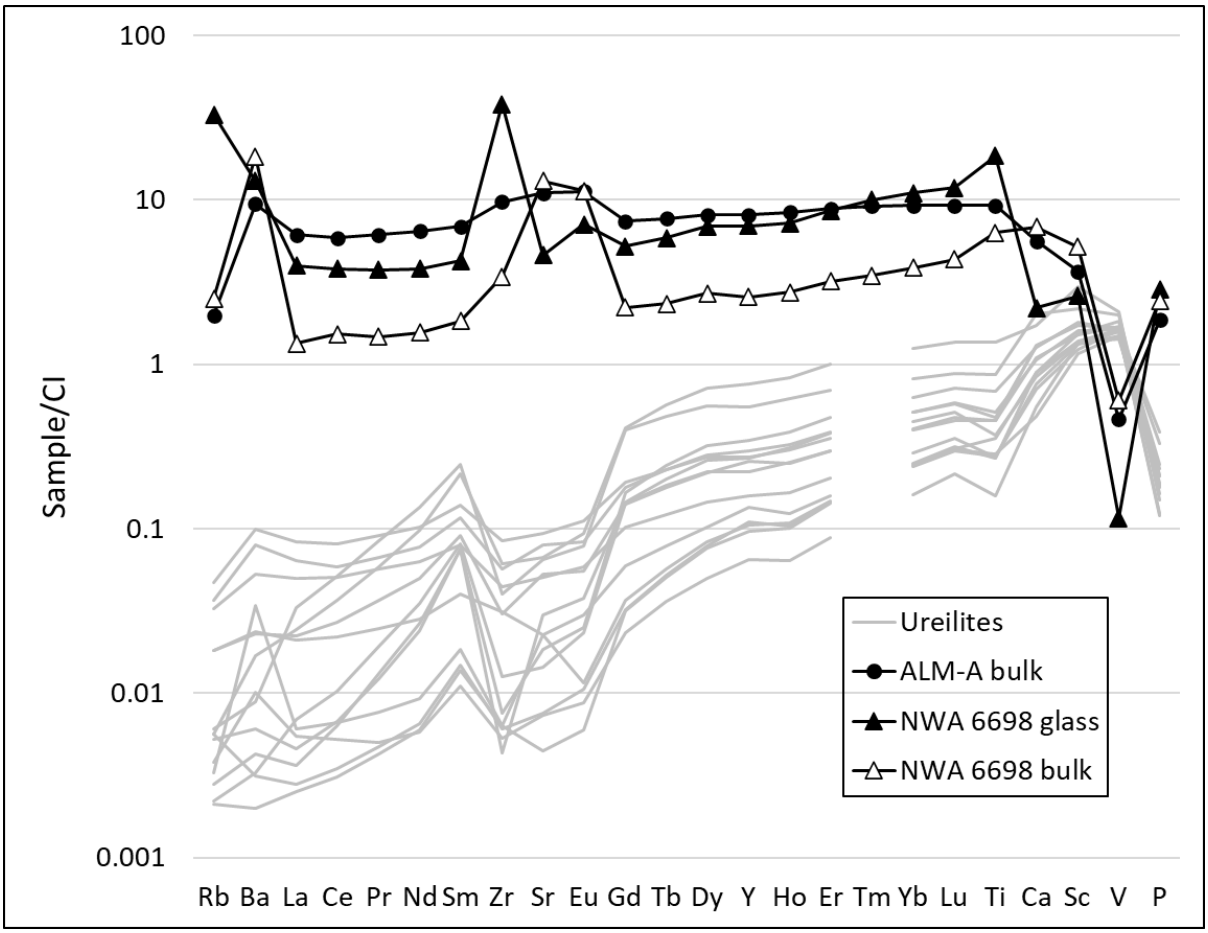

Figure 7. CI-normalized (Anders and Grevesse 1989) trace element patterns of NWA 6698 bulk raster and glass analyses, ALM-A bulk analysis (Bischoff et al. 2014), and ureilite bulk analyses (Barrat et al. 2016).

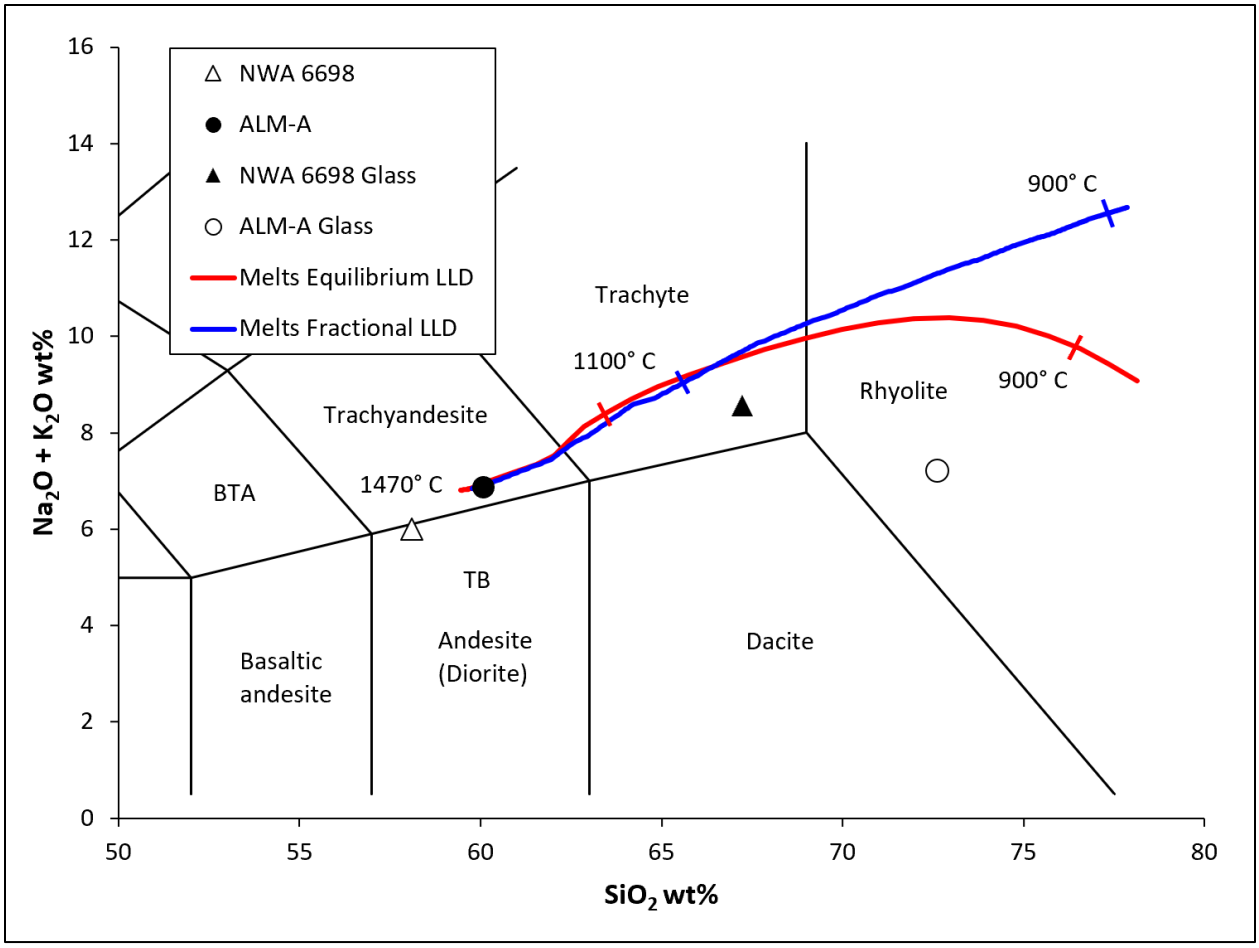

Figure 8. TAS diagram showing the liquid lines of descent (LLD) of Melts (Gualda et al. 2012) equilibrium and fractional crystallization models

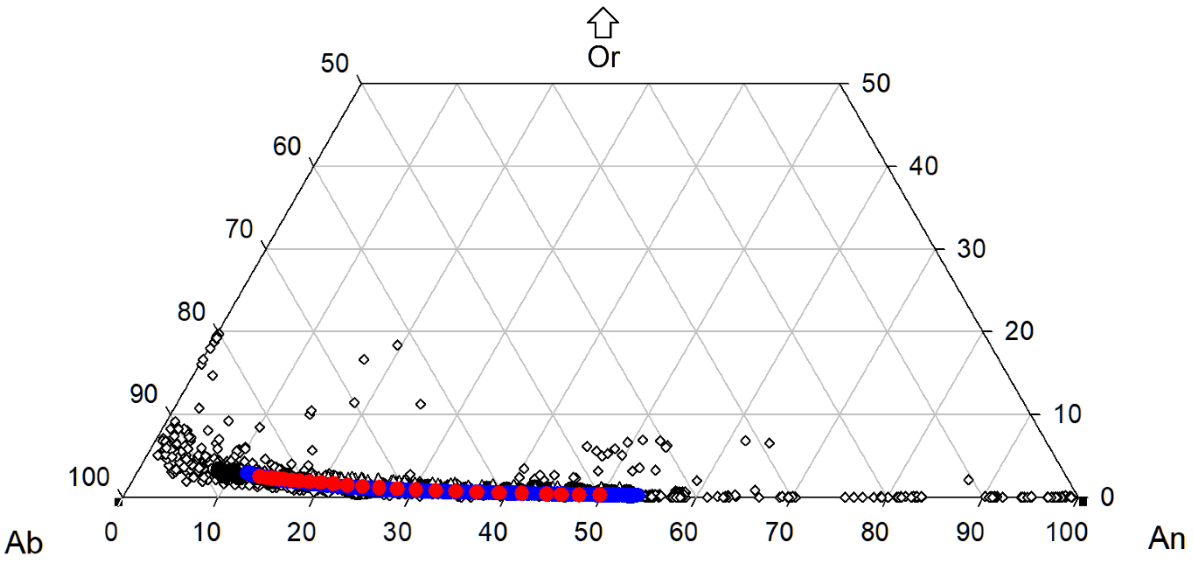

Fig. 9. Feldspar ternary diagram showing equilibrium (red) and fractional (blue) crystallization paths of solids produced in MELTS cooling models of NWA 6698.

References

Agee C. B. et al. 2013. Unique meteorite from early Amazonian Mars: water-rich basaltic breccia Northwest Africa 7034. *Science* 339:780–5. http://www.ncbi.nlm.nih.gov/pubmed/23287721.

Anders E., and Grevesse N. 1989. Abundances of the elements: Meteoritic and solar. *Geochimica et Cosmochimica Acta* 53:197–214.

Antonini A. S., Ganuza M. L., Ferracutti G., Gargiulo M. F., Matković K., Gröller E., Bjerg E. A., and Castro S. M. 2020. Spinel web: an interactive web application for visualizing the chemical composition of spinel group minerals. *Earth Science Informatics*.

Barrat J. A., Rouxel O., Wang K., Moynier F., Yamaguchi A., Bischoff A., and Langlade J. 2015. Early stages of core segregation recorded by Fe isotopes in an asteroidal mantle. *Earth and Planetary Science Letters* 419:93–100. http://dx.doi.org/10.1016/j.epsl.2015.03.026.

Barrat J. A., Jambon A., Yamaguchi A., Bischoff A., Rouget M. L., and Liorzou C. 2016. Partial melting of a C-rich asteroid: Lithophile trace elements in ureilites. *Geochimica et Cosmochimica Acta* 194:163–178.

Barrat J. A., Sansjofre P., Yamaguchi A., Greenwood R. C., and Gillet P. 2017. Carbon isotopic variation in ureilites: Evidence for an early, volatile-rich Inner Solar System. *Earth and Planetary Science Letters* 478:143–149. http://dx.doi.org/10.1016/j.epsl.2017.08.039.

Bischoff A., Horstmann M., Barrat J.-A., Chaussidon M., Pack A., Herwartz D., Ward D., Vollmer C., and Decker S. 2014. Trachyandesitic volcanism in the early Solar System. *Proceedings of the National Academy of Sciences* 111:12689–12692. http://www.pnas.org/cgi/doi/10.1073/pnas.1404799111.

Bland P. a, Zolensky M. E., Benedix G. K., and Sephton M. a. 2006. Weathering of chondritic meteorites. *Meteorites and the Early Solar System II* 853–867.

Borg L. E., Brennecka G. A., and Symes S. J. K. 2016. Accretion timescale and impact history of Mars deduced from the isotopic systematics of martian meteorites. *Geochimica et Cosmochimica Acta* 175:150–167. http://dx.doi.org/10.1016/j.gca.2015.12.002.

Bunch T. E., Irving A. J., Wittke J. H., and Rumble D. 2011. Northwest Africa 6698: A High Temperature “Dioritic” Achondrite with Oxygen Composition in the LL Chondrite Field. In *MetSoc* 74. p. 5224.

Clayton R. N., and Mayeda T. K. 1996. Oxygen isotope studies of achondrites. *Geochimica et Cosmochimica Acta* 60:1999–2017.

Clayton R. N. 2002. Solar System: Self-shielding in the solar nebula. *Nature* 415:860–861. papers://dee23da0-e34b-4588-b624-f878b46d7b3d/Paper/p646.

Cohen B. A., Goodrich C. A., and Keil K. 2004. Feldspathic clast populations in polymict ureilites: Stalking the missing basalts from the ureilite parent body. *Geochimica et Cosmochimica Acta* 68:4249–4266.

Collinet M., and Grove T. L. 2020. Incremental melting in the ureilite parent body: Initial composition, melting temperatures, and melt compositions. *Meteoritics and Planetary Science* 55:832–856.

Day J. M. D., Ash R. D., Liu Y., Bellucci J. J., Rumble D., McDonough W. F., Walker R. J., and Taylor L. A. 2009. Early formation of evolved asteroidal crust. *Nature* 457:179–182. http://dx.doi.org/10.1038/nature07651.

Day J. M. D. et al. 2012. Origin of felsic achondrites Graves Nunataks 06128 and 06129, and ultramafic brachinites and brachinite-like achondrites by partial melting of volatile-rich primitive parent bodies. *Geochimica et Cosmochimica Acta* 81:94–128. http://dx.doi.org/10.1016/j.gca.2011.12.017.

Debaille V., Brandon a D., Yin Q. Z., and Jacobsen B. 2007. Coupled 142Nd-143Nd evidence for a protracted magma ocean in Mars. *Nature* 450:525–528.

Gómez-Tuena A., Straub S. M., and Zellmer G. F. 2014. An introduction to orogenic andesites and crustal growth. Geological Society, London, Special Publications 385:1–13. http://sp.lyellcollection.org/lookup/doi/10.1144/SP385.16.

Goodrich C. A., Van Orman J. A., and Wilson L. 2007. Fractional melting and smelting on the ureilite parent body. *Geochimica et Cosmochimica Acta* 71:2876–2895.

Goodrich C. A., Ash R. D., Van Orman J. A., Domanik K., and McDonough W. F. 2013. Metallic phases and siderophile elements in main group ureilites: Implications for ureilite petrogenesis. *Geochimica et Cosmochimica Acta* 112:340–373. http://dx.doi.org/10.1016/j.gca.2012.06.022.

Goodrich C. A., Kita N. T., Sutton S. R., Wirick S., and Gross J. 2017. The Miller Range 090340 and 090206 meteorites: Identification of new brachinite-like achondrites with

implications for the diversity and petrogenesis of the brachinite clan. *Meteoritics and Planetary Science* 52:949–978.

Greenwood R. C., Burbine T. H., Miller M. F., and Franchi I. A. 2017. Melting and differentiation of early-formed asteroids: The perspective from high precision oxygen isotope studies. *Chemie der Erde - Geochemistry* 77:1–43. http://dx.doi.org/10.1016/j.chemer.2016.09.005.

Gualda G. A. R., Ghiorso M. S., Lemons R. V., and Carley T. L. 2012. Rhyolite-MELTS: A modified calibration of MELTS optimized for silica-rich, fluid-bearing magmatic systems. *Journal of Petrology* 53:875–890.

Hewins R. H. et al. 2017. Regolith breccia Northwest Africa 7533: Mineralogy and petrology with implications for early Mars. *Meteoritics and Planetary Science* 52:89–124.

Humayun M., Davis F. A., and Hirschmann M. M. 2010. Major element analysis of natural silicates by laser ablation ICP-MS. *Journal of Analytical Atomic Spectrometry* 25:998–1005. http://dx.doi.org/10.1039/C001391A.

Humayun M. 2012. Chondrule cooling rates inferred from diffusive profiles in metal lumps from the Acfer 097 CR2 chondrite. *Meteoritics and Planetary Science* 47:1191–1208.

Humayun M. et al. 2013. Origin and age of the earliest Martian crust from meteorite NWA 7533. *Nature* 503:513–516.

Irving A. J., Kuehner S. M., Bunch T. E., Ziegler K., Chen G., Herd C. D. K., Conrey R. M., and Ralew S. 2013. Ungrouped Mafic Achondrite Northwest Africa 7325: A Reduced, Iron-Poor Cumulate Olivine Gabbro from a Differentiated Planetary Parent Body. 4*4th Lunar and Planetary Science Conference* 2164.

Keil K. 2010. Enstatite achondrite meteorites (aubrites) and the histories of their asteroidal parent bodies. *Chemie der Erde* 70:295–317. http://dx.doi.org/10.1016/j.chemer.2010.02.002.

Keil K. 2012. Angrites, a small but diverse suite of ancient, silica-undersaturated volcanic-plutonic mafic meteorites, and the history of their parent asteroid. *Chemie der Erde* 72:191–218. http://dx.doi.org/10.1016/j.chemer.2012.06.002.

Kita N. T., Ikeda Y., Togashi S., Liu Y., Morishita Y., and Weisberg M. K. 2004. Origin of ureilites inferred from a SIMS oxygen isotopic and trace element study of clasts in the Dar al Gani 319 polymict ureilite. *Geochimica et Cosmochimica Acta* 68:4213–4235.

Kruijer T. S., Kleine T., Borg L. E., Brennecka G. A., Irving A. J., Bischoff A., and Agee C. B. 2017. The early differentiation of Mars inferred from Hf–W chronometry. *Earth and Planetary Science Letters* 474:345–354. http://dx.doi.org/10.1016/j.epsl.2017.06.047.

Kushiro I., and Mysen B. O. 2002. A possible effect of melt structure on the Mg-Fe2+ partitioning between olivine and melt. *Geochimica et Cosmochimica Acta* 66:2267–2272.

Mittlefehldt D. W. 2015. Asteroid (4) Vesta: I. The howardite-eucrite-diogenite (HED) clan of meteorites. *Chemie der Erde - Geochemistry* 75:155–183. http://dx.doi.org/10.1016/j.chemer.2014.08.002.

Nyquist L. E., Bogard D. D., Shih C. Y., Greshake A., Stöffler D., and Eugster O. 2001. Ages and geologic histories of martian meteorites. In *Chronology and Evolution of Mars*. pp. 105–164.

Oulton J., Humayun M., Fedkin A., and Grossman L. 2016. Chemical evidence for differentiation, evaporation and recondensation from silicate clasts in Gujba. *Geochimica et Cosmochimica Acta* 177:254–274.

Rankenburg K., Humayun M., Brandon A. D., and Herrin J. S. 2008. Highly siderophile elements in ureilites. *Geochimica et Cosmochimica Acta* 72:4642–4659.

Rosén Å. V., Pape J., Hofmann B. A., Gnos E., and Guillong M. 2019. Quenched primary melt in Ramlat as Sahmah 517 – Snapshot of ureilite anatexis in the early solar system. *Geochimica et Cosmochimica Acta* 246:1–20.

Santos A. R., Agee C. B., McCubbin F. M., Shearer C. K., Burger P. V., Tartèse R., and Anand M. 2015. Petrology of igneous clasts in Northwest Africa 7034: Implications for the petrologic diversity of the martian crust. *Geochimica et Cosmochimica Acta* 157:56–85.

Sautter V. et al. 2015. In situ evidence for continental crust on early Mars. *Nature Geoscience* 8:605–609.

Sharp Z. D. 1990. A laser-based microanalytical method for the in situ determination of oxygen isotope ratios of silicates and oxides. *Geochimica et Cosmochimica Acta* 54:1353–1357. http://linkinghub.elsevier.com/retrieve/pii/001670379090160M%5Cnpapers3://publication/doi/10.1016/0016-7037(90)90160-M.

Shearer C. K. et al. 2010. Non-basaltic asteroidal magmatism during the earliest stages of solar system evolution: A view from Antarctic achondrites Graves Nunatak 06128 and 06129.

Geochimica et Cosmochimica Acta 74:1172–1199. http://dx.doi.org/10.1016/j.gca.2009.10.029.

Singletary S. J., and Grove T. L. 2003. Early petrologic processes on the ureilite parent body. *Meteoritics and Planetary Science* 38:95–108.

Singletary S., and Grove T. L. 2006. Experimental constraints on ureilite petrogenesis. *Geochimica et Cosmochimica Acta* 70:1291–1308.

Srinivasan P., Dunlap D. R., Agee C. B., Wadhwa M., Coleff D., Ziegler K., Zeigler R., and McCubbin F. M. 2018. Silica-rich volcanism in the early solar system dated at 4.565 Ga. *Nature Communications* 9:1–8. http://dx.doi.org/10.1038/s41467-018-05501-0.

Warren P. H., and Kallemeyn G. W. 1992. Explosive volcanism and the graphite-oxygen fugacity buffer on the parent asteroid(s) of the ureilite meteorites. *Icarus* 100:110–126.

Warren P. H., Ulff-Møller F., Huber H., and Kallemeyn G. W. 2006. Siderophile geochemistry of ureilites: A record of early stages of planetesimal core formation. *Geochimica et Cosmochimica Acta* 70:2104–2126.

Warren P. H., and Huber H. 2006. Ureilite petrogenesis: A limited role for smelting during anatexis and catastrophic disruption. *Meteoritics and Planetary Science* 41:835–849.

Warren P. H., and Rubin A. E. 2010. Pyroxene-selective impact smelting in ureilites. *Geochimica et Cosmochimica Acta* 74:5109–5133. http://dx.doi.org/10.1016/j.gca.2010.05.026.

Yang S., Humayun M., Righter K., Jefferson G., Fields D., and Irving A. J. 2015. Siderophile and chalcophile element abundances in shergottites: Implications for Martian core formation. *Meteoritics and Planetary Science* 50:691–714.

Yang S., Humayun M., and Salters V. J. M. 2018. Elemental Systematics in MORB Glasses From the Mid-Atlantic Ridge. *Geochemistry, Geophysics, Geosystems* 19:4236–4259.

Zhu K., Moynier F., Schiller M., Wielandt D., Larsen K. K., van Kooten E. M. M. E., Barrat J.-A., and Bizzarro M. 2020. Chromium Isotopic Constraints on the Origin of the Ureilite Parent Body. *The Astrophysical Journal* 888:126. http://dx.doi.org/10.3847/1538-4357/ab5af7.

CHAPTER 3

Experimental constraints on evolved magmatism in the early Solar System

Abstract

Recently discovered ancient samples of dioritic, andesitic, and trachyandesitic achondrites challenge the paradigm of predominantly basaltic magmatism on small bodies in the early Solar System. The compositions of these rocks suggest the presence of evolved and silica-rich crusts on differentiated bodies in the first few million years of solar system history. On Earth, evolved magmatism requires the presence of plate tectonics, while petrologic experiments suggest the partial melting of chondritic material produces melts of primarily basaltic composition. To test the idea that lower oxygen fugacities produce more evolved melt compositions, 1-atmosphere melting experiments were performed on chondritic starting compositions at oxygen fugacities below the iron-wüstite (IW) buffer. Sodium contents were varied to examine the role of alkalis during partial melting.

1. Introduction

Achondrites are igneous meteorites that record the differentiation histories of their parent bodies. Other than the Shergottite-Nakhlite-Chassignite (SNC) meteorites, which are from Mars (Treiman et al. 2000), and lunar meteorites, achondrites originate from small bodies whose mostly shattered remnants comprise the asteroid belt. Historically, meteorite samples of these bodies have been primarily basaltic to ultramafic. For example, the over 2000 samples of Howardite-Eucrite-Diogenite (HED) meteorites are thought to originate from a differentiated

protoplanet or protoplanets, one of which might be the asteroid Vesta (McSween et al. 2013; Wasson 2013). These sample a basaltic crust (eucrites), an ultramafic lower crust or upper mantle (diogenites), and a regolith that contains a mixture of both (howardites). The angrites are an additional group of silica-undersaturated igneous meteorites of roughly basaltic composition, from an unknown parent body (Keil 2012). Primitive achondrites, including the ureilites, brachinites, acapulcoites, lodranites, and winonaites sample parent bodies that underwent lower degrees of partial melting, producing ultramafic residues depleted in siderophile and volatile lithophile elements relative to their chondritic protoliths (e.g. Warren et al. 2006; Keil and McCoy 2018). The prevailing paradigm is therefore that in the early solar system, chondritic material accreted and differentiated to varying degrees, at most segregating an ultramafic mantle from an FeNiS core and producing a basaltic crust.

Recently, more evolved and silica-rich ungrouped achondrites have been identified whose compositions challenge this assumption. Graves Nunataks (GRA) 06128/9 is an achondrite rich in sodic plagioclase that likely crystallized from a partial melt of a chondritic precursor (Shearer et al. 2010) and whose melting event possibly left behind the brachinites and brachinite-like achondrites as residues (Day et al. 2012a). Likewise, the trachyandesite ALM-A represents the extraction of an evolved melt from a chondritic precursor that left behind the ureilites as residues (Bischoff et al. 2014; Barrat et al. 2016). Finally, the andesite NWA 11119 is an extremely alkali-depleted extrusive volcanic rock, with ~30 wt.% silica, from an unknown parent body (Srinivasan et al. 2018). Although rare, these samples illustrate that planetesimal differentiation produced evolved and silica-rich crusts. On Earth, the generation of andesites and trachyandesites requires plate tectonics and complex melting scenarios (e.g. Gómez-Tuena et al. 2014). The differentiation of planetesimals, although likely simpler than that of terrestrial

planets, is poorly understood, and the generation of such silica-rich materials on small bodies is especially mysterious.

Chondritic materials have been experimentally melted to examine planetesimal differentiation and crust formation. Early 1-atmosphere experiments demonstrated that varying the oxygen fugacity resulted in differing melt compositions, with melts performed at one log unit below the iron-wüstite (IW-1) broadly reproducing eucritic compositions, while melts performed at IW+2 produced broadly angritic compositions (Jurewicz et al. 1991, 1993, 1995). At IW-1, with low degrees of partial malting, and with the addition of sodium, the silica contents of melts were increased, likely because lower oxygen fugacity sequesters Fe in the metal portion of the melt and alkalis stabilize the activity of plagioclase (Usui et al. 2015). These experiments potentially explain the petrogenesis of GRA 16128/9, while partial melting experiments that produced ureilite-like residues suggest that the ureilite parent body melted incrementally to produce the trachyandesite ALM-A (Collinet and Grove 2020a).

However, the andesite NWA 11119 has a uniquely magnesian and alkali-depleted composition that suggests it formed under more reducing and volatile-depleted conditions. While lower in FeO content than anything produced in the above experiments, its FeO is not as low as was produced by melting of an enstatite chondrite at an fO_2 of IW-5 (McCoy et al. 1999). If the FeO content of NWA 11119 reflects that of its source, which was presumably in equilibrium with metal, the fO_2 of its petrogenesis can be estimated with the following equation (McCubbin et al. 2012; Srinivasan et al. 2018)

$$\Delta IW = 2\log\left(\frac{\gamma_{FeO}^{silicate} \times X_{FeO}^{silicate}}{\gamma_{FeO}^{metal} \times X_{Fe}^{metal}}\right)$$

where γ is the activity and X is the mole fraction. Assuming both activities are unity and a pure Fe metal, the FeO content of NWA 11119 yields an fO_2 of ~IW-4. Since chondrite melting

experiments have not been conducted within this range, and to examine the conditions under which this and other evolved and silica-rich material formed, we conducted a series of 1 atmosphere melting experiments of chondritic materials at various starting compositions, melt fractions, and oxygen fugacities. This report concerns the first phase of our experimental campaign in which we reproduce and expand upon the work of Usui et al. (2015)

2. Methods

Partial melting experiments were performed using a Deltech 1-atmosphere gas mixing furnace equipped with $MoSi_2$ heating elements and a Eurotherm controller at the University of New Mexico. Starting compositions were modelled after Usui et al. (2015) in order to reproduce and build upon their results, and they included H and LL chondritic compositions with and without Na (Table 1). Reagent-grade oxide powders were mixed under ethanol in an agate mortar and pestle for 30 minutes to ensure homogeneity and allowed to air dry. Starting compositions were bound with 3% polyvinyl alcohol solution and loaded onto Re wire loops which were hung from Pt wires and suspended inside the furnace. All experiments were heated to 1350° C for 90 minutes to ensure they were completely melted before being brought down to their experimental temperatures where they were held for at least 20 hours before being drop-quenched into deionized water. Temperatures ranged from 1050 to 1250° C to generate varying degrees of partial melting.

Temperatures at the furnace hot spot where samples were hung were continually monitored with an S-type thermocouple and calibrated against the melting point of gold wire. Estimated temperature uncertainty was ±3° C. The fO_2 of the experiments were controlled using CO-CO_2 gas mixtures introduced into the furnace through a Matheson 7400 series gas flowmeter

and mixing manifold using a top-to-bottom flow-through scheme. The fO_2 of the gas mixtures was measured with a SIRO2 yttrium-stabilized zirconia (YSZ) electrochemical oxygen sensor placed at the furnace hot spot immediately before and after experiments were performed. The emf sensor's precision of ±1.5 mV defines an uncertainty of ±0.10 log units for reported fO_2 values.

Experimental run products were mounted in epoxy and polished for scanning electron microscopy (SEM) with a TeScan Vega and electron probe microanalysis (EPMA) with a JEOL 8200 Superprobe at the University of New Mexico. Constituent phase compositions were analyzed using quantitative wavelength-dispersive spectroscopy (WDS). An accelerating voltage of 15 kV, a beam current of 20 nA, and a spot size of 1 μm were used for analyses. Standards for WDS analysis were manufactured by the C.M. Taylor Standard Corporation in Sunnyvale, CA. Backscattered electron (BSE) mosaics of polished run products were constructed using digital imaging software. Modal mineralogy of phase assemblages was determined using ImageJ thresholding software, and these were combined with averaged microprobe analyses of constituent phases and mineral densities to formulate bulk compositions.

3. Results

3.1 Assessment of Experiments

A summary of experimental conditions and results is provided in Table 2. A thermodynamic model of Fe-Mg partitioning between olivine and liquid was used to check whether run products were at equilibrium, after Usui et al. (2015). Theoretical K_D equilibrium constants, defined as the molar Mg/Fe^{2+} of the liquid divided by the molar Mg/Fe^{2+} of coexisting olivine, were calculated using the thermodynamic model of (Toplis 2005) (Fig. 1). For

experimental charges in which no melt was observed, the silica content of plagioclase was used to calculate theoretical K_D values. Equilibrium was observed in all charges in which glass was present except for run #14, in which glass composition was too varied to calculate an accurate K_D. Electron beam overlap was also an issue for run products with small quantities of melt, such that adjacent olivine grains interfered with analyses so that true melt Mg# could not be measured in runs #8, #9, and #17.

Broad trends in mineral compositions and phase assemblages suggest that our experimental run products reflect equilibrium partial melting of ordinary chondritic material at IW-1. Olivine grains are unzoned and uniform in composition in all experiments ($Fo_{68\pm3}$). Measured olivine-melt K_D values are within ~10% of the modelled compositions except in instances of electron beam overlap. Pyroxene abundance and metal Fe:Ni ratios uniformly decrease with temperature, while melt abundance increases. Unlike Usui et al. (2015), who identified wüstite in their runs at IW-1, neither wüstite nor any other higher fO_2-associated phase was found within any experimental run products.

Alkalis are volatile elements, and especially at low fO_2, are known to volatilize readily from experimental charges (e.g. Stolper 1977). Loss of Na from run products is unavoidable in an open system experimental setup, and losses are documented in Table 2. However, the persistence of plagioclase and of weight percent levels of Na in the melts generated attest to the influence of alkali content on the experiments. There are also large uncertainties associated with determining Na contents based on modal mineralogy estimates from BSE images.

3.2 Phase Relationships

All experimental run products contain olivine as a major phase in euhedral habit, with crystal size ranging from 10-100 μm (Fig. 2). Modal olivine is generally lower in LL chondritic run products (29-50%) than in H chondritic run products (38-65%). Pyroxene is present in all experiments except for LL chondritic runs at the highest temperature step (1250° C), as larger (200-500 μm) oikocrysts that poikilitically enclose olivine chadacrysts. Modal pyroxene is generally higher in LL chondritic run products (2-57%) than in H chondritic run products (5-46%). While enstatite is the dominant phase, some pigeonite is found in H chondritic experiments at low temperatures (1050-1100° C) (Fig. 3).

Pigeonite is for the most part found interstitially to plagioclase lathes, which themselves occur interstitially to the major phases at low temperatures (1050-1100) in experiments with Na (Fig. 2). The composition of plagioclase is labradorite (An_{64-69}). Chromite is a trace phase (<0.4 mod.%) identified in LL chondritic, H chondritic, and H chondritic without Na experiments between 1050 and 1200° C. Metal abundances are generally higher at low temperatures and decrease as melting progresses along with Fe:Ni. Although P_2O_5 was included in the bulk compositions, no phosphorous-bearing phases were observed in any run products.

In experiments without Na, melt occurs interstitially as a high-Al_2O_3 (~35 wt.%) and low-SiO_2 (~44 wt.%) phase at low temperatures, and Al_2O_3 content gradually decreases with increasing temperature while SiO_2 contents increase and plateau at ~50 wt.% (Fig. 4). In experiments with Na, melt appears at low temperatures as a high SiO_2 phase, with the H chondritic experiments producing the most elevated SiO_2 contents (as high as 66 wt%). At low temperatures, plagioclase is the major Al_2O_3 bearing phase, which elevates SiO_2 in any melt that

is present. As plagioclase enters the melt at higher temperatures, the melts produced by Na bearing experiments resemble those of Na free experiments.

4. Discussion

4.1 Comparison with other Experiments

The results of partial melting experiments of LL and H chondritic material at IW-1 show broadly similar trends as previous experiments conducted on similar starting compositions and under similar conditions (Jurewicz et al. 1995; Usui et al. 2015). They also broaden the compositional range to include compositions without alkalis so that their effect on melt compositions can be effectively gauged. Generally, melts of chondritic materials at IW-1 generate tholeiitic or 'eucritic' melt compositions, while higher oxygen fugacities produce more FeO-rich, silica-undersaturated 'angritic' melts (Jurewicz et al. 1995). Reproducing and expanding upon these fundamentals is important to investigating the petrogenesis of evolved achondrites.

CIPW norms of experimental glasses were recalculated for projection onto the ol'-ne-'Q' diagram after Irvine and Baragar (1971) (Fig. 5). This projection separates silica over- and under-saturated magmas with the ol'-ab line, which no experimental melt compositions cross. Our results provide further evidence of the silica elevating effect of reduced fO_2 on experimental melts, as all of the melts produced at IW-1 are in the quartz-normative portion of the phase diagram. H chondritic melts are slightly more quartz-normative at 1050° C than those of Usui et al. (2015) at 1040° C, while H chondritic melts at 1100° C are more albite-normative than those of Usui et al. (2015) at 1090 and 1130° C. Thus, though the temperature intervals are larger than those of Usui et al. (2015), the trends shown by these experiments follow a more extreme pattern

of alkali and silica enrichments at low temperatures and small degrees of partial melting. At higher temperatures, and in all Na-free experiments and LL chondritic experiments, results overlap with those of Usui et al. (2015) and Jurewicz et al. (1995).

As in Usui et al. (2015), the presence of alkalis has a profound effect upon melt composition. The H chondritic melt experiments of Jurewicz et al. (1995) did not attempt to stabilize alkalis, and thus their melts were depleted in Na relative to our experiments with Na and those of Usui et al. (2015). Although alkali loss was greater in our experiments than in those of Usui et al. (2015), plagioclase is observed in greater modal abundances (Table 2), and one of the melts has a higher normative albite content than that of any previous chondritic partial melt experiment (Fig. 5). Interestingly, both this melt and the melts with the highest silica contents and normative quartz co-occur with plagioclase. This suggests that their quench temperatures capture the partial melting of plagioclase, and therefore they are elevated in incompatible elements relative to melts that form at temperatures too high for plagioclase stability or metastability.

Usui et al. (2015) observed that increasing the alkali and silica contents of the melts decreases the modal abundance of pyroxene in the residuum. This is confirmed by our experiments, as our modal pyroxene contents are much higher than theirs, even at higher temperatures. For example, three out of four of our experiments at 1150° C contain >30 mod.% pyroxene, while those of Usui et al. (2015) contain only 13 and 10 mod.% at 1130 and 1170° C, respectively. This suggests that by stabilizing normative feldspars in the melt compositions, alkalis suppress the activity of pyroxenes even in the absence of plagioclase, and the alkali losses in our experiments had the opposite effect. Additionally, LL chondritic compositions generated more modal pyroxene than H chondritic compositions, including in Na-free experiments. This

likely means that lowering Mg# decreases the size of the pyroxene stability field, as suggested by Longhi (1991).

In previous experiments (Jurewicz et al. 1995; Usui et al. 2015), a peritectic reaction was observed in which liquid and olivine were consumed to form pigeonite as temperatures were lowered from liquidus. Usui et al. (2015) observed a second peritectic reaction at lower temperatures in which liquid and pigeonite were consumed to produce olivine and augite. As no augite was identified in any of our experiments, this second peritectic reaction is absent from our results. As none of our melt compositions are olivine-normative, the first peritectic reaction is also not observed in any ternary projections (Fig. 6). This is potentially due to increased CaO contents in all of our melts which suppresses the activity of olivine relative to pyroxene in the CIPW norm calculation. However, in all experimental runs, a decrease in modal olivine and increase in modal pyroxene is observed as temperatures decrease, followed by the opposite at lower temperatures (Fig. 7), suggesting that this peritectic reaction is taking place.

4.2 Implications for Evolved Planetary Crusts

Experimental partial melting of chondritic material has been employed to study the petrogenesis of basaltic meteorites (Jurewicz et al. 1991, 1993, 1995; Longhi 1999), aubrites (McCoy et al. 1999), primitive achondrites (Gardner-Vandy et al. 2013; Collinet and Grove 2020b), and the evolved asteroidal crust GRA 06128/9 (Usui et al. 2015; Lunning et al. 2017). Our experiments serve to reinforce the results of Usui et al. (2015) by confirming that evolved and alkali-enriched melts can be produced by low degrees of partial melting of an H-chondritic precursor at low fO_2. As our Na-free experiments failed to produce silica-enriched melts, the importance of alkalis in generating evolved chondritic melts was reinforced. Despite alkali

depletion, our experiments also crystallized plagioclase, which was absent in the IW-1 experiments of (Usui et al. 2015). Additionally, since LL chondritic melts were less enriched in silica than H chondritic melts, chondritic material with a lower Mg# likely generates more evolved melt compositions due to being more sensitive to oxygen fugacity. Finally, unlike the IW-1 experiments by Usui et al. (2015), our experimental run products are free of any wüstite, whose presence complicated the interpretations of their results by raising the issues of fO_2 accuracy and metastability.

Lunning et al. (2017) questioned the conclusions of Usui et al. (2015) by arguing that the intrinsic oxygen fugacity of GRA 06128/9 is higher than IW-1 [IW+0.5 to +1.5 (Shearer et al. 2010)]. On this basis, they partially melted an R chondrite and produced melts comparable to GRA 06128/9 by disequilibrium partial melting. Their results potentially mirror our melts with the highest silica contents, whose individual analyses varied somewhat and might reflect the presence of some disequilibrium between plagioclase and melt. The higher fO_2 of GRA 01628/9 could also have been produced in an episode of secondary alteration or metamorphism (Shearer et al. 2010) that oxidized the primary igneous mineral assemblage, which was originally more reduced (Usui et al. 2015). While either of these scenarios seems feasible for GRA 06128/9, the petrogenesis of the extremely reduced andesitic to dacitic achondrite NWA 11119 demands additional constraints.

NWA 11119 is a porphyritic volcanic rock whose phenocrysts are composed of 30 mod.% tridymite, which is higher than that of any previously characterized achondrite, 56 mod.% feldspar, and 14 mod.% pyroxene (Srinivasan et al. 2018). Only our H chondritic partial melt at 1050° C approaches this composition with a CIPW normative quartz content of 27%. However, in NWA 11119, the extremely low pyroxene Fe/Mn of 4.6-7.8 and bulk FeO content

of 1.49 wt.% suggest that it formed at much more reducing conditions than those produced in any of our experiments. Therefore, based on the results of these and other experiments, it is not entirely clear whether partial melting of a chondritic protolith can produce melts as exotic in composition as NWA 11119.

The second phase of this experimental campaign will use the same starting compositions in sealed silica tube experiments using graphite as a C-CO buffer and silicon metal as a getter for any excess O_2. This setup will both eliminate any alkali loss via volatilization and allow for lower fO_2 in the vicinity of IW-3 to IW-4. By extending the lower limits oxygen fugacity in chondrite partial melting experiments, we hope to further constrain the petrogenesis of these silica-rich planetesimal crusts.

4. Conclusions

We have conducted a series of experiments at 1 atmosphere and an oxygen fugacity of IW-1 to simulate the partial melting of LL and H ordinary chondrites. These experiments extended the compositional range of chondrite melting experiments by including compositions both with and without Na. Our results are similar to the trends observed by Usui et al. (2015) and their predecessors Jurewicz et al. (1995). Notable differences include more extreme trends in silica and alkali enrichment observed in low temperature partial melts, persistence of plagioclase at 1050° C, absence of wüstite, the lack of a peritectic reaction involving augite, and significant alkali loss due to volatilization. We hope to further address these features and expand the range of experimental compositions and low-fO_2 melting conditions with the next phase of experiments which will use sealed silica tubes and a graphite buffer instead of CO-CO_2 gas.

Figures & Tables

Table 1: Starting compositions of chondrite partial melting experiments in wt.%

	LL Chondrite	LL Chondrite -Na	H Chondrite	H Chondrite -Na
SiO_2	40.66	41.08	35.05	35.45
TiO_2	0.10	0.10	0.10	0.10
Al_2O_3	2.37	2.39	2.00	2.00
Cr_2O_3	0.45	0.45	0.45	0.45
FeO	25.90	26.16	34.55	34.92
MgO	25.20	25.46	22.80	23.03
CaO	1.92	1.94	1.65	1.65
Na_2O	1.00	0.00	1.00	0.00
P_2O_5	0.40	0.40	0.40	0.40
NiO	2.00	2.02	2.00	2.00
Total	100.00	100.00	100.00	100.00

Table 2. Summary of experimental run products in chondritic partial melting experiments. * denotes where plagioclase SiO_2 content was used to calculate the modelled K_D in absence of any melt. Both compositions are listed in instances of co-occuring high- and low-Ca pyroxene.

Run #	Comp.	Target fO_2	Start fO_2 (IW)	End fO_2 (IW)	Dur. (h)	T (°C)	Na Loss (rel. %)	Model K_D	Meas. K_D
6	LL -Na	IW-1	-0.99	-1.00	23	1050	n/a	0.28	0.24
9	LL -Na	IW-1	-1.02	-0.97	22	1100	n/a	0.30	0.37
4	LL -Na	IW-1	-0.89	-0.86	23	1150	n/a	0.32	0.36
3	LL -Na	IW-1	-1.12	-1.09	22	1200	n/a	0.32	0.35
8	LL -Na	IW-1	-1.00	-1.09	23	1250	n/a	0.35	0.26
15	LL	IW-1	-0.99	-0.96	24	1050	47	0.33*	no melt
14	LL	IW-1	-1.00	-1.01	21	1100	62	0.29*	no eq.
13	LL	IW-1	-1.00	-1.01	23	1150	63	0.34	0.35
12	LL	IW-1	-1.01	-1.02	23	1200	91	0.34	0.36
11	LL	IW-1	-1.00	-1.03	23	1250	47	0.35	0.35
16	H -Na	IW-1	-1.00	-1.10	23	1050	n/a	0.30*	no melt
17	H -Na	IW-1	-0.99	-0.97	20	1100	n/a	0.28	0.22
18	H -Na	IW-1	-1.00	-0.96	22	1150	n/a	0.33	0.36
19	H -Na	IW-1	-1.01	-0.76	22	1200	n/a	0.34	0.31
20	H -Na	IW-1	-0.99	-0.92	23	1250	n/a	0.34	0.34
21	H	IW-1	-1.00	-0.99	23	1050	52	0.42	0.41
22	H	IW-1	-1.00	-0.83	20	1100	42	0.36*	no melt
23	H	IW-1	-1.01	-1.01	22	1150	74	0.35	0.34
24	H	IW-1	-1.01	-1.05	22	1200	76	0.36	0.36
25	H	IW-1	-1.02	-0.99	23	1250	86	0.34	0.33

Run #	Comp.	Ol. (md.%)	Fo	Px. (md.%)	Fs	Wo	Plag. (md.%)	An	Glass (md.%)	Metal (md.%)	Fe:Ni
6	LL -Na	34	71	57	18	0	0	n/a	4	5	6.5
9	LL -Na	29	68	56	20	0	0	n/a	11	3	4.0
4	LL -Na	44	67	35	28	1	0	n/a	20	2	2.8
3	LL -Na	36	73	36	23	1	0	n/a	24	4	4.7
8	LL -Na	48	70	22	25	1	0	n/a	28	2	2.1
15	LL	48	69	37	21	1	11	64	0	4	4.3
14	LL	45	68	42	22	1	6	69	3	4	3.8
13	LL	40	68	31	24	1	0	n/a	26	3	3.1
12	LL	47	71	18	26	1	0	n/a	32	2	2.2
11	LL	50	68	2	28	2	0	n/a	45	3	2.0
16	H -Na	47	71	39	20	1	6	100	0	8	12.4
17	H -Na	38	67	46	25	1	0	n/a	10	6	9.1
18	H -Na	49	66	30	29	2	0	n/a	13	6	7.3
19	H -Na	61	65	17	30	2	0	n/a	16	5	5.7
20	H -Na	56	65	0	n/a	n/a	0	n/a	39	4	3.8
21	H	52	67	31	26/30	2/11	10	67	0	7	11.6
22	H	45	67	35	27/29	3/10	12	68	0	7	8.7
23	H	51	67	26	30	3	0	n/a	15	6	6.7
24	H	65	64	5	31	3	0	n/a	27	3	3.7
25	H	59	64	0	n/a	n/a	0	n/a	38	3	4.1

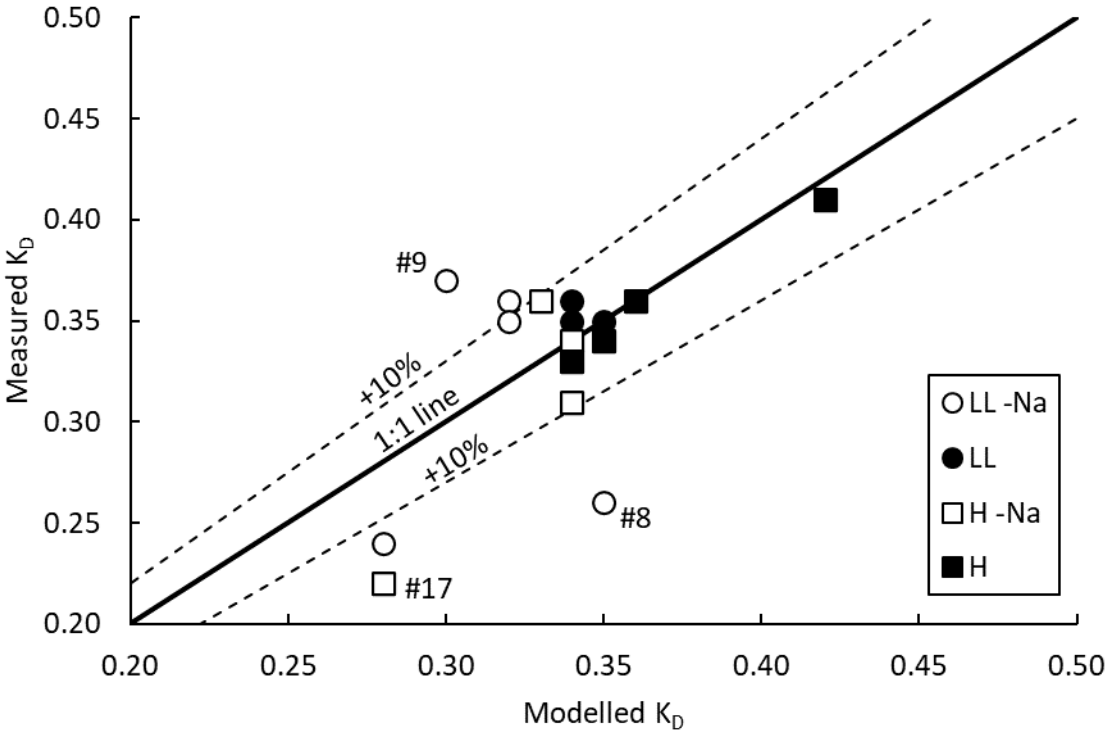

Figure 1. Measured vs. modelled K_D values for ordinary chondritic partial melting experimental runs conducted at IW-1. ±10% deviations from the 1:1 line are the uncertainties in the thermodynamic model (Toplis 2005).

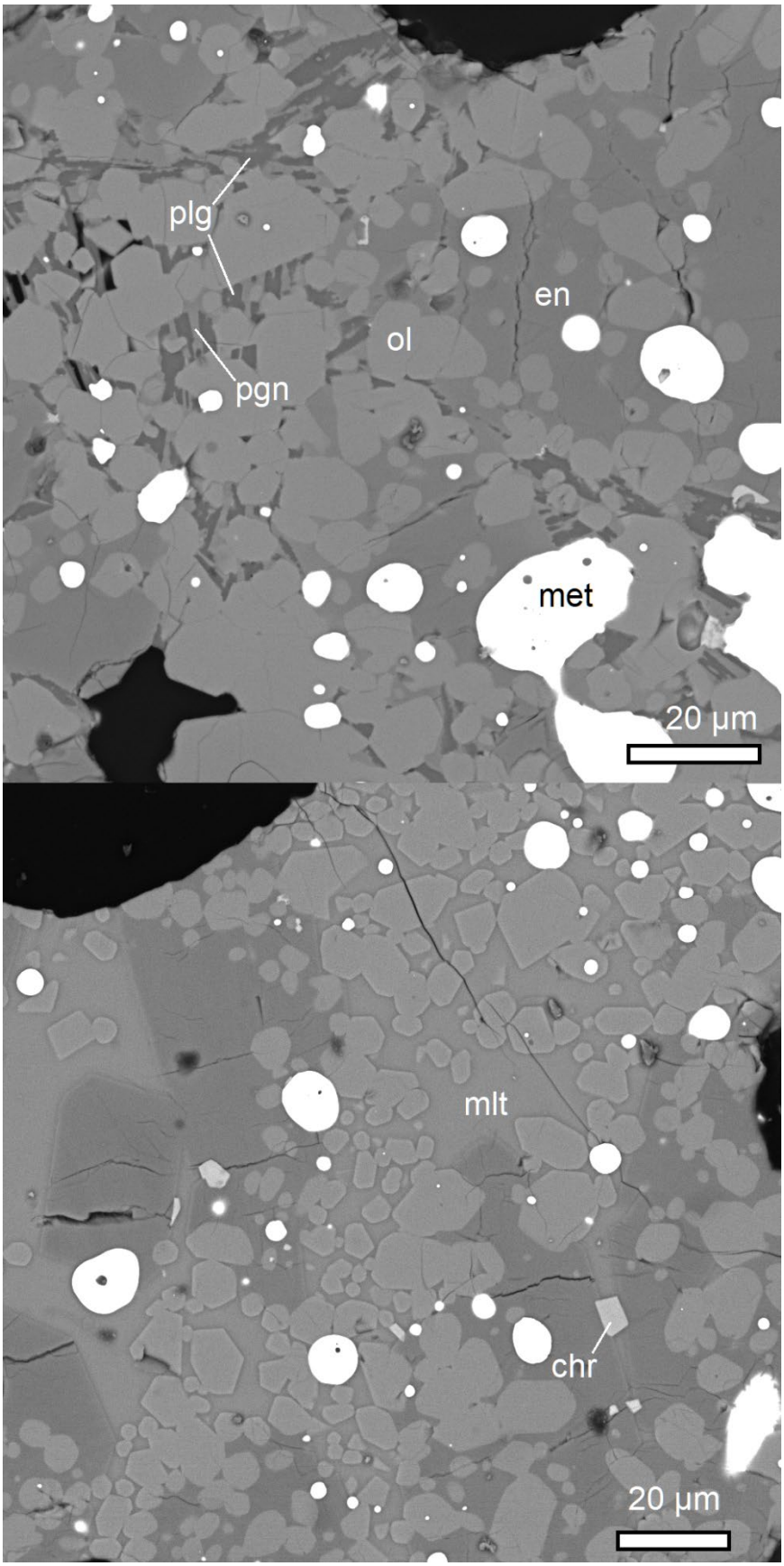
plg
pgn
ol
en
met
20 µm
mlt
chr
20 µm

Figure 2. BSE images of H chondritic partial melt run products at 1050 (top) and 1150° C (bottom). Plg = plagioclase; pgn = pigeonite; en = enstatite; ol = olivine; met = metal; mlt = melt; chr = chromite.

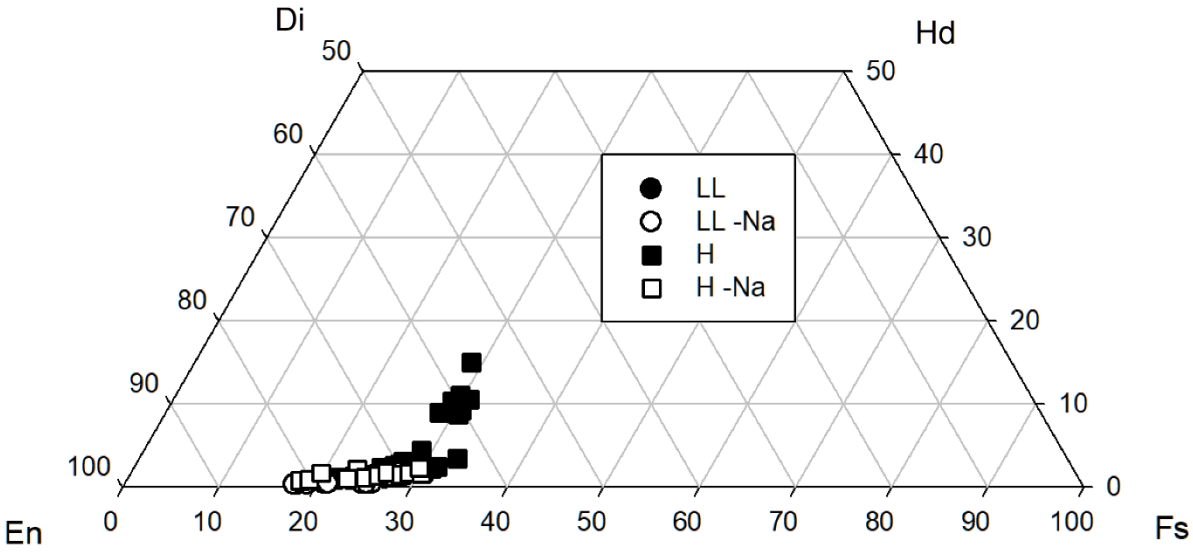

Figure 3. Pyroxene compositions in chondritic experimental partial melt run products at IW-1

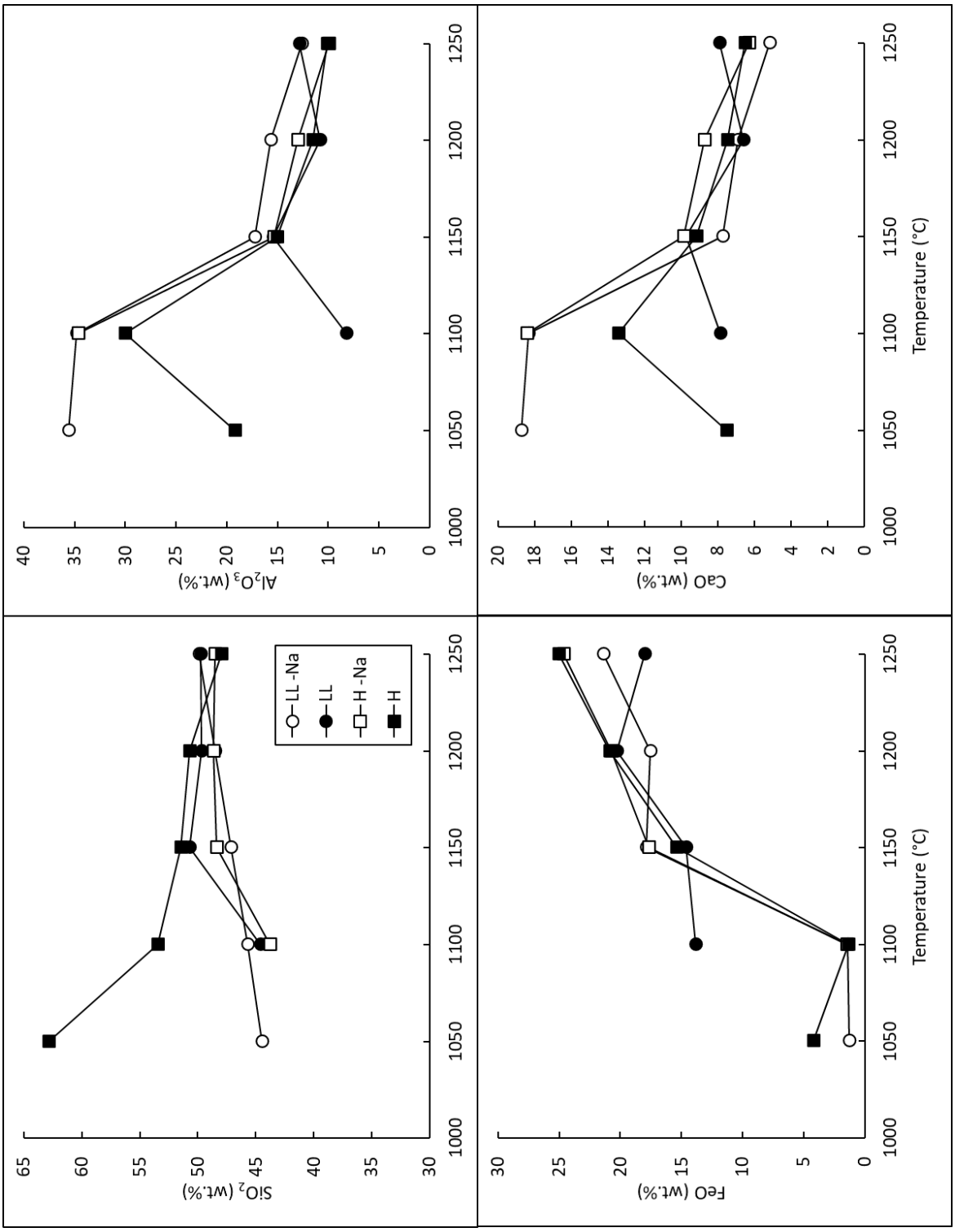

Figure 4. Major element contents of melts in chondritic partial melting experiments at different temperatures.

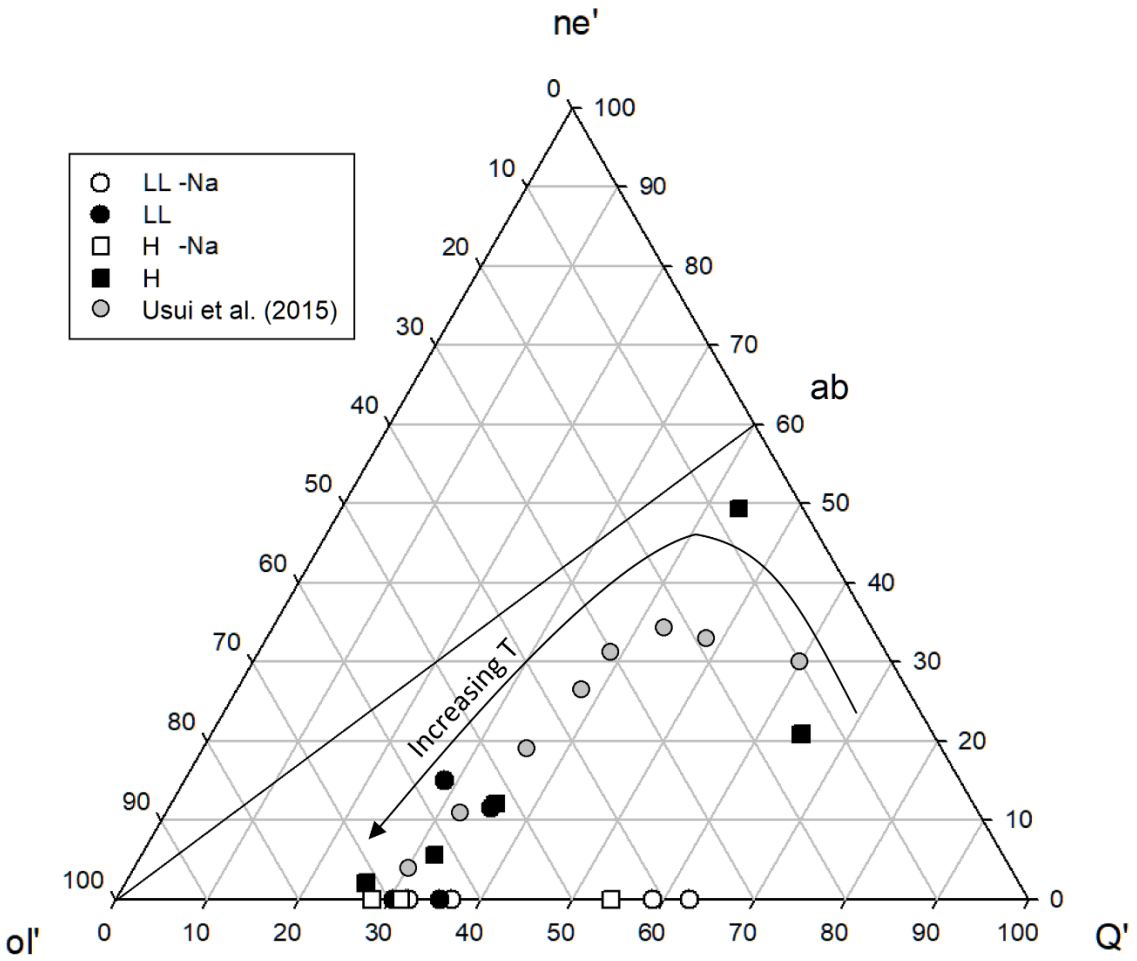

Figure 5. CIPW normative compositions of melts generated in chondritic partial melting experiments, along with IW-1 H chondrite melting experiments from Usui et al. (2015). The diagram is a projection from diopside after Irvine and Baragar (1971), in which ne' = ne + 3/5ab, ol' = ol + 3/4hy, and Q' = Q + 2/5ab + 1/4hy. Ne = nepheline; ol = olivine; Q = quartz; hy = hypersthene.

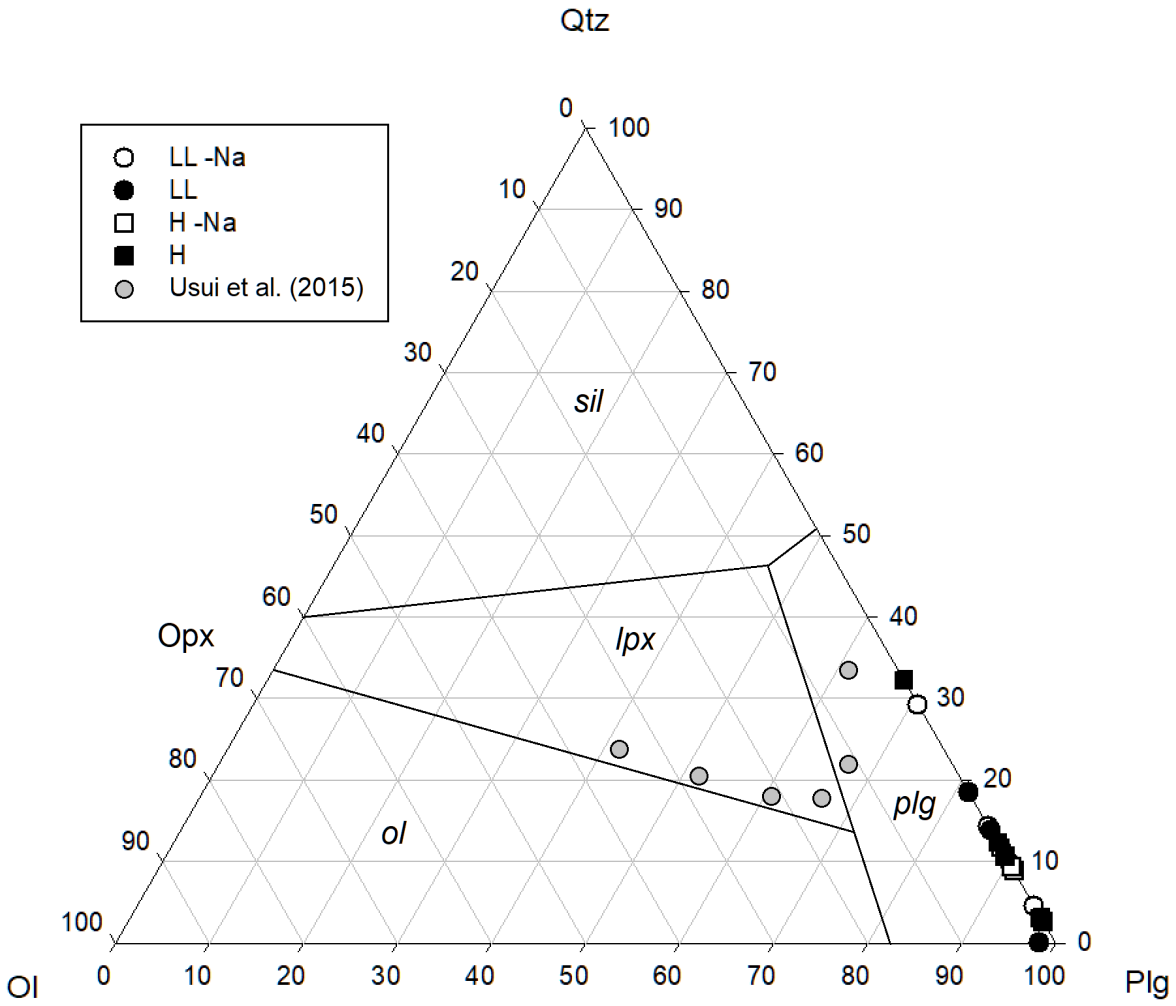

Figure 6. CIPW normative compositions of melts generated in chondritic partial melting experiments, along with IW-1 H chondrite melting experiments from Usui et al. (2015). The diagram is an Ol-Qtz-Plg system projected from Wo, after Longhi (1991). The solid lines are liquidus boundaries calculated using the bulk silicate composition of the H chondritic starting material. Ol = olivine; Qtz = quartz; Plg = plagioclase; lpx = low-Ca pyroxene; sil = silica phase.

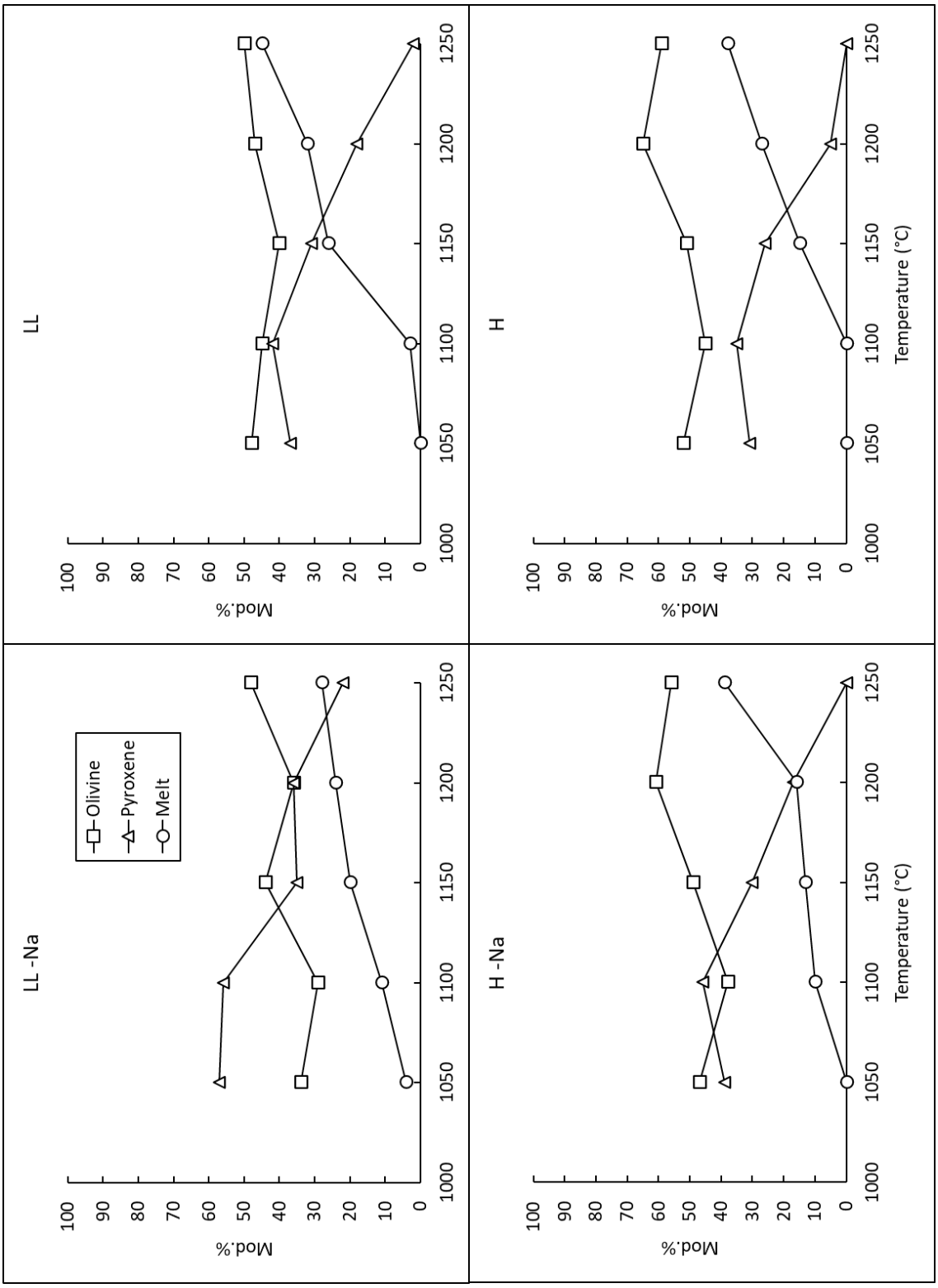

Figure 7. Modal phase abundances of olivine, pyroxene, and melt in chondritic partial melting experiments at different temperatures.

References

Barrat J. A., Jambon A., Yamaguchi A., Bischoff A., Rouget M. L., and Liorzou C. 2016. Partial melting of a C-rich asteroid: Lithophile trace elements in ureilites. *Geochimica et Cosmochimica Acta* 194:163–178.

Bischoff A., Horstmann M., Barrat J.-A., Chaussidon M., Pack A., Herwartz D., Ward D., Vollmer C., and Decker S. 2014. Trachyandesitic volcanism in the early Solar System. *Proceedings of the National Academy of Sciences* 111:12689–12692. http://www.pnas.org/cgi/doi/10.1073/pnas.1404799111.

Collinet M., and Grove T. L. 2020a. Incremental melting in the ureilite parent body: Initial composition, melting temperatures, and melt compositions. *Meteoritics and Planetary Science* 55:832–856.

Collinet M., and Grove T. L. 2020b. Formation of primitive achondrites by partial melting of alkali-undepleted planetesimals in the inner solar system. *Geochimica et Cosmochimica Acta* 277:358–376. https://doi.org/10.1016/j.gca.2020.03.004.

Day J. M. D. et al. 2012. Origin of felsic achondrites Graves Nunataks 06128 and 06129, and ultramafic brachinites and brachinite-like achondrites by partial melting of volatile-rich primitive parent bodies. *Geochimica et Cosmochimica Acta* 81:94–128. http://dx.doi.org/10.1016/j.gca.2011.12.017.

Gardner-Vandy K. G., Lauretta D. S., and McCoy T. J. 2013. A petrologic, thermodynamic and experimental study of brachinites: Partial melt residues of an R chondrite-like precursor. *Geochimica et Cosmochimica Acta* 122:36–57. http://dx.doi.org/10.1016/j.gca.2013.07.035.

Gómez-Tuena A., Straub S. M., and Zellmer G. F. 2014. An introduction to orogenic andesites and crustal growth. Geological Society, London, Special Publications 385:1–13. http://sp.lyellcollection.org/lookup/doi/10.1144/SP385.16.

Irvine T. N., and Baragar W. R. A. 1971. A Guide to the Chemical Classification of the Common Volcanic Rocks. *Canadian Journal of Earth Sciences* 8:523–548. http://www.nrcresearchpress.com/doi/abs/10.1139/e71-055.

Jurewicz A. J. G., Mittlefehldt D. W., and Jones J. H. 1991. Partial melting of the allende (CV3) meteorite: Implications for origins of basaltic meteorites. *Science* 252:695–698.

Jurewicz A. J. G., Mittlefehldt D. W., and Jones J. H. 1993. Experimental partial melting of the Allende (CV) and Murchison (CM) chondrites and the origin of asteroidal basalts. *Geochimica et Cosmochimica Acta* 57:2123–2139.

Jurewicz A. J. G., Mittlefehldt D. W., and Jones J. H. 1995. Experimental partial melting of the St. Severin (LL) and Lost City (H) chondrites. *Geochimica et Cosmochimica Acta* 59:391–408.

Keil K. 2012. Angrites, a small but diverse suite of ancient, silica-undersaturated volcanic-plutonic mafic meteorites, and the history of their parent asteroid. *Chemie der Erde* 72:191–218. http://dx.doi.org/10.1016/j.chemer.2012.06.002.

Keil K., and McCoy T. J. 2018. Acapulcoite-lodranite meteorites: Ultramafic asteroidal partial melt residues. *Chemie der Erde* 78:153–203. http://dx.doi.org/10.1016/j.chemer.2017.04.004.

Longhi J. 1991. Comparative liquidus equilibria of hypersthene-normative basalts at low pressure. *American Mineralogist* 76:785–800.

Longhi J. 1999. Phase equilibrium constraints on angrite petrogenesis. *Geochimica et Cosmochimica Acta* 63:573–585.

Lunning N. G., Gardner-Vandy K. G., Sosa E. S., McCoy T. J., Bullock E. S., and Corrigan C. M. 2017. Partial melting of oxidized planetesimals: An experimental study to test the formation of oligoclase-rich achondrites Graves Nunataks 06128 and 06129. *Geochimica et Cosmochimica Acta* 214:73–85. http://dx.doi.org/10.1016/j.gca.2017.07.004.

McCoy T. J., Dickinson T. L., and Lofgren G. E. 1999. Partial melting of the Indarch (EH4) meteorite: A textural, chemical, and phase relations view of melting and melt migration. *Meteoritics and Planetary Science* 34:735–746.

McCubbin F. M., Riner M. A., Vander Kaaden K. E., and Burkemper L. K. 2012. Is Mercury a volatile-rich planet? *Geophysical Research Letters* 39:1–5.

McSween H. Y. et al. 2013. Dawn; the Vesta-HED connection; and the geologic context for eucrites, diogenites, and howardites. *Meteoritics and Planetary Science* 48:2090–2104.

Shearer C. K. et al. 2010. Non-basaltic asteroidal magmatism during the earliest stages of solar system evolution: A view from Antarctic achondrites Graves Nunatak 06128 and 06129. *Geochimica et Cosmochimica Acta* 74:1172–1199. http://dx.doi.org/10.1016/j.gca.2009.10.029.

Srinivasan P., Dunlap D. R., Agee C. B., Wadhwa M., Coleff D., Ziegler K., Zeigler R., and McCubbin F. M. 2018. Silica-rich volcanism in the early solar system dated at 4.565 Ga. *Nature Communications* 9:1–8. http://dx.doi.org/10.1038/s41467-018-05501-0.

Stolper E. 1977. Experimental petrology of eucritic meteorites. *Geochimica et Cosmochimica Acta* 41:587–611. http://www.sciencedirect.com/science/article/pii/0016703777903003.

Toplis M. J. 2005. The thermodynamics of iron and magnesium partitioning between olivine and liquid: Criteria for assessing and predicting equilibrium in natural and experimental systems. *Contributions to Mineralogy and Petrology* 149:22–39.

Treiman A. H., Gleason J. D., and Bogard D. D. 2000. The SNC meteorites are from Mars. *Planetary and Space Science* 48:1213–1230. http://www.sciencedirect.com/science/article/pii/S0032063300001057.

Usui T., Jones J. H., and Mittlefehldt D. W. 2015. A partial melting study of an ordinary (H) chondrite composition with application to the unique achondrite Graves Nunataks 06128 and 06129. *Meteoritics and Planetary Science* 50:759–781.

Warren P. H., Ulff-Møller F., Huber H., and Kallemeyn G. W. 2006. Siderophile geochemistry of ureilites: A record of early stages of planetesimal core formation. *Geochimica et Cosmochimica Acta* 70:2104–2126.

Wasson J. T. 2013. Vesta and extensively melted asteroids: Why HED meteorites are probably not from Vesta. *Earth and Planetary Science Letters* 381:138–146. http://dx.doi.org/10.1016/j.epsl.2013.09.002.

CHAPTER 4

Constraints on Martian chronology from meteorites

Abstract

Martian meteorites provide the only direct constraints on the timing of Martian accretion, core formation, magmatic differentiation, and ongoing volcanism. While many radiogenic isotope chronometers have been applied to a wide variety of Martian samples, few, if any, techniques are immune to secondary effects from alteration and terrestrial weathering. This short review focuses on the most robust geochronometers that have been used to date Martian meteorites and geochemically model the differentiation of the planet, including $^{147}Sm/^{143}Nd$, $^{146}Sm/^{142}Nd$, $^{176}Lu/^{176}Hf$, $^{182}Hf/^{182}W$, and U-Th-Pb systematics.

1. Introduction

It is generally agreed that the inner solar system planets were formed by the collisional agglomeration of dust particles into cm- or m-sized objects which then grew into planetesimals up to 100 km in size via turbulent accretion triggered by gravitational instability. Gravitational interactions between planetesimals caused them to collide and produce Mars-sized planetary embryos, which then formed terrestrial planets via giant impacts (Chambers 2004; Raymond et al. 2009). Under this paradigm, Mars is a leftover planetary embryo which escaped the giant impacts that formed the other terrestrial planets (Dauphas and Chaussidon 2011). The timescales of the accretion, core formation, and silicate differentiation of Mars are best constrained using

the radiometric isotope systematics of the only available samples from the planet, Martian meteorites.

Since these meteorites are generally hot or cold desert finds that have spent a considerable amount of time exposed to terrestrial surface conditions, they are often heavily weathered (Crozaz et al. 2003). Isotopic chronometers can be highly sensitive to disruption by weathering, and for this reason this short review only focuses on the most pristine and uncompromised chronological data. Emphasis is placed on recent measurements employing the most robust chronometers. Isotopic systems employed include Sm-Nd, Lu-Hf, Hf-W, Ar-Ar, U-Th-Pb, and various noble gas exposure age chronometers such as cosmogenic ^{3}He, ^{21}Ne, and ^{38}Ar. All ages discussed below are reported with their two sigma uncertainties.

2. Overview of Martian Meteorites

The SNC (shergottite, nakhlite, chassignite) meteorite clan has been confirmed as originating from Mars on the basis of trapped noble gas compositions that match that of the Martian atmosphere (Treiman et al. 2000). These meteorites also plot along their own mass-dependent fractionation line in triple-oxygen isotope space, with a Δ^{17}O of ~0.3 (Clayton and Mayeda 1996). There are to date 150 meteorite pairing groups of Martian origin. While the traditional classification system divides these meteorites into shergottites (basalts constituting 89% of Martian meteorites (Udry et al. 2020)), nakhlites (clinopyroxene-rich cumulates), and chassignites (dunites) (McSween 1985), additional samples have contributed to the variety of the Martian igneous record. Allan Hills (ALH) 84001 is an orthopyroxene cumulate (Lapen et al. 2010), Northwest Africa (NWA) 7034 and its pairs are polymict breccias (Agee et al. 2013), and NWA 8159 and NWA 7635 are augite-rich shergottites with unique ages (Herd et al. 2017;

Lapen et al. 2017). Together, the crystallization ages of these meteorites roughly span the age of the planet (Fig. 1).

The shergottites, which represent the overwhelming majority of Martian meteorites, are subdivided into additional categories based on petrological and geochemical characteristics. Basaltic shergottites contain pyroxene and plagioclase in varying proportions and span grain sizes from gabbroic to fine-grained. Olivine-phyric shergottites are similar to basaltic shergottites but contain olivine phenocrysts, megacrysts, or xenocrysts, and poikilitic shergottites are mafic to ultramafic plutonic rocks with large-grained olivine and pyroxenes (Papike et al. 2009). Geochemically, shergottites are divided into enriched, intermediate, and depleted categories based on the level of depletion of their light rare earth elements (LREE) and their Sm-Nd and Hf-W radiogenic isotope systematics (Borg and Draper 2003; Debaille et al. 2007; Kruijer et al. 2017). While the majority of shergottites are young (<600 Ma), NWA 7635 and 8159 are 2.4 Ga exceptions (Herd et al. 2017; Lapen et al. 2017) which extend the age of shergottite volcanism to encompass nearly the entire Amazonian Period (3.0-0 Ga). The nakhlites and chassignites, on the other hand, are geochemically distinct from the shergottites and could represent melts and cumulates from a single differentiated igneous body (McCubbin et al. 2013; Shearer et al. 2018) or from several lava flows or shallow sills associated with a single volcano (Cohen et al. 2017; Udry and Day 2018). Allen Hills 84001 is an orthopyroxene cumulate with an age of 4.09 Ga (Lapen et al. 2010) that gives unique insight into the Noachian Period (4.1-3.7 Ga) of Martian history (Lapen et al. 2010), during which liquid water precipitated secondary carbonate (Borg et al. 1999). Finally, igneous clasts and zircons in the Martian regolith breccias NWA 7034 and its pairs record evidence of an ancient crust that must have formed on Mars within the first 20 Ma of the planet's formation (Bouvier et al. 2018).

Analyses from orbital and surface missions have greatly expanded the compositional diversity of Martian igneous rocks. With the exception of NWA 7034 and its pairs, Martian meteorites are all basaltic to ultramafic. Orbital measurements of volcanic provinces by Gamma Ray Spectroscopy (GRS) aboard Mars Odyssey show that the average Martian crust is basaltic to trachybasaltic (Taylor et al. 2010; Filiberto 2017). The igneous rocks at Gusev Crater examined by the Mars Exploration Rover (MER) Spirit are roughly basaltic but have much higher ranges of total alkalis than the SNC meteorites (McSween et al. 2006). The Mars Science Laboratory (MSL) has analyzed igneous rocks in Gale Crater and identified diorites, trachytes, trachyandesites, and quartz diorites (Cousin et al. 2017). Such diverse measurements suggest that Martian igneous geology is much more varied than implied by the SNC meteorites, involving large degrees of differentiation and fractional crystallization.

3. Crystallization and Ejection Ages

The radiometric age dating of Martian meteorites has been used to constrain the timing of Martian core formation and early silicate differentiation into distinct magmatic reservoirs. The subsequent melting and possible interaction of these reservoirs created the petrogenetic diversity of the Martian meteorite suite (Papike et al. 2009). Since Mars is a planet with a significant gravity well, large impacts and their associated shock pressures are required to loft material from the planet (Head et al. 2002; Artemieva and Ivanov 2004). Most Martian meteorites are moderately to heavily shocked (Fritz et al. 2005), resulting in partial melting and transformation of their plagioclase to the shock phase maskelynite. As the $^{40}Ar/^{39}Ar$ chronometer is sensitive to such disruptions (Kunz et al. 1997), the $^{40}Ar/^{39}Ar$ dating of Martian material must be carefully evaluated in regards to crystallization ages. Likewise, because most Martian meteorites are desert

finds, the $^{87}Rb/^{87}Sr$ chronometer is often disrupted by calcite deposition which contains terrestrial alkali and alkaline elements. Similarly, chronometers that employ the Sm-Nd system are susceptible to fluid mobilization and addition of these elements (as well as the rest of the rare earth elements) (Crozaz and Wadhwa 2001; Crozaz et al. 2003). Figure 2 summarizes the $^{147}Sm/^{143}Nd$ dating that has been performed on Martian meteorites.

$^{147}Sm/^{143}Nd$, $^{87}Rb/^{87}Sr$, and $^{176}Lu/^{176}Hf$ dating of the shergottites have shown crystallization ages that cluster according to their geochemical enrichment. The enriched shergottites have ages between ~165 and ~200 Ma (Shih et al. 1982, 2003, 2009; Borg et al. 2005; Marks et al. 2010; Shafer et al. 2010; Moser et al. 2013; Ferdous et al. 2017; Combs et al. 2019). The intermediate shergottites have overlapping and older crystallization ages between ~150 and ~350 Ma (Morikawa et al. 2001; Nyquist et al. 2001, 2009; Borg et al. 2002; Misawa et al. 2008; Liu et al. 2011; Shih et al. 2011). Depleted shergottites are the oldest group, with crystallization ages between ~327 and ~2400 Ma (Borg et al. 1997, 2003; Shih et al. 2004, 2007; Symes et al. 2005; Brennecka et al. 2014; Herd et al. 2017; Lapen et al. 2017). Prior to two recent studies, the depleted shergottites were all thought to have been younger than ~600 Ma. NWA 7635, with a $^{147}Sm/^{143}Nd$ crystallization age of 2403 ± 140 Ma (Lapen et al. 2017), and NWA 8159, with a $^{147}Sm/^{143}Nd$ crystallization age of 2300 ± 250 Ma (Herd et al. 2017), have greatly extended the potential magmatic history of the shergottites. Ejection ages for shergottites are all under 5 Ma (Herzog and Caffee 2014) with the exceptions of Dhofar 019 (18 Ma). Depleted shergottites and NWA 7635 have been suggested to originate from the same igneous body based on their nearly identical ejection ages of ~1.1 Ma (Herzog and Caffee 2014; Wieler et al. 2016; Lapen et al. 2017), and this suggests the existence of continuous Martian volcanism for half of the planet's history.

An additional complication in the Martian crystallization story is the "Old Shergottite Paradox." While the $^{147}Sm/^{143}Nd$, $^{87}Rb/^{87}Sr$, and $^{176}Lu/^{176}Hf$ chronometers show Amazonian ages for the shergottites, the Pb-Pb system has consistently yielded concordant ages older than 4 Ga (Bouvier et al. 2005, 2008, 2009). Given that aside from some young basaltic lava flows, the Martian surface appears to be predominantly ancient (>4 Ga) (Hartmann and Neukum 2001), the Pb-Pb ages of shergottites have been suggested to reflect primary crystallization of these ancient terrains. This would argue that the younger ages produced by the other chronometers were a result of later disruptions such as impact resetting, fluid percolation, the drying of lakes, or even the combination of impacts and wet soil, creating superheated steam which would more effectively reset phosphate-based chronometers (Bouvier et al. 2009).

Recent studies have called the old ages of the shergottites into question, disputing the presence of any >4 Ga Pb-Pb "isochron" with crystallization age significance. Secondary ion mass spectrometry (SIMS) Pb-Pb measurements of maskelynite grains in ALH 84001 and some enriched shergottites, interpreted to reflect initial Pb isotopic compositions since plagioclase incorporates very little U, showed significantly differing values, presumably due to crystallization ages separated by ~4 Ga (Bellucci et al. 2015a). In-situ SIMS Pb-Pb analyses of different phases in Chassigny revealed 3-component mixing array between initial Pb, radiogenic Pb along a 1.39 Ga isochron, and an unsupported radiogenic reservoir (Bellucci et al. 2016). This reservoir was heterogeneously present in phases whose major element compositions were otherwise homogenous, and its Pb composition plotted off the 1.39 Ga reservoir. Thus, it could not be explained by in-situ accumulation of radiogenic Pb and must represent non-igneous introduction of a likely crustal Martian reservoir. A hypothetical composition for this high μ

reservoir is provided by the Martian regolith breccias (Bellucci et al. 2015b), which the phases in Chassigny skew towards (Bellucci et al. 2016).

The $^{147}Sm/^{143}Nd$ and $^{87}Rb/^{87}Sr$ dating of nakhlites and chassignites have yielded crystallization ages around ~1300 Ma (Nakamura et al. 1982; Shih et al. 1998, 1999; Borg and Drake 2005; Misawa et al. 2006), with a mean age of 1340 ± 40 Ma (Udry and Day 2018). The ejection ages of most nakhlites and Chassigny cluster around ~10 Ma (Herzog and Caffee 2014; Cohen et al. 2017). Additionally, nakhlites and chassignites share similar trace element (Treiman 2005; Udry and Day 2018) and volatile-bearing phosphate (McCubbin et al. 2013) compositions. These lines of evidence and their similar petrologic texture suggest that they were formed in separate flows, sills, and dikes part of the same overall igneous complex (Udry and Day 2018) whose magmatic source reservoir is distinct from that of the shergottites.

The discovery of additional unique Martian meteorites has further complicated the magmatic history derived from study of the SNC suite. The $^{147}Sm/^{143}Nd$ ages determined for the orthopyroxene cumulate ALH 84001 have converged at ~4400 Ma (Nyquist et al. 2001). However, $^{176}Lu/^{176}Hf$ dating found a younger age of 4091 ± 30 Ma which concords with its $^{40}Ar/^{39}Ar$ and U-Pb ages (Lapen et al. 2010). The older ages were likely due to extensive alteration, but controversy over the true crystallization age still exists.

NWA 7034 and its pairs, the Martian regolith breccias, represent the oldest age dates yet found in Martian meteorites. Secondary ion mass spectrometry (SIMS) U-Pb dating of zircons in monzonitic clasts within one of its pairs, NWA 7533, revealed a discordia line with two intercepts at 4,428 ± 25 Ma and 1,712 ± 85 Ma, suggesting that the igneous clasts in the meteorite are sourced from an evolved Martian crust from the first ~100 Ma of solar system history (Humayun et al. 2013). The 1.7 Ga age is similar to a 2.1 Ga $^{87}Rb/^{87}Sr$ age (Agee et al.

2013), suggesting a major disturbance around that time. U-Pb dating of phosphates within the matrix also found a younger age of 1.357 ± 81 Ga, while Pb-Pb analyses of feldspars in igneous clasts identified a high μ ($^{238}U/^{204}Pb$) reservoir at least 4,428 Ma in age (Bellucci et al. 2015b), providing further evidence for an ancient enriched crust. $^{147}Sm/^{143}Nd$ dating of the igneous components of the regolith breccia provided additional confirmation with an age of 4,420 ± 70 Ma (Nyquist et al. 2016). Additional analyses of zircons within igneous clasts and matrix found two discrete sets of concordant U-Pb ages at 4,431 ± 27 Ma and 1,502 ± 98 Ma (McCubbin et al. 2016). Cl-apatite from igneous clasts and matrix analyses in the same study revealed a U-Pb age of 1,495 ± 88 Ma, suggesting a breccia-wide thermal event at that time such as an impact or volcanism.

The most precise zircon analyses conducted on the Martian regolith breccia, using acid dissolution and thermal ionization mass spectrometry (TIMS) instead of in-situ methods, yielded crystallization ages between 4,476.3 ± 0.9 Ma and 4,429.7 ± 1.0 Ma (Bouvier et al. 2018). Since the meteorite is only mildly shocked (<15 GPa) (Moser et al. 2019), $^{40}Ar/^{39}Ar$ analyses could also be used to extract reliable age information other than shock ages, as with the rest of the SNC suite. $^{40}Ar/^{39}Ar$ analysis of whole-rock fragments found several coherent plateau ages between 1,319 ± 16 Ma and 1,191 ± 32 Ma (Cassata et al. 2018). Rather than thermal metamorphism resulting from an impact, which would cool in a few 10's of Ma or less (Abramov and Kring 2005), these plateaus, along with the overlapping U-Pb ages, suggest a protracted period of metamorphism that varied spatially and temporally, such as that resulting from contact metamorphism due to volcanism (Cassata et al. 2018). An even younger event of ~225 Ma or earlier was identified via U-Th-Sm/He chronometry, suggested to be an impact that resulted in the brecciation and consolidation of the meteorites in their current form (Cassata et al. 2018).

Finally, an ejection event of ~5 Ma (Cartwright et al. 2014) brought the breccia into an Earth-crossing orbit. In summary, NWA 7034 and its pairs sample an ancient, evolved Noachian crust, distinct Amazonian volcanic and impact events, and a unique and recent ejection event, none of which are evident via the rest of the Martian meteorite suite.

4. Differentiation

Since they represent the only samples available from Mars, the Martian meteorite suite has been used in attempts to understand the large-scale magmatic processes that have shaped the planet's geologic history. For instance, the major and trace element compositions and isotopic systematics of shergottites have been used as constraints to test petrogenetic models of the magmatic differentiation of silicate Mars. One way to explain the geochemical diversity of shergottites is by assuming they formed by crustal assimilation and fractional crystallization (AFC) of mantle-derived magmas (Herd et al. 2002). However, the shergottites' bulk $^{87}Sr/^{86}Sr$ and $^{87}Rb/^{86}Sr$ values have been shown to plot along the ~4.5 Ga isochron known as the basaltic achondrite best initial (BABI) line (Papanastassiou and Wasserburg 1968; Shih et al. 1982). The AFC model would thus require the crustal assimilated material to have an age of ~4.5 Ga and remain undisturbed through the crystallization ages of all of the shergottites, which is unlikely (Borg et al. 2002) given the history of impact and volcanism experienced by the planet. In addition, the shergottites' incompatible trace element abundances, ratios, and isotopic compositions do not correlate well with their mineralogical or geochemical indices of differentiation, such as SiO_2 content or Mg# [molar Mg/(Mg+Fe)] (Borg and Draper 2003). The Martian regolith breccia, as its zircons and igneous fragments represent an enriched ancient crust, was likewise found to deviate from the shergottite mixing line in $\varepsilon^{143}Nd$-$\mu^{142}Nd$ space

(discussed further below), invalidating its role as an enriched end-member for shergottite crustal assimilation (Armytage et al. 2018).

Another model invoked to explain Martian basaltic volcanism involves equilibrium and fractional crystallization of the Martian magma ocean (MMO) into cumulate piles and enriched residual liquids (Borg and Draper 2003). The cumulate piles were then melted and mixed in varying proportions with the residual liquids to produce the diverse parent liquids of the shergottites. This two-stage model proposed a mixing relationship between geochemically enriched and depleted shergottite source regions early in Martian geologic history, which would satisfy the constraints imposed by the shergottites' bulk Rb-Sr systematics (Borg and Draper 2003). The compositions of cumulate packages were constrained using the bulk composition of Mars (Dreibus and Wanke 1985; Lodders and Fegley 1997) and petrological melting experiments at estimated pressures of the crystallizing MMO that included majoritic garnet as a near-liquidus phase (Draper et al. 2003). Partial melting of the cumulate piles was able to reproduce the major element concentrations and radiogenic parent/daughter ratios of the calculated parent liquid of ALH 77005 (McSween et al. 1988). Since this liquid was the most mafic of the Martian basalts, it was used as a least-differentiated end member in the model. More evolved compositions could then be reached through olivine fractionation. The trace incompatible element abundances of Martian basaltic liquids were reproduced by including a small fraction of residual liquid, solidified in the final stages of MMO crystallization, in the partial melting phase.

The combinations of several radiogenic isotope systems have been used to constrain the results of differentiation modeling. The short-lived isotope ^{146}Sm decays to ^{142}Nd with a half-life

of ~103 Ma[1] and thus imparts a ^{142}Nd anomaly on material that differentiated early enough in solar system history that it was still a live nuclide. When ^{146}Sm-^{142}Nd is combined with longer-lived isotopic systems such as ^{87}Rb/^{87}Sr and ^{147}Sm/^{143}Nd, the timing of both source differentiation and liquid crystallization can be constrained in a single model (Borg et al. 1997; Borg and Draper 2003). For example, the ε^{142}Nd ([^{142}Nd/^{144}Nd$_{sample}$ / ^{142}Nd/^{144}Nd$_{standard}$ -1] × 10000) of the basaltic shergottite Queen Alexandra Range (QUE) 94201 was found to be high enough to require fractionation of its source from bulk Mars no later than 33 Ma after the planet's formation (Borg et al. 1997). However, its calculated initial ε^{143}Nd ([^{143}Nd/^{144}Nd$_{sample\ initial}$ / ^{143}Nd/^{144}Nd$_{CHUR\ at\ T}$ -1] × 10000) required that its source remained relatively inactive until its crystallization age of ~327 Ma because any intermittent melting would have made the ε^{143}Nd value too high (Borg et al. 1997).

Early models of shergottite source crystallization combined the ^{146}Sm-^{142}Nd and ^{147}Sm-^{143}Nd chronometers for multiple Martian samples by plotting their initial ε^{143}Nd values, recalculated at 175 Ma, the average crystallization age of several shergottites, against their present-day measured ε^{142}Nd values (Borg et al. 2003). Several enriched and depleted shergottites formed an isochron that intersected with the chondritic uniform reservoir (CHUR) and converged on an age of ~4510 Ma, interpreted as the age of MMO differentiation from CHUR into geochemically enriched and depleted reservoirs. Other samples, such as the nakhlites and chassignites, plotted off this isochron, implying derivation from separate reservoirs or more complex igneous history (Borg and Draper 2003).

[1] This age has recently been questioned by Kinoshita (2012), who found a half-life of 68 Ma. Despite this, the present paper assumes the canonical value in reporting literature ages. The IUGS-IUPAC recommends using both half-lives to calculate ages until the discrepancy is resolved (Villa et al. 2020). For discussion see Borg et al. (2016).

The coupled ^{142}Nd-^{143}Nd chronometer was later refined in regards to shergottites with higher precision measurements of ^{142}Nd and additional sample measurements. An updated plot of enriched, intermediate, and depleted shergottites on the ε^{143}Nd vs. ε^{142}Nd graph formed a mixing line that missed the origin and thus is not likely to be an isochron (for an example of such a plot see Fig. 3) (Debaille et al. 2007). Instead, the coupled isotopic systematics for depleted and enriched shergottites were interpreted to constrain earlier and later Sm/Nd fractionation events, at ~4535 Ma and ~4457 Ma respectively. The calculated ^{147}Sm/^{144}Nd of the shergottite sources was found to be higher for each meteorite than the ^{147}Sm/^{144}Nd of the meteorites themselves, and this is the opposite of what is expected during partial melting since Nd is a more incompatible element than Sm (Debaille et al. 2007). Therefore, the source of the shergottites likely underwent a partial melting event immediately before melting to produce the shergottites, and the enriched and intermediate shergottites incorporated varying amounts of this depleted source and a distinct enriched source.

Additional analyses of shergottites have cast doubts on the need for multiple melting and differentiation events. The linear mixing line (Debaille et al. 2007) found between enriched and depleted shergottites in ^{147}Sm-^{144}Nd space has been obscured by newer data (Caro et al. 2008; Brennecka et al. 2014) showing variation in bulk rock ^{147}Sm/^{144}Nd in meteorites with similar calculated source ^{147}Sm/^{144}Nd values (Borg et al. 2016). Newer models showed that two separate 3-stage petrogenetic models using shergottite bulk rock ^{142}Nd, ^{147}Sm, and ^{143}Nd measurements converged on a source differentiation age of 4504 ± 6 Ma (Borg et al. 2016). The first model formed an isochron by plotting the measured bulk rock ^{142}Nd/^{144}Nd of the shergottites against their source ^{147}Sm/^{144}Nd, calculated from measured ^{143}Nd/^{144}Nd values. The second plotted the ^{142}Nd/^{144}Nd of each meteorite against their present-day source ε^{143}Nd, calculated from each

meteorite's initial $^{143}Nd/^{144}Nd$ (see Fig. 3). Importantly, neither model relied on an assumed initial $^{142}Nd/^{144}Nd$ for bulk Mars, and both allowed for binary mixing between depleted and enriched shergottite end members early in Martian history.

The Sm-Nd data from nakhlites and chassignites have been shown to diverge significantly from any model age isochrons formed by the shergottites (Debaille et al. 2009). Thus, the variation in Sm and Nd isotopic compositions between shergottites and nakhlites cannot be attributed to a single differentiation event early in Martian geologic history. Likewise, the crustal breccia NWA 7034 diverges from the shergottite mixing line in ^{142}Nd-^{143}Nd space, using either measured values from the meteorite or ones calculated for its source (Fig. 3) (Armytage et al. 2018). This suggests that it does not represent an enriched crustal end member for shergottite differentiation, and it casts doubts on the idea that the shergottite mixing line is in fact an isochron.

The extinct ^{182}Hf-^{182}W chronometer, which has a half-life of 9 Ma, has been coupled with the $^{142}Nd/^{144}Nd$ system to refine the time scale of magmatic source differentiation (Kruijer et al. 2017). The combined ^{182}W-^{143}Nd chronometer showed that instead of forming a binary contemporaneous mixing line between depleted and enriched shergottite sources, the shergottite source differentiation was instead spread between ~20-25 m.y. and ~40 m.y. after solar system formation (Fig. 4) (Kruijer et al. 2017). This was due primarily to a larger range in $\varepsilon^{182}W$ identified among depleted shergottites (+0.8 to +1.8). ^{142}Nd measurements of NWA 7034 and ALH 84001 also showed that these samples reflected the most enriched and early to differentiate (~20-25 Ma) source reservoir yet identified on Mars (Kruijer et al. 2017). The early differentiation of an enriched source coincides with modeling results obtained from U-Pb and Lu-Hf analyses performed on zircons in NWA 7034, which required an andesitic, rather than

basaltic, crustal reservoir to differentiate from CHUR in order to satisfy the $^{176}Lu/^{177}Hf$ values of concordant zircons (Bouvier et al. 2018). The U-Pb ages of these zircons converged at 4,475 Ma, while their Lu-Hf systematics suggested that an andesitic crust must have formed no later than 4,547 Ma. This early crust was completely reworked by impacts, including the one likely responsible for the formation of the Martian crustal dichotomy (Andrews-Hanna et al. 2008).

As this early crust predates meteorite magmatic source differentiation, its age also suggests that this differentiation did not occur under the regime of a crystallizing magma ocean. Instead, the crystallization of the MMO must have happened earlier, resulting in a stratified mantle susceptible to overturn, decompression melting of cumulate material, and extraction of an evolved andesitic crust (Elkins-Tanton et al. 2005; Scheinberg et al. 2014; Bouvier et al. 2018). Alternatively, the MMO may not have existed at all, as a recent study has found hydrogen isotopic heterogeneities within Martian mantle source reservoirs (Barnes et al. 2020). A series of later differentiation events must have formed the source reservoirs of the other Martian meteorites. The nakhlites, which have significantly more radiogenic $\varepsilon^{182}W$ values (~3) (Kleine et al. 2004; Foley et al. 2005), must have originated from a separate but roughly coeval magmatic source. The positive $\varepsilon^{182}W$ and $\varepsilon^{142}Nd$ values of SNC meteorites require that their sources formed from a garnet and clinopyroxene bearing mantle, since these phases fractionate Hf/W as well as Sm/Nd (Righter and Shearer 2003). The ongoing magmatism resulting from these differentiation events, along with impacts, completely resurfaced the planet.

5. Core Formation

Because W is a much more siderophile element than Hf, it fractionates completely from Hf during metal-silicate separation. The timing of the core formation of planetary bodies is

constrained by measuring ^{182}W anomalies from primitive chondritic values in silicates derived from material that underwent core formation while ^{182}Hf was still extant. Measuring the $\varepsilon^{182}W$ of Martian meteorites showed a small range in values for the shergottites (0.3 to 0.7) and a distinct and uniform value of ~3 for the nakhlites (Foley et al. 2005). By plotting $\varepsilon^{142}Nd$ values against $\varepsilon^{182}W$ values for the shergottites and solving the best-fit line for chondritic ^{142}Nd, a primitive Martian mantle (PMM) $\varepsilon^{182}W$ of 0.34±0.7 was determined (see Fig. 4). This value allowed for a two-stage model age for the Martian core formation of 11.6±0.4 m.y. after solar system formation (Foley et al. 2005). Other estimates for Martian core formation using W isotopes have ranged from ~3 to ~15 m.y. after solar system formation (Kleine et al. 2004; Nimmo and Kleine 2007).

A more recent study has found more variation in $\varepsilon^{182}W$ among the shergottites and that this variation correlates with $\varepsilon^{142}Nd$ (Kruijer et al. 2017). However, the new measurements did little to modify the bulk Mars $\varepsilon^{182}W$ value, since the Martian meteorites whose $\varepsilon^{142}Nd$ spanned the range of estimated bulk Mars $\varepsilon^{142}Nd$ values (Debaille et al. 2007; Borg et al. 2016) were relatively constrained in $\varepsilon^{182}W$. Thus, the new PMM $\varepsilon^{182}W$ was found to be +0.37 ± 0.04 (Fig. 4), within error of the old one. Combining this value with the bulk Martian $^{180}Hf/^{184}W$ ratio of 4.0 ± 0.5 (Dauphas and Pourmand 2011) yielded a two-stage model age for core formation of 4.1 ± 2.7 m.y. after solar system formation (Fig. 4) (Kruijer et al. 2017). This is consistent with the accretion timescale of a stranded planetary embryo, in which Mars attained half of its mass in ~2 m.y. or less (Dauphas and Pourmand 2011; Kruijer et al. 2017).

6. Conclusions

It is clear at this point that the 150 unpaired Martian samples that are currently available for study vastly undersample the igneous history of the planet Mars. The identification of petrologically diverse and evolved material by rovers suggests that the shergottites, nakhlites, chassignites, ALH 84001, and the Martian regolith breccias only offer a small window into the magmatic evolution of the planet (Table 1), and thus the need for sample return missions is highlighted by the study of Martian meteorites. There is now significant petrological and geochemical evidence that both the nakhlites and chassignites as a group, as well as the depleted shergottites, both originate from their own unique magma bodies. The Martian regolith breccias also sample a unique magmatic reservoir and possibly an ancient enriched crust that was later modified by impacts. These sources must have been separated since the earliest differentiation of Mars shortly after the birth of the solar system and stayed separate through the crystallization of the Martian igneous suite.

The need to better define the magmatic reservoirs present on Mars is another urgent reason to increase sample diversity. The Martian mantle is clearly heterogeneous, and its igneous products show a great deal of diversity in isotopic systematics, such that the timing for major events in the planet's history is likely subject to change (Fig. 5). This diversity is reflective of a silicate Mars that was inefficiently mixed during its early history. More unique magmatic source reservoirs are likely waiting to be discovered with additional samples from the planet. The wealth of research that the discovery of the Martian regolith breccias has generated is a testament to this, and new potential Noachian and Hesperian samples will likely again completely redefine our understanding of Martian igneous history.

Figures & Tables

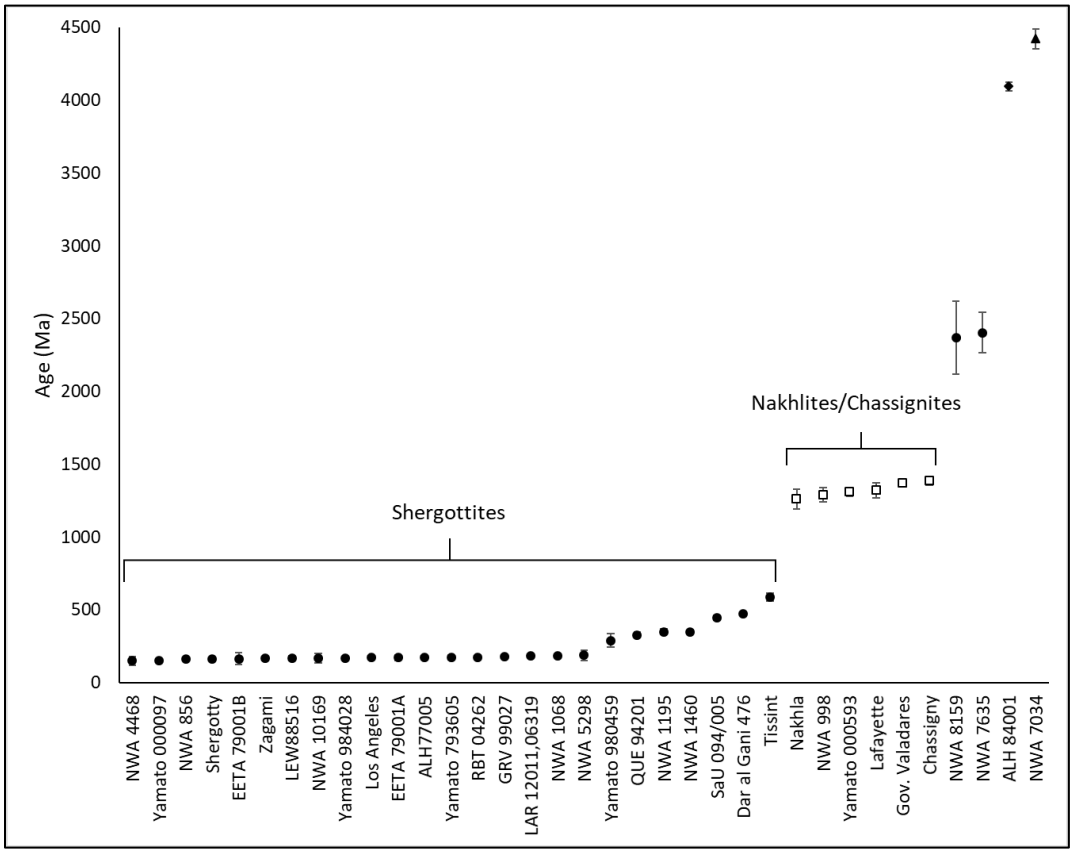

Figure 1. Crystallization ages of shergottites (black circles), nakhlites and chassignites (white squares), NWA 7034 (black), ALH 84001 (black diamond), and NWA 7034 (black triangle). The age shown for NWA 7034 corresponds to the oldest measured igneous clasts. Data are from Borg and Drake (2005); Herd et al. (2017); Lapen et al. (2017); Bouvier et al. (2018); Cassata et al. (2018); Udry and Day (2018) and references therein.

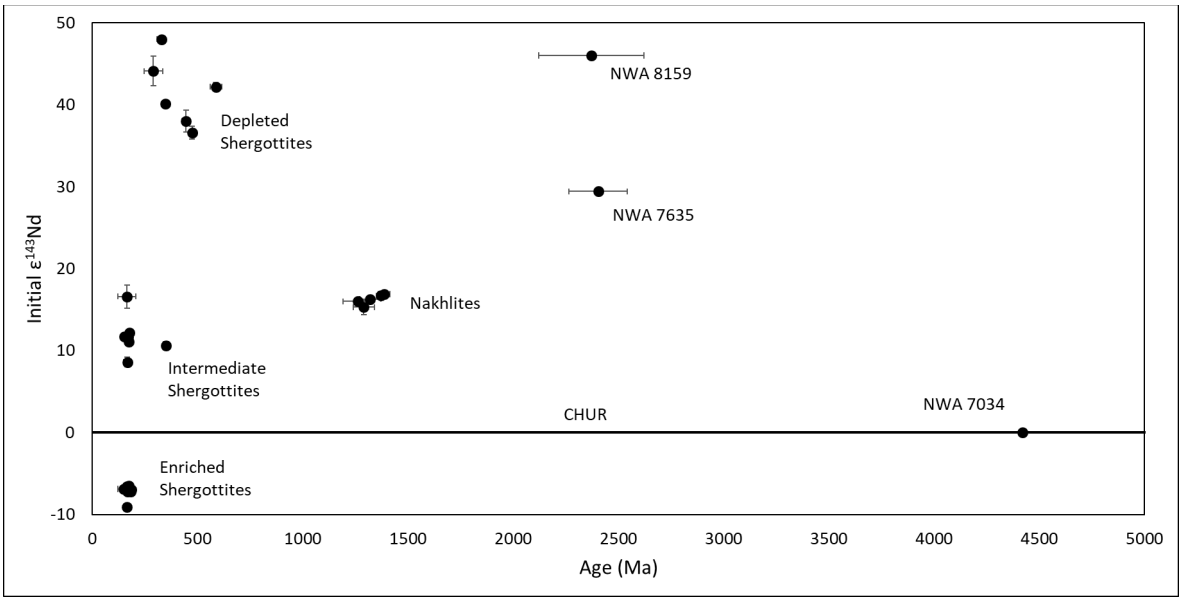

Figure 2. $^{147}Sm/^{143}Nd$ ages and calculated initial εNd values for Martian meteorites (Nakamura et al. 1982; Shih et al. 1982, 1998, 1999, 2003, 2004, 2007, 2009, 2011; Borg et al. 1997, 2002, 2003, 2005, 2008; Morikawa et al. 2001; Nyquist et al. 2001, 2009, 2016; Carlson and Irving 2004; Symes et al. 2005; Misawa et al. 2006, 2008; Shafer et al. 2010; Liu et al. 2011; Brennecka et al. 2014; Ferdous et al. 2017; Herd et al. 2017; Lapen et al. 2017).

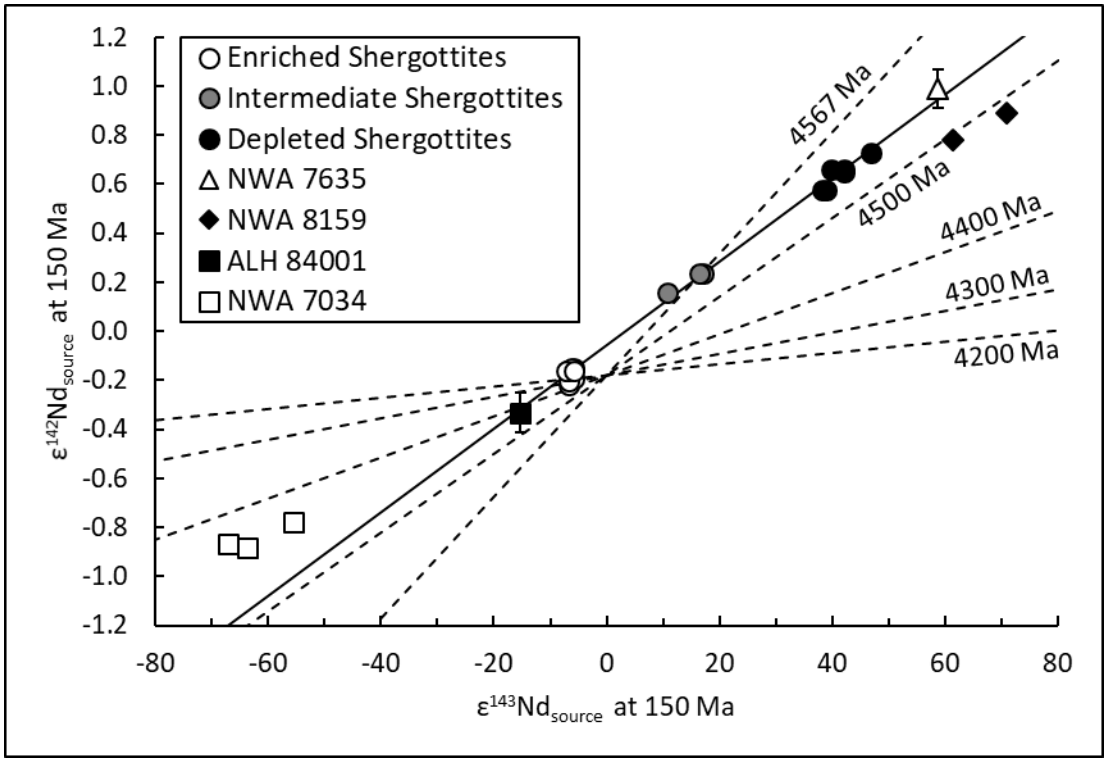

Figure 3. Calculated source ε^{142}Nd vs. ε^{143}Nd at 150 Ma for Martian meteorites. ε^{142}Nd values for ALH 84001 and the Martian regolith breccia sources are corrected for radiogenic growth of ^{142}Nd. Solid black line is the shergottite source regression line (SSRL) whose slope reflects the age of shergottite source differentiation [4506 ± 6 Ma (Borg et al. 2016)]. Dotted lines are model age isochrons which pass through the chondritic ε^{142}Nd value of -0.18 (Debaille et al. 2007). Since the SSRL does not intersect the model age origin, either it is not an isochron, or Mars' initial ^{142}Nd composition was not chondritic (Borg et al. 2016). The source of Martian regolith breccia does not intersect the SSRL, suggesting that the shergottite differentiation event was not a planet-wide event such as crystallization and overturn of a magma ocean. Data and models are from Borg et al. (2016) and Armytage et al. (2018) and references within. Errors are plotted when symbol is smaller than error.

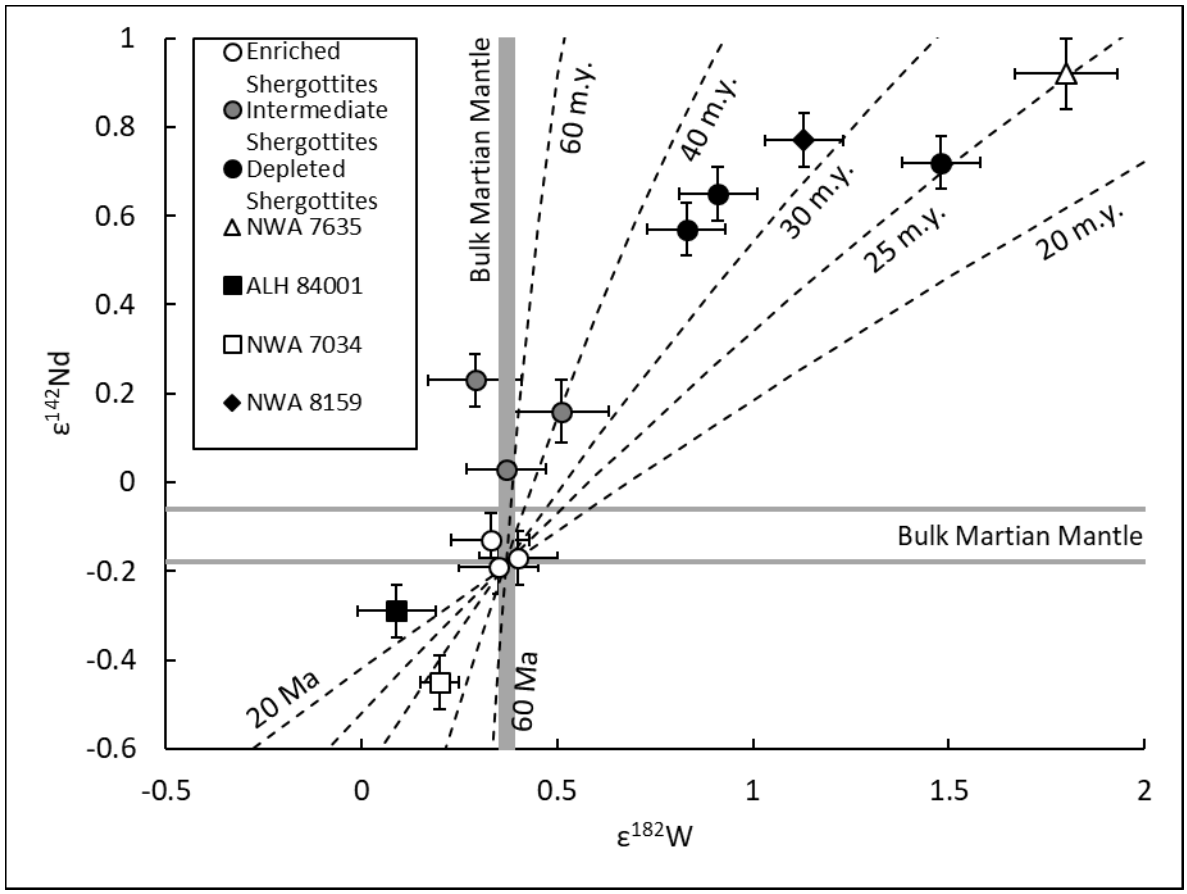

Figure 4. $\varepsilon^{182}W$ vs. $\varepsilon^{142}Nd$ for Martian meteorites. Grey horizontal lines are the ranges of potential Martian bulk $\varepsilon^{142}Nd$ values (Debaille et al. 2007; Borg et al. 2016), and grey vertical line is the range of Martian bulk $\varepsilon^{182}W$, deduced from these values and Martian meteorite $\varepsilon^{182}W$. Dashed lines represent model times for source differentiation after solar system formation. Data and model calculations from Kruijer et al. (2017) and references within.

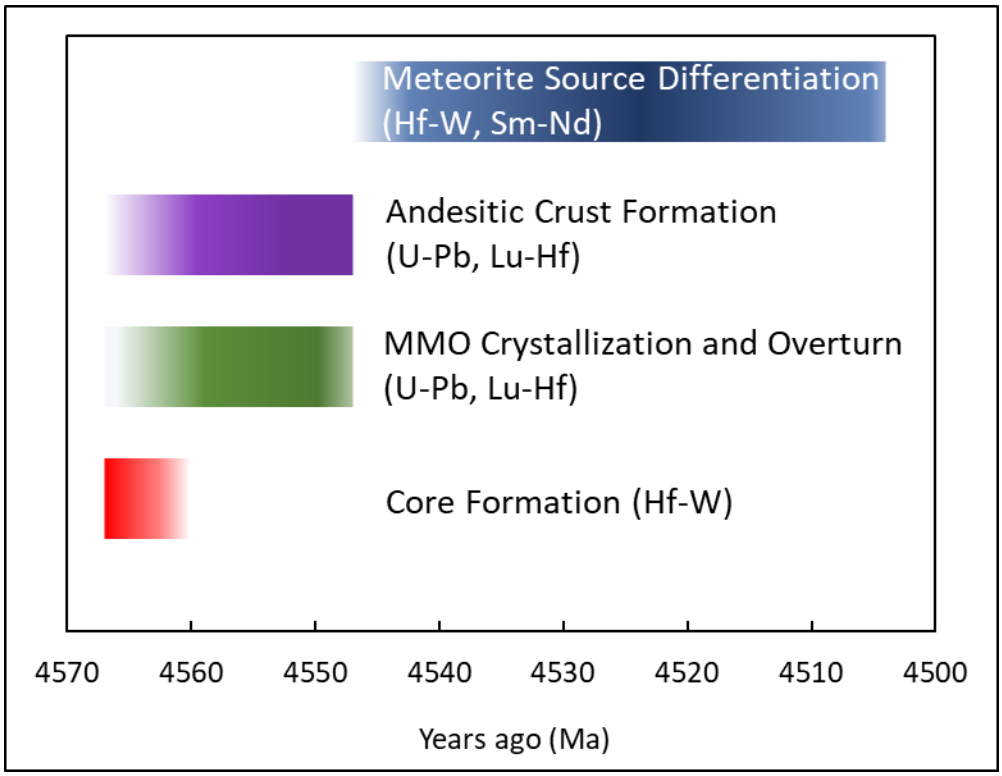

Figure 5. Summary of Early Martian events based on various chronometers (Foley et al. 2005; Debaille et al. 2008, 2009; Borg et al. 2016; Kruijer et al. 2017; Bellucci et al. 2018; Bouvier et al. 2018).

Table 1. Summary table of Martian meteorite ages, rock types, and geochemistry.

Meteorites	Ages	Rock Type(s)	Geochemistry
Shergottites	~150-600 Ma; ~2400 Ma	Gabbro, diabase, basalt	Depleted to Enriched in LREE
Nakhlites	~1300 Ma	Augite and olivine cumulate	Enriched in REE and LREE
Chassignites	~1300 Ma	Dunite	Enriched in LREE
NWA 8159	~2300 Ma	Augite basalt	Depleted in LREE
ALH 84001	~4100 Ma	Orthopyroxenite	Nearly chondritic REE
NWA 7034 and pairs	~4500 Ma	Polymict igneous breccia	Enriched in REE and LREE

References

Abramov O., and Kring D. A. 2005. Impact-induced hydrothermal activity on early Mars. *Journal of Geophysical Research: Planets* 110:1–19.

Agee C. B. et al. 2013. Unique meteorite from early Amazonian Mars: water-rich basaltic breccia Northwest Africa 7034. *Science* 339:780–5. http://www.ncbi.nlm.nih.gov/pubmed/23287721.

Andrews-Hanna J. C., Zuber M. T., and Banerdt W. B. 2008. The Borealis basin and the origin of the martian crustal dichotomy. *Nature* 453:1212–1215.

Armytage R. M. G., Debaille V., Brandon A. D., and Agee C. B. 2018. A complex history of silicate differentiation of Mars from Nd and Hf isotopes in crustal breccia NWA 7034. *Earth and Planetary Science Letters* 502:274–283. https://doi.org/10.1016/j.epsl.2018.08.013.

Artemieva N., and Ivanov B. 2004. Launch of martian meteorites in oblique impacts. *Icarus* 171:84–101.

Barnes J. J. et al. 2020. Multiple early-formed water reservoirs in the interior of Mars. *Nature* Geoscience 13:260–264. http://dx.doi.org/10.1038/s41561-020-0552-y.

Bellucci J. J., Nemchin A. A., Whitehouse M. J., Snape J. F., Bland P., and Benedix G. K. 2015a. The Pb isotopic evolution of the Martian mantle constrained by initial Pb in Martian meteorites. *Journal of Geophysical Research: Planets* 120:2224–2240.

Bellucci J. J., Nemchin A. A., Whitehouse M. J., Humayun M., Hewins R., and Zanda B. 2015b. Pb-isotopic evidence for an early, enriched crust on Mars. *Earth and Planetary Science Letters* 410:34–41. http://dx.doi.org/10.1016/j.epsl.2014.11.018.

Bellucci J. J., Nemchin A. A., Whitehouse M. J., Snape J. F., Kielman R. B., Bland P. A., and Benedix G. K. 2016. A Pb isotopic resolution to the Martian meteorite age paradox. *Earth and Planetary Science Letters* 433:241–248. http://dx.doi.org/10.1016/j.epsl.2015.11.004.

Borg L. E., Nyquist L. E., Taylor L. A., Wiesmann H., and Shih C. Y. 1997. Constraints on Martian differentiation processes from Rb-Sr and Sm-Nd isotopic analyses of the basaltic shergottite QUE 94201. *Geochimica et Cosmochimica Acta* 61:4915–4931.

Borg L. E., Connelly J. N., Nyquist L. E., Shih C. Y., Wiesmann H., and Reese Y. 1999. The age of the carbonates in martian meteorite ALH84001. *Science* 286:90–94.

Borg L. E., Nyquist L. E., Wiesmann H., and Reese Y. 2002. Constraints on the petrogenesis of Martian meteorites from the Rb-Sr and Sm-Nd isotopic systematics of the lherzolitic shergottites ALH77005 and LEW88516. *Geochimica et Cosmochimica Acta* 66:2037–2053.

Borg L. E., and Draper D. S. 2003. A petrogenetic model for the origin and compositional variation of the martian basaltic meteorites. *Meteoritics & Planetary Science* 38:1713–1731. http://doi.wiley.com/10.1111/j.1945-5100.2003.tb00011.x.

Borg L. E., Nyquist L. E., Wiesmann H., Shih C. Y., and Reese Y. 2003. The age of Dar al Gani 476 and the differentation history of the martian meteorites inferred from their radiogenic isotopic systematics. *Geochimica et Cosmochimica Acta* 67:3519–3536.

Borg L. E., Edmunson J. E., and Asmerom Y. 2005. Constraints on the U-Pb isotopic systematics of Mars inferred from a combined U-Pb, Rb-Sr, and Sm-Nd isotopic study of the Martian meteorite Zagami. *Geochimica et Cosmochimica Acta* 69:5819–5830.

Borg L., and Drake M. J. 2005. A review of meteorite evidence for the timing of magmatism and of surface or near-surface liquid water on Mars. *Journal of Geophysical Research E: Planets* 110:1–10.

Borg L. E., Brennecka G. A., and Symes S. J. K. 2016. Accretion timescale and impact history of Mars deduced from the isotopic systematics of martian meteorites. *Geochimica et Cosmochimica Acta* 175:150–167. http://dx.doi.org/10.1016/j.gca.2015.12.002.

Bouvier A., Blichert-Toft J., Vervoort J. D., and Albarède F. 2005. The age of SNC meteorites and the antiquity of the Martian surface. *Earth and Planetary Science Letters* 240:221–233.

Bouvier A., Blichert-Toft J., Vervoort J. D., Gillet P., and Albarède F. 2008. The case for old basaltic shergottites. *Earth and Planetary Science Letters* 266:105–124.

Bouvier A., Blichert-Toft J., and Albarède F. 2009. Martian meteorite chronology and the evolution of the interior of Mars. *Earth and Planetary Science Letters* 280:285–295. http://dx.doi.org/10.1016/j.epsl.2009.01.042.

Bouvier L. C. et al. 2018. Evidence for extremely rapid magma ocean crystallization and crust formation on Mars. *Nature* 558:586–589.

Brennecka G. A., Borg L. E., and Wadhwa M. 2014. Insights into the Martian mantle: The age and isotopics of the meteorite fall Tissint. *Meteoritics and Planetary Science* 49:412–418.

Caro G., Bourdon B., Halliday A. N., and Quitté G. 2008. Super-chondritic Sm/Nd ratios in Mars, the Earth and the Moon. *Nature* 452:336–339.

Cartwright J. A., Ott U., Herrmann S., and Agee C. B. 2014. Modern atmospheric signatures in 4.4 Ga Martian meteorite NWA 7034. *Earth and Planetary Science Letters* 400:77–87. http://dx.doi.org/10.1016/j.epsl.2014.05.008.

Cassata W. S., Cohen B. E., Mark D. F., Trappitsch R., Crow C. A., Wimpenny J., Lee M. R., and Smith C. L. 2018. Chronology of martian breccia NWA 7034 and the formation of the martian crustal dichotomy. *Science Advances* 4.

Chambers J. E. 2004. Planetary accretion in the inner Solar System. *Earth and Planetary Science Letters* 223:241–252.

Clayton R. N., and Mayeda T. K. 1996. Oxygen isotope studies of achondrites. *Geochimica et Cosmochimica Acta* 60:1999–2017.

Cohen B. E., Mark D. F., Cassata W. S., Lee M. R., Tomkinson T., and Smith C. L. 2017. Taking the pulse of Mars via dating of a plume-fed volcano. *Nature Communications* 8:1–8. http://dx.doi.org/10.1038/s41467-017-00513-8.

Combs L. M., Udry A., Howarth G. H., Righter M., Lapen T. J., Gross J., Ross D. K., Rahib R. R., and Day J. M. D. 2019. Petrology of the enriched poikilitic shergottite Northwest Africa 10169: Insight into the martian interior. *Geochimica et Cosmochimica Acta* 266:435–462. https://doi.org/10.1016/j.gca.2019.07.001.

Cousin A. et al. 2017. Classification of igneous rocks analyzed by ChemCam at Gale crater, Mars. *Icarus* 288:265–283. http://dx.doi.org/10.1016/j.icarus.2017.01.014.

Crozaz G., and Wadhwa M. 2001. The terrestrial alteration of saharan shergottites dar al ganid 476 and 489: A case study of weathering in a hot desert environment. *Geochimica et Cosmochimica Acta* 65:971–978.

Crozaz G., Floss C., and Wadhwa M. 2003. Chemical alteration and REE mobilization in meteorites from hot and cold deserts. *Geochimica et Cosmochimica Acta* 67:4727–4741.

Dauphas N., and Chaussidon M. 2011. A Perspective from Extinct Radionuclides on a Young Stellar Object: The Sun and Its Accretion Disk. *Annual Review of Earth and Planetary Sciences* 39:351–386. http://arxiv.org/abs/1105.5172%5Cnhttp://www.annualreviews.org/doi/abs/10.1146/annurev-earth-040610-133428.

Dauphas N., and Pourmand A. 2011. Hf-W-Th evidence for rapid growth of Mars and its status as a planetary embryo. *Nature* 473:489–492. http://dx.doi.org/10.1038/nature10077.

Debaille V., Brandon a D., Yin Q. Z., and Jacobsen B. 2007. Coupled 142Nd-143Nd evidence for a protracted magma ocean in Mars. *Nature* 450:525–528.

Debaille V., Brandon A. D., Oneill C., Yin Q. Z., and Jacobsen B. 2009. Early martian mantle overturn inferred from isotopic composition of nakhlite meteorites. *Nature Geoscience* 2:548–552. http://dx.doi.org/10.1038/ngeo579.

Draper D. S., Xirouchakis D., and Agee C. B. 2003. Trace element partitioning between garnet and chondritic melt from 5 to 9 GPa: Implications for the onset of the majorite transition in the martian mantle. *Physics of the Earth and Planetary Interiors* 139:149–169.

Dreibus G., and Wanke H. 1985. Mars, a volatile-rich planet. *Meteoritics* 20:367–381.

Elkins-Tanton L. T., Hess P. C., and Parmentier E. M. 2005. Possible formation of ancient crust on Mars through magma ocean processes. *Journal of Geophysical Research: Planets* 110:1–11.

Ferdous J., Brandon A. D., Peslier A. H., and Pirotte Z. 2017. Evaluating crustal contributions to enriched shergottites from the petrology, trace elements, and Rb-Sr and Sm-Nd isotope systematics of Northwest Africa 856. *Geochimica et Cosmochimica Acta* 211:280–306. http://dx.doi.org/10.1016/j.gca.2017.05.032.

Filiberto J. 2017. Geochemistry of Martian basalts with constraints on magma genesis. *Chemical Geology* 466:1–14. http://dx.doi.org/10.1016/j.chemgeo.2017.06.009.

Foley C. N., Wadhwa M., Borg L. E., Janney P. E., Hines R., and Grove T. L. 2005. The early differentiation history of Mars from ^{182}W-^{142}Nd isotope systematics in the SNC meteorites. *Geochimica et Cosmochimica Acta* 69:4557–4571.

Fritz J., Artemieva N., and Greshake A. 2005. Ejection of Martian meteorites. *Meteoritics & Planetary Science* 40:1393–1411. http://doi.wiley.com/10.1111/j.1945-5100.2005.tb00409.x.

Hartmann W. K., and Neukum G. 2001. Cratering chronology and the evolution of Mars. *Space Science Reviews* 96:165–194.

Head J. N., Melosh H. J., and Ivanov B. A. 2002. Martian meteorite launch: High-speed ejecta from small craters. *Science* 298:1752–1756.

Herd C. D. K., Borg L. E., Jones J. H., and Papike J. J. 2002. Oxygen fugacity and geochemical variations in the martian basalts: Implications for martian basalt petrogenesis and the oxidation state of the upper mantle of Mars. *Geochimica et Cosmochimica Acta* 66:2025–2036.

Herd C. D. K. et al. 2017. The Northwest Africa 8159 martian meteorite: Expanding the martian sample suite to the early Amazonian. *Geochimica et Cosmochimica Acta* 218:1–26.

Herzog G. F., and Caffee M. W. 2014. Cosmic-Ray Exposure Ages of Meteorites. In *Treatise on Geochemistry*. Elsevier Ltd. pp. 419–453.

Humayun M. et al. 2013. Origin and age of the earliest Martian crust from meteorite NWA 7533. *Nature* 503:513–516.

Kinoshita N. et al. 2012. A shorter 146Sm half-life measured and implications for 146Sm-142Nd chronology in the solar system. *Science* 335:1614–1617.

Kleine T., Mezger K., Münker C., Palme H., and Bischoff A. 2004. 182Hf-182W isotope systematics of chondrites, eucrites, and martian meteorites: Chronology of core formation and early mantle differentiation in Vesta and Mars. *Geochimica et Cosmochimica Acta* 68:2935–2946.

Kruijer T. S., Kleine T., Borg L. E., Brennecka G. A., Irving A. J., Bischoff A., and Agee C. B. 2017. The early differentiation of Mars inferred from Hf–W chronometry. *Earth and Planetary Science Letters* 474:345–354. http://dx.doi.org/10.1016/j.epsl.2017.06.047.

Kunz J., Falter M., and Jessberger E. K. 1997. Shocked meteorites: Argon-40-argon-39 evidence for multiple impacts. *Meteoritics and Planetary Science* 32:647–670.

Lapen T. J., Righter M., Brandon A. D., Debaille V., Beard B. L., Shafer J. T., and Peslier A. H. 2010. A younger age for ALH84001 and Its geochemical link to shergottite sources in mars. *Science* 328:347–351.

Lapen T. J., Righter M., Andreasen R., Irving A. J., Satkoski A. M., Beard B. L., Nishiizumi K., Jull A. J. T., and Caffee M. W. 2017. Two billion years of magmatism recorded from a single Mars meteorite ejection site. *Science Advances* 3:1–7.

Liu T., Li C., and Lin Y. 2011. Rb-Sr and Sm-Nd isotopic systematics of the lherzolitic shergottite GRV 99027. *Meteoritics and Planetary Science* 46:681–689.

Lodders K., and Fegley B. 1997. An oxygen isotope model for the composition of Mars. *Icarus* 126:373–394.

Marks N. E., Borg L. E., Gaffney A. M., and DePaolo D. 2010. The Relationship of Northwest Africa 4468 to the Other Incompatible Element-enriched Shergottites Inferred from its Rb-Sr and Sm-Nd Isotopic Systematics. *41st Lunar and Planetary Science Conference* #2064.

McCubbin F. M., Elardo S. M., Shearer C. K., Smirnov A., Hauri E. H., and Draper D. S. 2013. A petrogenetic model for the comagmatic origin of chassignites and nakhlites: Inferences from chlorine-rich minerals, petrology, and geochemistry. *Meteoritics and Planetary Science* 48:819–853.

McCubbin F. M. et al. 2016. Geologic history of Martian regolith breccia Northwest Africa 7034: Evidence for hydrothermal activity and lithologic diversity in the Martian crust. *Journal of Geophysical Research: Planets* 121:2120–2149.

McSween H. Y. 1985. SNC meteorites: Clues to martain petrogenic evolution? *Rev. Geophys.* 23:391–416.

McSween H. Y. J., Lundberg L., and Crozaz G. 1988. Crystallization of the ALHA77005 Shergottite: How is a Closed System. *Lunar and Planetary Science Conference XIX*.

McSween H. Y. et al. 2006. Alkaline volcanic rocks from the Columbia Hills, Gusev crater, Mars. *Journal of Geophysical Research: Planets* 111:1–15.

Misawa K., Shih C. Y., Reese Y., Bogard D. D., and Nyquist L. E. 2006. Rb-Sr, Sm-Nd and Ar-Ar isotopic systematics of Martian dunite Chassigny. *Earth and Planetary Science Letters* 246:90–101.

Misawa K., Park J., Shih C. Y., Reese Y., Bogard D. D., and Nyquist L. E. 2008. Rb-Sr, Sm-Nd, and Ar-Ar isotopic systematics of lherzolitic shergottite Yamato 000097. *Polar Science* 2:163–174. http://dx.doi.org/10.1016/j.polar.2008.08.001.

Morikawa N., Misawa K., Kondorosi G., Premo W. R., Tatsumoto M., and Nakamura N. 2001. Rb-Sr isotopic systematics of lherzolitic shergottite. *Antarct. Meteorite Res.* 14:47–60.

Moser D. E., Chamberlain K. R., Tait K. T., Schmitt A. K., Darling J. R., Barker I. R., and Hyde B. C. 2013. Solving the Martian meteorite age conundrum using micro-baddeleyite and launch-generated zircon. *Nature* 499:454–457.

Moser D. E. et al. 2019. Decline of giant impacts on Mars by 4.48 billion years ago and an early opportunity for habitability. *Nature Geoscience* 12:522–527. http://dx.doi.org/10.1038/s41561-019-0380-0.

Nakamura N., Unruh D. M., Tatsumoto M., and Hutchison R. 1982. Origin and evolution of the Nakhla meteorite inferred from the Sm-Nd and U-Pb systematics and REE, Ba, Sr, Rb and K abundances. *Geochimica et Cosmochimica Acta* 46:1555–1573. https://www.sciencedirect.com/science/article/pii/0016703782903143?via%3Dihub#aep-abstract-id7 (Accessed October 13, 2018).

Nimmo F., and Kleine T. 2007. How rapidly did Mars accrete? Uncertainties in the Hf-W timing of core formation. *Icarus* 191:497–504.

Nyquist L. E., Bogard D. D., Shih C. Y., Greshake A., Stöffler D., and Eugster O. 2001. Ages and geologic histories of martian meteorites. In *Chronology and Evolution of Mars*. pp. 105–164.

Nyquist L. E., Bogard D. D., Shih C. Y., Park J., Reese Y. D., and Irving A. J. 2009. Concordant Rb-Sr, Sm-Nd, and Ar-Ar ages for Northwest Africa 1460: A 346 Ma old basaltic shergottite related to "lherzolitic" shergottites. *Geochimica et Cosmochimica Acta* 73:4288–4309.

Nyquist L. E., Shih C. Y., Mccubbin F. M., Santos A. R., Shearer C. K., Peng Z. X., Burger P. V., and Agee C. B. 2016. Rb-Sr and Sm-Nd isotopic and REE studies of igneous components in the bulk matrix domain of Martian breccia Northwest Africa 7034. *Meteoritics and Planetary Science* 51:483–498.

Papanastassiou D. A., and Wasserburg G. J. 1968. Initial strontium isotopic abundances and the resolution of small time differences in the formation of planetary objects. *Earth and Planetary Science Letters* 5:361–376. https://www.sciencedirect.com/science/article/pii/S0012821X68800664 (Accessed October 30, 2018).

Papike J. J., Karner J. M., Shearer C. K., and Burger P. V. 2009. Silicate mineralogy of martian meteorites. *Geochimica et Cosmochimica Acta* 73:7443–7485. http://dx.doi.org/10.1016/j.gca.2009.09.008.

Raymond S. N., O'Brien D. P., Morbidelli A., and Kaib N. A. 2009. Building the terrestrial planets: Constrained accretion in the inner Solar System. *Icarus* 203:644–662. http://dx.doi.org/10.1016/j.icarus.2009.05.016.

Righter K., and Shearer C. K. 2003. Magmatic fractionation of Hf and W: Constraints on the timing of core formation and differentiation in the Moon and Mars. *Geochimica et Cosmochimica Acta* 67:2497–2507.

Scheinberg A., Elkins-Tanton L. T., and Zhong S. J. 2014. Timescale and morphology of Martian mantle overturn immediately following magma ocean solidification. *Journal of Geophysical Research: Planets* 119:454–467.

Shafer J. T., Brandon A. D., Lapen T. J., Righter M., Peslier A. H., and Beard B. L. 2010. Trace element systematics and ^{147}Sm-^{143}Nd and ^{176}Lu-^{176}Hf ages of Larkman Nunatak 06319: Closed-system fractional crystallization of an enriched shergottite magma. *Geochimica et Cosmochimica Acta* 74.

Shearer C. K., Messenger S., Sharp Z. D., Burger P. V, Nguyen A. N., and McCubbin F. M. 2018. Distinct chlorine isotopic reservoirs on Mars. Implications for character, extent and relative timing of crustal interactions with mantle-derived magmas, evolution of the martian atmosphere, and the building blocks of an early Mars. *Geochimica et Cosmochimica Acta* 234:24–36. https://doi.org/10.1016/j.gca.2018.04.034.

Shih C. Y., Nyquist L. E., Bogard D. D., McKay G. A., Wooden J. L., Bansal B. M., and Wiesmann H. 1982. Chronology and petrogenesis of young achondrites, Shergotty, Zagami, and ALHA77005: late magmatism on a geologically active planet. *Geochimica et Cosmochimica Acta* 46:2323–2344.

Shih C.-Y., Nyquist L. E., Reese Y., and Wiesmann H. 1998. The Chronology of the Nakhlite, Lafayette: Rb-Sr and Sm-Nd Isotopic Ages. *Lunar and Planetary Institute Science Conference XXIX* 1:14–15.

Shih C. Y., Nyquist L. E., and Wiesmann H. 1999. Samarium-neodymium and rubidium-strontium systematics of nakhlite Governador Valadares. *Meteoritics and Planetary Science* 34:647–655.

Shih C.-Y., Nyquist L. E., Wiesmann H., and Barrat J. A. 2003. Age and Petrogenesis of Picritic Shergottite NWA1068: Sm-Nd and Rb-Sr Isotopic Studies. *34th Annual Lunar and Planetary Science Conference* 1439.

Shih C.-Y., Nyquist L. E., Wiesmann H., and Misawa K. 2004. Rb-Sr and Sm-Nd Isotopic Studies of Shergottite Y980459 and a Petrogenetic Link Between Depleted Shergottites

and Nakhlites. In *35th Lunar and Planetary Science Conference*. pp. 8–9 https://www.lpi.usra.edu/meetings/lpsc2004/pdf/1814.pdf.

Shih Y., Nyquist L. E., and Reese Y. 2007. Rb-Sr and Sm-Nd Isotopic Studies of Martian Depleted Shergottites SaU 094/005. *38th Lunar and Planetary Science Conference* Abstract 1745.

Shih C.-Y., Nyquist L. E., and Reese Y. 2009. Rb-Sr and Sm-Nd Studies of Olivine-Phyric Shergottites RBT 04262 and LAR 06319: Isotopic Evidence for Relationship to Enriched Basaltic Shergottites. *Lunar and Planetary Institute Science Conference* Abstracts 40:1360.

Shih C. Y., Nyquist L. E., Reese Y., and Misawa K. 2011. Sm-Nd and Rb-Sr studies of lherzolitic shergottite Yamato 984028. *Polar Science* 4:515–529. http://dx.doi.org/10.1016/j.polar.2010.05.004.

Symes S. J., Borg L. E., Shearer C. K., Asmerom Y., and Irving A. J. 2005. Geochronology of NWA 1195 based on Rb-Sr and Sm-Nd Isotopic Systematics. In *LPSC 36*. p. 1435.

Taylor G. J., Martel L. M. V., Karunatillake S., Gasnault O., and Boynton W. V. 2010. Mapping Mars geochemically. *Geology* 38:183–186.

Treiman A. H., Gleason J. D., and Bogard D. D. 2000. The SNC meteorites are from Mars. *Planetary and Space Science* 48:1213–1230. http://www.sciencedirect.com/science/article/pii/S0032063300001057.

Treiman A. H. 2005. The nakhlite meteorites: Augite-rich igneous rocks from Mars. *Chemie der Erde* 65:203–270.

Udry A., and Day J. M. D. 2018. 1.34 billion-year-old magmatism on Mars evaluated from the co-genetic nakhlite and chassignite meteorites. *Geochimica et Cosmochimica Acta* 238:292–315. https://doi.org/10.1016/j.gca.2018.07.006.

Udry A., Howarth G. H., Herd C., Day J., Lapen T. J., and Filiberto J. 2020. What martian meteorites reveal about the interior and surface of Mars. *Earth and Space Science Open Archive* 55. https://doi.org/10.1002/essoar.10503123.2.

Villa I. M., Holden N. E., Possolo A., Ickert R. B., Hibbert D. B., and Renne P. R. 2020. IUPAC-IUGS recommendation on the half-lives of 147Sm and 146Sm. *Geochimica et Cosmochimica Acta* 285:70–77. https://doi.org/10.1016/j.gca.2020.06.022.

Wieler R. et al. 2016. Noble gases in 18 Martian meteorites and angrite Northwest Africa 7812-Exposure ages, trapped gases, and a re-evaluation of the evidence for solar cosmic ray-produced neon in shergottites and other achondrites. *Meteoritics and Planetary Science* 51:407–428.

APPENDIX

Table A1. Bulk major and trace element compositions of ultramafic achondrites.

(wt%)	NWA 12217	NWA 12319	NWA 12562
SiO_2	41.82	39.97	41.29
TiO_2	0.01	0.03	0.04
Al_2O_3	0.11	0.71	0.99
Fe_2O_{3total}	8.99	14.62	15.88
MgO	47.94	42.77	39.98
CaO	0.52	1.36	0.79
Na_2O	0.02	0.04	0.09
K_2O	0.05	0.02	0.08
Cr_2O_3	0.33	0.58	0.53
MnO	0.21	0.42	0.31
P_2O_5	0.02	0.06	0.02
Mg#	0.82	0.72	0.68
Fe/Mn	38.14	31.55	45.66
(ppm)			
Li	0.72	1.75	1.46
Sc	0.30	4.17	1.81
V	43.5	53.9	52.9
Cr	2199	3664	3389
Co	17.2	16.5	28.6
Ni	51.4	55.5	263.5
Cu	0.2	2.058	20.4
Zn	4.37	5.107	2.19
Ga	0.103	0.191	0.355
Ge	0.607	0.891	0.956
Rb	0.172	0.104	1.216
Sr	7.532	18.463	11.329
Y	0.215	0.693	0.866
Zr	7.769	2.427	14.202
Nb	0.028	0.107	0.427
Cs	0.005	0.002	0.019
Ba	20.427	9.320	14.777

(ppm)	NWA 12217	NWA 12319	NWA 12562
La	0.070	0.119	0.391
Ce	0.124	0.296	0.776
Pr	0.017	0.047	0.100
Nd	0.077	0.233	0.417
Sm	0.013	0.087	0.097
Eu	0.007	0.021	0.042
Gd	0.020	0.109	0.127
Tb	0.003	0.018	0.020
Dy	0.031	0.133	0.143
Ho	0.007	0.028	0.033
Er	0.022	0.079	0.098
Tm	0.003	0.013	0.017
Yb	0.025	0.086	0.116
Lu	0.004	0.016	0.018
Hf	0.218	0.086	0.487
Ta	0.002	0.011	0.032
W	0.036	0.011	0.032
Pb	0.061	0.068	0.228
Th	0.034	0.022	0.071
U	0.077	0.088	0.052

Table A2. Highly Siderophile Element (HSE) compositions of ultramafic achondrites.

Sample ID	Type	Re (ppb)	Pd (ppb)	Pt (ppb)	Ru (ppb)	Ir (ppb)	Os (ppb)
NWA 12217	Dunite	0.01	0.25	0.34	0.35	0.15	0.23
NWA 12217	Dunite	0.04	0.19	0.47	0.28	0.39	0.45
NWA 12562	Lherzolite	1.45	12.98	1.78	1.46	0.66	0.49
NWA 12562	Lherzolite	0.11	52.81	0.60	0.89	0.35	0.36
NWA 12319	Lherzolite	0.08	1.70	0.68	0.68	0.40	0.63

Table A3. Re/Os systematics and blank contributions (blk) of ultramafic achondrites.

Sample ID	$^{187}Re/^{188}Os$	2SE	$^{187}Os/^{188}Os$	2SE	Re Blk	Pd Blk	Pt Blk	Ru Blk	Ir Blk	Os Blk
NWA 12217	0.2081	0.0031	0.1358	0.0027	47%	71%	38%	55%	0.5%	10%
NWA 12217	0.3949	0.0059	0.1263	0.0004	57%	30%	28%	52%	0.2%	30%
NWA 12562	14.3383	0.2151	0.1337	0.0013	7%	2%	9%	16%	0.1%	1%
NWA 12562	1.4977	0.0225	0.1417	0.0003	40%	0%	22%	23%	0.2%	9%
NWA 12319	0.6418	0.0096	0.1306	0.0004	26%	4%	7%	11%	0.1%	4%

Table A4. Oxygen isotopic analyses for ultramafic achondrites.

	Mass (mg)	$\delta^{17}O'$	$\delta^{18}O'$	$\Delta^{17}O'$
NWA 12217	1.70	1.793	3.723	-0.173
NWA 12217	2.60	1.884	3.869	-0.159
NWA 12217	1.30	1.796	3.660	-0.136
NWA 12217	2.10	1.639	3.475	-0.196
NWA 12217	1.70	1.698	3.558	-0.181
NWA 12217	1.60	1.661	3.526	-0.201
NWA 12217	1.20	1.673	3.552	-0.203
Weighted Average		**1.744**	**3.639**	**-0.178**
NWA 12319		**1.681**	**3.613**	**-0.227**
NWA 12562	2.40	1.609	3.477	-0.227
NWA 12562	2.60	1.788	3.795	-0.216
NWA 12562	3.00	1.619	3.492	-0.225
NWA 12562	1.00	1.616	3.496	-0.230
NWA 12562	1.50	1.686	3.613	-0.222
NWA 12562	1.10	1.629	3.521	-0.230
NWA 12562	1.10	1.783	3.778	-0.211
Weighted Average		**1.674**	**3.593**	**-0.223**

Table A5. Chromium isotopic analyses for ultramafic achondrites.

	$\varepsilon^{53}Cr$	2SE	$\varepsilon^{54}Cr$	2SE
NWA 12217	0.70	0.04	-0.26	0.08
NWA 12319	0.64	0.05	0.02	0.13
NWA 12562	0.51	0.03	-0.13	0.10

Table A6. Individual microprobe analyses for ultramafic achondrites.

NWA 12217	Al_2O_3	SiO_2	Cr_2O_3	TiO_2	Na_2O	MgO	MnO	FeO	NiO	K_2O	CaO	TOTAL
Olivine	0.01	39.94	0.05	0.01	0.00	47.14	0.40	13.92	0.00	0.01	0.08	101.55
Olivine	0.04	40.72	0.06	0.02	0.01	49.13	0.30	10.91	0.03	0.03	0.10	101.35
Olivine	0.10	41.18	0.09	0.00	0.00	51.22	0.24	9.17	0.01	0.02	0.07	102.09
Olivine	0.01	40.40	0.08	0.02	0.00	49.90	0.30	10.45	0.02	0.02	0.07	101.26
Olivine	0.04	40.71	0.09	0.02	0.01	49.02	0.32	10.78	0.02	0.03	0.10	101.15
Olivine	0.03	41.19	0.09	0.00	0.00	50.92	0.27	9.51	0.01	0.01	0.08	102.12
Olivine	0.02	41.83	0.07	0.00	0.00	53.23	0.20	7.04	0.00	0.02	0.04	102.46
Olivine	0.03	41.38	0.09	0.00	0.00	52.24	0.20	7.10	0.00	0.02	0.08	101.13
Olivine	0.03	41.36	0.11	0.00	0.00	52.79	0.20	7.11	0.00	0.02	0.05	101.68
Olivine	0.02	41.85	0.10	0.00	0.01	53.18	0.18	6.86	0.00	0.02	0.05	102.26
Olivine	0.03	40.29	0.09	0.00	0.00	51.88	0.19	7.08	0.02	0.02	0.03	99.65
Olivine	0.01	40.83	0.09	0.00	0.00	51.94	0.22	7.70	0.00	0.00	0.06	100.86
Olivine	0.00	40.59	0.09	0.00	0.00	52.36	0.20	7.13	0.01	0.04	0.04	100.46
Olivine	0.00	40.23	0.09	0.00	0.00	52.41	0.20	7.04	0.00	0.02	0.04	100.04
Olivine	0.00	40.07	0.03	0.00	0.00	49.64	0.28	9.68	0.00	0.04	0.04	99.79
Olivine	0.01	40.71	0.08	0.00	0.00	52.33	0.20	6.90	0.00	0.03	0.05	100.31
Olivine	0.04	39.84	0.06	0.00	0.00	49.30	0.28	10.25	0.02	0.03	0.10	99.92
Olivine	0.00	38.90	0.09	0.00	0.00	52.56	0.18	7.06	0.01	0.02	0.04	98.87
Olivine	0.00	39.23	0.09	0.00	0.00	52.20	0.21	7.10	0.00	0.00	0.07	98.96
Olivine	0.02	38.97	0.07	0.00	0.00	49.72	0.26	9.83	0.00	0.03	0.05	98.98
Olivine	0.00	39.41	0.09	0.00	0.00	50.44	0.25	9.63	0.01	0.01	0.05	99.89
Olivine	0.01	39.03	0.06	0.00	0.00	50.17	0.27	9.49	0.00	0.02	0.06	99.13
Olivine	0.01	39.90	0.10	0.00	0.00	52.49	0.21	7.06	0.01	0.03	0.03	99.87
Olivine	0.01	38.44	0.11	0.00	0.00	52.81	0.20	6.91	0.00	0.02	0.06	98.58
Olivine	0.03	38.34	0.11	0.00	0.00	52.46	0.19	6.96	0.01	0.04	0.01	98.16
Olivine	0.01	38.63	0.10	0.00	0.00	51.83	0.19	7.10	0.00	0.01	0.07	97.93
Olivine	0.04	38.19	0.08	0.00	0.00	49.45	0.26	9.87	0.01	0.03	0.06	98.02
Olivine	0.04	38.81	0.06	0.00	0.00	51.65	0.21	7.14	0.00	0.01	0.08	98.00
Olivine	0.03	38.71	0.10	0.00	0.00	52.31	0.21	7.24	0.00	0.03	0.04	98.68
Olivine	0.01	38.45	0.09	0.00	0.00	52.01	0.20	7.35	0.00	0.02	0.06	98.19
Olivine	0.06	40.25	0.11	0.00	0.01	50.50	0.20	7.35	0.00	0.02	0.07	98.57
Olivine	0.04	40.44	0.09	0.01	0.02	48.78	0.27	10.29	0.00	0.02	0.12	100.07
Olivine	0.03	41.17	0.12	0.00	0.00	51.84	0.20	7.22	0.00	0.01	0.07	100.67
Olivine	0.02	40.91	0.12	0.01	0.00	52.33	0.18	7.27	0.00	0.03	0.07	100.93
Olivine	0.05	40.87	0.23	0.01	0.01	49.94	0.25	8.87	0.00	0.01	0.07	100.31
Olivine	0.05	41.06	0.12	0.00	0.01	51.56	0.17	7.17	0.03	0.01	0.07	100.25
Olivine	0.03	40.35	0.09	0.00	0.00	49.28	0.28	10.11	0.00	0.02	0.07	100.24
Olivine	0.02	40.39	0.09	0.02	0.00	49.54	0.29	10.13	0.00	0.02	0.06	100.58
Olivine	0.03	41.15	0.11	0.02	0.00	51.73	0.21	7.27	0.00	0.01	0.08	100.62
Olivine	0.05	40.21	0.03	0.01	0.02	46.72	0.35	13.10	0.01	0.02	0.09	100.60
Olivine	0.20	41.54	0.09	0.01	0.01	50.99	0.24	7.91	0.00	0.01	0.07	101.06
Olivine	0.09	40.50	0.64	0.04	0.02	48.40	0.27	10.29	0.01	0.02	0.51	100.80

NWA 12217	Al_2O_3	SiO_2	Cr_2O_3	TiO_2	Na_2O	MgO	MnO	FeO	NiO	K2O	CaO	TOTAL
Olivine	0.03	40.98	0.11	0.00	0.00	51.32	0.21	7.90	0.02	0.02	0.08	100.68
Olivine	0.04	41.30	0.12	0.00	0.00	52.22	0.18	7.08	0.00	0.02	0.07	101.03
Olivine	0.02	41.24	0.12	0.01	0.00	52.32	0.21	6.94	0.02	0.02	0.05	100.94
Olivine	0.02	41.15	0.10	0.00	0.01	52.27	0.23	7.03	0.00	0.02	0.06	100.89
Olivine	0.03	40.47	0.07	0.01	0.01	49.67	0.31	10.08	0.02	0.02	0.06	100.75
Olivine	0.02	41.25	0.10	0.00	0.00	52.31	0.19	7.19	0.02	0.02	0.06	101.17
Olivine	0.02	40.41	0.16	0.01	0.00	49.15	0.28	10.50	0.02	0.01	0.08	100.64
Olivine	0.09	41.08	0.40	0.00	0.03	51.66	0.18	7.16	0.03	0.02	0.13	100.76
Olivine	0.08	41.01	0.09	0.01	0.00	52.11	0.19	7.05	0.02	0.02	0.05	100.63
Olivine	0.08	40.50	0.08	0.00	0.00	49.89	0.25	8.90	0.01	0.02	0.05	99.78
Olivine	0.04	40.66	0.11	0.00	0.00	49.21	0.29	10.14	0.02	0.02	0.11	100.61
Olivine	0.04	41.30	0.10	0.01	0.01	52.04	0.18	7.33	0.00	0.02	0.04	101.08
Olivine	0.02	41.28	0.07	0.00	0.00	52.19	0.21	7.01	0.00	0.02	0.05	100.85
Olivine	0.01	41.08	0.11	0.00	0.00	51.53	0.16	7.03	0.00	0.01	0.04	99.98
Olivine	0.06	40.56	0.09	0.02	0.00	48.60	0.29	10.60	0.00	0.02	0.12	100.36
Olivine	0.02	41.21	0.11	0.00	0.00	51.57	0.20	7.09	0.00	0.02	0.05	100.27
Olivine	0.03	40.47	0.07	0.01	0.00	48.80	0.30	10.73	0.01	0.02	0.05	100.48
Olivine	0.03	41.26	0.08	0.00	0.00	51.88	0.20	7.22	0.00	0.02	0.08	100.76
Olivine	0.02	41.27	0.12	0.00	0.01	51.80	0.20	7.14	0.01	0.01	0.06	100.65
Olivine	0.03	40.77	0.06	0.01	0.00	48.76	0.27	10.72	0.01	0.02	0.06	100.71
Olivine	0.02	40.61	0.07	0.01	0.00	48.79	0.29	10.44	0.00	0.02	0.08	100.33
Olivine	0.06	41.43	0.10	0.02	0.00	51.79	0.19	7.06	0.00	0.02	0.06	100.74
Olivine	0.04	39.76	0.05	0.01	0.00	44.70	0.42	15.33	0.03	0.01	0.06	100.40
Olivine	0.03	39.50	0.06	0.01	0.01	44.52	0.40	15.21	0.02	0.01	0.05	99.81
Olivine	0.04	41.14	0.10	0.00	0.00	51.46	0.20	7.19	0.00	0.02	0.08	100.24
Olivine	0.04	40.48	0.08	0.02	0.00	48.55	0.30	10.36	0.00	0.02	0.09	99.95
Olivine	0.02	40.43	0.09	0.00	0.00	48.29	0.30	10.15	0.04	0.02	0.05	99.41
Olivine	0.03	40.44	0.12	0.00	0.00	48.76	0.27	9.25	0.03	0.02	0.09	98.99
Olivine	0.01	41.35	0.11	0.00	0.00	51.32	0.20	7.41	0.00	0.02	0.08	100.51
Olivine	0.05	40.12	0.07	0.01	0.02	48.60	0.26	9.71	0.01	0.02	0.06	98.92
Olivine	0.08	40.58	0.06	0.00	0.00	48.87	0.31	11.30	0.00	0.02	0.04	101.26
Olivine	0.02	41.28	0.11	0.02	0.00	51.77	0.21	7.37	0.00	0.01	0.06	100.86
Olivine	0.02	41.14	0.13	0.00	0.01	51.44	0.21	7.49	0.00	0.01	0.08	100.52
Olivine	0.03	41.12	0.12	0.00	0.01	51.58	0.21	7.41	0.00	0.01	0.05	100.53
Olivine	0.02	40.51	0.09	0.00	0.00	49.07	0.29	10.43	0.00	0.01	0.06	100.49
Olivine	0.25	40.40	0.09	0.01	0.01	48.57	0.25	10.21	0.00	0.02	0.13	99.94
Olivine	0.03	40.86	0.10	0.01	0.00	50.55	0.26	8.99	0.01	0.02	0.05	100.88
Olivine	0.01	39.94	0.05	0.02	0.00	46.58	0.38	13.18	0.03	0.02	0.08	100.29
Olivine	0.01	39.67	0.04	0.00	0.00	46.08	0.36	13.23	0.01	0.02	0.08	99.52
Olivine	0.03	40.44	0.05	0.02	0.00	48.43	0.32	11.32	0.03	0.02	0.03	100.68
Olivine	0.03	40.43	0.05	0.01	0.00	48.22	0.30	11.25	0.01	0.02	0.06	100.37

NWA 12217	Al_2O_3	SiO_2	Cr_2O_3	TiO_2	Na_2O	MgO	MnO	FeO	NiO	K_2O	CaO	TOTAL
Opx	0.79	55.72	0.80	0.11	0.03	29.09	0.49	13.05	0.00	0.01	1.18	101.28
Opx	1.29	55.65	0.46	0.11	0.02	28.65	0.50	12.79	0.00	0.02	1.46	100.95
Opx	0.52	51.97	0.34	0.30	0.03	16.95	1.01	27.27	0.02	0.02	2.11	100.53
Opx	0.55	51.73	0.38	0.38	0.10	16.39	0.92	25.50	0.02	0.02	3.94	99.93
Opx	0.48	51.50	0.34	0.39	0.02	17.12	1.13	28.44	0.00	0.02	1.00	100.44
Opx	0.49	51.73	0.34	0.45	0.04	16.49	1.01	27.24	0.01	0.03	2.20	100.03
Opx	0.37	51.72	0.27	0.39	0.04	16.61	1.10	28.44	0.00	0.03	1.19	100.17
Opx	0.12	52.04	0.16	0.34	0.06	19.27	1.02	24.07	0.01	0.01	1.46	98.57
Opx	0.94	54.01	0.71	0.14	0.03	24.80	0.72	16.77	0.00	0.02	2.01	100.14
Opx	1.05	53.04	0.77	0.12	0.05	27.45	0.51	12.70	0.02	0.02	1.72	97.46
Opx	0.89	52.54	0.83	0.13	0.05	27.45	0.47	12.70	0.01	0.02	1.44	96.53
Opx	0.99	51.36	0.79	0.12	0.03	27.43	0.50	12.67	0.00	0.02	1.51	95.42
Cpx	0.29	54.01	1.11	0.01	0.41	21.11	0.09	2.34	0.00	0.05	17.21	96.64
Cpx	0.45	52.53	1.10	0.02	0.42	20.27	0.12	4.47	0.00	0.07	17.33	96.79
Cpx	0.86	53.35	0.92	0.11	0.40	18.43	0.12	2.02	0.00	0.03	20.99	97.23
Cpx	1.45	52.70	1.59	0.52	0.72	17.94	0.21	3.02	0.04	0.02	18.99	97.19
Cpx	0.93	53.63	1.12	0.20	0.54	18.25	0.17	2.59	0.01	0.01	20.28	97.74
Chromite	4.13	0.02	64.52	0.35	0.00	6.52	0.75	21.89	0.00	0.02	0.00	98.20
Chromite	16.58	0.00	54.98	0.05	0.00	12.78	0.47	14.57	0.00	0.03	0.00	99.46
Chromite	17.63	0.00	54.05	0.09	0.00	12.89	0.47	14.28	0.03	0.03	0.01	99.47
Chromite	18.90	0.00	53.02	0.13	0.00	13.98	0.45	13.14	0.00	0.03	0.00	99.65
Chromite	14.98	0.00	56.52	0.10	0.00	12.76	0.49	14.65	0.00	0.04	0.00	99.53
Chromite	8.61	0.04	61.96	0.14	0.00	9.50	0.58	17.82	0.00	0.03	0.02	98.70
Chromite	3.24	0.05	64.56	0.04		8.09	0.64	19.18	0.00		0.03	95.84
Chromite	3.37	0.00	65.08	0.06		8.17	0.72	19.20	0.00		0.05	96.65
Chromite	3.47	0.18	63.51	0.01		7.41	0.73	19.78	0.00		0.14	95.22
Chromite	4.02	0.03	64.92	0.38		6.36	0.75	21.62	0.02		0.03	98.13
Chromite	6.99	0.02	62.61	0.20		8.06	0.64	19.71	0.08		0.02	98.33
Chromite	9.39	0.05	60.82	0.16		10.52	0.54	16.26	0.00		0.03	97.77
Chromite	15.87	0.01	55.68	0.08		12.58	0.48	14.48	0.00		0.01	99.18
Chromite	14.61	0.02	56.89	0.09		11.90	0.52	14.80	0.00		0.02	98.85
Chromite	15.33	0.00	55.96	0.12		11.97	0.52	14.75	0.00		0.02	98.66
Chromite	8.13	0.22	61.43	0.16		9.62	0.59	17.59	0.06		0.01	97.81
Chromite	4.44	0.04	63.19	0.41		5.38	0.88	23.21	0.03		0.03	97.61
Chromite	8.28	0.07	60.58	0.29		8.96	0.69	18.42	0.00		0.01	97.29
Chromite	14.95	0.15	53.29	0.12		11.87	0.52	16.94	0.00		0.02	97.86
Chromite	5.36	0.04	62.26	0.56		6.05	0.77	22.49	0.00		0.03	97.57
Chromite	6.61	0.02	62.07	0.77		7.31	0.71	20.69	0.00		0.15	98.32
Chromite	5.18	0.05	63.31	0.53		6.75	0.71	20.96	0.00		0.25	97.74
Chromite	9.03	0.03	58.62	1.21		8.60	0.69	19.73	0.00		0.01	97.92
Chromite	11.00	0.02	59.20	0.28		10.02	0.58	17.05	0.02		0.04	98.20

NWA 12217	Al_2O_3	SiO_2	P_2O_5	Cl	Na_2O	MgO	F	FeO	K_2O	CaO	TOTAL
Plagioclase	26.83	58.11	0.04	0.01	6.39		0.03		0.23	8.41	100.16
Plagioclase	27.24	55.71	0.01	0.00	6.09		0.00		0.30	9.55	99.14
Plagioclase	28.19	55.26	0.03	0.01	5.64		0.03		0.32	9.57	99.33
Plagioclase	22.97	63.55	0.00	0.00	9.29		0.07		0.44	3.99	100.51
K-Feldspar	17.81	69.58	0.05	0.04	4.06		0.01		9.13	0.50	101.39
K-Feldspar	18.16	67.95	0.01	0.05	4.49		0.05		10.01	0.47	101.37
K-Feldspar	18.75	67.18	0.04	0.02	5.27		0.00		8.98	0.48	100.88
K-Feldspar	15.28	68.97	0.01	0.18	2.54		0.02		10.61	0.43	98.21
K-Feldspar	17.67	65.70	0.03	0.15	3.07		0.01		11.32	0.39	98.48
K-Feldspar	16.32	72.94	0.07	0.01	2.74		0.01		10.73	0.46	103.44
K-Feldspar	15.06	66.91			5.73				8.88	0.52	97.32
K-Feldspar	14.24	71.50			4.64				7.31	0.74	98.62
Merrillite	0.01	0.06	44.95	0.00	2.51	3.59	0.50	0.26	0.06	46.06	98.02
Merrillite	0.02	0.05	46.42	0.00	2.53	3.57	0.52	0.27	0.08	46.26	99.72
Merrillite	0.01	0.06	44.85	0.00	2.57	3.56	0.50	0.29	0.07	46.97	98.87
Merrillite	0.00	0.05	45.00	0.00	2.41	3.62	0.58	0.25	0.07	46.05	98.03

NWA 12217	Al	Si	Cr	Ti	Na	MgO	Mn	Fe	Ni	K	Ca	TOTAL
Metal Traverse	0.00	0.01	0.00	0.00	0.00	0.00	0.01	91.72	7.05	0.04	0.00	98.82
Metal Traverse	0.00	0.01	0.00	0.00	0.00	0.00	0.01	91.56	6.94	0.04	0.00	98.56
Metal Traverse	0.00	0.01	0.00	0.00	0.00	0.00	0.00	91.72	7.03	0.03	0.00	98.79
Metal Traverse	0.00	0.01	0.00	0.00	0.00	0.00	0.00	91.64	6.95	0.03	0.00	98.63
Metal Traverse	0.00	0.00	0.00	0.00	0.00	0.00	0.01	91.63	7.07	0.02	0.02	98.75
Metal Traverse	0.00	0.01	0.00	0.00	0.00	0.00	0.00	91.31	6.91	0.03	0.00	98.26
Metal Traverse	0.00	0.00	0.00	0.00	0.00	0.00	0.00	91.40	7.02	0.02	0.00	98.44
Metal Traverse	0.00	0.01	0.00	0.00	0.01	0.00	0.00	91.69	7.03	0.02	0.00	98.76
Metal Traverse	0.00	0.00	0.00	0.00	0.01	0.00	0.00	92.54	7.04	0.05	0.00	99.64
Metal Traverse	0.00	0.01	0.00	0.00	0.00	0.00	0.00	91.58	7.16	0.02	0.00	98.77
Metal Traverse	0.00	0.00	0.00	0.00	0.00	0.00	0.00	91.56	7.08	0.03	0.02	98.69
Metal Traverse	0.00	0.01	0.00	0.00	0.00	0.00	0.01	91.54	7.01	0.02	0.00	98.59
Metal Traverse	0.01	0.01	0.00	0.00	0.00	0.00	0.00	91.52	7.07	0.01	0.00	98.62
Metal Traverse	0.00	0.01	0.00	0.00	0.00	0.00	0.00	91.76	7.14	0.04	0.00	98.95
Metal Traverse	0.00	0.01	0.00	0.00	0.02	0.00	0.00	89.20	10.15	0.02	0.00	99.40
Metal Traverse	0.00	0.00	0.00	0.00	0.00	0.00	0.00	81.79	17.69	0.03	0.02	99.52
Metal Traverse	0.00	0.01	0.00	0.00	0.00	0.00	0.01	84.63	14.84	0.04	0.00	99.54
Metal Traverse	0.00	0.00	0.00	0.00	0.00	0.00	0.00	81.68	17.48	0.01	0.00	99.17
Metal Traverse	0.00	0.01	0.00	0.00	0.01	0.00	0.00	84.94	14.61	0.02	0.00	99.59
Metal Traverse	0.00	0.01	0.00	0.00	0.00	0.00	0.00	79.63	19.64	0.04	0.00	99.31
Metal Traverse	0.00	0.01	0.00	0.00	0.00	0.00	0.00	79.94	19.35	0.02	0.00	99.32
Metal Traverse	0.00	0.01	0.00	0.00	0.00	0.00	0.00	70.92	27.96	0.03	0.01	98.93
Metal Traverse	0.00	0.00	0.00	0.00	0.00	0.00	0.00	91.68	7.15	0.03	0.00	98.86
Metal Traverse	0.00	0.01	0.00	0.00	0.00	0.00	0.01	92.16	7.06	0.01	0.01	99.26

NWA 12217	Co	Cr	Ti	Fe	Ni	TOTAL
Metal	1.23	0.00	0.00	93.59	7.00	101.82
Metal	1.16	0.00	0.00	91.56	7.12	99.84
Metal	0.67	0.01	0.00	78.35	20.78	99.81
Metal	1.15	0.00	0.00	91.01	7.18	99.33
Metal	1.20	0.00	0.00	92.94	7.06	101.20
Metal	1.10	0.00	0.00	92.88	6.91	100.89
Metal	1.12	0.00	0.00	92.50	7.19	100.81
Metal	0.46	0.01	0.00	72.08	26.00	98.54
Metal	0.39	0.01	0.01	71.98	25.42	97.82
Metal	0.42	0.00	0.00	70.44	28.95	99.81
Metal	0.37	0.01	0.00	68.90	29.28	98.57
Metal	0.37	0.01	0.00	70.61	29.18	100.17
Metal	1.08	0.23	0.00	91.13	6.98	99.42

NWA 12319	Al_2O_3	SiO_2	TiO_2	Cr_2O_3	Na_2O	MgO	MnO	FeO	NiO	K_2O	CaO	CoO	TOTAL
Olivine	0.03	38.95	0.03	0.03	0.01	42.94	0.44	17.11	0.00	0.02	0.07	0.03	99.65
Olivine	0.01	39.45	0.01	0.03	0.00	44.50	0.35	14.66	0.00	0.02	0.08	0.03	99.15
Olivine	0.02	40.23	0.00	0.03	0.00	45.89	0.36	13.34	0.01	0.03	0.06	0.03	100.03
Olivine	0.02	40.40	0.01	0.03	0.00	46.46	0.31	12.53	0.01	0.02	0.05	0.01	99.85
Olivine	0.02	40.82	0.01	0.04	0.01	45.62	0.33	13.47	0.00	0.02	0.07	0.01	100.41
Olivine	0.01	39.71	0.02	0.02	0.00	41.63	0.40	17.50	0.00	0.03	0.07	0.00	99.38
Olivine	0.01	39.79	0.00	0.04	0.01	41.68	0.42	17.65	0.04	0.03	0.10	0.00	99.76
Olivine	0.03	42.07	0.01	0.07	0.00	49.69	0.21	8.39	0.02	0.02	0.03	0.01	100.55
Olivine	0.01	41.64	0.00	0.04	0.01	47.13	0.28	11.04	0.00	0.02	0.05	0.01	100.24
Olivine	0.00	41.86	0.01	0.05	0.00	47.21	0.29	10.99	0.00	0.02	0.06	0.00	100.49
Olivine	0.04	39.69	0.02	0.04	0.01	39.24	0.49	20.32	0.00	0.02	0.18	0.05	100.10
Olivine	0.03	42.41	0.00	0.05	0.00	49.81	0.19	8.38	0.00	0.02	0.02	0.00	100.93
Olivine	0.03	42.10	0.00	0.06	0.00	49.75	0.22	8.38	0.00	0.01	0.01	0.01	100.59
Olivine	0.02	42.43	0.00	0.07	0.00	49.73	0.25	8.38	0.00	0.02	0.03	0.03	100.95
Olivine	0.01	40.46	0.02	0.03	0.00	43.51	0.39	15.27	0.00	0.02	0.05	0.01	99.76
Olivine	0.00	40.21	0.01	0.04	0.01	42.28	0.38	17.01	0.00	0.01	0.05	0.04	100.06
Olivine	0.03	40.47	0.03	0.04	0.01	42.29	0.39	17.07	0.02	0.03	0.07	0.02	100.46
Olivine	0.01	39.61	0.03	0.15	0.02	39.56	0.53	19.78	0.00	0.03	0.03	0.02	99.75
Olivine	0.03	41.32	0.00	0.02	0.00	46.82	0.25	11.56	0.00	0.02	0.05	0.00	100.08
Olivine	0.03	40.64	0.01	0.07	0.02	43.44	0.37	15.36	0.00	0.01	0.03	0.01	100.00
Olivine	0.03	42.03	0.01	0.06	0.00	49.68	0.21	8.28	0.04	0.02	0.04	0.00	100.41
Olivine	0.01	40.88	0.00	0.01	0.00	43.92	0.38	14.92	0.00	0.01	0.03	0.00	100.18
Olivine	0.00	39.50	0.02	0.04	0.00	38.43	0.51	21.02	0.00	0.02	0.10	0.04	99.67
Olivine	0.00	40.03	0.02	0.03	0.01	39.35	0.51	19.47	0.01	0.02	0.12	0.03	99.59
Olivine	0.03	41.72	0.00	0.08	0.00	46.91	0.29	11.20	0.01	0.03	0.07	0.00	100.34
Olivine	0.03	41.89	0.01	0.06	0.00	49.71	0.22	8.39	0.00	0.02	0.01	0.03	100.39
Olivine	0.01	40.41	0.01	0.05	0.00	43.43	0.37	15.21	0.02	0.02	0.06	0.01	99.61
Olivine	0.03	40.87	0.00	0.03	0.01	43.39	0.37	15.30	0.01	0.02	0.04	0.02	100.09
Olivine	0.02	40.31	0.00	0.04	0.01	41.14	0.41	17.61	0.00	0.02	0.07	0.06	99.68
Olivine	0.02	40.36	0.01	0.03	0.01	40.63	0.44	18.19	0.01	0.02	0.06	0.05	99.83
Olivine	0.00	41.18	0.01	0.03	0.00	44.37	0.32	13.74	0.02	0.01	0.06	0.04	99.79
Olivine	0.00	40.42	0.03	0.10	0.00	41.63	0.44	16.80	0.01	0.02	0.04	0.05	99.55
Olivine	0.01	40.01	0.02	0.03	0.01	38.85	0.50	19.38	0.03	0.03	0.12	0.00	99.00
Olivine	0.01	42.34	0.00	0.13	0.00	47.82	0.25	9.89	0.00	0.02	0.04	0.02	100.53
Olivine	0.01	42.57	0.00	0.06	0.00	48.32	0.22	9.12	0.01	0.01	0.06	0.01	100.40
Olivine	0.01	40.11	0.03	0.02	0.00	38.95	0.46	19.58	0.00	0.02	0.07	0.01	99.28
Olivine	0.02	40.75	0.01	0.02	0.00	43.72	0.40	15.13	0.00	0.02	0.05	0.03	100.14
Olivine	0.01	40.72	0.00	0.03	0.00	43.73	0.37	14.87	0.03	0.03	0.04	0.03	99.85
Olivine	0.03	42.19	0.01	0.05	0.00	48.93	0.26	8.89	0.01	0.02	0.06	0.00	100.46
Olivine	0.03	40.30	0.03	0.15	0.02	40.90	0.40	18.06	0.00	0.02	0.10	0.04	100.04
Olivine	0.03	40.94	0.03	0.08	0.00	43.17	0.37	14.98	0.00	0.02	0.06	0.00	99.68
Olivine	0.01	40.67	0.02	0.04	0.00	41.52	0.42	17.05	0.03	0.02	0.05	0.04	99.86
Olivine	0.01	42.01	0.01	0.03	0.01	47.27	0.29	11.01	0.00	0.02	0.02	0.03	100.71

NWA 12319	Al_2O_3	SiO_2	TiO_2	Cr_2O_3	Na_2O	MgO	MnO	FeO	NiO	K_2O	CaO	CoO	TOTAL
Olivine	0.05	41.44	0.02	0.07	0.01	44.57	0.32	12.78	0.01	0.02	0.09	0.03	99.40
Olivine	0.01	40.32	0.03	0.02	0.01	39.15	0.46	19.70	0.00	0.03	0.07	0.01	99.81
Olivine	0.01	41.26	0.02	0.02	0.01	43.68	0.36	14.26	0.02	0.02	0.02	0.02	99.69
Olivine	0.00	41.30	0.00	0.01	0.01	44.06	0.37	13.94	0.00	0.02	0.05	0.00	99.77
Olivine	0.01	42.34	0.00	0.04	0.00	48.86	0.24	8.53	0.01	0.02	0.03	0.00	100.10
Olivine	0.14	39.75	0.01	0.05	0.02	37.74	0.47	19.67	0.00	0.02	0.16	0.06	98.08
Olivine	0.01	40.70	0.02	0.05	0.01	42.62	0.42	16.27	0.00	0.03	0.09	0.01	100.23
Olivine	0.02	42.14	0.00	0.06	0.01	48.84	0.20	8.53	0.00	0.02	0.01	0.00	99.83
Olivine	0.03	42.12	0.00	0.06	0.00	49.28	0.23	8.59	0.01	0.01	0.05	0.01	100.40
Olivine	0.01	41.87	0.02	0.04	0.00	49.39	0.23	8.59	0.00	0.01	0.02	0.02	100.21
Olivine	0.01	41.88	0.00	0.07	0.00	49.32	0.22	8.55	0.00	0.02	0.06	0.02	100.15
Olivine	0.03	40.09	0.07	0.13	0.00	53.27	0.24	8.78		0.00	0.02		102.62
Olivine	0.15	39.41	0.06	0.05	0.01	45.84	0.39	15.39		0.01	0.10		101.41
Olivine	0.03	40.18	0.01	0.05	0.01	46.64	0.40	13.90		0.00	0.07		101.29
Olivine	0.03	39.94	0.07	0.06	0.00	44.79	0.42	15.79		0.00	0.07		101.17
Olivine	0.07	41.18	0.00	0.08	0.02	47.69	0.37	11.40		0.00	0.08		100.87
Olivine	0.03	41.17	0.00	0.10	0.01	50.28	0.26	8.83		0.00	0.06		100.75
Olivine	0.05	40.24	0.00	0.08	0.00	46.90	0.34	13.05		0.00	0.06		100.72
Olivine	0.01	39.81	0.00	0.06	0.03	44.64	0.37	15.76		0.00	0.04		100.71
Olivine	0.02	40.06	0.02	0.09	0.00	45.52	0.42	14.49		0.00	0.07		100.69
Olivine	0.04	39.88	0.05	0.05	0.02	46.12	0.37	14.03		0.01	0.06		100.62
Olivine	0.04	40.11	0.00	0.05	0.03	46.97	0.32	12.93		0.00	0.06		100.51
Olivine	0.05	39.91	0.05	0.07	0.02	47.18	0.34	12.83		0.00	0.05		100.49
Olivine	0.02	40.07	0.01	0.01	0.01	46.60	0.31	13.39		0.00	0.03		100.45
Olivine	0.02	39.50	0.11	0.02	0.03	44.67	0.43	15.62		0.00	0.04		100.44
Olivine	0.03	40.61	0.00	0.06	0.01	50.37	0.20	8.99		0.00	0.04		100.32
Olivine	0.03	40.97	0.00	0.07	0.02	49.76	0.22	9.15		0.00	0.07		100.29
Olivine	0.04	39.78	0.00	0.01	0.02	45.35	0.33	14.57		0.00	0.05		100.14
Olivine	0.02	40.36	0.00	0.05	0.01	46.83	0.33	12.50		0.00	0.02		100.11
Olivine	0.04	40.85	0.10	0.08	0.00	49.82	0.26	8.92		0.00	0.05		100.11
Olivine	0.10	39.84	0.00	0.05	0.04	45.10	0.41	14.44		0.01	0.09		100.07
Olivine	0.04	40.71	0.00	0.06	0.00	50.03	0.28	8.89		0.00	0.03		100.05
Olivine	0.04	40.55	0.00	0.07	0.00	50.21	0.26	8.84		0.00	0.04		100.00
Olivine	0.03	40.02	0.01	0.00	0.03	46.31	0.32	13.25		0.00	0.03		100.00
Olivine	0.03	40.94	0.03	0.03	0.01	49.95	0.22	8.74		0.02	0.02		99.98
Olivine	0.04	39.71	0.00	0.04	0.01	44.81	0.35	14.85		0.01	0.07		99.89
Olivine	0.03	40.76	0.00	0.08	0.02	49.81	0.27	8.87		0.01	0.04		99.89
Olivine	0.02	39.67	0.01	0.07	0.00	43.51	0.40	16.13		0.01	0.05		99.87
Olivine	0.04	40.82	0.00	0.08	0.00	49.85	0.22	8.79		0.00	0.04		99.85
Olivine	0.02	39.73	0.00	0.06	0.00	43.90	0.42	15.59		0.00	0.11		99.83
Olivine	0.04	40.95	0.05	0.10	0.01	49.60	0.24	8.80		0.00	0.04		99.83
Olivine	0.03	40.15	0.03	0.00	0.00	46.83	0.33	12.42		0.00	0.02		99.80
Olivine	0.03	39.90	0.08	0.06	0.00	46.19	0.34	13.11		0.00	0.06		99.77

NWA 12319	Al_2O_3	SiO_2	TiO_2	Cr_2O3	Na_2O	MgO	MnO	FeO	NiO	K_2O	CaO	CoO	TOTAL
Olivine	0.03	40.22	0.00	0.07	0.02	47.69	0.26	11.39		0.00	0.04		99.71
Olivine	0.04	40.27	0.08	0.02	0.01	46.51	0.35	12.37		0.01	0.05		99.70
Olivine	0.04	40.07	0.00	0.01	0.03	45.77	0.28	13.34		0.00	0.06		99.61
Olivine	0.03	39.49	0.03	0.08	0.01	44.57	0.33	14.96		0.00	0.08		99.58
Olivine	0.02	39.81	0.00	0.01	0.02	46.14	0.37	13.14		0.00	0.05		99.56
Olivine	0.03	39.89	0.00	0.07	0.00	45.89	0.33	13.20		0.01	0.08		99.51
Olivine	0.02	40.68	0.00	0.01	0.01	49.58	0.25	8.70		0.00	0.05		99.30
Olivine	0.04	39.42	0.03	0.03	0.00	43.63	0.43	15.64		0.01	0.06		99.29
Olivine	0.05	39.91	0.05	0.08	0.03	45.99	0.34	12.71		0.01	0.07		99.25
Olivine	0.08	39.76	0.02	0.09	0.01	44.19	0.36	14.64		0.00	0.09		99.24
Olivine	0.04	40.64	0.00	0.09	0.00	49.18	0.23	8.91		0.00	0.07		99.15
Olivine	0.03	38.28	0.00	0.05	0.02	47.36	0.36	12.96		0.00	0.06		99.12
Olivine	0.03	39.01	0.02	0.09	0.00	46.51	0.31	12.59		0.00	0.04		98.59
Olivine	0.05	39.50	0.00	0.01	0.00	45.58	0.30	12.93		0.00	0.05		98.42
Olivine	0.02	40.87	0.07	0.00	0.03	47.91	0.22	8.93		0.00	0.03		98.07
Olivine	0.29	40.24	0.00	0.10	0.07	42.08	0.41	14.45		0.03	0.37		98.03
Opx	0.36	51.72	0.12	0.16	0.02	16.45	0.91	27.08	0.02	0.02	1.92	0.06	98.85
Opx	1.07	54.10	0.14	0.64	0.01	26.16	0.49	14.87	0.00	0.02	1.51	0.02	99.03
Opx	0.56	53.07	0.18	0.48	0.01	20.30	0.78	22.69	0.01	0.02	1.66	0.06	99.80
Opx	0.62	49.51	0.51	0.24	0.02	12.69	0.99	31.35	0.01	0.02	3.67	0.03	99.66
Opx	0.71	57.63	0.04	0.83	0.02	28.94	0.42	11.56	0.03	0.02	0.69	0.01	100.90
Opx	0.63	55.70	0.23	0.35	0.00	24.68	0.69	17.05	0.00	0.03	1.22	0.00	100.58
Opx	1.14	56.56	0.12	0.77	0.02	26.61	0.49	13.72	0.01	0.02	1.44	0.04	100.92
Opx	0.40	54.26	0.20	0.22	0.02	20.62	0.80	22.18	0.01	0.03	1.08	0.01	99.81
Opx	0.93	55.95	0.05	0.73	0.01	25.26	0.53	15.97	0.00	0.02	1.09	0.02	100.55
Opx	0.88	57.64	0.05	0.83	0.03	28.88	0.42	11.68	0.01	0.02	0.80	0.03	101.28
Opx	0.90	57.44	0.05	0.90	0.02	28.93	0.37	11.38	0.00	0.02	0.86	0.03	100.90
Opx	0.82	57.52	0.06	0.78	0.02	28.52	0.37	11.04	0.00	0.02	0.85	0.03	100.02
Opx	1.20	56.11	0.18	0.75	0.03	26.00	0.48	14.19	0.01	0.02	1.48	0.07	100.50
Opx	0.82	55.72	0.15	0.58	0.05	24.73	0.55	15.48	0.02	0.01	2.07	0.01	100.20
Opx	1.13	53.11	0.19	0.42	0.01	18.44	0.84	23.90	0.02	0.01	1.17	0.00	99.25
Opx	0.85	55.91	0.06	0.70	0.05	30.40	0.46	11.89		0.00	0.96		101.28
Opx	1.35	54.65	0.18	0.84	0.05	27.05	0.53	13.03		0.00	2.19		99.87
Opx	0.73	54.76	0.10	0.75	0.02	28.55	0.44	13.64		0.00	0.76		99.73
Opx	0.65	53.44	0.12	0.45	0.04	23.85	0.68	18.38		0.01	1.63		99.25
Opx	1.37	52.94	0.62	0.76	0.30	16.67	0.31	5.38		0.01	20.90		99.26
Cpx	0.80	49.23	1.15	0.10	0.08	1.98	0.72	27.97	0.00	0.02	18.08	0.02	100.16
Cpx	1.77	51.19	0.32	1.13	0.23	14.56	0.38	7.89		0.00	20.53		98.00

NWA 12319	Al_2O_3	SiO_2	TiO2	Cr_2O_3	Na_2O	MgO	MnO	FeO	NiO	K_2O	CaO	CoO	TOTAL
Chromite	1.15	0.33	0.01	68.35	0.00	5.65	0.76	21.93	0.04	0.03	0.03	0.02	98.29
Chromite	12.18	0.04	0.62	54.18	0.03	4.77	0.68	25.82	0.00	0.03	0.06	0.03	98.43
Chromite	24.79	0.03	0.11	46.49	0.02	14.19	0.40	13.86	0.00	0.03	0.03	0.00	99.94
Chromite	0.01	0.11	0.03	70.90	0.03	6.39	0.94	21.01	0.00	0.03	0.02	0.04	99.50
Chromite	17.96	0.06	1.08	46.71	0.00	5.81	0.65	25.87	0.00	0.03	0.02	0.05	98.23
Chromite	15.89	0.02	1.51	50.34	0.01	8.17	0.59	22.21	0.03	0.03	0.00	0.01	98.83
Chromite	15.62	0.24	0.12	49.86	0.00	4.58	0.67	26.47	0.00	0.03	0.03	0.00	97.64
Chromite	1.17	0.07	0.02	69.46	0.01	5.63	0.76	22.10	0.03	0.03	0.02	0.00	99.30
Chromite	10.33	0.34	1.48	53.33	0.02	3.71	0.75	27.94	0.00	0.03	0.04	0.06	98.02
Chromite	24.47	0.01	0.12	46.09	0.01	13.95	0.40	13.65	0.00	0.03	0.01	0.05	98.77
Chromite	16.00	0.58	1.48	49.06	0.02	8.95	0.56	22.40		0.02	0.04		99.11
Chromite	0.01	0.07	0.11	70.86	0.04	6.82	0.99	21.60		0.00	0.00		100.50
Chromite	1.84	0.38	0.00	64.43	0.00	3.36	0.86	27.11		0.00	0.03		98.01
Plagioclase	30.18	52.29	0.05	0.00	3.94	0.09	0.01	0.50		0.19	13.09		100.34
Plagioclase	32.65	49.10	0.00	0.00	2.95	0.00	0.00	0.45		0.06	14.96		100.17
Plagioclase	32.07	49.26	0.00	0.01	3.02	0.05	0.05	0.33		0.08	15.13		100.01
Plagioclase	32.14	49.32	0.03	0.02	2.95	0.01	0.05	0.34		0.07	14.85		99.79

NWA 12562	Al_2O_3	SiO_2	TiO_2	Cr_2O_3	Na_2O	MgO	MnO	FeO	NiO	K_2O	CaO	TOTAL
Olivine	0.03	39.65	0.01	0.04	0.00	45.95	0.35	14.16	0.02	0.01	0.05	100.27
Olivine	0.02	38.97	0.02	0.02	0.00	40.83	0.47	20.03	0.00	0.01	0.11	100.48
Olivine	0.02	41.10	0.02	0.04	0.01	49.51	0.21	9.94	0.03	0.02	0.04	100.94
Olivine	0.01	39.41	0.01	0.01	0.00	40.72	0.49	20.32	0.03	0.02	0.08	101.10
Olivine	0.02	41.28	0.00	0.12	0.00	50.26	0.21	9.11	0.03	0.02	0.06	101.11
Olivine	0.01	39.05	0.01	0.04	0.00	41.61	0.48	19.15	0.02	0.03	0.10	100.49
Olivine	0.07	40.66	0.00	0.05	0.00	48.98	0.26	10.49	0.00	0.02	0.06	100.60
Olivine	0.01	40.15	0.01	0.04	0.00	45.02	0.37	15.19	0.02	0.02	0.08	100.90
Olivine	0.02	41.37	0.00	0.05	0.00	49.16	0.25	9.30	0.01	0.02	0.05	100.24
Olivine	0.01	40.03	0.00	0.03	0.00	45.80	0.34	14.34	0.01	0.02	0.08	100.67
Olivine	0.00	40.02	0.00	0.03	0.00	44.96	0.36	14.29	0.00	0.02	0.06	99.73
Olivine	0.02	39.66	0.01	0.04	0.00	43.81	0.38	15.54	0.00	0.02	0.03	99.51
Olivine	0.03	40.42	0.00	0.08	0.00	48.91	0.24	9.17	0.00	0.01	0.05	98.92
Olivine	0.01	37.69	0.01	0.02	0.00	36.42	0.58	24.57	0.00	0.01	0.06	99.36
Olivine	0.03	40.33	0.00	0.05	0.00	47.95	0.29	12.06	0.02	0.01	0.06	100.80
Olivine	0.01	39.84	0.00	0.02	0.00	42.74	0.36	16.67	0.01	0.01	0.04	99.72
Olivine	0.03	39.70	0.00	0.06	0.00	44.98	0.33	14.32	0.00	0.01	0.08	99.50
Olivine	0.00	40.19	0.02	0.01	0.01	44.54	0.36	15.60	0.03	0.03	0.05	100.83
Olivine	0.01	40.64	0.00	0.03	0.00	42.80	0.39	16.70	0.01	0.02	0.08	100.67
Olivine	0.02	39.63	0.03	0.02	0.00	44.55	0.37	15.32	0.00	0.02	0.07	100.01
Olivine	0.03	40.92	0.01	0.06	0.00	49.56	0.26	9.69	0.00	0.01	0.05	100.58
Olivine	0.00	40.61	0.01	0.01	0.00	45.27	0.36	14.73	0.01	0.02	0.03	101.05
Olivine	0.03	38.92	0.02	0.04	0.00	39.48	0.42	21.33	0.03	0.02	0.09	100.38
Olivine	0.03	38.47	0.02	0.00	0.00	37.80	0.52	22.61	0.00	0.01	0.05	99.51
Olivine	0.01	39.86	0.00	0.09	0.00	51.22	0.22	9.14	0.00	0.02	0.04	100.61
Olivine	0.02	40.49	0.00	0.13	0.00	50.76	0.23	8.73	0.01	0.01	0.02	100.39
Olivine	0.06	40.04	0.01	0.30	0.00	49.78	0.23	9.16	0.00	0.02	0.27	99.88
Olivine	0.01	40.46	0.00	0.15	0.00	48.91	0.27	11.24	0.00	0.02	0.08	101.13
Olivine	0.02	39.68	0.00	0.15	0.00	48.77	0.27	11.08	0.02	0.02	0.09	100.11
Olivine	0.03	38.86	0.03	0.03	0.00	37.30	0.54	24.00	0.00	0.03	0.13	100.95
Olivine	0.00	40.43	0.00	0.04	0.01	45.03	0.33	14.53	0.02	0.02	0.06	100.46
Olivine	0.02	41.19	0.01	0.04	0.02	49.98	0.20	9.83	0.02	0.01	0.05	101.37
Olivine	0.03	40.76	0.02	0.03	0.00	44.11	0.36	15.29	0.01	0.02	0.08	100.71
Olivine	0.03	39.46	0.04	0.05	0.00	39.91	0.49	20.18	0.02	0.01	0.11	100.29
Olivine	0.01	40.00	0.01	0.03	0.01	43.49	0.35	15.51	0.02	0.02	0.06	99.51
Olivine	0.02	40.12	0.02	0.04	0.00	48.04	0.27	9.91	0.05	0.03	0.08	98.59
Olivine	0.02	39.14	0.04	0.05	0.01	40.00	0.50	20.04	0.00	0.02	0.09	99.91
Olivine	0.02	40.26	0.03	0.02	0.00	42.44	0.41	18.42	0.02	0.01	0.02	101.66
Olivine	0.00	38.97	0.00	0.02	0.00	43.57	0.42	17.68	0.00	0.02	0.05	100.73
Olivine	0.02	39.93	0.00	0.06	0.00	49.97	0.24	9.57	0.00	0.01	0.04	99.84
Olivine	0.02	39.94	0.01	0.05	0.00	50.31	0.19	9.61	0.00	0.01	0.02	100.16
Olivine	0.00	39.87	0.01	0.01	0.00	44.93	0.35	15.77	0.00	0.02	0.03	101.00
Olivine	0.03	39.82	0.00	0.06	0.00	43.08	0.39	16.75	0.03	0.02	0.09	100.26

NWA 12562	Al_2O_3	SiO_2	TiO_2	Cr_2O_3	Na_2O	MgO	MnO	FeO	NiO	K_2O	CaO	TOTAL
Olivine	0.01	38.93	0.01	0.03	0.00	41.69	0.46	19.34	0.00	0.02	0.07	100.56
Olivine	0.05	41.37	0.00	0.07	0.00	51.03	0.22	8.61	0.00	0.02	0.04	101.40
Olivine	0.01	38.42	0.04	0.01	0.00	38.80	0.53	22.65	0.00	0.02	0.07	100.56
Olivine	0.02	41.21	0.00	0.07	0.00	50.02	0.24	9.35	0.00	0.01	0.04	100.96
Olivine	0.03	39.99	0.01	0.07	0.02	44.30	0.41	16.18	0.03	0.01	0.08	101.13
Olivine	0.04	39.82	0.00	0.07	0.01	50.93	0.25	9.32	0.04	0.02	0.07	100.57
Olivine	0.04	40.90	0.02	0.05	0.00	50.95	0.25	9.26	0.01	0.01	0.07	101.57
Olivine	0.00	39.53	0.00	0.03	0.00	45.57	0.37	14.29	0.00	0.01	0.06	99.88
Olivine	0.00	39.25	0.04	0.04	0.00	38.22	0.53	23.36	0.00	0.02	0.13	101.60
Olivine	0.02	38.46	0.00	0.02	0.00	40.34	0.48	20.70	0.02	0.02	0.05	100.10
Olivine	0.01	39.11	0.01	0.02	0.00	44.95	0.44	15.96	0.00	0.01	0.09	100.61
Olivine	0.02	40.85	0.02	0.09	0.00	50.03	0.23	9.25	0.00	0.02	0.00	100.52
Olivine	0.02	39.32	0.00	0.02	0.00	44.79	0.38	15.64	0.02	0.02	0.05	100.26
Olivine	0.01	38.79	0.00	0.02	0.00	44.24	0.39	15.56	0.01	0.02	0.03	99.08
Olivine	0.02	40.64	0.01	0.05	0.00	51.09	0.23	8.44	0.00	0.02	0.04	100.55
Olivine	0.00	40.36	0.01	0.05	0.00	50.51	0.22	8.41	0.00	0.01	0.05	99.62
Olivine	0.02	39.89	0.01	0.03	0.00	48.50	0.28	10.77	0.00	0.02	0.07	99.60
Olivine	0.01	39.67	0.03	0.05	0.00	48.78	0.26	10.95	0.00	0.02	0.06	99.83
Olivine	0.01	39.23	0.00	0.05	0.00	48.24	0.29	10.93	0.02	0.02	0.07	98.87
Olivine	0.02	39.48	0.02	0.02	0.00	45.36	0.36	14.26	0.03	0.02	0.07	99.63
Olivine	0.01	39.43	0.00	0.03	0.00	45.41	0.35	14.38	0.00	0.01	0.06	99.68
Olivine	0.01	39.22	0.00	0.03	0.00	44.93	0.36	14.25	0.01	0.02	0.06	98.89
Olivine	0.00	38.36	0.03	0.01	0.01	40.66	0.48	19.79	0.00	0.03	0.08	99.45
Olivine	0.01	38.59	0.01	0.01	0.00	40.24	0.46	19.49	0.02	0.02	0.04	98.90
Olivine	0.01	41.04	0.01	0.07	0.00	49.84	0.24	8.91	0.01	0.02	0.06	100.21
Olivine	0.02	40.29	0.00	0.04	0.00	49.23	0.23	9.10	0.03	0.02	0.05	99.02
Olivine	0.00	38.59	0.00	0.02	0.00	48.74	0.27	11.40	0.02	0.03	0.02	99.09
Olivine	0.01	38.44	0.00	0.01	0.00	47.58	0.24	11.52	0.03	0.02	0.02	97.88
Olivine	0.01	39.02	0.01	0.02	0.01	41.33	0.46	18.73	0.00	0.02	0.08	99.67
Olivine	0.01	38.80	0.01	0.00	0.00	42.47	0.46	18.24	0.00	0.02	0.06	100.08
Olivine	0.02	40.44	0.00	0.09	0.00	51.81	0.23	8.46	0.01	0.02	0.03	101.10
Olivine	0.02	38.86	0.01	0.07	0.01	50.47	0.21	8.46	0.00	0.02	0.03	98.17
Olivine	0.01	39.20	0.01	0.03	0.00	41.50	0.44	19.25	0.00	0.03	0.07	100.53
Olivine	0.02	38.68	0.00	0.02	0.00	41.15	0.47	19.21	0.01	0.02	0.07	99.65
Olivine	0.01	40.70	0.02	0.04	0.00	45.06	0.40	14.70	0.04	0.01	0.07	101.05
Olivine	0.01	39.81	0.03	0.04	0.00	44.39	0.39	14.88	0.00	0.02	0.05	99.60
Olivine	0.02	40.58	0.00	0.07	0.00	51.13	0.23	8.54	0.01	0.02	0.05	100.65
Olivine	0.04	41.25	0.00	0.05	0.00	50.70	0.22	8.36	0.04	0.02	0.05	100.72
Olivine	0.01	40.61	0.00	0.03	0.00	47.03	0.32	12.52	0.00	0.03	0.06	100.62
Olivine	0.02	40.62	0.01	0.07	0.00	46.20	0.31	12.41	0.01	0.02	0.04	99.72
Olivine	0.01	38.89	0.03	0.08	0.00	45.11	0.37	14.62	0.02	0.02	0.05	99.20

NWA 12562	Al_2O_3	SiO_2	TiO_2	Cr_2O_3	Na_2O	MgO	MnO	FeO	NiO	K_2O	CaO	TOTAL
Opx	0.91	55.40	0.04	0.78	0.03	29.14	0.41	12.63	0.03	0.02	0.89	100.30
Opx	1.35	55.48	0.17	0.74	0.05	30.09	0.35	9.56	0.02	0.02	1.74	99.57
Opx	1.43	52.56	0.15	0.58	0.07	19.93	0.77	20.66	0.00	0.02	4.03	100.20
Opx	1.39	52.70	0.13	0.59	0.07	20.32	0.78	20.73	0.01	0.02	3.85	100.59
Opx	1.22	51.11	0.12	0.75	0.03	20.35	0.73	19.52	0.02	0.02	4.77	98.63
Opx	0.94	53.22	0.13	0.59	0.03	22.07	0.73	20.36	0.00	0.01	1.81	99.89
Opx	1.01	53.99	0.08	0.77	0.03	26.77	0.50	14.75	0.00	0.02	1.54	99.47
Opx	0.90	55.42	0.20	0.62	0.04	26.86	0.46	11.06	0.00	0.02	5.16	100.74
Opx	0.44	49.67	0.20	0.19	0.00	13.05	1.09	32.86	0.00	0.02	1.93	99.46
Opx	0.86	52.84	0.14	0.43	0.02	21.69	0.74	21.46	0.00	0.02	1.57	99.77
Opx	0.80	56.15	0.04	0.78	0.01	28.95	0.41	12.25	0.02	0.01	0.60	100.02
Opx	0.80	53.65	0.23	0.74	0.03	24.59	0.60	16.69	0.00	0.01	2.14	99.49
Opx	0.65	52.34	0.26	0.32	0.03	18.78	0.92	24.82	0.00	0.02	2.18	100.32
Opx	0.78	49.69	0.41	0.26	0.06	8.42	1.05	33.42	0.00	0.02	7.14	101.25
Opx	0.91	54.88	0.15	0.81	0.03	27.17	0.49	14.02	0.02	0.02	1.69	100.18
Opx	0.71	54.16	0.13	0.53	0.02	25.68	0.52	15.55	0.00	0.02	2.00	99.32
Opx	0.79	53.93	0.18	0.61	0.02	25.57	0.50	15.47	0.00	0.02	2.25	99.34
Opx	0.65	53.90	0.13	0.63	0.01	25.42	0.53	15.95	0.00	0.02	1.67	98.91
Opx	1.29	54.14	0.09	0.92	0.03	31.38	0.37	9.25	0.04	0.02	1.03	98.56
Opx	1.22	55.50	0.08	0.93	0.02	31.24	0.38	9.23	0.00	0.02	1.04	99.66
Opx	1.26	55.39	0.10	0.90	0.03	30.95	0.38	9.18	0.00	0.02	0.97	99.18
Opx	0.94	54.72	0.14	0.81	0.01	27.15	0.49	14.22	0.00	0.03	1.49	99.99
Opx	0.92	54.27	0.14	0.83	0.02	26.63	0.47	14.17	0.00	0.01	1.62	99.08
Opx	0.78	54.62	0.05	0.81	0.01	30.39	0.41	11.47	0.00	0.02	0.55	99.10
Opx	0.85	54.75	0.03	0.84	0.01	29.73	0.39	11.44	0.00	0.02	0.57	98.63
Opx	0.74	52.16	0.18	0.38	0.02	19.75	0.83	22.77	0.00	0.02	2.77	99.62
Opx	1.20	56.75	0.22	0.91	0.04	31.89	0.32	8.20	0.03	0.01	1.69	101.27
Opx	0.76	51.68	0.14	0.32	0.05	16.03	0.83	24.88	0.00	0.02	4.78	99.48
Opx	1.02	55.03	0.07	0.81	0.01	26.89	0.45	14.22	0.01	0.02	1.14	99.67
Opx	0.85	54.26	0.17	0.66	0.02	26.49	0.54	15.10	0.02	0.02	1.87	100.01
Opx	0.32	58.05	0.03	0.54	0.02	36.64	0.21	5.39	0.00	0.01	0.34	101.55
Opx	0.89	51.88	0.17	0.35	0.03	18.03	0.73	22.96	0.00	0.02	4.47	99.53
Opx	2.55	51.50	0.17	0.72	0.03	21.53	0.68	21.09	0.00	0.02	1.60	99.88
Cpx	0.93	49.16	0.32	0.44	0.06	8.83	0.95	29.15	0.00	0.02	9.78	99.64
Cpx	0.93	49.16	0.32	0.44	0.06	8.83	0.95	29.15	0.00	0.02	9.78	99.64
Cpx	1.64	49.82	0.87	0.54	0.19	9.29	0.64	18.66	0.01	0.01	16.81	98.48

NWA 12562	Al_2O3	SiO_2	TiO_2	Cr2O3	Na_2O	MgO	MnO	FeO	NiO	K_2O	CaO	TOTAL
Chromite	9.29	0.11	0.70	54.21	0.00	5.08	0.71	27.42	0.02	0.02	0.03	97.58
Chromite	8.15	0.04	1.30	55.44	0.01	3.03	0.65	29.10	0.00	0.02	0.03	97.78
Chromite	0.34	0.07	0.05	67.51	0.00	5.59	0.69	23.26	0.00	0.02	0.00	97.53
Chromite	1.12	0.02	0.54	65.95	0.01	4.54	0.80	24.80	0.00	0.02	0.01	97.81
Chromite	12.51	0.05	0.73	54.09	0.00	6.53	0.66	23.72	0.00	0.03	0.05	98.38
Chromite	11.96	0.02	1.08	53.17	0.01	5.06	0.75	26.09	0.00	0.02	0.03	98.18
Plagioclase	34.06	45.94	0.00	0.00	1.36	0.35	0.04	0.85	0.02	0.02	17.68	100.31
Plagioclase	33.39	49.41	0.03	0.03	2.72	0.08	0.01	0.65	0.04	0.02	15.73	102.11
Plagioclase	32.04	49.43	0.05	0.00	3.12	0.11	0.02	0.44	0.01	0.05	14.89	100.14
Plagioclase	30.14	52.01	0.06	0.01	4.39	0.20	0.01	0.46	0.01	0.07	12.98	100.36
Plagioclase	29.54	52.68	0.02	0.00	4.15	0.03	0.00	0.39	0.02	0.18	12.89	99.90
Plagioclase	33.53	46.21	0.02	0.00	1.76	0.03	0.00	0.09	0.00	0.05	17.41	99.10
Plagioclase	33.62	46.93	0.03	0.00	2.05	0.01	0.02	0.23	0.02	0.04	16.94	99.89
Plagioclase	31.59	49.89	0.04	0.00	3.56	0.01	0.00	0.28	0.00	0.05	14.55	99.96
Plagioclase	32.99	47.18	0.02	0.00	1.92	0.11	0.00	0.45	0.00	0.03	17.04	99.75
Plagioclase	31.08	50.15	0.02	0.01	3.25	0.06	0.02	0.56	0.03	0.09	14.76	100.04
Plagioclase	33.44	47.38	0.01	0.01	2.21	0.04	0.01	0.20	0.00	0.05	16.58	99.92
Plagioclase	33.22	47.93	0.01	0.01	2.50	0.05	0.00	0.34	0.00	0.05	16.34	100.45

Table A6. Oxygen isotopic analyses of NWA 6698.

	Mass (mg)	$\delta^{17}O'$	$\delta^{18}O'$	$\Delta^{17}O'$
NWA 6698	1.40	2.954	7.527	-1.020
NWA 6698	1.50	3.008	7.671	-1.042
NWA 6698	1.50	3.191	7.989	-1.027
NWA 6698	1.40	3.037	7.657	-1.005
NWA 6698	1.80	3.143	7.937	-1.048
NWA 6698	3.00	3.267	8.113	-1.017
NWA 6698	3.30	3.270	8.135	-1.026
Weighted Average		**3.161**	**7.929**	**-1.026**

Table A7. Individual LA-ICP-MS analyses of mineral phases and area rasters of NWA 6698. Several analyses overlap with adjacent phases and were not used in the study. Oxides are in wt.% and elements are in ppm; bdl = below detection limit.

NWA 6698	Plagioclase 1	Plagioclase 2	Plagioclase 3	Plagioclase 4	Plagioclase 5	Plagioclase 6	Plagioclase 7
Li	1.1	1.3	0.8	0.6	0.9	3.0	3.3
Be	1.1	0.6	0.2	0.4	0.0	0.1	0.0
B	0.1	0.4	0.7	0.4	0.3	0.8	0.7
Na_2O	7.96	8.96	8.62	7.01	8.11	8.64	7.39
MgO	0.04	0.03	0.04	0.03	0.04	0.05	0.04
Al_2O_3	29.94	28.14	27.39	29.20	26.65	23.45	25.50
SiO_2	52.83	56.11	56.52	53.69	57.79	62.58	59.51
P_2O_5	0.020	0.020	0.076	0.017	0.033	0.027	0.028
K_2O	0.19	0.32	0.27	0.16	0.23	0.35	0.21
CaO	8.83	6.24	6.87	9.69	7.00	4.55	7.22
Sc	bdl	bdl	bdl	bdl	bdl	2.3	2.0
TiO_2	0.10	0.11	0.14	0.06	0.07	0.10	0.05
V	0.3	0.5	0.5	0.3	0.6	0.5	0.3
Cr	3.6	1.0	3.3	3.8	10.8	102.4	5.0
MnO	0.006	0.003	0.004	0.006	0.004	0.003	0.005
FeOT	0.09	0.06	0.07	0.13	0.08	0.24	0.07
Co	bdl	bdl	0.45	0.85	0.03	bdl	bdl
Ni	bdl	bdl	4	31	0.8	2.7	1.3
Cu	0.1	0.4	0.7	0.8	0.1	0.6	0.3
Zn	6.5	6.6	7.9	7.0	8.6	10.6	9.3
Ga	30	34	33	27	33	39	33
Ge	bdl	bdl	0.13	0.21	0.20	0.22	0.22
As	bdl	bdl	bdl	bdl	bdl	bdl	bdl
Se	0.18	bdl	0.18	0.21	0.15	0.35	0.12
Rb	0.8	1.7	1.4	0.6	1.2	2.1	1.0
Sr	197	173	174	193	177	149	180
Y	0.11	0.03	0.17	0.07	0.05	0.04	0.06
Zr	1.06	0.33	0.28	0.12	0.09	0.18	0.14
Nb	0.104	0.007	0.021	0.003	0.005	0.007	0.009
Mo	bdl	bdl	bdl	bdl	bdl	bdl	bdl
Ag	bdl	bdl	bdl	bdl	bdl	bdl	bdl
Cd	0.052	bdl	0.032	0.053	0.014	0.031	0.068
In	bdl	bdl	bdl	bdl	bdl	bdl	bdl
Sn	0.05	0.03	0.03	0.02	0.04	0.04	0.03
Sb	bdl	bdl	0.04	0.03	0.02	0.02	0.02

NWA 6698	Plagioclase 1	Plagioclase 2	Plagioclase 3	Plagioclase 4	Plagioclase 5	Plagioclase 6	Plagioclase 7
Cs	bdl	bdl	bdl	bdl	bdl	bdl	bdl
Ba	22	25	29	21	24	26	23
La	0.10	0.06	0.09	0.12	0.07	0.04	0.10
Ce	0.19	0.10	0.13	0.17	0.11	0.09	0.17
Pr	0.02	0.01	0.02	0.02	0.01	0.01	0.02
Nd	bdl	0.05	0.14	0.13	0.01	0.01	0.08
Sm	0.02	bdl	0.02	bdl	0.02	0.01	0.01
Eu	1.05	0.99	0.98	1.15	1.13	0.98	1.11
Gd	0.025	bdl	0.023	bdl	0.025	0.011	0.020
Tb	0.004	0.003	0.005	0.006	0.003	0.002	0.003
Dy	0.059	0.008	0.035	0.025	0.018	0.013	0.010
Ho	bdl	bdl	0.004	bdl	0.004	bdl	bdl
Er	0.007	bdl	0.013	bdl	0.012	bdl	bdl
Tm	bdl	0.005	bdl	bdl	0.005	bdl	bdl
Yb	0.021	0.004	0.003	0.004	0.009	0.014	0.010
Lu	bdl	bdl	bdl	bdl	bdl	bdl	bdl
Hf	0.043	bdl	bdl	bdl	bdl	0.007	0.003
Ta	bdl	bdl	bdl	bdl	bdl	bdl	bdl
W	bdl	bdl	0.041	bdl	bdl	bdl	0.002
Tl	bdl	bdl	0.002	0.003	bdl	0.003	0.002
Pb	0.08	0.08	0.13	0.08	0.07	0.07	0.05
Bi	0.005	0.006	0.007	0.003	0.003	0.066	0.002
Th	0.002	bdl	0.011	bdl	0.005	0.009	bdl
U	bdl	0.006	0.005	0.002	0.001	0.005	0.001

NWA 6698	Cpx 1	Cpx 2	Cpx 3	Cpx 4	Cpx 5	Cpx 6	Cpx 7	Cpx 8
Li	2.8	2.1	2.0	2.9	2.7	2.4	2.6	2.6
Be	bdl	bdl	bdl	bdl	bdl	bdl	bdl	bdl
B	0.6	0.5	0.8	0.8	0.7	0.5	0.6	0.6
Na_2O	0.44	0.52	0.68	0.57	0.93	0.51	0.54	0.50
MgO	17.99	15.26	14.69	15.35	14.07	14.71	14.90	15.02
Al_2O_3	0.90	0.81	1.08	0.90	1.68	0.64	0.66	0.69
SiO_2	47.41	47.04	48.96	50.24	51.36	51.00	50.71	50.90
P_2O_5	0.029	0.032	0.020	0.038	0.029	0.020	0.016	0.017
K_2O	0.022	bdl	0.035	0.021	0.032	bdl	bdl	bdl
CaO	15.61	22.41	21.00	18.01	18.94	18.90	19.49	19.36
Sc	103	141	122	100	101	105	114	110
TiO_2	1.10	1.31	1.24	1.10	1.12	1.06	1.09	1.13
V	82	113	166	98	105	111	109	107
Cr	5016	6100	6058	5475	5550	5819	5848	5819
MnO	0.947	0.740	0.737	0.791	0.709	0.750	0.743	0.748
FeOT	15.54	11.88	11.55	12.99	11.13	12.40	11.86	11.63
Co	1.2	0.8	0.8	5.2	1.5	1.1	0.7	0.6
Ni	4.9	2.6	2.6	80.5	13.0	3.9	1.9	2.2
Cu	0.6	1.9	1.1	3.9	0.6	3.7	0.9	0.3
Zn	297	200	216	271	230	266	263	250
Ga	4.34	5.17	5.93	5.56	7.37	5.89	5.87	5.73
Ge	0.05	0.02	0.07	0.10	0.11	0.12	0.11	0.09
As	0.04	0.03	0.02	0.02	0.08	0.06	0.03	0.03
Se	0.06	0.15	0.22	0.22	0.08	0.30	0.13	0.12
Rb	0.97	bdl	1.18	1.01	1.00	0.07	bdl	bdl
Sr	4.9	6.1	6.9	6.4	13.5	5.9	6.0	6.8
Y	8.6	12.0	10.1	8.6	8.6	8.6	9.5	9.1
Zr	16.7	20.5	24.7	18.4	17.7	14.9	14.3	17.4
Nb	0.21	0.05	0.44	0.23	0.23	0.06	0.06	0.06
Mo	0.07	0.09	0.05	0.06	0.04	0.07	0.08	0.07
Ag	0.008	0.003	0.005	0.006	0.004	0.010	0.009	0.004
Cd	0.03	0.03	0.07	0.06	0.05	0.05	0.05	0.08
In	0.004	0.002	bdl	bdl	bdl	bdl	bdl	bdl
Sn	0.03	0.03	0.03	0.03	0.03	0.05	0.03	0.03
Sb	0.009	0.002	0.016	0.012	0.015	0.012	0.015	0.013

NWA 6698	Cpx 1	Cpx 2	Cpx 3	Cpx 4	Cpx 5	Cpx 6	Cpx 7	Cpx 8
Cs	0.026	bdl	bdl	0.056	0.036	bdl	bdl	bdl
Ba	2.9	0.14	6.3	13.1	6.4	0.6	1.2	1.4
La	0.11	0.15	0.08	0.09	0.08	0.07	0.08	0.07
Ce	0.34	0.40	0.32	0.36	0.35	0.33	0.33	0.32
Pr	0.07	0.10	0.07	0.07	0.08	0.07	0.08	0.07
Nd	0.48	0.67	0.57	0.55	0.53	0.58	0.62	0.56
Sm	0.35	0.41	0.39	0.30	0.34	0.34	0.39	0.37
Eu	0.05	0.07	0.08	0.07	0.11	0.07	0.08	0.07
Gd	0.59	1.02	0.81	0.70	0.72	0.75	0.85	0.79
Tb	0.13	0.19	0.17	0.16	0.15	0.16	0.18	0.17
Dy	1.05	1.54	1.35	1.21	1.23	1.34	1.47	1.41
Ho	0.27	0.36	0.32	0.30	0.30	0.33	0.37	0.35
Er	1.02	1.35	1.06	1.02	1.06	1.11	1.19	1.21
Tm	0.15	0.21	0.19	0.17	0.18	0.19	0.20	0.21
Yb	1.19	1.50	1.42	1.30	1.27	1.33	1.48	1.49
Lu	0.22	0.27	0.23	0.22	0.22	0.23	0.26	0.27
Hf	0.566	0.611	0.756	0.647	0.680	0.567	0.588	0.763
Ta	0.007	bdl	0.025	0.010	0.012	0.002	0.002	0.001
W	0.002	bdl	bdl	bdl	bdl	0.002	bdl	bdl
Tl	0.001	bdl	0.002	bdl	0.001	0.001	0.001	0.001
Pb	0.106	0.075	0.070	0.133	0.055	0.105	0.063	0.048
Bi	0.002	0.000	0.001	0.006	bdl	0.001	0.002	0.003
Th	0.023	0.006	0.006	0.018	0.013	0.004	0.004	0.004
U	0.009	0.001	0.007	0.005	0.006	0.002	0.005	0.002

NWA 6698	Cpx 9	Cpx 10	Opx 1	Opx 2	Opx 3	Opx 4	Opx 5	Opx 6
Li	3.4	2.7	3.1	3.5	4.4	4.1	3.0	2.9
Be	bdl	bdl	bdl	bdl	bdl	bdl	bdl	bdl
B	0.7	0.5	0.5	0.5	0.9	0.7	0.5	0.4
Na_2O	0.58	0.52	0.12	0.13	0.18	0.13	0.14	0.12
MgO	14.79	14.93	18.51	19.08	18.79	18.95	19.70	19.20
Al_2O_3	0.84	0.67	0.29	0.31	0.38	0.32	0.36	0.30
SiO_2	50.65	50.97	53.38	52.80	53.23	53.25	52.05	50.92
P_2O_5	0.027	0.015	0.010	0.009	0.022	0.015	0.008	1.153
K_2O	0.034	bdl	bdl	bdl	0.022	0.008	bdl	bdl
CaO	18.84	19.07	3.90	4.05	3.94	4.31	4.58	5.66
Sc	108	113	38	38	38	40	42	42
TiO_2	1.11	1.12	0.51	0.52	0.50	0.52	0.57	0.54
V	107	109	38	38	41	37	40	37
Cr	5811	5817	3202	3151	3195	3080	3244	3075
MnO	0.752	0.751	1.214	1.220	1.242	1.208	1.225	1.184
FeOT	12.38	11.96	22.06	21.88	21.69	21.29	21.36	20.94
Co	1.5	0.5	1.1	2.1	4.4	1.3	1.4	0.8
Ni	11.0	0.2	1.1	10.9	62.2	8.9	5.8	0.5
Cu	4.3	0.3	0.9	0.6	2.1	0.4	0.1	bdl
Zn	273	270	744	704	692	718	610	567
Ga	6.26	6.04	2.98	2.76	3.06	2.73	2.62	2.56
Ge	0.12	0.10	0.16	0.18	0.12	0.17	0.11	0.16
As	0.04	0.02	0.04	0.06	0.06	0.08	0.04	0.05
Se	0.33	0.09	0.20	0.23	0.19	0.18	0.08	bdl
Rb	1.20	bdl	bdl	bdl	0.7	0.2	0.3	bdl
Sr	6.9	6.0	0.8	0.9	1.0	2.3	0.6	4.4
Y	9.1	9.2	2.5	2.5	2.4	2.6	2.8	36.9
Zr	18.7	15.8	2.9	3.6	3.0	2.9	3.7	3.3
Nb	0.17	0.04	0.04	0.07	0.06	0.04	0.06	0.03
Mo	0.07	0.06	0.18	0.10	0.22	0.12	0.08	0.10
Ag	0.012	0.001	0.008	0.003	0.009	0.004	0.005	0.002
Cd	0.09	0.07	0.09	0.04	0.11	0.11	0.06	0.05
In	bdl	bdl	bdl	bdl	bdl	bdl	bdl	bdl
Sn	0.03	0.02	0.03	0.02	0.04	0.03	0.24	0.02
Sb	0.017	0.013	0.037	0.004	0.016	0.017	0.007	0.019

NWA 6698	Cpx 9	Cpx 10	Opx 1	Opx 2	Opx 3	Opx 4	Opx 5	Opx 6
Cs	0.034	bdl	bdl	bdl	bdl	bdl	bdl	bdl
Ba	3.0	0.03	0.98	6.80	5.53	3.81	2.33	0.27
La	0.08	0.07	0.01	0.01	0.03	0.02	0.01	3.23
Ce	0.34	0.33	0.03	0.05	0.09	0.09	0.04	7.97
Pr	0.08	0.08	0.01	0.01	0.01	0.01	0.01	1.24
Nd	0.58	0.60	0.05	0.09	0.09	0.07	0.06	6.55
Sm	0.32	0.40	0.04	0.05	0.06	0.06	0.04	2.78
Eu	0.08	0.07	0.01	0.01	0.01	0.01	0.01	0.24
Gd	0.80	0.84	0.13	0.13	0.13	0.14	0.14	4.65
Tb	0.17	0.19	0.04	0.03	0.03	0.04	0.04	0.82
Dy	1.48	1.49	0.38	0.33	0.31	0.32	0.37	5.53
Ho	0.35	0.36	0.10	0.10	0.09	0.11	0.10	1.23
Er	1.17	1.21	0.41	0.38	0.37	0.41	0.41	3.57
Tm	0.20	0.21	0.08	0.07	0.07	0.08	0.08	0.53
Yb	1.49	1.52	0.65	0.60	0.56	0.68	0.63	3.11
Lu	0.26	0.26	0.12	0.13	0.12	0.13	0.12	0.46
Hf	0.783	0.656	0.14	0.13	0.13	0.12	0.15	0.13
Ta	0.014	0.002	bdl	0.004	0.002	0.003	0.005	bdl
W	bdl	0.018	bdl	bdl	0.004	0.004	0.002	0.003
Tl	0.005	bdl	bdl	0.0009	0.0010	0.0024	0.0008	bdl
Pb	0.120	0.025	0.07	0.06	0.18	0.25	0.06	0.11
Bi	0.002	0.002	0.008	0.001	0.003	0.007	0.002	bdl
Th	0.012	0.001	0.004	0.009	0.017	0.011	0.005	0.173
U	0.006	0.001	0.002	0.002	0.015	0.005	0.004	0.026

NWA 6698	Phosphate 1	Phosphate 2	Glass 1	Glass 2	Glass 3	Raster	Raster Corrected
Li	bdl	7.5	16.0	18.9	16.1	3.52	4.54
Be	bdl	bdl	0.4	0.3	0.4	0.05	0.04
B	6.6	4.7	14.9	14.4	16.1	1.23	2.13
Na_2O	1.05	0.85	7.34	7.24	6.92	5.29	4.96
MgO	0.63	2.98	1.66	1.69	1.63	6.09	6.83
Al_2O_3	2.06	0.13	12.98	13.54	12.05	15.86	14.06
SiO_2	7.17	1.30	66.51	65.40	66.85	55.30	55.72
P_2O_5	43.95	52.62	0.808	0.819	0.766	0.628	0.680
K_2O	0.07	0.05	1.33	1.57	1.88	0.20	0.28
CaO	43.88	39.30	2.88	2.91	2.76	9.21	8.87
Sc	5	51	15	16	14	28	30
TiO_2	0.04	0.01	1.42	1.31	1.30	0.37	0.46
V	3	11	6.5	7.1	6.2	32	34
Cr	745	245	336	301	360	1745	1877
MnO	0.161	0.209	0.204	0.217	0.222	0.345	0.398
FeOT	0.98	2.54	4.87	5.31	5.62	6.71	7.75
Co	3	19	1.4	0.8	0.4	17	17
Ni	42	256	bdl	4.0	0.4	495	500
Cu	2	8	1.4	2.7	2.6	15	15
Zn	18	46	188	215	234	160	195
Ga	7.19	10.32	31.1	31.4	31.7	24	23
Ge	1.80	1.53	0.16	0.17	0.17	0.13	0.13
As	1.37	0.85	0.04	0.12	0.04	0.18	0.19
Se	2.59	1.10	0.10	0.17	0.09	0.46	0.46
Rb	0.3	0.4	79.8	64.7	82.4	1.29	5.77
Sr	205	159	35.5	35.6	36.5	116	102
Y	34	1218	11.5	10.5	10.6	3.3	4.0
Zr	9.1	1.8	178.4	137.1	135.8	4.2	13.4
Nb	0.08	0.07	14.4	12.2	12.3	0.08	0.87
Mo	bdl	0.4	0.01	0.02	0.03	0.14	0.15
Ag	bdl	0.1	0.05	0.04	0.04	0.03	0.03
Cd	bdl	0.2	0.09	0.09	0.08	0.06	0.06
In	bdl	bdl	0.02	0.02	0.08	0.003	0.006
Sn	0.14	0.16	0.17	0.14	0.21	0.09	0.10
Sb	0.03	0.05	0.40	0.03	0.01	0.02	0.03

NWA 6698	Phosphate 1	Phosphate 2	Glass 1	Glass 2	Glass 3	Raster	Raster Corrected
Cs	0.03	0.04	4.2	3.3	4.4	0.08	0.32
Ba	22	50	25.4	38.5	27.7	43	43
La	3.95	149.80	0.988	0.925	0.896	0.26	0.31
Ce	9.49	344.85	2.235	2.328	2.318	0.79	0.92
Pr	1.59	57.51	0.330	0.340	0.336	0.11	0.13
Nd	8.88	307.94	1.679	1.756	1.720	0.60	0.71
Sm	3.02	107.81	0.600	0.647	0.633	0.23	0.27
Eu	1.54	9.26	0.339	0.350	0.397	0.71	0.63
Gd	5.52	172.31	1.100	1.072	1.029	0.36	0.43
Tb	0.89	29.14	0.201	0.222	0.213	0.07	0.08
Dy	5.72	205.72	1.678	1.665	1.668	0.54	0.66
Ho	1.24	43.46	0.404	0.402	0.398	0.12	0.15
Er	3.51	126.59	1.368	1.422	1.315	0.41	0.51
Tm	0.49	17.14	0.275	0.229	0.222	0.07	0.08
Yb	3.10	94.61	1.817	1.757	1.790	0.50	0.63
Lu	0.45	13.94	0.275	0.297	0.291	0.08	0.11
Hf	0.11	0.13	4.52	3.81	3.62	0.17	0.41
Ta	0.006	0.002	0.834	0.680	0.637	0.005	0.048
W	0.011	0.022	0.020	0.028	0.022	0.055	0.055
Tl	bdl	0.011	0.044	0.050	0.055	0.006	0.009
Pb	0.547	5.081	0.316	0.729	0.475	0.800	0.834
Bi	0.006	0.008	0.003	0.012	0.023	0.025	0.025
Th	0.693	10.06	0.402	0.403	0.380	0.043	0.067
U	0.807	0.712	0.198	0.211	0.311	0.055	0.070

Table A8. Individual microprobe analyses for NWA 6698.

NWA 6698	Al_2O_3	SiO_2	TiO_2	Cr_2O_3	Na_2O	MgO	MnO	FeO	NiO	K_2O	CaO	TOTAL
Feldspar	21.26	63.41	0.09	0.00	9.78	0.04	0.00	0.14	0.00	0.30	4.65	99.66
Feldspar	22.10	65.35	0.12	0.00	9.39	0.03	0.00	0.10	0.01	0.32	4.38	101.81
Feldspar	22.92	61.01	0.06	0.00	8.84	0.05	0.02	0.09	0.00	0.25	6.30	99.53
Feldspar	25.24	56.52	0.04	0.00	6.90	0.02	0.03	0.04	0.04	0.13	9.46	98.42
Feldspar	21.40	64.01	0.11	0.00	10.00	0.05	0.00	0.08	0.00	0.31	4.27	100.25
Feldspar	23.09	61.15	0.10	0.00	8.76	0.04	0.00	0.06	0.01	0.22	6.46	99.89
Feldspar	22.25	62.18	0.09	0.01	9.16	0.04	0.00	0.07	0.01	0.25	5.46	99.53
Feldspar	23.44	59.32	0.06	0.00	8.16	0.04	0.02	0.05	0.00	0.18	7.31	98.58
Feldspar	21.28	62.62	0.09	0.00	9.68	0.04	0.00	0.08	0.00	0.29	4.70	98.77
Feldspar	20.52	63.51	0.11	0.01	9.78	0.04	0.00	0.09	0.01	0.28	4.16	98.51
Feldspar	21.66	63.87	0.11	0.00	9.51	0.03	0.00	0.17	0.00	0.29	4.76	100.39
Feldspar	21.52	64.37	0.12	0.00	9.84	0.04	0.02	0.16	0.00	0.28	4.48	100.82
Feldspar	22.66	65.36	0.10	0.00	8.81	0.05	0.00	0.03	0.00	0.34	4.44	101.78
Feldspar	24.97	61.83	0.11	0.00	7.70	0.05	0.00	0.07	0.00	0.22	6.60	101.56
Feldspar	23.89	62.75	0.09	0.00	8.41	0.03	0.00	0.07	0.00	0.26	5.86	101.36
Feldspar	28.56	55.31	0.01	0.00	5.56	0.01	0.01	0.08	0.01	0.12	10.93	100.59
Feldspar	22.64	65.28	0.11	0.00	8.75	0.04	0.02	0.10	0.00	0.36	4.34	101.65
Feldspar	22.90	64.74	0.07	0.00	8.60	0.03	0.00	0.07	0.02	0.31	4.89	101.62
Feldspar	23.54	61.86	0.08	0.01	8.15	0.01	0.00	0.10	0.00	0.24	6.43	100.43
Feldspar	22.62	65.49	0.11	0.00	8.68	0.04	0.00	0.07	0.03	0.33	4.53	101.91
Feldspar	24.30	61.74	0.07	0.00	8.19	0.04	0.00	0.05	0.01	0.25	5.94	100.60
Feldspar	23.20	61.76	0.11	0.01	8.70	0.03	0.00	0.05	0.01	0.33	4.50	98.70
Feldspar	23.62	63.44	0.09	0.00	8.64	0.05	0.01	0.08	0.00	0.28	5.29	101.48
Feldspar	22.34	63.82	0.13	0.00	8.65	0.04	0.01	0.09	0.00	0.30	5.15	100.53
Feldspar	22.96	60.79			9.27	0.05		0.09		0.38	4.00	97.54
Feldspar	24.26	61.85			8.62	0.04		0.05		0.28	5.14	100.25
Feldspar	24.88	57.18			8.25	0.06		0.06		0.26	6.12	96.82
Feldspar	23.12	61.07			9.02	0.04		0.09		0.36	4.24	97.94
Feldspar	24.53	58.46			7.76	0.05		0.11		0.21	6.86	97.99
Feldspar	23.39	65.31			9.05	0.05		0.10		0.36	4.44	102.68
Feldspar	23.55	64.69			9.11	0.05		0.08		0.35	4.37	102.19
Feldspar	27.27	59.00			7.15	0.03		0.11		0.19	8.14	101.89
Feldspar	23.91	64.84			9.00	0.04		0.10		0.33	4.47	102.69
Feldspar	23.83	63.75			9.02	0.04		0.11		0.32	4.69	101.76
Feldspar	23.81	64.67			9.07	0.05		0.15		0.32	4.48	102.55
Feldspar	29.66	55.72			5.77	0.07		0.09		0.12	10.46	101.89
Feldspar	27.72	57.59			6.94	0.02		0.09		0.19	8.65	101.21
Feldspar	23.19	64.70			9.26	0.08		0.09		0.36	4.16	101.83
Feldspar	24.14	64.81			8.79	0.04		0.10		0.31	4.86	103.05
Feldspar	27.21	59.99			7.64	0.06		0.09		0.22	7.29	102.51

NWA 6698	Al_2O_3	SiO_2	TiO_2	Cr_2O_3	Na_2O	MgO	MnO	FeO	NiO	K_2O	CaO	TOTAL
Feldspar	24.18	65.43			8.20	0.04		0.15		0.32	4.55	102.86
Feldspar	27.48	56.58			7.17	0.05		0.08		0.18	7.77	99.30
Feldspar	25.87	61.69			7.98	0.04		0.10		0.25	5.96	101.89
Feldspar	24.37	64.61			8.54	0.05		0.08		0.34	4.28	102.27
Feldspar	25.16	62.15			8.38	0.06		0.09		0.28	5.40	101.52
Feldspar	25.28	62.84			8.09	0.06		0.06		0.30	5.24	101.86
Feldspar	24.91	64.21			8.33	0.04		0.09		0.31	4.88	102.77
Feldspar	24.57	64.20			8.43	0.05		0.05		0.32	4.58	102.20
Feldspar	24.93	64.06			8.25	0.04		0.08		0.30	4.87	102.52
Feldspar	25.86	62.20			8.17	0.03		0.07		0.27	5.75	102.35
Feldspar	24.47	63.78			8.75	0.06		0.11		0.31	4.58	102.07
Feldspar	26.88	58.73			7.69	0.05		0.06		0.22	7.21	100.84
Glass	13.71	68.54	1.01	0.04	7.78	1.34	0.18	4.13	0.01	1.09	2.14	99.98
Glass	12.57	67.37	1.27	0.05	7.03	1.36	0.19	4.96	0.00	1.14	2.69	98.63
Glass	11.45	66.99	1.12	0.03	6.72	1.78	0.29	6.17	0.01	1.07	2.92	98.56
Glass	13.32	67.61	1.11	0.04	7.99	1.49	0.15	4.20	0.02	0.87	2.52	99.31
Glass	13.53	67.10	1.22	0.04	8.21	1.34	0.18	4.30	0.07	0.93	2.48	99.40
Glass	14.50	67.15	1.16	0.04	7.31	1.52	0.18	4.65	0.00	1.04	2.85	100.39
Glass	14.26	67.35	1.13	0.05	7.64	1.36	0.16	4.21	0.00	1.19	2.34	99.68
Glass	13.81	67.02	1.27	0.02	7.36	1.14	0.20	4.95	0.01	0.83	2.48	99.09
Glass	14.84	66.55	1.14	0.00	7.75	1.17	0.19	5.55	0.00	0.92	2.32	100.44
Glass	13.11	67.32	1.23	0.03	6.95	1.56	0.23	5.48	0.02	1.42	2.25	99.61
Glass	14.07	66.69	1.20	0.05	7.40	1.59	0.19	4.55	0.00	1.14	2.87	99.75
Glass	14.96	67.11	1.05	0.01	7.96	0.78	0.14	4.19	0.00	1.06	2.08	99.35

NWA 6698	Al_2O_3	SiO_2	TiO_2	Cr_2O_3	Na_2O	MgO	MnO	FeO	NiO	K_2O	CaO	TOTAL
Opx	0.33	52.77	0.56	0.43	0.16	19.65	1.20	20.35	0.01	0.02	4.23	99.71
Opx	0.32	52.78	0.52	0.43	0.15	19.82	1.18	20.23	0.00	0.01	4.20	99.63
Opx	0.33	53.11	0.53	0.44	0.13	19.70	1.17	20.25	0.00	0.03	4.21	99.91
Opx	0.32	52.52	0.56	0.44	0.15	19.49	1.18	20.11	0.04	0.02	4.26	99.09
Opx	0.32	53.98	0.57	0.46	0.13	19.46	1.15	20.13	0.01	0.02	4.27	100.51
Opx	0.34	53.08	0.56	0.48	0.14	19.55	1.17	20.29	0.00	0.03	4.28	99.92
Opx	0.34	53.23	0.52	0.44	0.16	19.09	1.16	20.55	0.01	0.03	4.23	99.75
Opx	0.36	53.09	0.55	0.44	0.14	19.18	1.13	20.38	0.00	0.02	4.22	99.51
Opx	0.33	53.03	0.53	0.44	0.16	19.08	1.18	20.44	0.01	0.02	4.15	99.37
Opx	0.34	52.76	0.51	0.44	0.14	19.17	1.20	20.65	0.00	0.02	4.24	99.47
Opx	0.36	53.35	0.55	0.45	0.16	19.09	1.13	20.42	0.01	0.02	4.30	99.85
Opx	0.34	52.85	0.55	0.44	0.14	19.18	1.16	20.44	0.00	0.02	4.21	99.34
Opx	0.35	53.31	0.57	0.44	0.15	19.21	1.20	20.47	0.01	0.03	4.19	99.94
Opx	0.35	52.90	0.54	0.44	0.15	19.14	1.13	20.34	0.02	0.02	4.17	99.21
Opx	0.33	52.92	0.58	0.43	0.14	19.29	1.15	20.16	0.00	0.02	4.32	99.34
Cpx	0.66	52.27	1.13	0.83	0.55	14.90	0.70	11.38	0.02	0.02	17.67	100.13
Cpx	0.71	52.69	1.20	0.86	0.55	14.76	0.74	11.25	0.01	0.02	17.66	100.46
Cpx	0.70	52.00	1.15	0.82	0.55	14.75	0.70	11.20	0.00	0.01	17.82	99.71
Cpx	0.69	52.04	1.14	0.84	0.53	14.83	0.72	11.16	0.00	0.03	17.61	99.57
Cpx	0.69	52.92	1.16	0.84	0.53	14.71	0.72	11.14	0.00	0.03	17.59	100.35
Cpx	0.68	53.35	1.12	0.83	0.53	14.70	0.74	11.24	0.00	0.02	17.58	100.79
Cpx	0.71	52.56	1.16	0.83	0.57	14.78	0.73	11.25	0.04	0.02	17.75	100.40
Cpx	0.79	52.30	1.18	0.83	0.55	14.76	0.69	11.22	0.00	0.05	17.61	99.98
Cpx	0.72	52.73	1.18	0.84	0.56	14.64	0.75	11.43	0.00	0.02	17.73	100.61
Cpx	0.71	53.20	1.15	0.87	0.55	14.74	0.76	11.20	0.00	0.03	17.54	100.73
Cpx	0.73	52.75	1.13	0.86	0.53	14.66	0.75	11.44	0.02	0.04	17.62	100.51
Cpx	0.73	53.09	1.12	0.82	0.56	14.89	0.71	11.23	0.00	0.03	17.68	100.86
Cpx	0.73	52.94	1.16	0.86	0.54	14.55	0.69	11.23	0.02	0.03	17.69	100.43
Cpx	0.70	52.44	1.17	0.82	0.54	14.84	0.74	11.16	0.00	0.03	17.91	100.35
Cpx	0.69	52.14	1.17	0.88	0.55	14.89	0.73	11.21	0.00	0.02	17.69	99.96
Cpx	0.65	53.03	1.12	0.83	0.53	14.62	0.69	11.33	0.00	0.02	17.71	100.54
Cpx	0.73	53.04	1.11	0.81	0.50	14.34	0.70	11.37	0.00	0.02	17.69	100.31
Cpx	0.77	52.67	1.14	0.84	0.51	14.18	0.68	11.23	0.02	0.02	17.71	99.77
Cpx	0.74	52.78	1.08	0.84	0.53	14.35	0.72	11.32	0.00	0.02	17.46	99.86
Cpx	0.76	52.63	1.16	0.85	0.52	14.20	0.76	11.22	0.00	0.02	17.60	99.72
Cpx	0.75	53.01	1.15	0.83	0.51	14.22	0.73	11.23	0.00	0.02	17.64	100.07
Cpx	0.74	53.05	1.17	0.82	0.50	14.27	0.75	11.24	0.00	0.02	17.65	100.22
Cpx	0.73	52.61	1.15	0.82	0.53	14.27	0.71	11.25	0.01	0.02	17.57	99.68
Cpx	0.71	53.02	1.14	0.83	0.48	14.16	0.73	11.32	0.00	0.03	17.71	100.14
Cpx	0.73	52.83	1.10	0.86	0.54	14.98	0.68	11.27	0.00	0.02	17.45	100.45

NWA 6698	Al_2O_3	SiO_2	TiO_2	Cr_2O_3	Na_2O	MgO	MnO	FeO	NiO	K_2O	CaO	TOTAL
Oxide	3.66	0.04	15.43	37.13	0.00	4.80	0.98	35.77	0.03	0.02	0.00	97.89
Oxide	3.37	0.05	15.37	38.09	0.03	4.93	0.99	35.69	0.04	0.02	0.01	98.60
Oxide	3.38	0.04	14.96	38.50	0.04	5.07	1.01	34.94	0.00	0.02	0.01	97.96
Oxide	3.46	0.05	15.80	37.29	0.02	5.59	0.99	34.81	0.00	0.03	0.03	98.06
Oxide	3.31	0.04	15.96	37.62	0.03	5.41	1.06	34.87	0.00	0.04	0.01	98.36
Oxide	3.22	0.05	15.87	37.31	0.00	5.23	0.96	35.46	0.00	0.03	0.02	98.15
Oxide	3.41		15.59	37.86		4.96	1.04	34.65	0.02		0.01	98.09
Oxide	3.26		15.29	37.65		4.09	1.02	36.45	0.00		0.07	98.29
Oxide	3.34		15.52	37.53		5.12	1.01	35.16	0.00		0.01	98.17
Oxide	3.56		15.48	38.15		5.37	0.99	34.36	0.02		0.01	98.67
Oxide	3.56		15.63	37.80		4.93	0.99	35.17	0.00		0.03	98.84
Oxide	3.58		15.17	38.22		4.94	1.02	34.82	0.03		0.03	98.45
Oxide	3.84		15.24	37.85		5.15	1.01	34.74	0.01		0.00	98.52
Oxide	3.67		15.59	38.44		5.43	1.02	34.60	0.00		0.00	99.47
Oxide	3.55		15.43	38.22		5.02	1.04	35.18	0.02		0.00	99.23
Oxide	3.91		15.23	38.08		4.91	0.99	35.30	0.01		0.02	99.06

NWA 6698	CaO	P_2O_5	F	Cl	MgO	Na_2O	FeO	TOTAL
Apatite	52.76	41.78	1.73	3.23	0.47	0.58	0.96	101.51
Apatite	52.79	42.01	1.70	3.05	0.58	0.62	0.77	101.52
Apatite	53.04	40.96	1.88	2.97	0.51	0.60	0.88	100.84
Apatite	52.99	40.42	1.77	3.00	0.50	0.57	0.77	100.03
Apatite	52.97	42.39	1.99	2.94	0.54	0.59	0.82	102.23
Apatite	52.74	39.51	1.74	3.13	0.36	0.45	1.22	99.15
Apatite	52.66	39.98	1.80	3.19	0.53	0.54	0.91	99.61
Apatite	52.63	40.81	1.63	3.15	0.56	0.52	0.80	100.11
Apatite	53.15	41.16	1.79	3.15	0.41	0.63	0.74	101.04
Apatite	52.79	39.26	1.81	3.11	0.60	0.62	0.67	98.86
Apatite	52.75	41.01	1.86	3.13	0.50	0.60	0.66	100.50
Apatite	52.69	41.66	1.81	3.13	0.53	0.64	0.77	101.24
Merrillite	47.08	44.27	0.42	0.00	2.87	1.64	2.01	98.28
Merrillite	46.87	44.91	0.41	0.00	3.26	1.68	1.59	98.71
Merrillite	46.99	45.23	0.47	0.00	3.15	1.54	1.78	99.15
Merrillite	46.79	47.38	0.42	0.00	3.19	1.70	1.75	101.23
Merrillite	47.06	44.84	0.36	0.00	3.27	1.22	1.85	98.60
Merrillite	47.38	44.57	0.43	0.00	2.95	1.65	1.95	98.92
Merrillite	47.15	46.00	0.55	0.00	3.40	1.78	1.22	100.10
Merrillite	47.33	45.11	0.37	0.00	2.98	1.55	2.02	99.36
Merrillite	47.03	42.52	0.27	0.00	3.33	1.24	1.70	96.08
Merrillite	47.19	45.32	0.50	0.00	3.32	1.64	1.42	99.40
Merrillite	47.17	46.53	0.39	0.00	3.30	1.33	1.34	100.06
Merrillite	46.86	45.30	0.33	0.00	3.13	1.56	1.81	99.00
Merrillite	47.05	44.99	0.47	0.00	3.08	1.36	1.87	98.82
Merrillite	47.17	45.26	0.47	0.01	3.17	1.41	1.87	99.35
Merrillite	46.97	46.22	0.56	0.00	3.19	1.17	1.88	99.99
Merrillite	46.88	44.95	0.39	0.00	2.95	1.63	2.09	98.89

Table A9. Individual microprobe analyses for experimental run products. Ol = olivine; Px = pyroxene; Plg = plagioclase; MLT = melt; Chr = chromite; Met = metal.

LL	Al_2O_3	SiO_2	TiO_2	Cr_2O_3	MgO	FeO	NiO	CaO	Na_2O	TOTAL
1050 Ol	0.02	31.29	0.02	0.28	34.54	26.64	0.04	0.17	0.00	92.99
1050 Ol	0.05	31.29	0.03	0.31	33.80	26.66	0.05	0.24	0.00	92.43
1050 Px	0.54	47.14	0.05	0.68	28.76	14.22	0.06	0.56	0.00	92.00
1050 Px	0.78	55.13	0.06	0.72	28.73	13.60	0.00	0.51	0.00	99.52
1050 Px	0.77	55.62	0.06	0.69	28.17	13.81	0.05	0.51	0.00	99.67
1050 Px	0.61	55.54	0.04	0.61	28.49	14.14	0.04	0.53	0.00	100.01
1050 Ol	0.01	37.48	0.03	0.26	34.35	26.31	0.06	0.17	0.00	98.65
1050 Ol	0.02	38.53	0.03	0.25	34.33	26.24	0.05	0.19	0.00	99.65
1050 Ol	0.02	36.98	0.04	0.17	31.88	29.58	0.03	0.21	0.00	98.91
1050 Mlt	1.45	52.51	0.85	0.46	19.18	16.75	0.01	8.76	0.03	99.99
1050 Mlt	2.35	49.93	1.11	0.55	18.73	15.62	0.07	10.04	0.06	98.47
1050 Mlt	1.60	52.09	0.92	0.51	20.24	16.65	0.03	7.95	0.08	100.06
1050 Mlt	1.65	53.44	0.13	1.04	25.27	16.43	0.03	1.51	0.00	99.49
1050 Met	0.00	0.04	0.03	0.04	0.03	101.54	24.74	0.06	0.00	98.50
1050 Plg	27.58	53.09	0.12	0.03	1.30	1.74	0.01	12.49	3.68	100.03
1050 Plg	28.10	54.12	0.09	0.01	0.83	1.59	0.05	12.49	3.74	101.01
1050 Plg	28.39	54.09	0.06	0.01	0.86	1.49	0.00	12.63	3.87	101.42
1050 Plg	27.66	58.29	0.24	0.02	0.60	1.75	0.02	11.26	3.59	103.43
1100 Ol	0.03	37.17	0.04	0.22	32.83	28.59	0.06	0.26	0.00	99.19
1100 Ol	0.04	37.67	0.03	0.20	33.02	28.12	0.07	0.31	0.00	99.46
1100 Ol	0.03	37.73	0.03	0.33	33.84	26.97	0.07	0.23	0.00	99.22
1100 Px	0.70	55.52	0.06	0.70	27.79	14.26	0.00	0.51	0.00	99.53
1100 Px	0.65	55.44	0.05	0.67	27.91	14.40	0.04	0.53	0.00	99.68
1100 Px	0.49	56.08	0.06	0.59	29.07	13.88	0.02	0.40	0.00	100.59
1100 Chr	24.10	0.32	0.87	41.03	7.89	25.23	0.02	0.10	0.00	99.55
1100 Chr	23.54	0.23	0.83	40.79	7.86	25.13	0.04	0.11	0.00	98.52
1100 Chr	22.39	2.15	0.87	39.99	8.42	24.89	0.05	0.13	0.01	98.88
1100 Met	0.03	0.05	0.01	0.06	0.03	99.01	27.41	0.04	0.00	98.63
1100 Plg	30.68	52.72	0.05	0.01	0.51	1.67	0.07	14.03	3.22	102.98
1100 Plg	30.32	52.83	0.05	0.02	0.54	1.35	0.03	13.51	3.39	102.04
1100 Plg	28.53	52.09	0.05	0.03	1.46	2.30	0.03	12.79	3.08	100.36
1100 Plg	30.02	52.88	0.06	0.02	0.43	1.29	0.05	13.57	3.42	101.76
1100 Plg	29.96	52.43	0.04	0.01	0.41	1.28	0.03	13.55	3.40	101.10
1100 Mlt	11.19	45.31	2.36	0.18	6.39	15.38	0.07	11.50	0.90	93.29
1100 Mlt	7.57	42.45	1.80	0.17	15.01	20.29	0.03	7.29	0.69	95.31
1100 Mlt	11.32	44.82	3.09	0.15	6.03	15.43	0.04	11.45	0.99	93.32
1100 Mlt	8.77	42.10	1.97	0.19	11.38	18.18	0.02	9.13	0.93	92.67

LL	Al_2O_3	SiO_2	TiO_2	Cr_2O_3	MgO	FeO	NiO	CaO	Na_2O	TOTAL
1150 Ol	0.02	37.06	0.01	0.25	33.61	27.82	0.07	0.24	0.00	99.07
1150 Ol	0.02	37.80	0.00	0.24	31.81	27.35	0.03	0.26	0.00	97.51
1150 Ol	0.04	37.49	0.03	0.26	32.76	27.39	0.02	0.26	0.00	98.25
1150 Px	0.74	55.16	0.06	0.71	27.43	14.78	0.05	0.54	0.00	99.46
1150 Px	0.90	54.82	0.07	0.80	25.91	15.93	0.02	0.73	0.00	99.18
1150 Px	0.75	55.13	0.05	0.73	27.71	15.16	0.04	0.53	0.00	100.10
1150 Chr	27.04	0.16	0.67	38.31	8.59	23.48	0.05	0.12	0.00	98.42
1150 Chr	27.83	0.18	0.65	37.83	9.08	23.86	0.07	0.07	0.00	99.56
1150 Chr	27.50	0.18	0.68	38.15	8.65	23.57	0.05	0.06	0.00	98.85
1150 Mlt	15.40	50.70	0.59	0.21	6.28	14.75	0.05	9.70	1.14	98.83
1150 Mlt	15.67	50.65	0.63	0.21	5.72	14.46	0.06	9.77	1.10	98.26
1150 Mlt	15.36	50.89	0.61	0.21	6.15	14.65	0.02	9.70	1.10	98.69
1200 Ol	0.02	36.79	0.03	0.38	35.52	25.81	0.08	0.18	0.00	98.80
1200 Ol	0.02	37.06	0.01	0.39	35.11	25.91	0.08	0.19	0.00	98.76
1200 Ol	0.02	37.17	0.01	0.37	34.91	25.63	0.06	0.20	0.00	98.36
1200 Ol	0.03	37.45	0.01	0.36	34.79	25.79	0.07	0.19	0.00	98.70
1200 Met	0.03	0.07	0.00	0.05	0.01	86.21	40.15	0.04	0.00	98.68
1200 Px	0.89	53.54	0.05	0.68	25.52	16.79	0.04	0.78	0.00	98.29
1200 Px	0.91	53.73	0.06	0.79	25.60	16.64	0.05	0.68	0.02	98.48
1200 Px	0.94	54.28	0.07	0.65	25.76	16.61	0.01	0.72	0.00	99.04
1200 Mlt	10.40	49.23	0.40	0.41	11.22	20.38	0.05	6.13	0.22	98.44
1200 Mlt	11.14	50.02	0.47	0.42	9.18	20.20	0.02	6.89	0.22	98.55
1200 Mlt	10.98	49.78	0.46	0.40	9.73	20.33	0.04	6.80	0.23	98.77
1250 Met	0.03	0.10	0.01	0.07	0.05	81.72	44.09	0.09	0.00	98.38
1250 Ol	0.04	36.94	0.02	0.37	33.64	28.34	0.05	0.22	0.00	99.61
1250 Ol	0.04	37.58	0.02	0.35	33.41	28.39	0.05	0.24	0.00	100.08
1250 Ol	0.01	37.17	0.02	0.35	34.12	28.04	0.09	0.23	0.00	100.03
1250 Px	1.04	53.46	0.08	0.83	25.27	17.62	0.07	0.94	0.00	99.32
1250 Px	0.97	53.59	0.07	0.78	24.54	17.77	0.10	1.01	0.00	98.84
1250 Px	0.95	54.87	0.06	0.81	25.43	17.48	0.07	0.81	0.00	100.48
1250 Mlt	13.15	50.91	0.51	0.36	7.58	18.00	0.03	7.88	0.87	99.29
1250 Mlt	12.66	49.54	0.51	0.36	7.47	17.95	0.03	7.98	0.89	97.40
1250 Mlt	12.66	48.77	0.53	0.35	7.50	18.03	0.05	7.91	0.91	96.69
1250 Mlt	0.06	0.13	0.01	0.07	0.03	87.22	46.37	0.07	0.00	133.96

LL -Na	Al_2O_3	SiO_2	TiO_2	Cr_2O_3	MgO	MnO	FeO	NiO	CaO	TOTAL
1050 Met	0.01	0.07	0.00	0.04	0.03	0.02	108.92	17.46	0.04	98.51
1050 Ol	0.03	36.28	0.05	0.10	35.48	0.15	26.97	0.08	0.11	99.24
1050 Ol	0.02	37.52	0.02	0.14	36.21	0.15	25.10	0.04	0.09	99.28
1050 Ol	0.01	36.88	0.03	0.10	35.25	0.12	26.97	0.06	0.13	99.56
1050 Px	0.79	56.31	0.04	0.51	30.97	0.07	11.90	0.00	0.24	100.82
1050 Px	0.55	56.41	0.03	0.35	30.90	0.08	12.12	0.03	0.21	100.67
1050 Px	0.60	55.93	0.05	0.41	31.25	0.09	11.92	0.05	0.21	100.50
1050 Mlt	34.78	44.71	0.05	0.01	0.45	0.00	1.34	0.07	18.46	99.89
1050 Mlt	35.44	44.58	0.07	0.01	0.43	0.00	1.23	0.02	18.65	100.42
1050 Mlt	36.60	44.18	0.07	0.00	0.35	0.02	1.21	0.02	19.05	101.50
1100 Met	0.00	0.05	0.01	0.02	0.04	0.02	100.11	25.78	0.04	98.19
1100 Ol	0.04	36.70	0.03	0.09	34.06	0.12	28.47	0.03	0.10	99.64
1100 Ol	0.04	36.33	0.04	0.08	34.34	0.13	28.39	0.05	0.11	99.51
1100 Ol	0.03	35.77	0.02	0.06	33.80	0.13	28.17	0.05	0.10	98.14
1100 Px	0.59	53.55	0.04	0.20	30.22	0.11	14.10	0.09	0.25	99.13
1100 Px	0.85	52.21	0.08	0.28	29.48	0.10	14.10	0.07	0.26	97.43
1100 Px	0.50	55.77	0.05	0.14	30.45	0.08	12.78	0.05	0.20	100.03
1100 Mlt	36.19	44.73	0.06	0.00	0.42	0.02	1.39	0.03	18.76	101.59
1100 Mlt	28.98	43.15	0.03	0.02	7.03	0.03	6.43	0.10	14.46	100.24
1100 Mlt	32.34	45.31	0.15	0.03	2.04	0.00	3.51	0.05	16.73	100.16
1150 Met	0.04	0.08	0.00	0.03	0.00	0.01	91.72	34.45	0.04	98.48
1150 Ol	0.03	36.02	0.01	0.11	33.29	0.13	29.58	0.08	0.15	99.41
1150 Ol	0.04	35.76	0.00	0.11	32.82	0.12	29.16	0.05	0.17	98.23
1150 Ol	0.05	36.49	0.02	0.12	34.82	0.11	29.46	0.07	0.17	101.30
1150 Px	2.03	52.40	0.09	0.37	25.34	0.08	17.31	0.01	0.60	98.23
1150 Px	0.98	54.05	0.09	0.18	26.36	0.11	17.35	0.09	0.56	99.76
1150 Px	5.22	51.22	0.21	0.47	24.13	0.07	17.48	0.03	0.63	99.46
1150 Mlt	17.33	47.01	0.78	0.08	7.86	0.10	18.14	0.02	7.63	98.94
1150 Mlt	17.18	47.15	0.81	0.08	7.21	0.14	17.60	0.01	7.90	98.08
1150 Mlt	17.30	47.25	0.68	0.09	7.19	0.12	17.80	0.10	7.68	98.21

LL -Na	Al_2O_3	SiO_2	TiO_2	Cr_2O_3	MgO	MnO	FeO	NiO	CaO	TOTAL
1200 Met	0.00	0.04	0.00	0.04	0.01	0.00	103.24	22.82	0.02	98.24
1200 Ol	0.05	36.65	0.03	0.14	37.31	0.12	24.48	0.07	0.16	99.02
1200 Ol	0.18	35.75	0.02	0.16	37.10	0.13	24.29	0.06	0.15	97.82
1200 Ol	0.05	36.64	0.01	0.17	37.28	0.13	24.47	0.01	0.14	98.90
1200 Px	2.41	52.28	0.11	0.41	27.58	0.12	15.10	0.07	0.56	98.63
1200 Px	1.97	51.78	0.10	0.51	28.07	0.09	15.14	0.00	0.49	98.16
1200 Px	2.82	53.24	0.12	0.49	27.42	0.12	15.03	0.00	0.50	99.75
1200 Mlt	13.82	41.40	0.56	0.15	10.52	0.12	17.68	0.02	6.52	90.79
1200 Mlt	13.39	40.24	0.58	0.16	10.42	0.15	17.34	0.02	6.73	89.02
1200 Mlt	5.75	35.41	0.21	0.14	27.87	0.12	22.04	0.06	2.27	93.88
1200 Mlt	11.78	38.78	0.49	0.16	14.44	0.12	18.33	0.02	5.49	89.62
1250 Met	0.00	0.08	0.00	0.03	0.01	0.00	84.00	41.65	0.02	98.11
1250 Ol	0.06	30.54	0.03	0.19	35.40	0.12	26.55	0.04	0.12	93.05
1250 Ol	0.08	30.73	0.03	0.20	35.37	0.10	26.45	0.09	0.13	93.19
1250 Ol	0.01	37.70	0.01	0.19	35.31	0.13	26.90	0.08	0.11	100.44
1250 Ol	0.05	37.89	0.02	0.21	35.07	0.11	26.72	0.13	0.12	100.30
1250 Ol	0.04	37.80	0.02	0.20	35.15	0.12	26.79	0.07	0.11	100.31
1250 Px	0.75	55.35	0.05	0.37	27.66	0.10	16.19	0.07	0.23	100.76
1250 Px	0.82	55.69	0.04	0.34	27.14	0.10	16.79	0.06	0.28	101.26
1250 Px	0.75	55.77	0.04	0.35	27.30	0.08	16.42	0.04	0.25	101.01
1250 Mlt	12.30	49.74	0.56	0.26	7.70	0.14	21.35	0.03	4.99	97.07
1250 Mlt	12.91	49.90	0.53	0.24	7.07	0.13	21.38	0.00	5.23	97.39
1250 Mlt	12.68	50.06	0.57	0.25	6.86	0.13	21.51	0.06	5.26	97.37
1200 Mlt	11.30	43.87	0.46	0.16	15.25	0.11	20.63	0.04	5.17	96.97
1300 Met	0.00	0.05	0.02	0.03	0.01	0.00	85.25	38.26	0.03	96.42
1300 Ol	0.03	38.70	0.01	0.19	37.48	0.10	24.11	0.09	0.10	100.80
1300 Ol	0.02	36.45	0.01	0.20	38.16	0.11	23.91	0.06	0.09	99.01
1300 Ol	0.02	29.80	0.00	0.18	37.84	0.10	23.51	0.07	0.10	91.63
1300 Px	0.61	53.80	0.04	0.28	28.18	0.11	15.27	0.07	0.23	98.58
1300 Px	0.51	56.25	0.05	0.25	28.37	0.10	15.77	0.06	0.24	101.61
1300 Px	0.57	56.81	0.05	0.26	28.19	0.08	15.96	0.08	0.23	102.24
1300 Mlt	9.67	50.98	0.44	0.25	10.77	0.13	22.80	0.08	3.80	98.93
1300 Mlt	10.16	48.66	0.41	0.26	11.19	0.15	22.50	0.00	3.56	96.90
1300 Mlt	9.11	50.25	0.41	0.25	12.46	0.12	22.58	0.01	3.58	98.77

H	Al_2O_3	SiO_2	TiO_2	Cr_2O_3	MgO	FeO	NiO	CaO	Na_2O	TOTAL
1050 Ol	0.01	37.06	0.04	0.29	32.96	28.54	0.00	0.20	0.00	99.10
1050 Ol	0.01	37.81	0.04	0.29	33.19	28.50	0.01	0.19	0.00	100.03
1050 Ol	0.01	37.12	0.04	0.31	32.91	29.59	0.04	0.21	0.00	100.22
1050 Px	1.60	53.58	0.12	1.31	24.83	16.97	0.00	1.27	0.01	99.69
1050 Px	1.91	50.26	1.01	0.58	19.69	17.94	0.04	7.31	0.01	98.76
1050 Px	1.79	53.87	0.14	1.20	24.32	17.30	0.04	1.52	0.00	100.19
1050 Px	2.12	52.75	1.14	0.62	20.86	18.90	0.06	4.46	0.03	100.95
1050 Px	1.30	53.51	0.11	1.07	26.07	16.60	0.01	1.22	0.00	99.89
1050 Px	1.67	50.81	0.88	0.59	21.31	18.26	0.04	5.07	0.00	98.63
1050 Px	0.91	55.14	0.09	0.88	26.58	15.81	0.02	0.72	0.00	100.14
1050 Px	1.95	51.74	1.22	0.65	20.12	18.85	0.02	5.07	0.02	99.64
1050 Plg	27.44	54.87	0.10	0.02	0.94	1.89	0.09	12.28	3.47	101.10
1050 Plg	28.40	53.96	0.07	0.01	0.65	1.60	0.00	12.99	3.72	101.41
1050 Plg	26.81	54.18	0.09	0.02	1.43	2.40	0.04	12.35	3.33	100.67
1050 Plg	28.45	54.25	0.07	0.02	0.65	1.48	0.01	13.12	3.43	101.49
1050 Mlt	22.52	59.50	0.39	0.03	2.13	3.01	0.04	8.92	2.89	99.42
1050 Mlt	22.11	63.33	0.62	0.00	1.48	3.10	0.01	8.30	2.81	101.76
1050 Mlt	27.51	55.15	0.18	0.02	0.86	1.93	0.01	12.08	3.29	101.03
1050 Met	0.00	0.10	0.00	0.05	0.00	120.23	13.77	0.04	0.00	134.19
1050 Chr	23.82	2.10	1.32	38.71	7.91	25.05	0.01	0.44	0.00	99.36
1050 Chr	24.10	1.76	1.04	38.79	8.48	25.43	0.05	0.28	0.03	99.96
1100 Ol	0.02	36.58	0.01	0.34	32.38	29.57	0.04	0.23	0.00	99.17
1100 Ol	0.03	36.78	0.04	0.21	33.77	29.20	0.05	0.24	0.00	100.31
1100 Ol	0.04	36.23	0.04	0.26	33.35	28.48	0.02	0.32	0.00	98.74
1100 Ol	0.01	35.73	0.05	0.21	33.07	29.96	0.05	0.27	0.00	99.35
1100 Ol	1.53	53.35	0.15	1.13	25.28	17.57	0.04	1.18	0.00	100.21
1100 Px	1.26	53.62	0.12	1.02	24.30	16.99	0.04	1.11	0.03	98.48
1100 Px	1.66	53.97	0.13	1.08	24.72	17.30	0.03	1.36	0.00	100.26
1100 Px	3.09	52.64	0.42	0.87	20.32	18.21	0.02	4.10	0.04	99.71
1100 Px	3.58	52.28	0.39	0.98	21.39	17.35	0.01	4.26	0.02	100.26
1100 Px	2.32	52.31	0.63	0.73	21.01	18.70	0.00	5.44	0.05	101.19
1100 Plg	29.71	53.49	0.04	0.01	0.38	1.26	0.02	13.01	3.48	101.39
1100 Plg	29.92	53.42	0.05	0.02	0.46	1.32	0.03	13.66	3.28	102.15
1100 Plg	30.54	53.41	0.07	0.00	0.44	1.38	0.00	13.62	3.49	102.94
1100 Met	0.00	0.26	0.00	0.03	0.12	112.28	13.47	0.06	0.00	98.12
1100 Chr	27.04	0.44	1.02	37.46	8.54	24.75	0.06	0.09	0.00	99.41
1100 Chr	35.92	1.07	0.72	28.60	10.61	23.93	0.01	0.10	0.00	100.96

H	Al_2O_3	SiO_2	TiO_2	Cr_2O_3	MgO	FeO	NiO	CaO	Na_2O	TOTAL
1150 Ol	0.03	37.52	0.03	0.26	33.45	29.26	0.02	0.26	0.00	100.84
1150 Ol	0.03	36.80	0.00	0.28	33.08	28.71	0.05	0.21	0.00	99.16
1150 Ol	0.04	37.03	0.01	0.27	33.26	28.72	0.03	0.27	0.00	99.63
1150 Px	2.26	53.18	0.20	1.26	23.08	17.81	0.00	2.12	0.00	99.92
1150 Px	1.11	54.42	0.12	1.12	25.09	17.59	0.01	1.11	0.00	100.58
1150 Px	2.13	50.88	0.18	1.06	22.77	21.16	0.45	1.71	0.00	100.34
1150 Mlt	15.21	51.54	0.70	0.22	6.07	15.19	0.04	9.15	1.26	99.37
1150 Mlt	15.21	51.90	0.70	0.21	6.02	15.36	0.03	9.29	1.24	99.96
1150 Mlt	14.98	51.42	0.70	0.22	5.99	15.59	0.03	9.13	1.16	99.23
1150 Mlt	14.88	51.12	0.68	0.23	6.15	15.44	0.00	9.19	1.26	98.97
1150 Met	0.00	0.05	0.00	0.06	0.02	109.47	17.01	0.06	0.00	98.58
1150 Chr	24.99	0.16	0.89	39.98	8.26	24.65	0.06	0.06	0.00	99.05
1150 Chr	23.80	0.50	0.92	40.25	8.07	24.98	0.03	0.15	0.00	98.69
1200 Ol	0.03	36.91	0.00	0.42	31.42	31.31	0.06	0.24	0.00	100.41
1200 Ol	0.03	36.98	0.02	0.40	30.88	31.83	0.07	0.25	0.00	100.46
1200 Ol	0.04	36.99	0.00	0.40	31.34	31.10	0.10	0.20	0.00	100.16
1200 Px	1.46	54.19	0.11	0.92	22.85	19.47	0.01	1.22	0.00	100.23
1200 Px	1.52	54.84	0.10	0.89	23.63	19.60	0.04	1.21	0.00	101.83
1200 Px	1.24	54.01	0.09	0.86	23.67	19.60	0.01	1.13	0.00	100.62
1200 Mlt	11.53	51.50	0.57	0.44	7.53	20.50	0.00	7.41	0.67	100.18
1200 Mlt	11.52	49.98	0.60	0.40	7.43	21.21	0.00	7.59	0.63	99.36
1200 Mlt	11.55	50.70	0.61	0.40	7.35	20.91	0.04	7.50	0.68	99.73
1200 Chr	18.82	0.19	0.94	45.64	6.80	26.31	0.13	0.03	0.00	98.86
1200 Chr	18.42	0.15	0.95	46.48	6.77	26.25	0.03	0.08	0.00	99.15
1200 Met	0.01	0.14	0.01	0.87	0.28	98.14	27.80	0.04	0.00	99.00
1250 Ol	0.06	37.09	0.01	0.39	31.76	30.83	0.07	0.21	0.00	100.42
1250 Ol	0.06	36.94	0.00	0.41	30.80	30.98	0.03	0.20	0.00	99.42
1250 Ol	0.08	36.98	0.02	0.42	31.18	31.28	0.03	0.20	0.00	100.18
1250 Mlt	10.50	47.33	0.56	0.52	7.63	25.57	0.05	6.87	0.23	99.25
1250 Mlt	9.98	47.88	0.53	0.47	8.82	25.02	0.05	6.37	0.29	99.41
1250 Mlt	9.96	48.80	0.51	0.44	8.89	24.50	0.02	6.38	0.25	99.76
1250 Met	0.00	0.08	0.00	0.05	0.05	101.18	25.62	0.05	0.00	98.92

H -Na	Al2O3	SiO2	TiO2	Cr2O3	MgO	MnO	FeO	NiO	CaO	TOTAL
1050 Ol	0.01	38.38	0.02	0.23	35.95	0.22	25.49	0.03	0.15	100.48
1050 Ol	0.01	37.72	0.05	0.20	35.37	0.16	25.53	0.00	0.20	99.24
1050 Ol	0.01	38.28	0.04	0.23	35.22	0.20	25.77	0.03	0.20	99.97
1050 Px	0.56	57.06	0.04	0.51	30.97	0.21	12.30	0.05	0.45	102.15
1050 Px	0.37	56.65	0.03	0.54	30.00	0.15	12.61	0.04	0.50	100.90
1050 Px	0.50	56.43	0.09	0.20	29.46	0.21	13.28	0.09	0.90	101.16
1050 Px	1.71	55.26	0.08	0.94	27.32	0.17	15.24	0.00	1.11	101.84
1050 Plg	31.98	44.17	0.40	2.63	1.39	0.05	2.94	0.04	15.98	99.58
1050 Plg	29.86	50.04	0.08	0.03	0.96	0.02	1.85	0.05	17.26	100.15
1050 Plg	26.43	49.50	0.30	0.13	5.64	0.05	4.55	0.04	14.55	101.20
1050 Plg	28.72	50.80	0.12	0.04	2.39	0.06	1.92	0.05	16.65	100.75
1050 Met	0.00	0.06	0.02	0.07	0.03	0.03	117.51	9.88	0.06	99.28
1050 Chr	10.49	3.62	8.59	31.64	8.17	0.24	29.74	0.04	0.24	92.76
1100 Ol	0.01	37.30	0.04	0.20	31.87	0.16	29.00	0.13	0.25	98.96
1100 Ol	0.01	36.68	0.02	0.24	33.88	0.17	28.69	0.04	0.24	99.97
1100 Ol	0.09	38.11	0.07	0.22	33.82	0.17	30.04	0.09	0.34	102.94
1100 Px	1.01	55.07	0.08	0.88	26.99	0.12	16.03	0.01	0.59	100.77
1100 Px	0.94	54.21	0.05	0.80	24.94	0.11	15.84	0.00	0.67	97.56
1100 Px	1.61	54.20	0.12	1.06	25.16	0.15	17.40	0.09	0.99	100.77
1100 Px	0.81	56.33	0.06	0.80	28.57	0.12	15.30	0.05	0.55	102.59
1100 Px	1.31	54.48	0.11	1.00	25.68	0.19	17.01	0.12	0.89	100.79
1100 Plg	33.10	44.09	0.01	0.02	2.50	0.01	2.22	0.03	17.60	99.58
1100 Plg	34.13	43.53	0.05	0.03	0.40	0.00	1.45	0.03	18.10	97.73
1100 Plg	35.55	44.83	0.04	0.01	0.31	0.01	1.39	0.00	18.24	100.38
1100 Plg	0.00	0.05	0.00	0.10	0.00	0.00	117.18	12.76	0.02	130.11
1100 Met	0.00	0.06	0.01	0.03	0.01	0.00	112.94	13.18	0.03	98.22

H -Na	Al_2O_3	SiO_2	TiO_2	Cr_2O_3	MgO	MnO	FeO	NiO	CaO	TOTAL
1150 Ol	0.06	37.64	0.01	0.22	32.69	0.19	29.97	0.00	0.27	101.06
1150 Ol	0.04	37.23	0.01	0.19	32.89	0.18	30.48	0.04	0.22	101.28
1150 Ol	0.07	37.63	0.00	0.24	33.01	0.19	29.80	0.04	0.22	101.18
1150 Px	1.72	53.76	0.07	1.14	24.41	0.16	18.18	0.00	0.93	100.39
1150 Px	1.35	54.04	0.08	1.08	25.01	0.15	17.95	0.00	0.73	100.39
1150 Px	1.50	53.91	0.09	0.99	24.87	0.16	18.56	0.01	0.86	100.96
1150 Mlt	15.43	48.77	0.63	0.22	7.01	0.12	17.50	0.00	9.79	99.47
1150 Mlt	15.20	48.11	0.68	0.27	7.00	0.18	18.16	0.04	9.79	99.42
1150 Mlt	15.37	48.32	0.65	0.23	6.87	0.14	17.46	0.00	10.07	99.10
1150 Met	0.01	0.03	0.00	0.09	0.03	0.00	110.94	15.75	0.03	98.74
1150 Chr	35.71	0.12	0.50	30.52	9.89	0.19	23.47	0.06	0.09	100.55
1200 Ol	0.04	37.55	0.03	0.38	32.15	0.15	30.27	0.07	0.20	100.85
1200 Ol	0.03	37.51	0.00	0.38	32.33	0.18	30.21	0.04	0.21	100.90
1200 Ol	0.05	37.63	0.01	0.38	32.21	0.13	30.86	0.04	0.23	101.54
1200 Px	1.67	54.02	0.09	0.96	24.14	0.19	19.23	0.01	0.94	101.24
1200 Px	1.43	54.33	0.07	0.93	24.29	0.18	19.20	0.12	0.84	101.38
1200 Px	1.32	54.10	0.11	0.89	24.29	0.18	18.90	0.00	1.15	100.92
1200 Chr	22.76	0.17	0.62	44.06	7.44	0.15	24.81	0.05	0.13	100.21
1200 Mlt	12.73	48.23	0.58	0.48	7.49	0.19	20.87	0.00	8.40	98.99
1200 Mlt	13.94	49.80	0.65	0.44	5.36	0.17	20.12	0.02	9.45	99.95
1200 Mlt	12.41	48.01	0.58	0.44	7.41	0.15	21.30	0.01	8.42	98.72
1200 Met	0.01	0.05	0.00	0.03	0.01	0.00	107.45	19.77	0.00	99.11
1250 Ol	0.07	37.14	0.02	0.46	32.05	0.17	30.78	0.01	0.18	100.88
1250 Ol	0.06	37.13	0.01	0.46	32.07	0.15	30.54	0.03	0.22	100.68
1250 Ol	0.06	37.03	0.03	0.46	31.92	0.12	30.45	0.00	0.18	100.25
1250 Mlt	8.39	40.71	0.36	0.51	8.16	0.12	33.91	1.87	5.24	99.27
1250 Mlt	10.15	48.00	0.46	0.59	8.43	0.16	24.90	0.14	6.38	99.21
1250 Mlt	9.71	48.21	0.44	0.55	9.32	0.15	24.42	0.00	6.15	98.94
1250 Mlt	9.88	49.29	0.44	0.57	8.24	0.16	24.52	0.02	6.46	99.58
1250 Met	0.02	0.07	0.03	0.05	0.01	0.02	100.51	27.67	0.03	100.00